MULTI-DECADAL SURFACE TEMPERATURE TRENDS IN EAST ANTARCTICA INFERRED FROM BOREHOLE FIRN TEMPERATURE MEASUREMENTS AND GEOPHYSICAL INVERSE METHODS

by

Atsuhiro Muto
B.Sc., Chiba University, Japan, 2003
M.Sc., Chiba University, Japan, 2005

A thesis submitted to the
Faculty of the Graduate School of the
University of Colorado in partial fulfillment
of the requirement for the degree of
Doctor of Philosophy
Department of Geography
2010

This thesis entitled:

Multi-decadal surface temperature trends in East Antarctica inferred from borehole firn temperature measurements and geophysical inverse methods

written by Atsuhiro Muto

has been approved for the Department of Geography by

_____

Konrad Steffen

_____

Theodore A. Scambos

Date _____

The final copy of this thesis has been examined by the signatories, and we find that both the content and the form meet acceptable presentation standards of scholarly work in the above mentioned discipline.

Muto, Atsuhiro (Ph.D., Geography)

Multi-decadal surface temperature trends in East Antarctica inferred from borehole firn temperature measurements and geophysical inverse methods

Thesis directed by Professor Konrad Steffen

Abstract

The climate trend of the Antarctic interior remains unclear relative to the rest of the globe because of a lack of long-term weather records. Recent studies by other authors utilizing sparse available records, satellite data, and models have estimated a significant warming trend in the near-surface air temperature in West Antarctica and weak and poorly constrained warming trend in East Antarctica for the past 50 years. In this dissertation, firn thermal profiling was used to detect multi-decadal surface temperature trends in the interior of East Antarctica where few previous records of any kind exist. The surface temperature inversion from firn temperature profiles provides a climate reconstruction independent of firn chemistry, sparse weather data, satellite data, or ice cores, and therefore may be used in conjunction with these data sources for corroboration of climate trends over the large ice sheets.

During the Norwegian-U.S. IPY Scientific Traverse of East Antarctica, in the austral summers of 2007-08 and 2008-09, thermal-profiling telemetry units were installed at five locations. Each unit consists of 16 PRTs (Platinum Resistance Thermometers) distributed in a back-filled borehole of 80 to 90 m deep. The accuracy of the temperature measurement is 0.03 K.

Geophysical inverse methods (linearized and Monte Carlo inversion) were applied to one full year of data collected from three units installed near the ice divide in the Dome Fuji/ Pole of Inaccessibility region and one on Recovery Lake B, situated >500 km south to

south-west of and >1000 m lower in altitude than sites near the ice divide. Three sites near the ice divide indicate that the mean surface temperatures have increased approximately 1 to 1.5 K within the past ~50 years although the onset and the duration of this warming vary by site. On the other hand, slight cooling to no change was detected at the Recovery Lake B site. Although uncertainties remain due to limitations of the method, these results raise the possibility of an interesting recent climate pattern in East Antarctica; significant warming trend near the ice divide and cooling to no change off the divide.

Acknowledgements

This dissertation could not have been made possible without support of many individuals and organizations. First and foremost, I am most grateful to my co-advisors, Prof. Konrad Steffen and Dr. Ted Scambos. In particular, I can not thank Ted enough for his inspiration, encouragement and exemplary passion for science, as well as providing the financial support for all my time spent here at the Univ. of Colorado. This research started with his idea and he has been patient with me taking so long to develop and finally presenting it as this dissertation. I've had a pleasure of interacting with my committee members, Peter Blanken, Gary Clow, Glen Liston and Tad Pfeffer. Their helpful comments and insights are greatly appreciated. I am also grateful for Prof. Fumihiko Nishio of Chiba University, Japan, for preparing me to go in to the doctoral study.

As you will see, participating in the Norwegian-U.S. IPY Scientific Traverse of East Antarctica was a vital part of this research. For this, I am indebted to the agencies, organizations and people for provided support in conducting the traverse; the U.S. National Science Foundation, the Norwegian Research Council, the Norsk Polarinstitutt (Norwegian Polar Institute), Raytheon Polar Services Company, the 109th Air National Guard, Antarctic Logistics Center International, and members of the traverse teams of 2007-08 and 2008-09. I would like to express my sincere gratitude to Frank Urban and Mark Ohms of the USGS for their help in calibrating temperature sensors. I would also like to thank Cindy Brekke and Ted DeMaria who helped me tremendously in purchasing the field equipment.

I would like to thank a few individuals at the NSIDC. Dr. Drew Slater spent so much time with me in my office, discussing mostly science but also about skiing and biking gears. The 'Whiteboard Sessions' with him were essential in checking my knowledge on all aspects of my research. Terry Haran, Jennifer Bohlander and Rob Bauer of the 'Team Scambos'

helped me with processing remote sensing imagery and gathering historical data. I was able to stay healthy and relatively fit by going on bike rides with Andy Barrett, Dave Kindig, and Drew.

My fellow graduate students, John Adler (now Dr. Adler), Liam Colgan, Dan McGrath, Thomas Phillips (now Dr. Phillips) and Kevin Sampson, have kept me distracted enough and hold my sanity during tough times. Thanks, guys. I will cherish the friendship with you for a long, long time to come.

My parents allowed me to pursue almost whatever I wanted to do all my life. I would like to express my gratitude and apology to them for being a little rogue by a Japanese standard. I promise to start giving back to the society with the education you provided me with. Lastly but not least, I could not have done it all without the love and support of my partner, Kathryn Urbanowicz. Thank you so much, Kat.

This dissertation research was financially supported by the U.S. National Science Foundation grant OPP-0538103 to the University of Colorado.

Table of contents

Chapter

List of Tables

Table

List of figures

Figure

Chapter 1

ANTARCTIC CLIMATE CHANGE

1.1 Global climate change and cryopshere

Warming of the climate system is unequivocal, as is now evident from observations of increases in global average air and ocean temperatures, widespread increases in melting of snow and ice and rising global average sea level (IPCC, 2007). The linear trend of global mean surface temperature between 1906 and 2005 is 0.74 ± 0.18 K, or 0.07 ± 0.02 K per decade. The rate of warming over the last 50 years is 0.13 ± 0.03 K per decade which is almost double that over the last 100 years (Trenberth et al., 2007). IPCC (2007) concluded that most of the observed increase in global average temperature since the mid-20th century is very likely (90% probability) due to the observed increase in anthropogenic greenhouse gas concentrations. Observed global mean temperature changes over the 20th century are only reproduced by GCMs (General Circulation Models) when they include anthropogenic forcings, and they fail to do so when they exclude anthropogenic forcings (Hegerl et al., 2007).

In light of the growing evidence of anthropogenic global warming, polar regions have seen increased attention from the scientific community, policymakers, and the public. This is largely because the increase in global temperature is expected to be amplified near the poles, and this is observed for the Arctic (e.g. Manabe et al., 1992; Serreze and Francis, 2006; Meehl et al., 2007). Warming of the polar regions has important societal implications because of potential sea level rise due to fresh water discharge from glaciers, ice caps and ice sheets that could jeopardize more than 200 million people living in coastal areas around the world

and $1 trillion worth of assets located less than 1-m elevation above current sea level (Stearn, 2007). The estimate of the rate of global average sea level rise was 3.1 ± 0.7 mm per year from 1993 to 2003; 57% is due to the thermal expansion of the oceans and changes in their salinity (steric sea level contribution) with decreases in glaciers and ice caps contributing about 28% and losses from the polar ice sheets contributing the remainder (IPCC, 2007). Although the Greenland and Antarctic Ice Sheets contribute only ~15% to the total global sea level rise, a series of satellite observations reveals a recent acceleration in their rate of mass loss (e.g. Shepherd and Wingham, 2007; Rignot et al., 2008; Velicogna, 2009). Because of this, the land-ice contribution to the global sea level rise has nearly doubled to ~60% since about 2003 and now has surpassed the steric sea level contribution (Nicholls and Cazenave, 2010; Cazenave 2010).

1.2 Antarctic climate change - surface temperature

It is important to understand how surface temperatures across the Antarctic Ice Sheet have changed in recent decades as an input, or validation, for climate models, and because of the impact that temperature changes may have on accumulation and net mass balance (e.g. Schneider et al., 2006) and, consequently, sea level changes (e.g. Giovinetto et al. 1990; van Lipzig et al., 2002). The model-estimated responses to these external factors are detectable in the 20th-century climate globally and in each individual continent except Antarctica, where there are insufficient observations (Hegerl et al., 2007).

One of the regions on earth with the largest warming rate is the Antarctic Peninsula (van Lipzig et al., 2009) where the surface temperature has risen at a rate of 0.37 ± 0.16 K per decade over the past 50 years (Vaughan et al., 2003). Dramatic changes occurring to ice shelves in the Peninsula area are considered to be a direct result of the strong warming. Over

the last few decades, particularly within the last 10 to 20 years, several ice shelves in the region have rapidly retreated or collapsed (e.g. Cook and Vaughan, 2009). Although ice shelf retreats and collapses have been attributed to both atmospheric and oceanic effects (e.g. Shepherd et al., 2003; Vieli et al., 2007), a key process observed during the collapses of ice shelves appears to be the extensive formation of melt ponds on the surface. Surface melt in the Antarctic Peninsula has high positive correlation with the summer near-surface air temperature (e.g. Torinesi et al., 2003; Liu et al., 2006) and it is probable, in the case of Larsen B Ice Shelf at least, that percolating meltwater has propagated fracturing of the ice shelf, which eventually resulted in its disintegration (Scambos et al., 2004).

Beyond the Antarctic Peninsula, the climate trend is far less clear. Sparse distribution of long-term weather station records over the ice sheet, as can be seen in Figure 1.1, together with the large inter-annual to decadal variability of Antarctic climate, make it difficult to establish surface temperature trends (Turner et al., 2005; 2007). In particular, the interior of Antarctica remains almost a complete blank, both spatially and temporally. Over a region the size of the United States and Mexico combined, just two occupied station records exist with multi-decadal continuous measurements: Amundsen-Scott Station at the South Pole (hereinafter South Pole) and Vostok. Although Automated Weather Stations (AWSs) are now widely scattered around the Antarctic interior, their use began only in the 1980s, and most stations in the high polar plateau were deployed in the 1990s and 2000s. There are also frequent gaps in the data when systems fail during the winter (Turner et al., 2009).

Despite the modest amount of available weather records, a number of investigations have examined near-surface temperature trends for Antarctica as a whole, using the two stations in the ice sheet interior and the several coastal records (e.g. Raper et al., 1984; Jacka and Budd, 1991, 1998; Jones, 1995, Comiso, 2000, Turner et al, 2005). The general findings of these studies are that, contrary to the Peninsula region, high variability and small cooling

and warming trends seem to be the rule. Of the 19 stations examined by Turner et al. (2005), 11 showed warming trends in their annual data and 7 showed cooling (Turner et al., 2007). Moreover, in some cases, warming and cooling trends coexist within the same general region. For example, trends at Mawson (69°S, 39.59°E) and Davis (67.68°S, 46.13°E), both located on the coast near Amery Ice Shelf and separated by about 650 km, were -0.11 ± 0.23 K and +0.03 ± 0.35 K per decade, respectively, for 1955-2000. As can be seen in the large uncertainty estimates, above trends are not statistically significant, a fact that is true for all trends at stations except those in the Antarctic Peninsula, and Novolazarevskaya and South Pole which show trends of +0.25 ± 0.27 K and -0.17 ± 0.21 K per decade, respectively, statistically significant at 10% level. The low levels of statistical significance in mean annual temperature trends partly stem from different seasonal trends seen at most of stations analyzed. Outside of the Peninsula, only Novolazarevskaya and South Pole have the same sign in trends for all seasons with positive trends for the former and negative trends for the latter.

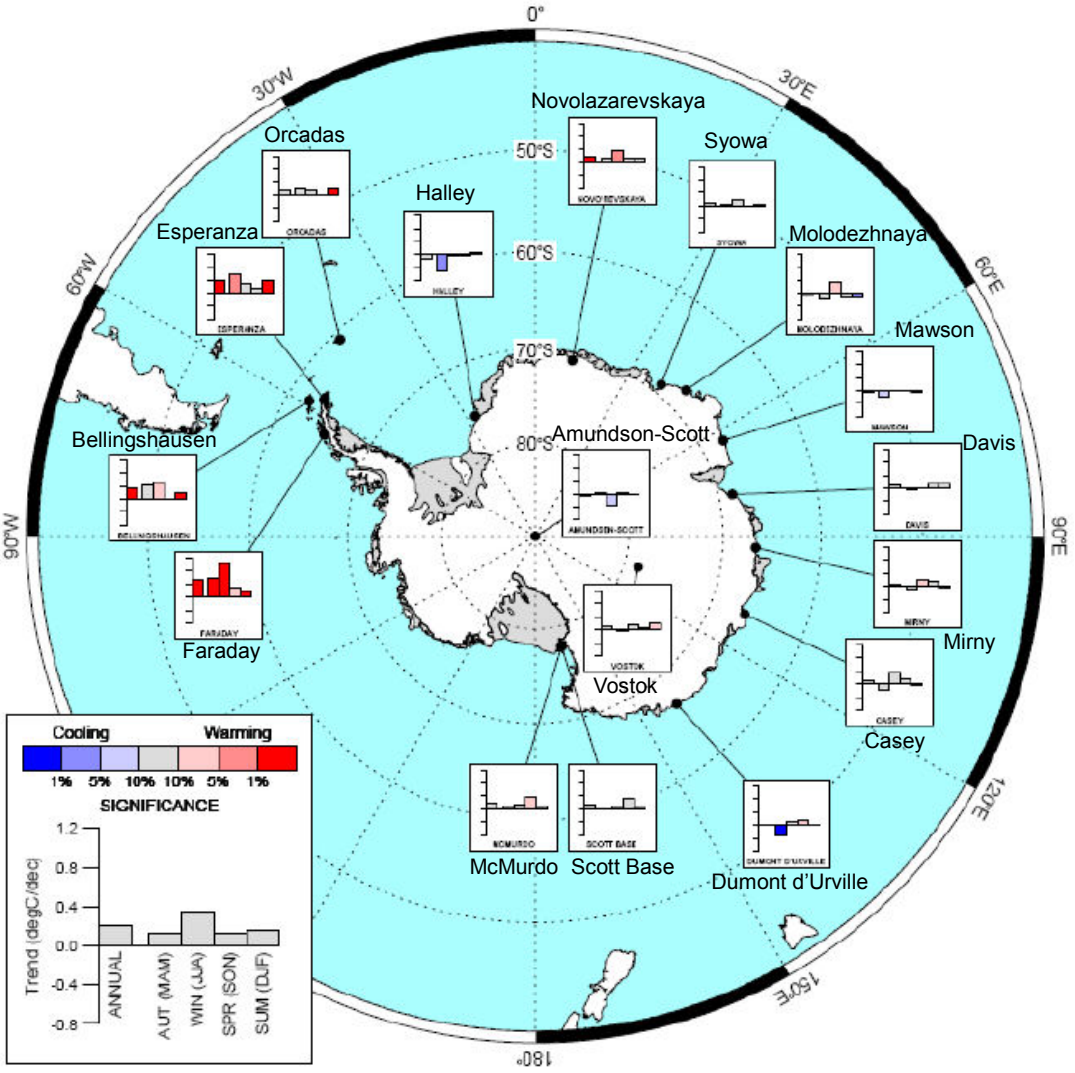

Figure 1.1. Annual and seasonal temperature trends at Antarctic stations with long records. From Turner et al. (2009).

Another key feature of surface temperature trends at continental locations is the large variability in inter-decadal time scale. Comiso (2000) analyzed trends for 45-year (1953-98) and 20-year (1979-98) period separately and found that 9 out of 12 stations changed the sign between the two different periods. Turner et al. (2005) conducted a similar analysis but using 1961-90 and 1971-2000 time periods for 10 stations where there are enough records in both time periods. Out of those 10 stations, 5 exhibited the change in sign. It is worth noting that

all trends that showed a sign-change in Turner et al. (2005) did so from positive trends in 1961-90 and negative trends in 1971-2000 (Table 1.1). This is suggestive of the warming trends in earlier decades of records and conversely a general cooling in the last few decades of the 20th century.

Table 1.1. Trends in the annual mean surface temperature during two time periods. Stations with trends calculated for both time periods were selected. Stations that showed a sign change are in bold. Adapted from Turner et al. (2005).

	Temperature trend (K per decade)	
station	1961-90	1971-2000
Novolazarevskaya	+0.41 ± 0.38	+0.10 ± 0.41
Molodehnaya	**+0.16 ± 0.45**	**-0.26 ± 0.49**
Mawson	-0.13 ± 0.52	-0.15 ± 0.43
Mirny	**+0.16 ± 0.45**	**-0.26 ± 0.49**
Vostok	**+0.11 ± 0.53**	**-0.31 ± 0.51**
Casey	**+0.37 ± 0.54**	**-0.37 ± 0.57**
Dumont Durville	**+0.14 ± 0.41**	**-0.33 ± 0.46**
Scott Base	+0.32 ± 0.67	+0.05 ± 0.60
Halley	**+0.41 ± 0.65**	**-0.56 ± 0.71**
South Pole	-0.06 ± 0.39	-0.36 ± 0.46

When no *in situ* measurements are available, infrared (IR) imagery from polar-orbiting satellites can provide useful data with high spatial coverage, although there are limitations. The length of record is limited to the period since the early 1980s. Data are only gained under clear-sky conditions and IR imagery provides the surface skin temperature which can differ significantly from the standard 2-m height near-surface temperature. Nevertheless, there is a good agreement in trends of surface skin temperatures and near-surface temperatures recorded at stations across Antarctica (Comiso, 2000). Kwok and Comiso (2002) provide a map of surface skin temperature trends derived from monthly averaged satellite IR records

for the period 1982-1998. Much of East Antarctica showed moderate cooling between 0.0 to -0.1 K per decade while a region around South Pole and Victoria Land and eastern Wilkes Land cooled at a higher rate of up to 0.2 K per decade. Regions of relatively strong warming (0.1 to 0.2 K per decade) are identified in the area corresponding to the high-altitude ridge in East Antarctica and parts of West Antarctica.

Surface temperature reconstruction from firn and ice cores is another method used often to fill gaps of *in situ* observations and to extend temporal lengths. Isotopic ratios of oxygen and hydrogen in polar ice cores have been used extensively as the temperature proxies (Schneider et al., 2005). Based on the 'stacking' of 5 ice cores around Antarctica, Schneider et al. (2006) concluded that there is a significant interannual to decadal scale variability but the continent-wide temperature increase of about 0.2 K over the last 200 years can be identified. One must keep in mind, however, that ice cores used by Schneider et al. (2006) are scattered with a highly non-uniform pattern, with three cores from the interior of West Antarctica and only two cores from East Antarctica. Although a high correlation between the temperatures variations derived from a composite of 8 station records and the ice core stack have been demonstrated, this study also suffers from the lack of records from the interior of both West and East Antarctica.

Recently, new techniques have been applied to spatially extrapolate from sparse station records, using either distance-weighting or spatial covariance of the surface temperature variability, to reconstruct a fuller picture of continent-wide surface temperature trends. Positive trends for much of Antarctica were found for periods 1958-2002 by Chapman and Walsh (2007) and for 1960-2005 by Monaghan et al. (2008), but these were again determined to be not statistically significant. The shift in the trends from slight warming to cooling suggested by Turner et al. (2005) was shown to extend for the majority of Antarctic continent by both Chapman and Walsh (2007) and Monaghan et al. (2008). Through three different

time periods analyzed (1960-2002, 1970-2002 and 1980-2002), trends over the continental Antarctica became gradually more negative as time progressed (Monaghan et al., 2008). The 1960-2002 period shows both positive and negative trends scattered over the continent whereas negative trend of around -0.1 to -0.5 K per decade covers most of the continent which increases to between -0.4 to -1.0 K per decade in 1980-2002 period (Monaghan et al., 2008). Chapman et al. (2007) shows the same general features of wide spread negative trend but with smaller magnitudes than Monaghan et al. (2008). The trend takes a sharp turn from negative to positive in the most recent decade of 1992-2005, displaying +0.5 to 1.0 K per decade. While varying signs and magnitudes of the trends are seen for much of the continent in the different analyses, both reconstructions of Chapman et al. (2007) and Monaghan et al. (2008) indicate the Antarctic Peninsula has warmed at ~0.5 K per decade throughout the time periods examined.

Steig et al. (2009), examining slightly longer period than Chapman and Walsh (2007) and Monaghan et al. (2008), found that the warming trend extends beyond the Peninsula area and over the entire Antarctic Ice Sheet with the rate of 0.12 ± 0.07 K between 1957 and 2006. In particular, a larger magnitude of warming (0.17 ± 0.06 K per decade) was seen in West Antarctica (Figure 1.2b). The West Antarctic warming trend is concurrent with the shorter-period record compiled from AWS and satellite microwave observations at Siple Station (1.1 ± 0.07 K) and Byrd Station (0.45 ± 1.3 K) for 1979-1997 although the magnitudes of the interpolated trends in the Steig et al. (2009) study are smaller. During a shorter time period of 1967-2000, the warming trend is confined to West Antarctica with the majority of East Antarctica showing cooling but not statistically significant (Figure 1.3b). Cooling of the majority of the continent between 1960s to 1990s was indicated by Chapman and Walsh (2007) and Monaghan et al. (2008). However, Steig et al. (2009) points out that the trends in West Antarctica shown by Monaghan et al. (2008) become positive and statistically

significant when the complete set of AWS data from West Antarctica is included. In general, the three reconstructions agree on the trends seen in Antarctica for the past 40 to 50 years.

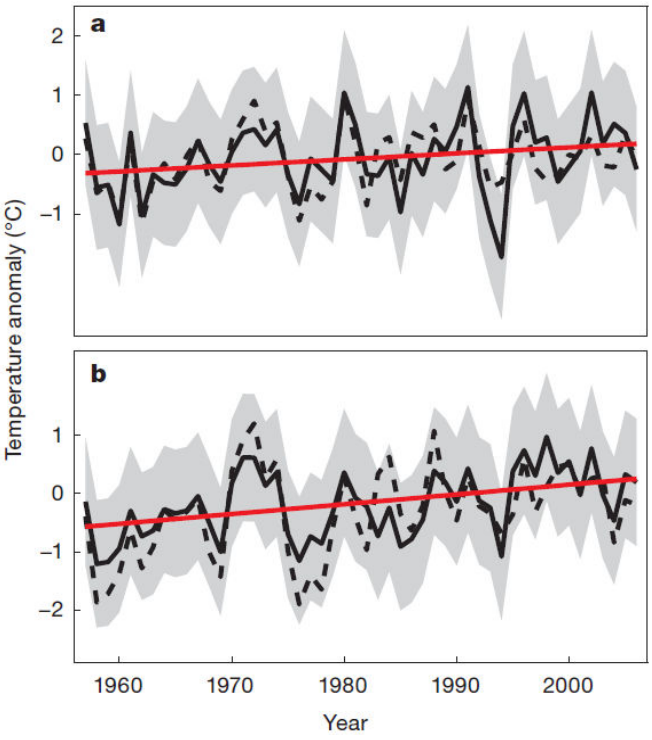

Figure 1.2. Reconstructed mean annual temperature anomaly for **a**, East Antarctica and **b**, West Antarctica for 1957-2006. Solid black lines show results from reconstruction using infrared satellite data (T_{IR}), averaged over all grid points for each region. Dashed lines show the average of reconstructed AWS data in each region. Straight red lines show average trends of the T_{IR} reconstruction. From Steig et al. (2009).

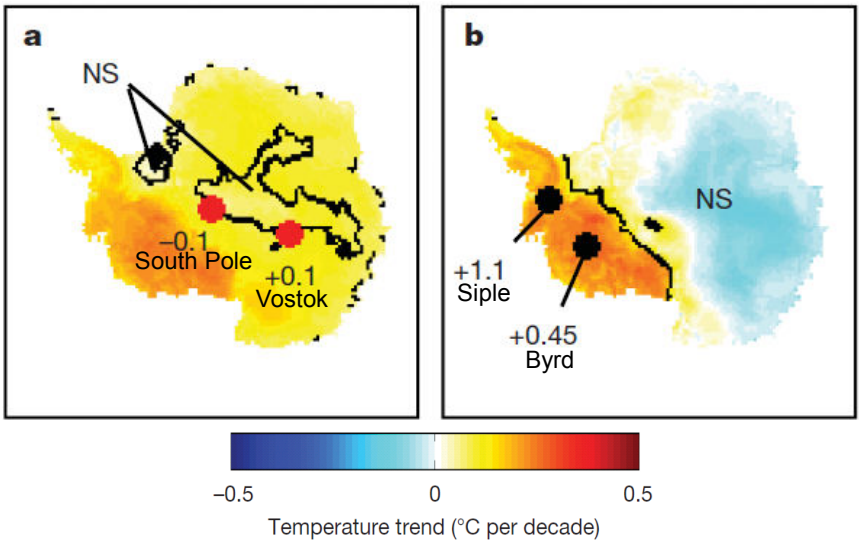

Figure 1.3. a, mean annual trends for 1957-2006 and **b**, for 1967-2000. NS refers to areas of below-significance trends at the 95% confidence level. Red circles and adjacent numbers in **a** show the locations of the South Pole and Vostok weather stations and their respective trends (°C per decade) during the same time interval as the reconstruction (1957–2006). Black circles in **b** show the locations of Siple and Byrd Stations, and the adjacent numbers show their respective trends for 1979–1997. From Steig et al. (2009).

1.3 Antarctic climate change - atmospheric pressure and circulations

Contrary to the surface temperature, mean annual Mean Sea Level Pressure (MSLP) shows decrease in all parts of Antarctica including the Antarctic Peninsula, with Orcadas, located in the South Orkney Islands, being the only station with no overall trend (Turner et al., 2005; 2007, Figure 1.4). Trends at stations located on the coast of East Antarctica tend to show stronger negative trends compared to the rest of the continent and the Peninsula, varying between -0.48 hPa to -0.98 hPa per decade with two stations (Novolazarevskaya and Mawson) showing trends statistically significant at the 5% level and two more (Molodezhnaya and Mirny) at the 1% level. In the Peninsula region, trends are generally smaller and statistically not significant, with the trend at Bellingshausen being the strongest

(-0.57 hPa per decade).

Most variability in the MSLP trend is seen in the spring when 8 out of 17 stations have positive trends. Summer shows uniformly negative trends, with 8 stations having the largest negative trends in this season. A few positive trends are found in fall (4 stations) and winter (3 stations). In fall, the four stations with positive trends are in the Peninsula which is the only indication of spatial pattern seen in MSLP.

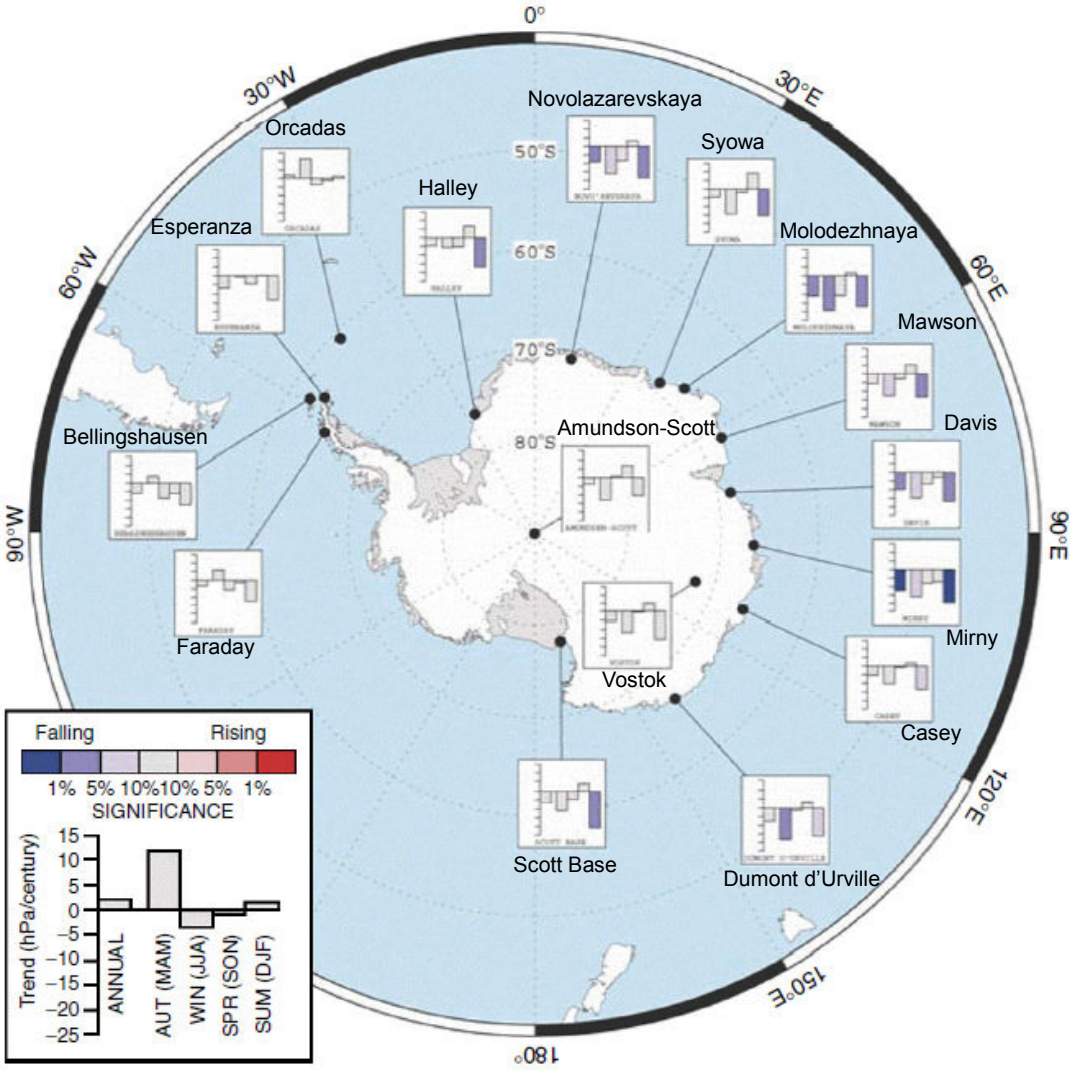

Figure 1.4. Annual and seasonal mean sea level pressure trends at Antarctic stations with long records. From Turner et al. (2007).

The major mode of atmospheric variability across the mid and high latitude of Southern Hemisphere is the Southern Annular Mode (SAM), also known as the AAO or the high-latitude mode (e.g. Turner et al., 2007; Mayewski et al., 2009). The SAM is revealed as the leading empirical orthogonal function (EOF) in many atmospheric fields, including surface pressure, geopotential heights and zonal wind (Marshall, 2003) and typically describes ~35% of total Southern Hemisphere climate variability (Marshall, 2007). When pressures are higher (lower) than average over the Southern Hemisphere mid-latitudes (Antarctica), the SAM is said to be in its positive (negative) phase (Turner et al., 2009). Changes in the SAM over time can be traced using the SAM index which can be defined in several ways. For example, Thompson and Wallace (2000) define it as the EOF-1 of 850 hPa geopotential height for 20-90°S and Gong and Wang (1999) use the difference between the zonally averaged MSLP between 40°S and 65°S. Marshall (2003) defined the SAM index as the difference in MSLP at stations located at around 40°S and 65°S, realizing that using reanalysis data such as National Center for Environmental Prediction-National Center for Atmospheric Research (NCEP-NCAR) Reanalysis and European Center for Medium-Range Weather Forecasts 40-year Re-Analysis (ERA-40) can be problematic due to inaccuracies before the assimilation of satellite data started in late 1970s (e.g. Bromwich and Fogt, 2004; Hines et al. 2000).

Based on the SAM index of Marshall (2003), the general trend of the SAM on annual basis is toward the positive phase from the mid-1960s to the end of the 20th century, as can be seen in Figure 1.5. Investigations by seasons reveal significant positive trends during summer and fall (e.g. Thompson et al., 2000; Marshall 2007; Jones et al, 2009), summarized in Table 1.2. Furthermore, the changes in the SAM observed over the last 50 years are greater than any changes in the SAM found in a 1000-year control run of the Hadley Center climate model (Turner et al., 2007).

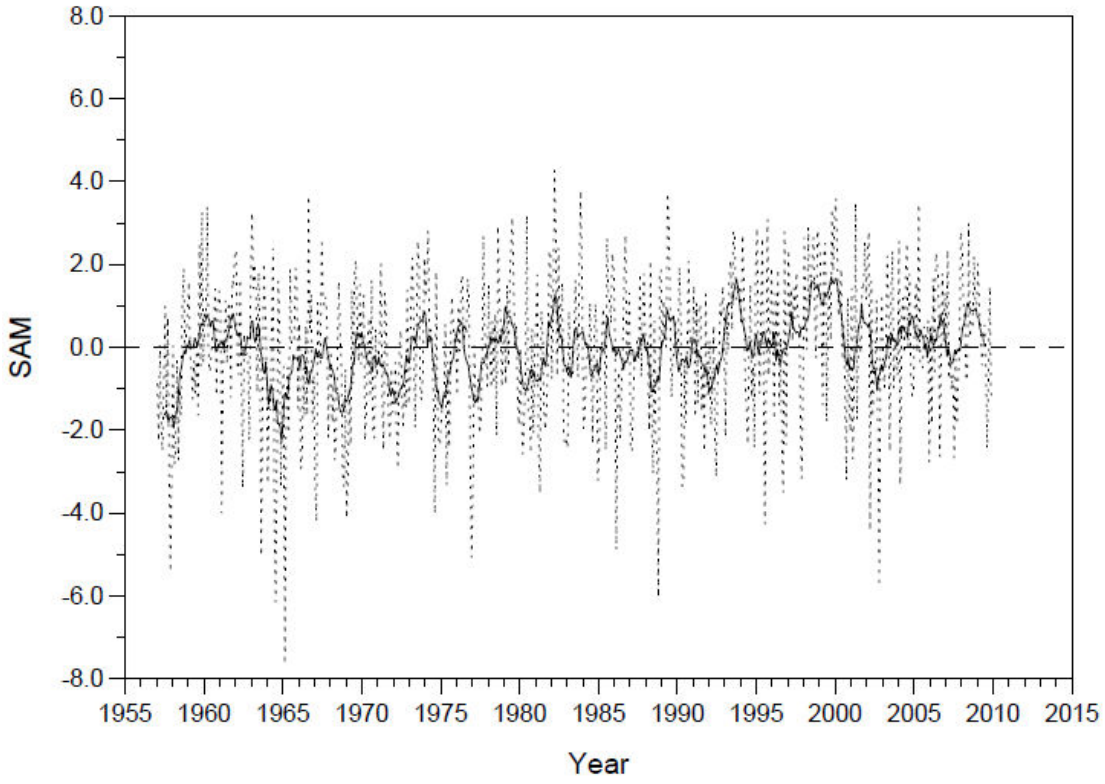

Figure 1.5. Annual (solid line) and monthly (dotted line) SAM index of Marshall (2003) from 1957 to 2009. From the website *An observation-based Southern Hemisphere Annular Mode Index* (http://www.antarctica.ac.uk/met/gjma/sam.html)

Table 1.2. Annual and seasonal trends in the SAM from 1957 to 2004. Units are per decade. Significant trends are shown by asterisks; ** <1% and * <5%. Annual trend is calculated from data obtained from Marshall (2010). Seasonal trends are from Marshall (2007).

Annual	Fall (MAM)	Winter (JJA)	Spring (SON)	Summer (DJF)
+0.53 ± 0.35**	+0.45 ± 0.27**	+0.21 ± 0.38	+0.00 ± 0.35	+0.45 ± 0.39*

One of the characteristics of atmospheric circulation associated with SAM is the north-south seesaw of atmospheric mass between high and mid-latitudes. This is shown by

the regression of SAM index on 850 hPa geopotential height where over Antarctica south of around 60-65°S shows negative anomaly and to the north is the positive anomaly (e.g. Thompson and Wallace, 2000). Another feature again shown through regression of the SAM index is the zonal mean geostrophic wind, where positive anomaly in the upper troposphere zonal wind around 60°S is associated with positive SAM index (Thompson and Wallace, 2000). This indicates that the positive SAM index is congruent with a strengthening of the polar vortex. The SAM-polar vortex relationship has been shown to extend to the near-surface level by Thompson and Solomon (2002), through the linear regression of the near-surface (925 hPa level) wind onto the SAM index. The study found a high contribution of SAM index in the trend of wind speed in December to May over the period of 1979-2000. van den Broeke and van Lipzig (2004) corroborates this result through the use of a regional atmospheric climate model and showed a high positive correlation between the SAM index and the westerly component of 10 m wind speeds off the coast of Antarctica.

1.4 Attribution of Antarctic temperature changes

All studies to date lack an extensive record from the vast interior of Antarctica. South Pole and Vostok are the only two meteorological stations operating since the IGY (1957-58). Therefore caution needs to be taken in discussing the temperature changes and their causes in Antarctica as a whole. However, 'warming Peninsula, little change to some cooling across the rest of the continent (Turner et al., 2009)' is the statement that has been made broadly speaking, particularly of the last few decades of the 20th century. For the MSLP, results point to the general negative trend over the continent. These two have been linked to suggest the overriding mechanism of climate change seen in Antarctica as a whole, which is the broad-scale atmospheric circulation. A number of studies showed that SAM index have been

increasing since 1950s but particularly since the mid-1960s, as mentioned in section 1.3. These results are in accordance with decreasing trends of MSLP found at Antarctic stations. Juxtaposed with the temperature trends in some seasons between the 1960s and 1990s, results are suggestive of relationship between the SAM and temperature changes across Antarctica.

Thompson and Solomon (2002) examined the contribution of SAM to changes in near-surface temperatures for 1969-2000. SAM has been noticed to increase most during summer months (December to May) although all seasons do show positive trends (Marshall, 2007). For summer months, when the temperature records from stations are regressed on the SAM index, negative contribution of SAM to temperature is revealed at continental stations and positive contribution at stations on the Peninsula (Thompson and Solomon, 2002). More detailed investigation considering four separate seasons and a longer time period (1957-2004) shows that in each season there are positive correlations between the SAM and near-surface temperatures in the Peninsula region and negative correlations across East Antarctica (Marshall, 2007). Seasonal regression coefficients between the SAM and temperatures are generally largest in fall and winter, and smallest in spring and summer (Marshall, 2007). Fall has the largest trend in the SAM (Table 1.2) and Marshall (2007) further finds that the resultant temperature changes are greater in fall than other seasons at most stations. Kwok and Comiso (2002) found similar results using the satellite infrared surface temperature mapping.

A modelling study of van den Broeke and van Lipzig (2004) indicates that a positive shift in SAM can reduce the near-surface air temperature on the Antarctic ice sheet. They regressed the SAM index onto the results of regional climate model (RACMO/ANT1) forced by ERA-15 data. Significant cooling over much of the continent and warming over Antarctic Peninsula was again indicated to be associated with positive SAM index (Figure 4c of ven den Broeke and van Lipzig, 2004). They also performed the regression on the 10 m wind and

found a reduction in the wind speed over the continent and an increase in a belt just off of the continent around 60°S (van den Broeke and van Lipzig, 2004). Strengthening of polar vortex with positive index of SAM is a robust feature found in other studies as mentioned already, and the result of van den Broeke and van Lipzig (2004) show that this feature may extend down through the troposphere to the surface. Strengthening of polar vortex has been attributed as a main cause in reduced surface temperatures through the suppressed meridional heat transport from the mid-latitudes. Also, van den Broeke and van Lipzig (2004) suggest the possibility of less turbulent heat flux to the surface because of reduced 10m wind speed as the cause of the drop in surface temperatures.

The strong warming trends for the Antarctic Peninsula may also be connected to changes in the extent of sea ice cover. Temperatures at Faraday are linked closely to the sea ice extent over the eastern Bellingshausen Sea with winters of extensive (little) sea ice being cold (warm) (Turner and others, 2007). Such associations are suggested using sea ice extent derived from passive microwave satellite data. Some studies report that the sea ice extent in the Bellingshausen Sea in the pre-satellite era was further to north (King and Harangozo, 1998; Kukla and Gavin, 1981; both quoted in Turner and others, 2007), indicating the reduction in the sea ice extent in recent decades.

The shift in SAM index towards a positive phase between 1960s and 1990s is driven in part, at least between December and May for 1968-2000 period, by the depletion of stratospheric ozone in spring time which has led to the negative trend in geopotential height and temperature anomalies through the lower stratosphere to troposphere over the Antarctic continent (Thompson and Solomon, 2002). There is a downward trend in the total column ozone observed at Halley station for 1968-98 (Thompson and Solomon, 2002) and various data sets including satellite and station data (Bodeker, 2005). Breakdown of polar vortex at the end of winter that is normally caused by the rise of the sun after the polar darkness has

been delayed because of less photochemical reaction in the lower stratosphere which increases the temperature at that level (~100-200 hPa geopotential height). The resulting heat transport towards Antarctica through meridional circulation and temperature increase occurs later in summer.

Modelling studies since Thompson and Solomon (2002) also show responses in the SAM index and Antarctic near-surface temperatures, both from ozone depletion and from greenhouse gas increases as well (Arblaster and Meehl, 2006; Gillet et al., 2008). Cooling in East Antarctica for 1969-2000, although confined to fall (March, April and May) and not statistically significant, was also found by Steig et al. (2009).

1.5 Summary

Climate trends in Antarctica and their causes have long been ambiguous due to the sparse distribution of long-term weather records. Recent studies utilizing spatial extrapolation of available observational records and climate models have advanced our knowledge of the nature of the surface temperature changes in Antarctica. However, an outstanding issue is the lack of long-term observations on which these techniques rely from the vast interior and climate trends there still remain unclear. This is depicted well by Steig et al. (2009) who showed a large region of no statistical significance in the surface temperature trend (Figure 1.3). Also, the most recent and comprehensive modelling study of anthropogenic influence on temperature changes (Gillett et al., 2008) is still limited to 5° by 5° grid cells containing stations with available observational records. In order to better understand the Antarctic-wide climate changes, continuation of weather observations and improved models, as well as more *in situ* sources of the climate reconstruction are needed.

Chapter 2

OBJECTIVES

Antarctica is a pervasive component in the global climate system yet changes occurring there are poorly understood compared to other continents. For example, anthropogenic influence has been detected in every continent except Antarctica which has insufficient observational coverage to make an assessment (Hegerl et al., 2007). Despite recent developments in spatial extrapolation techniques and climate models, an uncertainty still exists for the interior Antarctic surface temperature trend because of the lack of long-term observations.

Climate reconstructions from proxies of air temperature, such as stable water isotopes in firn and ice cores, are widely used when *in situ* or co-temporal observations are not available. However, the direct interpretation of isotopic variations as local temperature variations is generally recognized as overly simplistic (e.g., Noone, 2008). Isotopic compositions are fundamentally coupled with large-scale circulation patterns (e.g. Jouzel et al., 1997; Cole et al., 1999; Werner and Heimann, 2002) and isotope records at different locations are not always influenced by the same set of climate variables (e.g. Noone and Simmonds, 2002; Werner and Heimann, 2002). Examination of isotopes in ice cores from West Antarctica and the surface temperature derived from satellite infrared measurements by Schneider et al. (2005) reveal that while the correlation between the two on seasonal time scale is high, the correlation coefficients are not statistically significant inter-annually and the Antarctic-wide temperature index (the first principle component of the Antarctic-wide temperature variations) explains at least as much variance in local isotopic records as the site temperature. Caution needs to be taken in interpreting isotopic records particularly in low accumulation

areas that occupy most of the Antarctic interior (e.g. Vaughan et al., 1999; Arthern et al., 2006) because of the observed bias in timing and condition of snow deposition at for example Dome Fuji in East Antarctica (Fujita and Abe, 2006).

A source of the surface temperature reconstruction that is independent of any other techniques such as spatial interpolation/extrapolation and proxies in ice cores is the use of subsurface temperatures measured in boreholes and geophysical inverse methods. The variation of temperature in the ice sheet with depth is known to provide information about past changes in the surface temperature (Paterson, 1994). Several studies (e.g. Dahl-Jensen and Johnsen, 1986; MacAyeal et al., 1991; Dahl-Jensen et al., 1998; Barrett et al, 2009) have demonstrated the value of this technique, often referred to as 'borehole paleothermometry' (MacAyeal et al., 1991). Commonly, temperature profiles measured over several hundred to a few thousand meters are obtained after deep ice core drillings, using fluid-filled holes that are allowed to re-equilibrate for at least one year. These records have been used to reconstruct the past temperature history extending over the Holocene and sometimes into the last glacial period. For example, Dahl-Jensen and Johnsen (1986) reconstructed the surface temperature record for the past 115,000 years at Dye 3 in Greenland (65°N, 44°W) using the measured temperature profile of the 2037 m borehole. Climatic events of the recent past such as the A.D. 1920-50 maximum, the little ice age (A.D. 1400-1900) and the medieval warm period (A.D. 900-1400) were well represented in the reconstructed history. Dahl-Jensen et al. (1998) then applied a Monte Carlo inverse method to the temperature profile at Greenland Ice Core Project (GRIP) site and resolved similar events.

However, the wealth of information about past climate gained from temperature measurements in fluid-filled deep boreholes comes at the expense of fairly intensive field logistics. Boreholes need to remain fluid-filled for at least more than one year before measurements for thermal re-equilibration. To evaluate and subsequently correct for the

drilling disturbance within a few years of borehole completion, temperatures should be measured annually with a precision of at least 1 mK level (Clow et al., 1996). Besides, deep boreholes are sparsely located, and require at least three to four years to drill.

During the recent International Polar Year (March 2007 to March 2009), the 'Norwegian-U.S. IPY Scientific Traverse of East Antarctica' (hereinafter referred to as 'the Traverse') was conducted. This was a collaborative project by polar scientists from Norway and the United States, comprising two overland traverses in Dronning Maud Land, one departing from the Norwegian research station Troll near the coast and ending near South Pole, and a return traverse taking a different route (see Figures 2.1 and 2.2). These traverses went through areas that were rarely visited in the past. A series of ice cores that are 80 to 90 m long were drilled during traverses to investigate century- to millennial-scale variations in accumulation rate and atmospheric chemistry. This project presented a unique opportunity to carry out borehole paleothermometry in the interior of East Antarctica, and provide an important piece of climate information regarding the continent.

Objectives of this dissertation are:

1) To determine the surface temperature trends in the interior of East Antarctica for the past several decades;
2) In order to achieve 1), develop an automated firn temperature profiling system that is easily deployed in a traverse set-up, and make high-precision firn temperature profile measurements and;
3) Apply geophysical inverse methods to the obtained firn temperature profiles.

Reconstruction of decadal to century scale surface temperature history from intermediate depth (~100-300 m) temperature measurements has been done before in Antarctica (Nicholls

and Paren, 1993; Barret et al., 2009). However, there are only a couple of examples, limited to the area near the Antarctic Peninsula where climatic conditions such as the accumulation rate and the mean annual temperature which control the subsurface thermal signature, as will be discussed in later chapters, are very different from those of the interior of East Antarctica. Therefore, the borehole paleothermometry using firn temperature profiles in the high Antarctic plateau is demonstrated by this dissertation for the first time. Also, past temperature measurement systems used were different from the one developed in this dissertation, which has a capability for long-term firn temperature monitoring without revisits. There are a number of intermediate depth boreholes made from ice core drillings in the recent years, resulting from projects such as the International Trans-Antarctic Scientific Expeditions (ITASE), and these numbers are expected to increase in the future as the scientific community continue to gather ice cores in an attempt to better understand the past changes of the Antarctic Ice Sheet. The borehole paleothermometry technique developed here could be applied to existing and future boreholes and potentially be an important measurement protocol that provides a source of climate reconstruction that is independent and additional to existing ones.

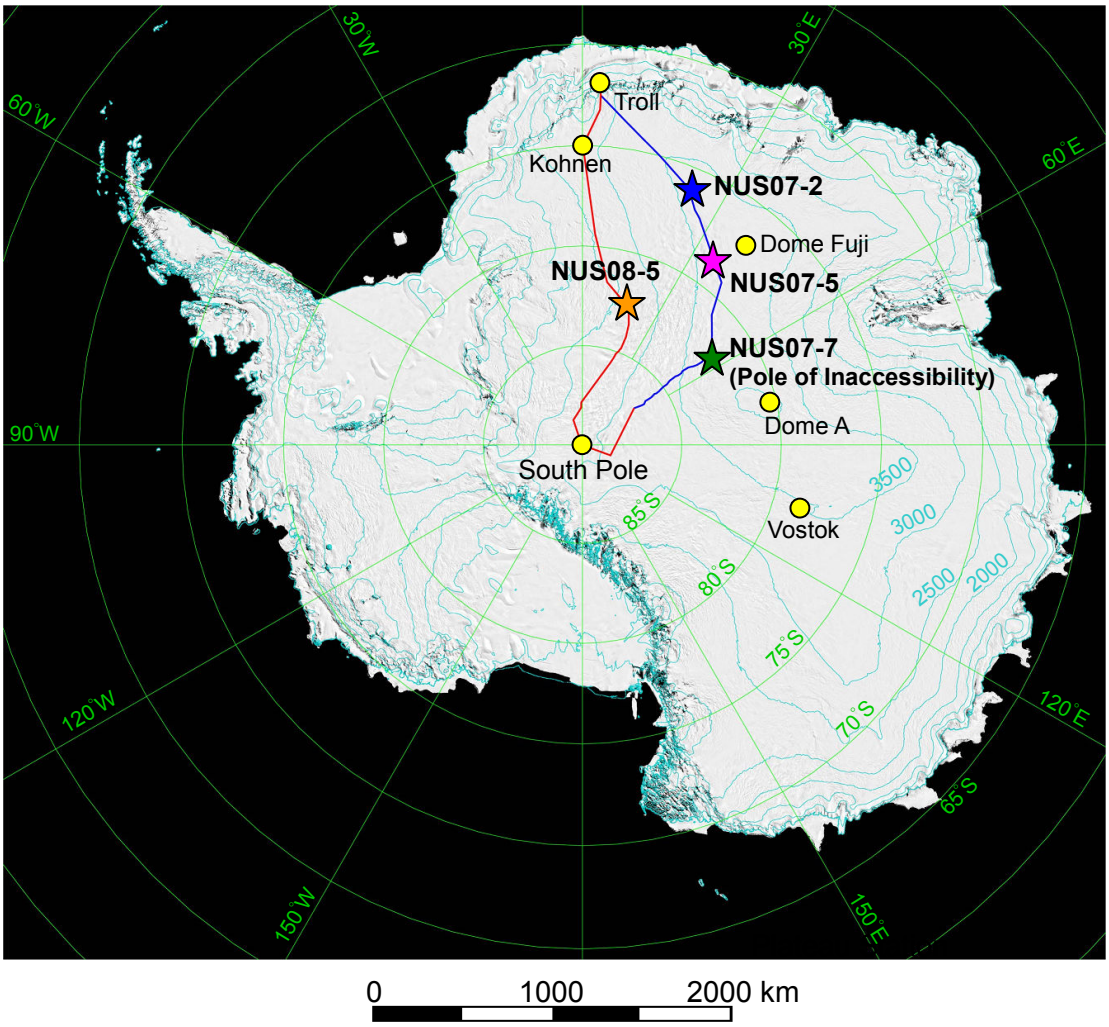

Figure 2.1. A map of Antarctica with the study sites indicated by stars and the Traverse routes of the 2007-08 season (blue solid line) and the 2008-09 season (red solid line). The figure was created from MOA (MODIS Mosiac of Antarctica; Haran et al., 2006) by laying the elevation contours from the Digital Elevation Model of Bamber et al. (2009).

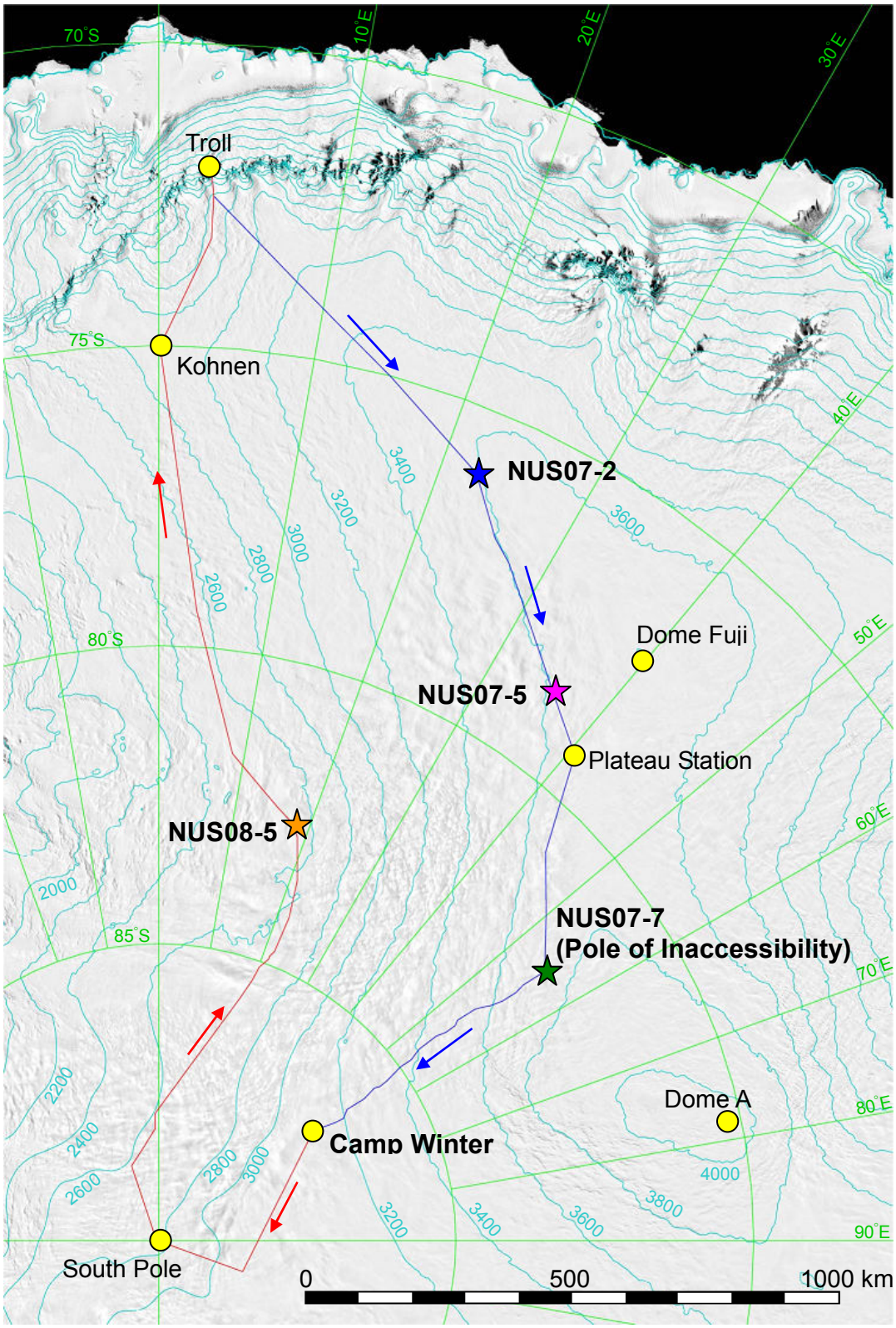

Figure 2.2. A map of Dronning Maud Land sector of East Antarctica with study sites indicated by stars and the Traverse routes of the 2007-08 season (blue solid line) and the 2008-09 season (red solid line). Contour lines are altitudes in meters.

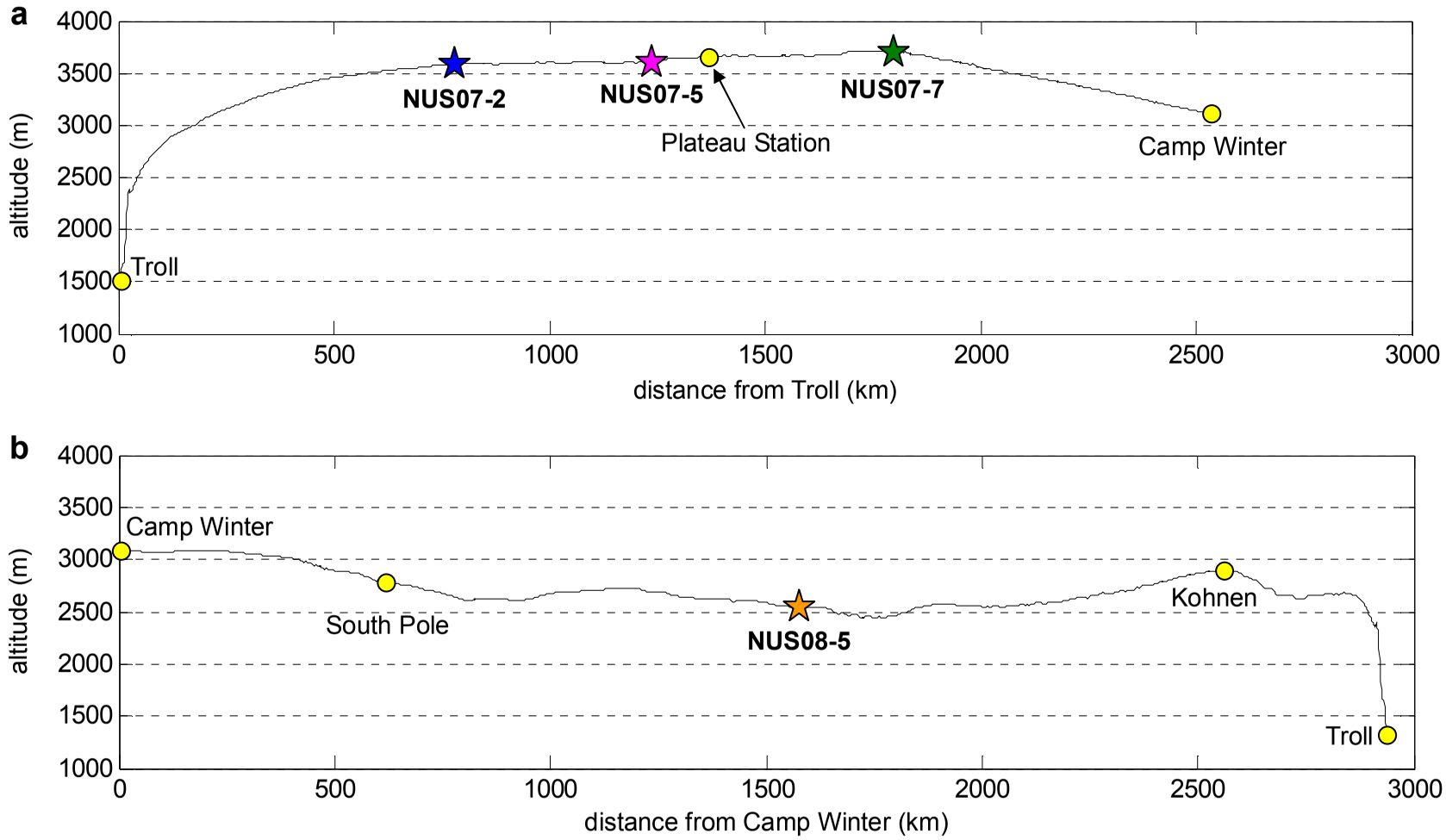

Figure 2.3. Altitude profiles along the Traverse routes of **a**. 2007-08 and **b**. 2008-09 seasons.

Chapter 3

FIRN TEMPERATURE MEASUREMENT

3.1 Temperature measurement system, Automated Temperature Profiling Unit (ATPU)

3.1.1 Data logger and multiplexer

Temperature is measured with the CR1000 data logger and the AM16/32 multiplexer, both manufactured by Campbell Scientific Inc. AM16/32 is a channel-switching device that is attached to the CR1000 data logger to increase the number of channels on the logger. A maximum of 16 sensors can be attached to one AM16/32 for measurements using a 4-wire half-bridge circuit (details on this circuit and how measurements are made are in section 3.2). 4-wire half-bridge circuit is completed with a 4WPB1K terminal input module, also manufactured by Campbell Scientific Inc,. that is attached to CR1000. 4WPB1K has a reference 1000-Ω reference and 10k-Ω current-reducing resistors built in. ARGOS transmitter (Campbell Scientific Inc. ST-20) is also connected to each CR1000 to facilitate transmission of data through satellite telemetry system.

Each data logger is powered by 3 photovoltaic sealed lead-acid batteries (Sun Xtender PVX-1040T, 12V, 104 Ah). Batteries are connected to two 20-W solar panels (BP Solar SUX20).

3.1.2 Temperature sensor and conductor cable

Temperature sensors used in this study were 1000-Ω PRTs, HEL-705-U-0-12-00, manufactured by Honeywell Sensing and Control Inc. Each PRTs consist of partially supported platinum wires in a ceramic housing and two lead wires. To increase the

ruggedness, each PRT was put inside an Aluminum tube (2 cm long, 4 mm diameter) using an epoxy adhesive (Scotch-Weld DP-270). The thermal conductivity of Aluminum is 241 and 236 $Wm^{-1}K^{-1}$ at -100 and 0°C, respectively (Kaye and Laby, 1995) which is several orders of magnitude larger than that of firn and ice. The thermal conductivity of DP-270 is 0.175 $Wm^{-1}K^{-1}$ at 45°C (manufacturer's specification) although its value for the typical temperature range in this research (-60 to -40°C) could not be found. Since the thermal conductivity of a similar epoxy resin is 0.18 and 0.22 $Wm^{-1}K^{-1}$ at -80 and 27°C, respectively (Garrett and Rosenberg, 1974), it is assumed that the thermal conductivity of DP-270 at -60 to -40°C range is not significantly different than the value at 45°C. Those values are comparable to the thermal conductivity of firn or ice. Therefore, the use of Aluminum and epoxy are considered to have negligible effect on temperature measurements.

Each PRT sensor was soldered to 4-wire conductor cables of lengths corresponding to depths of deployment. One pair of wires was soldered to each lead of a PRT. Conductor cables consist of 4 wires that are each covered with extruded ethylene-tetrafluorethylene (ETFE) copolymer. All 4 wires are then shielded by tin-coated copper and jacketed with ETFE.

PRTs were calibrated at the USGS thermal calibration facility at USGS in Lakewood, Colorado, following the procedures described in Clow (2008). However, Clow (2008) describes the calibration procedure for thermistors rather than PRTs used in this research. Therefore, a resistance readout instrument specific for PRTs (Hart Scientific PRT module 2567) was used.

Briefly, a 25.5-Ω quartz-sheath standard platinum resistance thermometer (SPRT) was used as the calibration standard. SPRT and PRTs (upto 4 at a time) were placed in a copper equilibration block in a bath filled with temperature-controlled Halocarbon fluid. The temperature in the bath is varied from -60°C to 10°C, recording the temperature of the SPRT

and the resistance of PRTs at calibration points that were places at 5°C intervals. Least squares method is applied to the calibration data (SPRT temperature vs. sensor resistance) to obtain coefficients a_i in equation (3.4) that define a resistance-temperature conversion curve unique to each PRT.

3.2 Resistance (temperature) measurement

Firn temperatures were obtained by measuring resistances of Platinum Resistance Thermometers (PRTs), then converting resistances to temperatures. Temperature can be measured with PRTs because of the resistance-temperature relationship of Platinum i.e. the resistance of Platinum increases with increasing temperature.

Ohm's law suggests that resistance (R) can be measured by measuring the voltage (V) across a resistor and the current (I) through it, and then calculating the ratio $R = V/I$ (Nicholas and White, 2001). However, electrical current is not easily measured or defined except in terms of a voltage and resistance. In practice, resistance is often measured by comparison with another resistance to eliminate the need to know or measure the current directly (Nicholas and White, 2001). If a reference resistor of a known resistance is used, the resistance of the sensor (R_s) can be found from the ratio of the voltage of the sensor (V_s) and the reference resistor (V_{ref}), then converted to resistance using voltage-resistance relationship. R_s is given by

$$R_s = \frac{V_s}{V_{ref}} R_{ref} , \tag{3.1}$$

where R_{ref} is the resistance of the reference resistor.

In this research, resistance was measured with a 4-wire half-bridge circuit, by applying

a voltage across a PRT sensor and a reference resistor (Figure 3.1). In this circuit, one pair of lead wires carries the current and the voltage drop across the PRT (V_s) is measured using another pair. Measurement of V_s is not affected by the resistance of lead wires since there is no current passing through the pair of wires measuring V_s. Excitation voltage (V_{ex}) is passed through a 10k-Ω current-limiting resistor which reduces the effect of noise in the excitation voltage and keeps the current low so self-heating of PRT sensor is kept to a minimum.

The CR1000 data logger determines the ratio V_s/V_{ref} internally. However, V_s is needed for evaluating the uncertainty of resistance measurements (details in section 3.5.2). In order to obtain V_s, the current I running through the whole circuit is needed. Using the Ohms Law, I is given by,

$$I = \frac{V_{ex}}{R_K + R_{ref} + R_s}, \tag{3.2}$$

where V_{ex} is the excitation voltage and R_K is the resistance of the current-limiting resistor. V_s is then,

$$V_s = R_s I. \tag{3.3}$$

The resistance of the reference resistor (R_{ref}) is nominally 1000 Ω at 0°C. However, there is a small amount of drift in R_{ref} with temperature which needs to be corrected for when calculating R_s using equation (3.1). Although the manufacturer of the reference resistor provides a temperature coefficient that could be used for this correction, reference resistors were calibrated in order to better characterize the temperature drift. Reference resistors were calibrated in the same manner as for PRTs to obtain an equation to calculate R_{ref} at different temperatures which is a cubic polynomial in the form,

$$R_{ref} = a_1 + a_2 T_{ref} + a_3 {T_{ref}}^2 + a_4 {T_{ref}}^3, \quad (3.4)$$

where a_i are coefficients unique to each reference resistor determined by the calibration and T_{ref} is the temperature of the reference resistor. The temperature measured by a thermistor inside a CR1000 data logger (panel temperature) is used as T_{ref}.

Before the resistances are converted to temperatures, they need to be corrected for a systematic error. A source of a systematic error in the resistance measurements by ATPUs is self-heating of PRTs. Because a current is passed through the sensor to measure its resistances, sensor dissipates heat, which in turn causes the temperature of the sensor to increase (Nicholas and White, 2001). The resistance increase due to self-heating (δR_h) can be modeled as,

$$\delta R_h = \frac{\alpha_T (I R_s)^2}{P_d}, \quad (3.5)$$

where α_T is the sensor's temperature coefficient and P_d is the sensor's power dissipation constant (Clow, 2008). α_T and P_d of PRTs used in this research are 0.0375 Ω/K and 15 mW/K maximum, respectively, given by the manufacturer. Self-heating causes the resistance increase by 6.810×10^{-3} Ω at -60°C and 0.011 Ω at 0°C, which in temperatures are 1.7 mK and 2.9 mK, respectively.

Another potential source of a systematic error, as discussed in Clow (2008), is the leakage current along the circuit which can be caused for example by imperfect insulation of conductor cables or soldered joints. The potential for the leakage current was not realized until after ATPUs were deployed in the field and the amount of the leakage for each sensor-conductor cable assembly was not measured. To rectify this problem, leakage

measurements were made on 8 sensor-cable assemblies of the same design that were intended for Automated Met-Ice-Geophysics Observation Stations (AMIGOS, see Scambos et al. 2008 for details) planned to be deployed in the Antarctic Peninsula. Those 8 assemblies were made in October and November of 2009 then sent to Antarctica. However, they returned to Boulder, CO, in June 2010 since some AMIGOS were not deployed as planned. It is considered that they experienced rough handling and large temperature variations during the transportation, similar to ones deployed as parts of ATPUs have experienced. Therefore, the leakage current of those 8 assemblies are estimated to be of the same level as the ones on ATPUs. The leakage current measured on the 8 sensor-conductor cable assemblies were 0. For this reason, it is considered that there is no leakage on sensor-conductor cable assemblies on ATPUs.

To obtain a temperature (T) from a resistance measurement (R_s), a conversion equation derived from the calibration of the sensor is used. Resistance-temperature conversion equation is also a cubic polynomial in the form,

$$T = a_1 + a_2 R_s + a_3 R_s^{\,2} + a_4 R_s^{\,3}. \tag{3.6}$$

Coefficients a_1, a_2, a_3 and a_4 which are unique for each PRT sensor are determined by the sensor calibration.

The resolution of resistance measurements depend on the resolution of the voltage change that can be detected by the data logger. The manufacturer's specification states that the resolution of the voltage detection by CR1000 is 33.3 μV which corresponds to 0.157 Ω and 0.160 Ω at -60°C and 0°C, respectively, in resistance. However, the smallest resistance change that was actually measured was much better at 0.018 Ω in the temperature range most commonly measured by ATPUs (-56°C to -45°C). Although reasons for the discrepancy between the manufacturer's specification and the actual measurements are not clearly known,

the empirical value (0.018 Ω) will be adopted as the resolution of the resistance measurement.

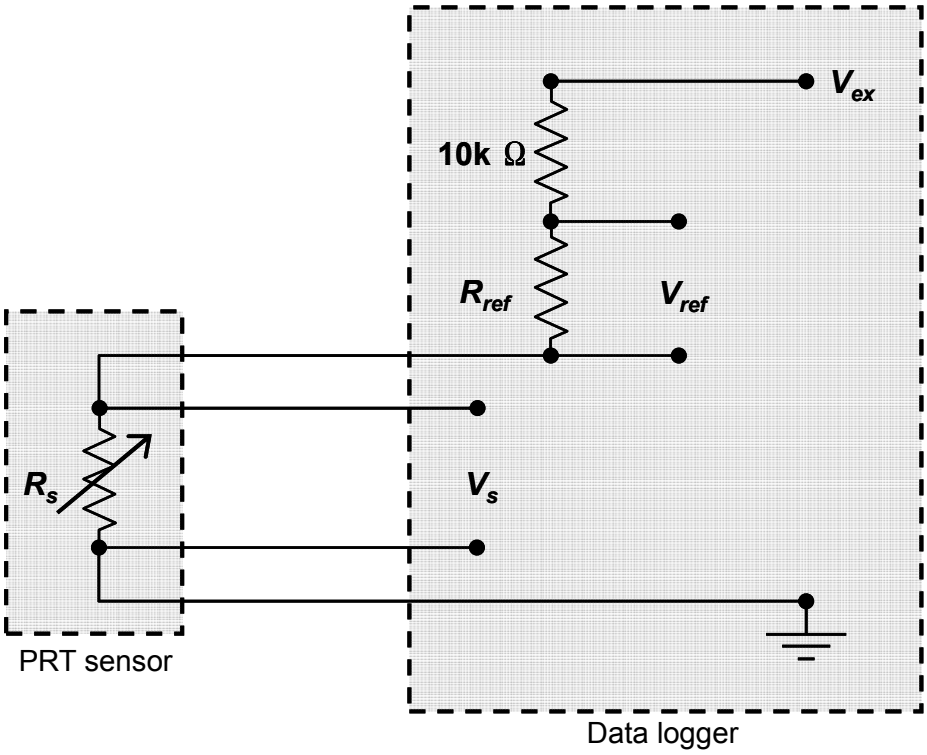

Figure 3.1. Schematic diagram of the 4-wire half-bridge circuit used for resistance measurements. R_s and R_{ref} are resistances of the PRT and the reference resistor, respectively, and V_s and V_{ref} are voltage drops across the PRT and the reference resistor, respectively. V_{ex} is the excitation voltage applied to the whole circuit. 10k Ω denotes the current-limiting resistor. Adapted from Tanner (1990).

3.3 Deployment in the field

Three ATPUs were deployed during the 2007-08 season and 1 ATPU in the 2008-09 season of the Traverse. Figure 3.2 is a schematic diagram of the ATPU deployment. A pit that is 2 m long by 1.5 m wide by 2 m deep (all approximate measurements) was dug directly above the borehole to place a water-tight case that houses the data logger, multiplexer, transmitter and batteries. To avoid thermal disturbances that could be caused by this pit-digging, a separate

hole was drilled by a hand auger 3 m away from the deep hole to place sensors in the top ~3 m.

Conductor cables with PRTs were attached to a steel cable, placing sensors at intervals corresponding to spacing between depths of sensors. Depths of PRTs at NUS07-2, -5 and -7 are 0.15, 0.65, 1.65, 2.65 and 3.15 m in the shallow hole, and 2.5, 3, 5, 10, 16, 24, 32, 40, 55, 70 and 90 m in the deep hole. At NUS08-5, the deepest sensor was placed at 80 m instead of 90 m since the hole did not quite reach 90 m. Bamboo sticks were attached to the top-end of the steel wire for anchoring the cable-wire assembly on top of the borehole. A dumbbell was attached to the bottom-end of the steel wire as a weight so there would be no kinks when hanging in the borehole.

Both deep and shallow boreholes were filled with granulated snow after the sensor-cable assembly was placed to prevent air convection and provide good conduction between sensors and the surrounding firn. To ensure that the deep borehole is in fact filled, temperatures were recorded throughout the period of back-filling process which varied between ~1.3 and 4.5 hours. At every site, sudden changes in temperatures were observed sequentially starting from the bottom-most sensor. Such observations indicate that there were no blockages in the borehole and each PRT sensors were buried. Further details and temperature data recorded during the back-filling are in Appendix A. For the shallow 3-m borehole, back-filling was confirmed by visual observations since the bottom of the borehole was visible and the change in the borehole depth as it was being filled could be tracked visually.

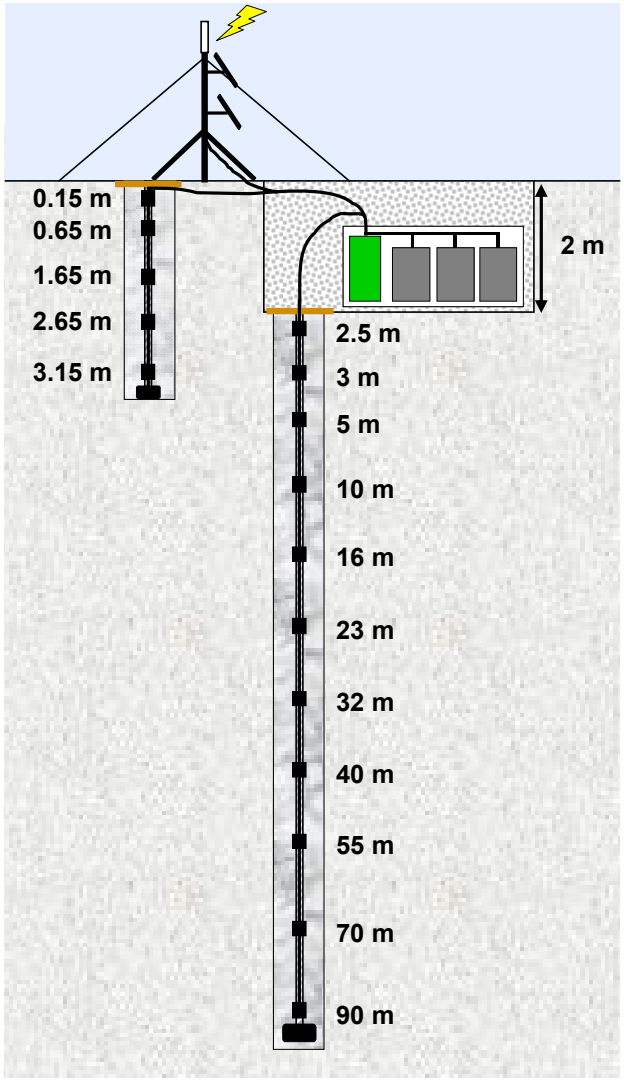

Figure 3.2. Schematic diagram of ATPU. At NUS08-5, the deepest sensor was placed at 80 m instead of 90 m.

3.4 Data retrieval

Resistance and the data logger panel temperature measurements are transmitted via ARGOS satellite telemetry system using the ARGOS transmitter. The use of AROGS system eliminates the need for revisits to study sites that are located in extremely remote areas of

East Antarctica. Data retrieval would be difficult logistically and financially if data are stored at study sites.

Data were first stored in CR1000 with Campbell Scientific 2 byte floating point format. With this format, data values can be between -7999 and 7999 with decimal point located anywhere. In order to store as many digits as possible, each resistance and panel temperature values were divided into two parts; integer and fraction multiplied by 1000. For example, resistance of 835.7892 Ω is stored as 835 and 789.2.

With the ARGOS system, a maximum of 31 bytes of data can be transmitted at one time. This limits the number of data values that can be included in one transmission to 15. Since each resistance measurement and the panel temperature is divided into two parts, and also date and time of the measurement need to be transmitted, not all data can be included in one transmission. In order to overcome this issue, measurement and data transmission are carried out in four separate time-blocks that are cycled through in one hour. This means that measurements of all 16 sensors and panel temperature are made at the start of an hour. Then, data from a set of four sensors along with panel temperature, year, day of year, time (hour and minute) battery voltage and a block ID, are transmitted for 15 minutes. After the first 15 minutes, measurements of 16 sensors and panel temperature are made again. Then, this time, data from a set of four sensors differing from the first 15 minutes together with other data parameters are transmitted for the next 15 minutes. And this is repeated until the next hour. Block ID is a number 1 through 4 that are included in a transmission to identify which set of sensor-data is included in a transmission. Table 3.1 shows data parameters included in each transmission. ST-20 is programmed to transmit every 200 seconds. During the 15-minute interval, the same set of data parameters is being transmitted at 200-second intervals.

Table 3.1. Data parameters included in each transmission blocks. Time under block numbers indicate the time interval in an hour when a particular block is transmitted. A numbers after a dash denote the either the first or the second part of divided data e.g. 10-1 denotes the first part of the value from the sensor at 10 m.

1 00:00 - 00:14	2 00:15 - 00:29	3 00:30 - 00:44	4 00:45-00:59
Year	Year	Year	Year
day of year	day of year	day of year	day of year
hour and minute	hour and minute	hour and minute	hour and minute
Panel temperature-1	Panel temperature-1	Panel temperature-1	Panel temperature-1
panel temperature-2	panel temperature-2	panel temperature-2	panel temperature-2
0.15S-1	3.15S-1	10-1	40-1
0.15S-2	3.15S-2	10-2	40-2
0.65S-1	2.5-1	16-1	55-1
0.65S-2	2.5-2	16-2	55-2
1.65S-1	3-1	24-1	70-1
1.65S-2	3-2	24-2	70-2
2.65S-1	5-1	32-1	90-1
0.15S-1	5-2	32-2	90-2
Block ID (1)	Block ID (2)	Block ID (3)	Block ID (4)
Battery voltage	Battery voltage	Battery voltage	Battery voltage

AROGS telemetry system uses polar orbiting satellites to receive transmission from ARGOS transmitters and relay data to ground receiving stations. Currently, NOAA-15 through to 18 of the National Oceanic and Atmospheric Administration (NOAA), and METOP-A of the European Organization for the Exploration of Meteorological Satellites (Eumesat) carry ARGOS instruments. Those five satellites are polar orbiting. Therefore the data transmitted from each ATPU is frequently received by satellites hence the data retrieval rate from ATPUs is high. The average number of measurements retrieved from each sensor per day for the period of time from which the data are used for analyses (March 1, 2008 to February 28, 2009) is 16.5. However, there are periods of time in late austral winter when data retrieval rate drops significantly, and to 0 in some cases, when the power reserve in the battery is low. No data were retrieved from the ATPU at NUS07-5 for period of August 24 -

September 27, 2008. ATPUs at NUS07-5 and -7, and NUS08-5 transmitted throughout a year.

Firn temperatures obtained at each site by the method described thus far are shown in Figures 3.3-6. For the inversion of surface temperatures to be presented in later chapters, mean temperatures over one year for 5 m and below are used. This is because temperatures measured at depths above 5 m are dominated by seasonal signals that are not the target of this research.

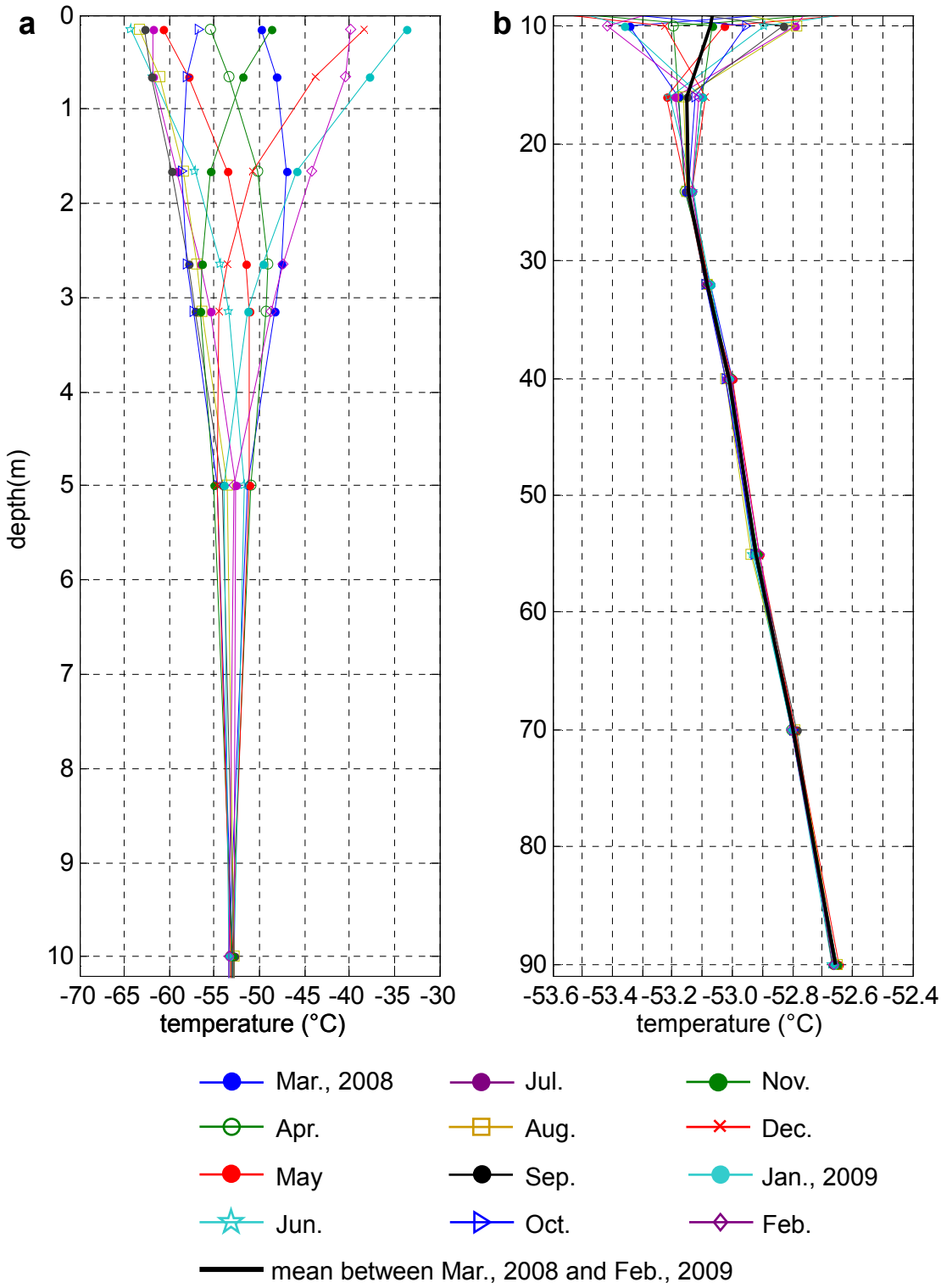

Figure 3.3. Measured firn temperature profiles at NUS07-2 for **a**. top 10 m and **b**. 10 to 90 m. Thick black line in **b** is the mean between March, 2008 and February 2009 which is used in the analyses.

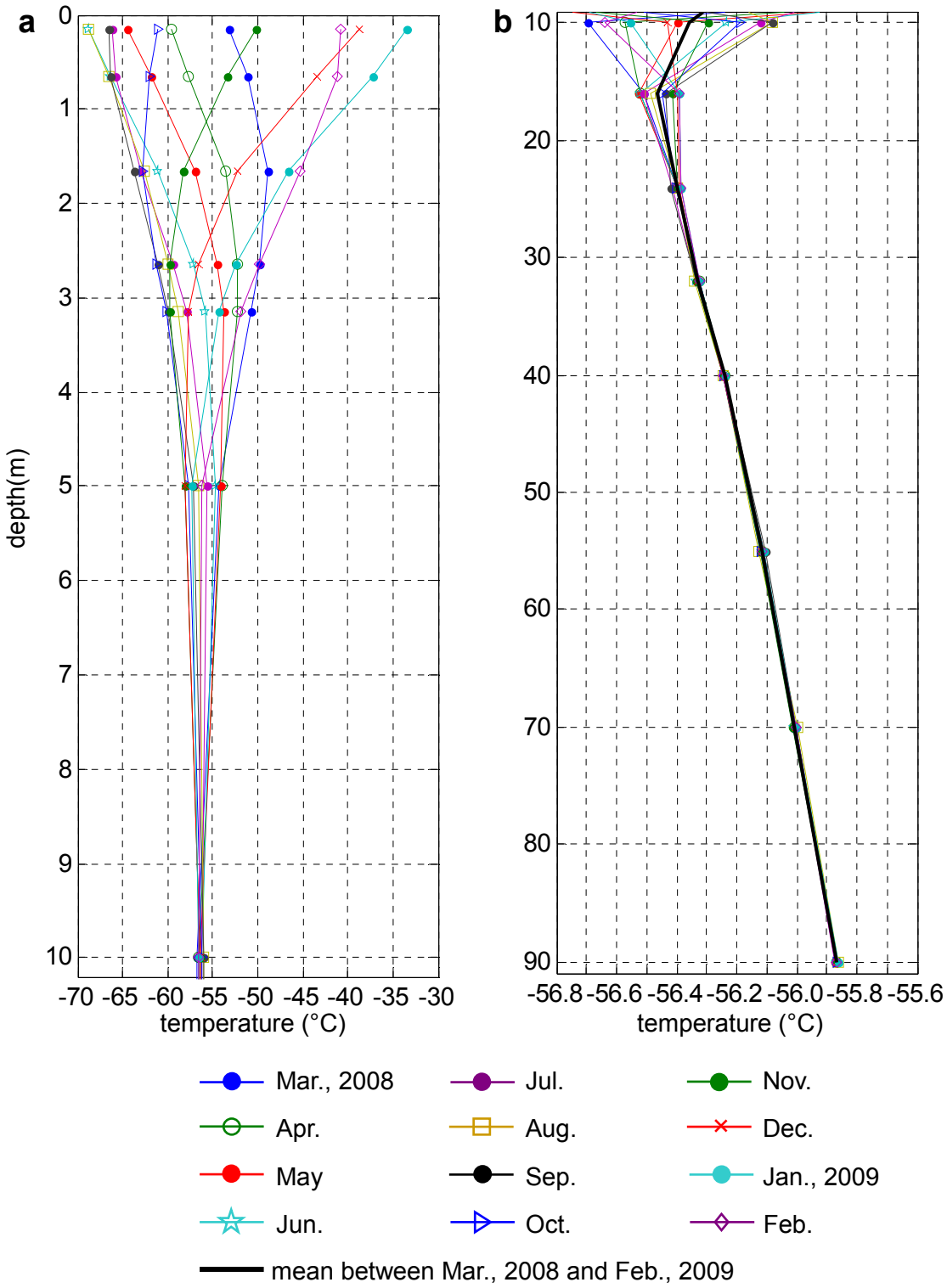

Figure 3.4. Measured firn temperature profiles at NUS07-5 for **a**. top 10 m and **b**. 10 to 90 m. Thick black line in **b** is the mean between March, 2008 and February 2009 which is used in the analyses.

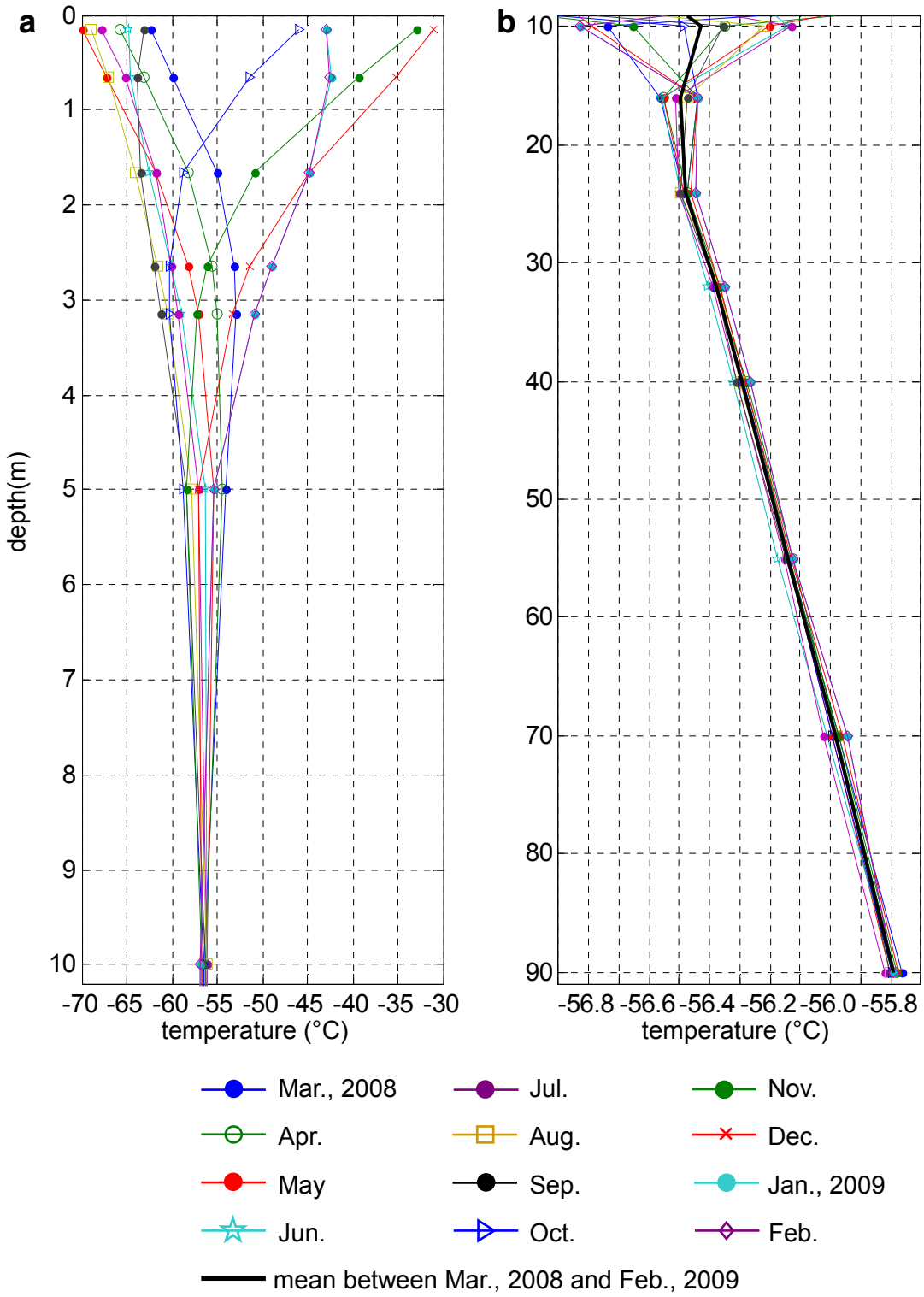

Figure 3.5. Measured firn temperature profiles at NUS07-7 for **a**. top 10 m and **b**. 10 to 90 m. Thick black line in **b** is the mean between March, 2008 and February 2009 which is used in the analyses.

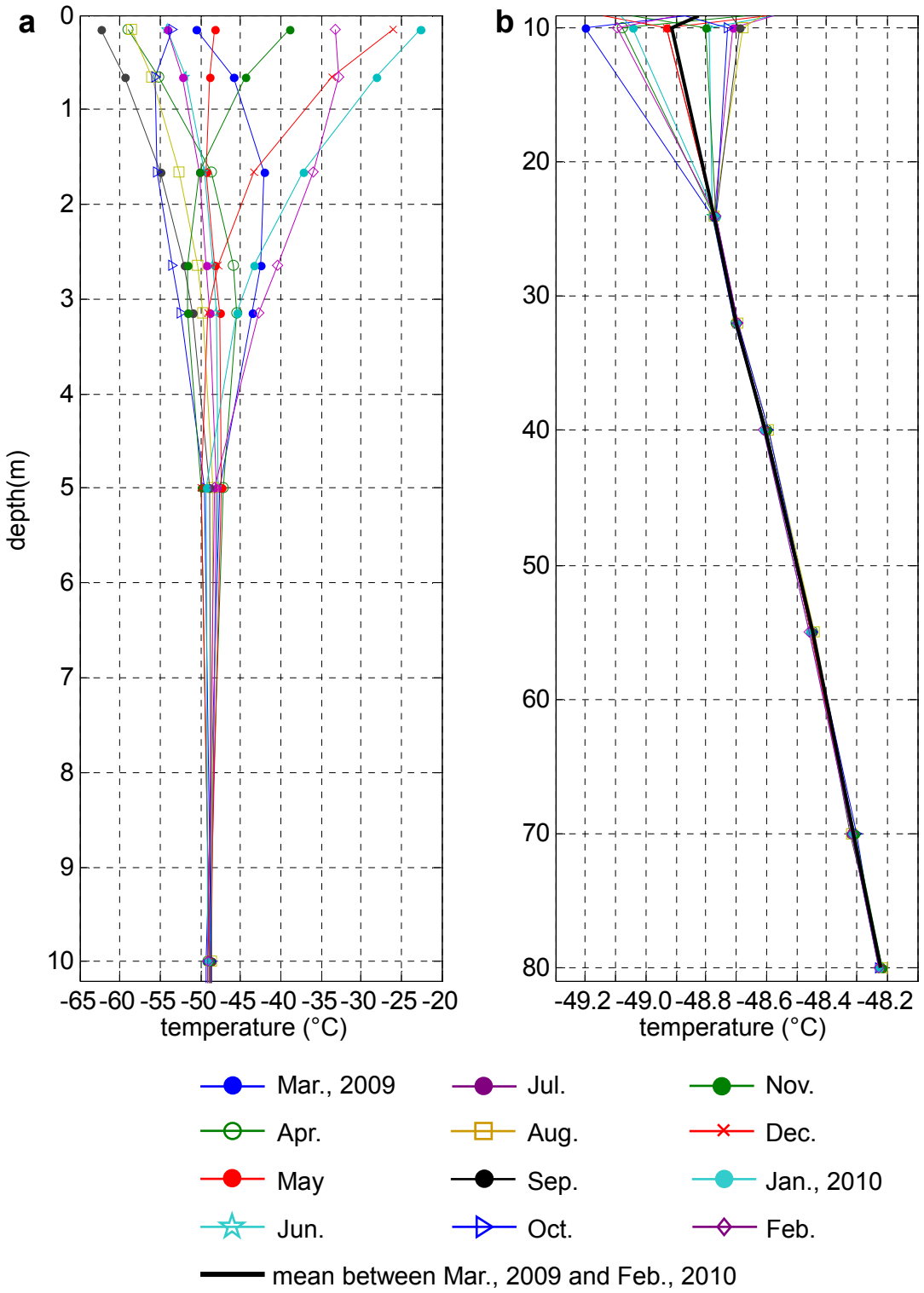

Figure 3.6. Measured firn temperature profiles at NUS08-5 for **a**. top 10 m and **b**. 10 to 80 m. Thick black line in **b** is the mean between March, 2009 and February 2010 which is used in the analyses.

3.5 Uncertainties in temperature measurements

Significant sources of uncertainties identified in temperature measurements using ATPU are sensor calibration (u_c), resistance measurement (u_{TRs}), resistance correction (u_{cRs}) resolution of the resistance measurement ($u_{T\Delta Rs}$) and noise (u_n).

Uncertainties in temperature measurements are presented here following the guidelines of International Committee for Weights and Measures (CIPM). CIPM guidelines are adopted by the U.S. National Institute of Standards and Technology (NIST) and are succinctly presented in Taylor and Kuyatt (1994). With the CIPM guideline, components of the uncertainty of a result of a measurement are categorized into Type A and Type B. Type A uncertainty is evaluated by statistical analysis. Type B uncertainty is evaluated by means other than statistics which may be, for example, physical theory, information from hand books and manufacturer's specifications. Each components of uncertainty that contributes to the uncertainty of a measurement result are represented by the 'standard uncertainty', which is an estimated standard deviation of a quantity i.e. the interval within which a quantity should occur with 67 percent probability (Clow, 2008). Individual standard uncertainties, whether Type A or Type B, are combined to give the standard uncertainty of the temperature measurement. The method used to combine standard uncertainties is the 'law of propagation of uncertainty' (Taylor and Kuyatt, 1994, Appendix A) which is also known as the root-sum-of-squares (RSS).

Often times, the manufacturer of a measurement instrument provides the 'accuracy' of the instrument with statements such as "±0.05% of the measured value". Typically, this indicates the range within which the true value could lie with a uniform probability density function (PDF) and differs from the standard uncertainty as discussed above. If we define X_H and X_L as the upper and lower limits, respectively, of the accuracy range of a quantity of interest X, the standard uncertainty u_X can be calculated from the accuracy range as (Nicholas

and White, 2001),

$$u_X = \frac{1}{\sqrt{3}} \frac{\left(X_H - X_L\right)}{2} = \frac{\text{accuracy range}}{\sqrt{3}}. \quad (3.7)$$

For example, if the accuracy range was ±0.05% of the measured value, the standard uncertainty is 0.05%/√3 ≈ 0.029% of the measured value. In following sections, there are a number of examples of the standard uncertainty being calculated from the accuracy range in this manner.

3.5.1 Sensor calibration (u_c)

The USGS thermal calibration system consists of several electronics and equipment. Therefore, there are several components of the standard uncertainty of sensor calibration, namely, SPRT reference temperature (u_{RT}), the temperature-sensor resistance reading (u_r), bath temperature fluctuation (u_f) and the non-uniformity of the temperature field in the bath (u_u). Detailed discussion of derivation on each of the above components is in Clow (2008). To avoid reiteration, each of the standard uncertainties at -60°C and 0°C are summarized in Table 3.2. u_r differs from that of Clow (2008) since a different resistance readout instrument was used. The basic accuracy of this instrument provided by the manufacturer is ±25 ppm of the reading which corresponds to the standard uncertainty of ±14.4 ppm based on a uniform PDF. This was then converted to temperatures to obtain 2.9 mK and 3.8 mK at -60°C and 0°C, respectively. Combining $u_{RT,}$ u_r, u_f and u_u using the RSS, u_c is estimated to be 4.0 mK at -60°C and 4.8 mK at 0°C. u_c is a Type A, B uncertainty since both Type A and B methods were used to evaluate components of u_c (Clow, 2008).

Table 3.2. Uncertainty components contributing to the standard uncertainty of the temperature sensor calibration, u_c: SPRT reference temperature (u_{RT}), temperature-sensor resistance reading (u_r), bath temperature fluctuation (u_f) and non-uniformity of the temperature field in the bath (u_u).

	Standard uncertainty (mK)	
	At -60°C	At 0°C
u_{RT}	2.77	2.9
u_r	2.9	3.8
u_f	0.2	0.2
u_u	0.06	0.06

3.5.2 Resistance measurement (u_{TRs})

The resistance of the sensor (R_s) is given by equation (3.1). If we let $V_s/V_{ref} = X$ and using the law of propagation of uncertainty, the standard uncertainty of the resistance (u_{Rs}) is in the form,

$$u_{Rs} = \sqrt{\left(R_{ref}\, u_X\right)^2 + \left(X\, u_{Rref}\right)^2}\,. \tag{3.8}$$

The uncertainty of the reference resistance (u_{Rref}) results from the calibration of the reference resistors (u_{cRref}) and the uncertainty in the reference temperature (u_{Tref}) that is used to correct for the temperature drift of reference resistance (R_{ref}). Applying the law of propagation to equation (3.4) and combining with u_{cRref} using the RSS, u_{Rref} is,

$$u_{Rref} = \sqrt{{u_{cRref}}^2 + \left(a_2\, u_{Tref} + 2\, a_3\, T_{ref}\, u_{Tref} + 3\, a_4\, {T_{ref}}^2\, u_{Tref}\right)^2}\,. \tag{3.9}$$

Since reference resistors were calibrated with the same procedure as for PRT sensors, u_{cRref} is similar to u_c presented in the previous section with u_r recalculated with appropriate resistance

readings and all components (u_{RT}, u_r, u_f and u_u) expressed in resistance. u_{cRref} is 1.09×10^{-4} Ω and 1.07×10^{-5} Ω at -60°C and 0°C, respectively, which is the mean of three reference resistors used in each ATPU. The accuracy of the temperature measured by the built-in thermistor of CR1000 as given by the manufacturer is ±0.8°C. Based on a uniform PDF, this corresponds to u_{Tref} of 0.46°C. Although this accuracy is defined for the temperature range of -55 to +85°C by the manufacturer, it was extended to temperature ranges experienced by reference resistors in the field, down to approximately -65°C at the most (see temperatures at 2 m depth in Figures 3.3 to 3.6). The accuracy appears to be below 0.8°C if the panel temperature accuracy curve given by the manufacturer (Figure 3.7) is extrapolated to -65°C. u_{Rref} is then 3.47×10^{-3} Ω and 4.29×10^{-4} Ω at -60°C and 0°C, respectively. These values are again the mean of five reference resistors.

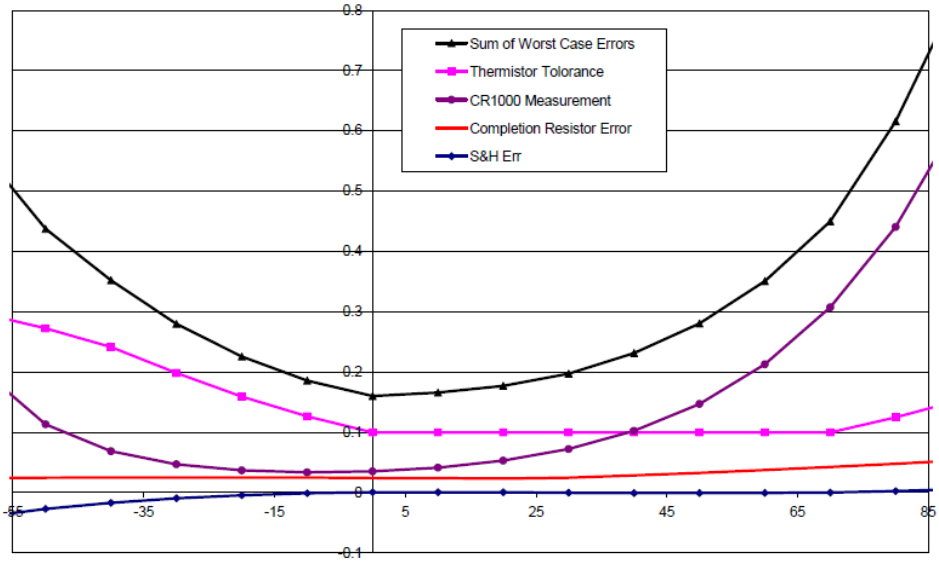

Figure 3.7. Panel temperature accuracy given by Campbell Scientific Inc. Sum of Worst Case Errors is defined as the accuracy here. From CR1000 Operator's Manual by Campbell Scientific Inc.

The accuracy of X is provided by the manufacturer as,

$$\pm \frac{0.04\% \text{ of } V_s + \delta_V}{V_{ex}}, \tag{3.10}$$

where δ_V is the offset to X (50.5 μV), V_{ex} is the excitation voltage (2.5 V). The accuracy calculated from the above is $\pm 4.66\times10^{-5}$ and $\pm 5.37\times10^{-5}$ at -60°C and 0°C, respectively. u_X is then 2.69×10^{-5} and 3.10×10^{-5} at -60°C and 0°C, respectively, based on a uniform PDF. Substituting u_{Rref} and u_X into equation (3.8), u_{Rs} is 0.027 Ω and 0.031 Ω at -60°C and 0°C, respectively.

u_{TRs}, the standard uncertainty of temperature measurement due to u_{Rs} is characterized by u_{Rs} propagating to temperature when R_s is converted to temperature. u_{TRs} is calculated by applying the law of propagation to equation (3.4) as,

$$u_{TRs} = a_2\, u_{Rs} + 2\, a_3\, R_s\, u_{Rs} + 3\, a_4\, {R_s}^2\, u_{Rs}\,. \tag{3.11}$$

Using coefficients a_i of all 48 sensors used in this research and taking the mean, u_{TRs} is 0.01 K at -60°C and 0.011 K at 0°C. u_{TRs} is a type B uncertainty since it was calculated using the manufacturer's specifications.

3.5.3 Resistance correction (u_{cRs})

Applying the law of propagation to equation (3.5), the uncertainty due to resistance correction for self-heating (u_h) can be calculated as,

$$u_h = \frac{\alpha_T I^2 {R_s}^2}{P_d} \sqrt{4\left(\frac{u_I}{I}\right)^2 + 4\left(\frac{u_{R_s}}{R_s}\right)^2 + \left(\frac{u_{P_d}}{P_d}\right)^2}\,. \tag{3.12}$$

u_I is given by,

$$u_I = \frac{1}{\left(R_k + R_{ref} + R_s\right)^2}\left\{\left[\left(R_k + R_{ref} + R_s\right)u_{V_{ex}}\right]^2 + \left[V_{ex}\left(u_{R_K} + u_{R_{ref}} + u_{R_s}\right)\right]^2\right\}^{1/2}, \quad (3.13)$$

The manufacturer's specification on the accuracy of the excitation voltage (V_{ex}) and current-limiting resistor (R_K) are $\pm 5.5\times10^{-3}$ V and ±500 Ω, respectively. Based on a uniform PDF, the standard uncertainties u_{Vex} and u_{RK} are 3.18×10^{-3} V and 289 Ω, respectively. u_{Rref} and u_{Rs} are the same as those given in the previous section. Substituting u_{Vex}, $u_{RK,}$, u_{Rref} and u_{Rs} in to equation (3.13), u_I ranges from 5.22×10^{-6} A at -60°C and 5.02×10^{-6} A at 0°C. The accuracy of the dissipation constant (u_{Pd}) is unknown since there is no specification provided by the manufacturer. In such a situation, the best practice is to assume the accuracy is as large as the dissipation constant itself. Hence the accuracy is assumed to be 0.15 mW/K. The standard uncertainty u_{Pd} is then 8.66 mW/K, based on a uniform PDF. Substituting u_I, u_{Rs} and u_{Pd}, into equation (3.12), the standard uncertainty of the correction for self-heating is 4 mK and 6.3 mK at -60°C and 0°C, respectively.

3.5.4 Resolution of resistance measurement ($u_{T\Delta Rs}$)

The resolution of the resistance measurement as discussed in section 3.2 is 0.018 Ω. The standard uncertainty associated with this resolution based on a uniform PDF is 0.010 Ω. Propagation of this uncertainty to temperature is calculated in the same manner as for u_{TRs} using equation (3.11). $u_{T\Delta Rs}$ is then 2.6 mK.

3.5.5 Noise (u_n)

There are also random noises in the received data, sources of which could not be identified. To determine the uncertainty due to noises, a statistical approach was applied to the resistance

data.

Firn temperature at some depths can be assumed to stay constant over intervals of several days. Following the analysis of Paterson (1994) on the propagation of cyclical variation in surface temperature, assuming that the temperature variations at the surface takes sinusoidal form, annual and any shorter time-scale variations are dampened far beyond the detectable limit of ATPU at the two deepest sensors (70 and 90 m for NUS07-2, -5 and 7, and 70 and 80 m for NUS08-5). For example, amplitude of annual variations at the surface is dampened by a factor of 10^{-10} at 70 m. Based on this fact, temperatures at the two deepest sensors are assumed to stay constant over a 1-month period. The root mean square error (RMSE) of the linear fit to temperature data over 1 month was repeatedly calculated over the period of the data set, shifting by one day each time and the maximum RMSE for each depth was defined as u_n. The thermal re-equilibration was assumed to have taken place 1 month after the installations hence the first month of each data set is not used in the above calculation. Table 3.3 shows the maximum RMSE's for each site at 70 and 90m for NUS07-2, -5 and -7, and 70 and 80 m for NUS08-5. Temperature measurements of the two deepest sensors are made simultaneously so the effect of noise to both readings is considered equal. The different values of RMSE may be the result of noises inherent in sensors. To stay conservative, the worst value 0.024 K was taken as the estimate of u_n for all ATPUs. Since a statistical analysis was used, u_n is a type A uncertainty.

Table 3.3. RMSE's of a linear fit to 1 month of temperatures measured by the two deepest sensors at each site.

	RMSE (K)	
	70 m	90 m
NUS07-2	0.022	0.024
NUS07-5	0.015	0.019
NUS07-7	0.022	0.020
	70 m	80 m
NUS08-5	0.014	0.015

3.5.6 Combined standard uncertainty of temperature measurements (u_T)

Combining u_c, u_{TRs}, u_{cRs}, $u_{\Delta R}$ and u_n as the root sum of squares, u_T ranges from 0.026 K at -60°C and 0.028 K at 0°C. Figure 3.3 shows the combined standard uncertainty of temperature measurements (u_T) as well u_c, u_{TRs}, u_{cRs}, $u_{\Delta R}$ and u_n between -60°C and 0°C, which are the average of all 64 sensors and 4 ATPUs used in this research. For the convenience of calculations, temperature dependence of u_T will be ignored and rounded up to 0.03 K. u_T is a Type A,B uncertainty.

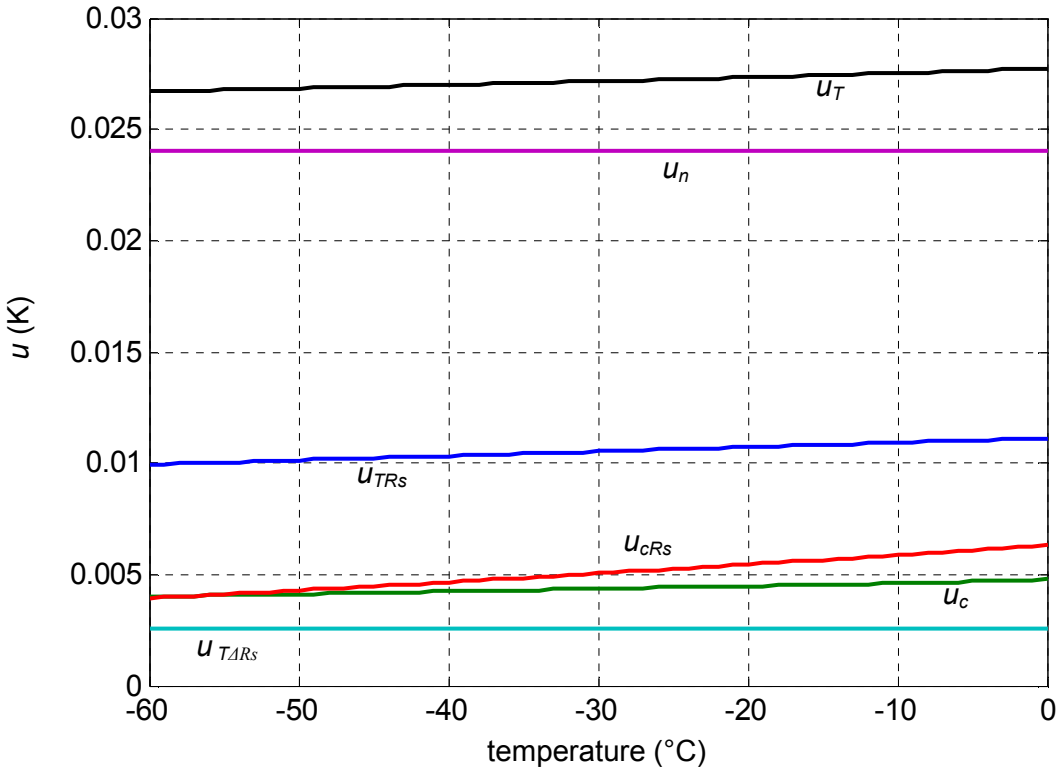

Figure 3.8. Combined standard uncertainty of the temperature measurement by ATPU (u_T) and components contributing to u_T: sensor calibration (u_c), resistance measurements (u_{TRs}), resistance correction (u_{cRs}) resolution of resistance measurements ($u_{T\Delta Rs}$) and noise (u_n).

Chapter 4

GEOPHYSICAL INVERSE METHOD

4.1 Introduction

The surface temperature history will be obtained by applying geophysical inverse methods to the one-year mean of measured firn temperatures. In this research, linearized and Monte Carlo inversion techniques will be used.

In order to solve the inverse problem, either with the linearized or Monte Carlo method, a forward model of heat transfer process in firn and ice is needed. Therefore, this chapter starts with a description of the forward problem and its solution procedure. Then, the two inverse methods are presented and are applied to a synthetic problem simulating the conditions in East Antarctica.

4.2 Forward model

The forward model used here is based on a one-dimensional heat diffusion-advection equation in the form,

$$\rho c \frac{\partial T}{\partial t} = K \frac{\partial^2 T}{\partial z^2} - \rho c w \frac{\partial T}{\partial z}, \tag{4.1}$$

where is T is the temperature, t is time, z is depth (positive downwards), ρ is the density, c is the specific heat capacity, K is the thermal conductivity and w is the vertical velocity. ρ, c, K and w are depth and/or temperature dependent and the following section describes their

parameterizations. This equation is a simplified form of Paterson (1994), from two dimensions to one dimension and neglecting the internal heat source.

The possible sources of heat generation within firn and ice are solar penetration near the surface (e.g. Brandt and Warren, 1997; Liston and Winther, 2005), strain heating due to the ice deformation and firn compaction (Paterson, 1994). Contribution of the solar penetration to the heat transfer within the high polar-plateau snow is only a few percent (Brandt and Warren, 1997). Heat produced by the strain heating at Vostok, which has geographical and glaciological settings comparable to the study sites of this research, were shown to be 10 to 20 times smaller than the heat transported by vertical advection (Goujon et al., 2003). Heat produced by firn compaction can be calculated using the procedure given by Paterson (1994). Applying this method to one of the study sites (NUS07-2), the maximum temperature change in one year due to heat produced by firn compaction was approximately 0.1 mK at 10 m depth. Therefore, the three heat sources are considered negligible.

A partial differential equation (4.1) is numerically solved by following the control volume method of Patankar (1980). The control volume method divides the solution domain (one-dimensional firn-ice column here) into a number of non-overlapping control volumes with a grid point inside each control volume. The partial differential equation is integrated over each control volume, resulting in the discretization equation for calculating the energy flow at interfaces of each control volume and determining temperature T at each grid point. Figure 4.1 is a graphical representation of the control volume grid covering the solution domain. The solution domain is divided into 1000 control volumes, resulting in 1001 grid points, regardless of the thickness of the firn-ice column at a specific site. Grid points are spaced at 5-cm intervals for the top 10 m, increasing to ~7 m about half way through the column and decreasing to 5cm again at the bottom of the domain. A cosine function was used to place the grid points below 10 m depth to ensure that no abrupt change in grid spacing

occurred. Derivation of the discretization equation and solution technique is presented in Appendix B.

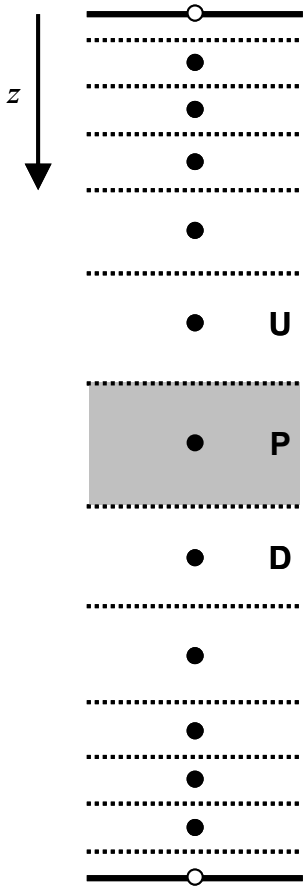

Figure 4.1. Graphical representation of control volume grids used to model 1-D heat diffusion-advection. U, P and D are grid points upwards, inside and downwards of the control volume of interest, respectively.

4.2.1 Model inputs

Density (ρ)

The dimension and the weight of each firn core were measured immediately after the core recovery in the field from which the bulk density was calculated. Those data were provided by Dr. Joe McConnell of the Desert Research Institute, the University of Nevada and Dr. Tom

Neumann of the NASA Goddard Space Flight Center. The density profile for each site was derived by performing a quadratic or exponential fit to bulk density data, by a method modified from that used by Severinghaus et al. (2010). Density data is divided into three segments according to the three stages of transition of snow to ice (e.g. Arthern and Wingham, 1998; Goujon, et al., 2003): $\rho < 550$ kgm^{-3}, $550 < \rho < 830$ kgm^{-3} and $830 < \rho < 917$ kgm^{-3}. Then, a quadratic fit for the first two stages and an exponential fit for the third stage were performed. The exponential fit to the third stage has a condition that the derivatives of the quadratic and exponential must equal at $\rho = 830$ kgm^{-3}. For NUS07-5 and -7, the boundary of the 2nd and 3rd stages were extrapolated from the quadratic fit since the highest density measured from cores at the two sites did not exceed 830 kgm^{-3}. Figure 4.2 shows the measured and parameterized density profiles for each site.

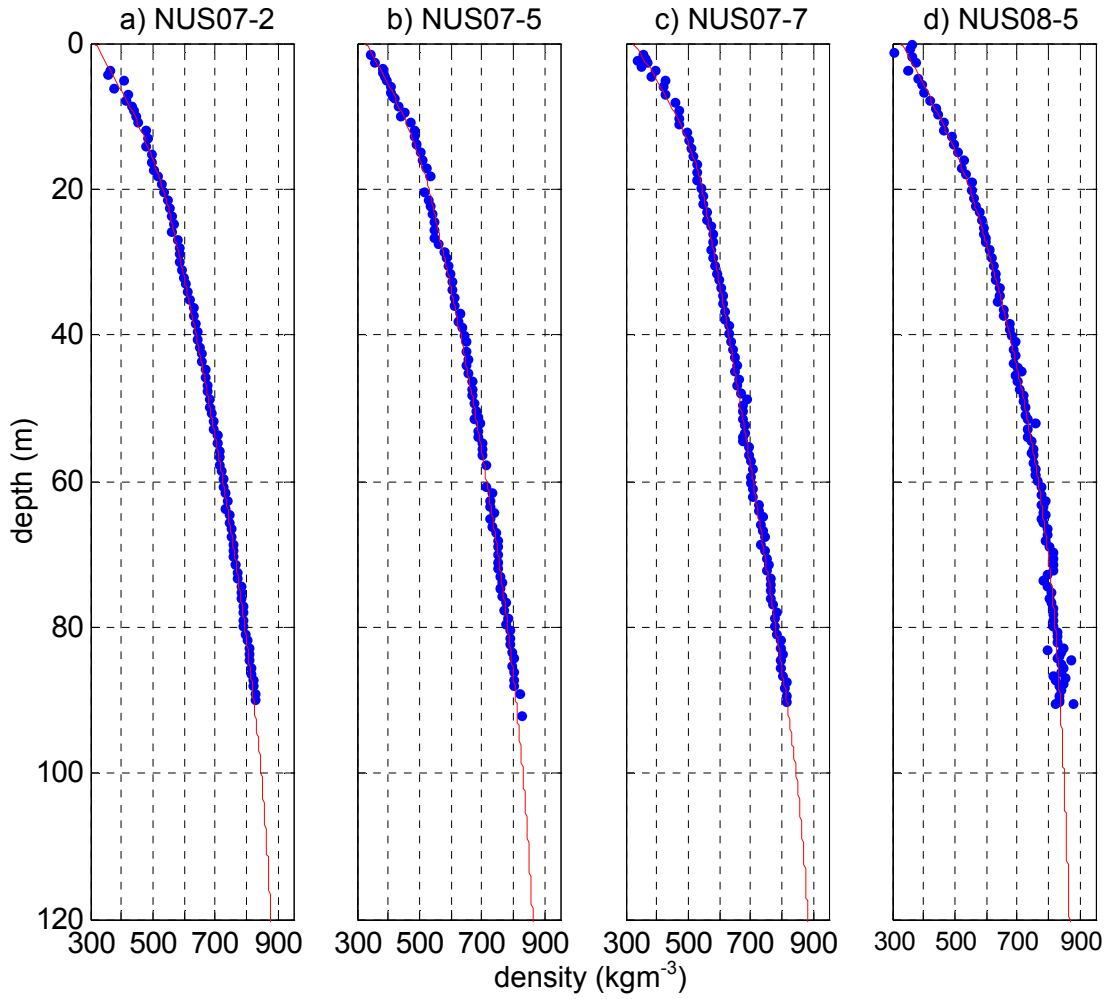

Figure 4.2. Measured (blue dots) and parameterized (red solid line) density profiles from a) NUS07-2, b) NUS07-5, c) NUS07-7 and d) NUS08-5.

Specific heat capacity (c)

Specific heat capacity of ice (c_i) in $Jkg^{-1}K^{-1}$ was given by the following equation of Paterson (1994):

$$c_i = 152.5 + 7.122\,T\,, \tag{4.2}$$

where T is temperature in Kelvin. Specific heat capacity of firn (c_{firn}) was calculated from the percentage of ice and air in firn,

$$c_{firn} = c_i \frac{\rho}{\rho_i} + c_a \left(1 - \frac{\rho}{\rho_i}\right), \tag{4.3}$$

where ρ_i is the density of ice (917 kgm^{-3}) and is c_a the specific heat capacity of dry air. c_a is not temperature-dependent in the range of temperatures typical for the study sites (e.g. van den Broeke et al., 2005) and 1005 $Jkg^{-1}K^{-1}$ is used.

Thermal conductivity (K)

Thermal conductivity of firn and ice were determined based on density and temperatures measured over one year. The temperature-dependent thermal conductivity of ice (K_i,) in $Wm^{-1}K^{-1}$ is given by,

$$K_i = 2.22\left(1 - 0.0067\,T\right), \tag{4.4}$$

where T is temperature in degrees Celsius (Weller and Schwerdtfeger, 1977).

The thermal conductivity of firn used in this research is the 'effective thermal conductivity' that includes the effects of both regular conduction through linked grains of firn and the transfer of latent heat by water vapor sublimation, diffusion and deposition (Arons and Colbeck, 1995).

Thermal conductivity of firn (K_f) is parameterized by a modified version of an equation used by Schwander et al. (1997),

$$K_f = K_i \left(\frac{\rho}{\rho_i} \right)^{\alpha - \beta \frac{\rho}{\rho_i}}, \tag{4.5}$$

where α and β are site-specific coefficients determined by a global optimization method. Schwander et al. (1997) used equation (4.5) with $\alpha = 2$ and $\beta = 0.5$ which were obtained from a fit through data collected by Mellor (1977), for finding the gas age scale in ice cores from GRIP and GISP2 in Greenland. Mellor (1977) presents a collection of effective thermal conductivities of a wide range of snow and firn types not limited to those found on the Antarctic plateau. Therefore, it is considered appropriate to modify the equation used by Schwander et al. (1997), treating α and β as tuning parameters.

Values of α and β are determined by minimizing the least-squares performance constraint J, describing the mean square misfit between observed and modeled temperatures:

$$J = \frac{1}{N} \sum_{j=1,L} \sum_{i=1,M} \left[\frac{T^{obs}(t_j, z_i) - T^{est}(t_j, z_i)}{u_T + \sigma_i} \right]^2, \tag{4.6}$$

where $T^{obs}(t_j, z_i)$ is the measured firn temperatures at time t_j and depth z_i, $T^{est}(t_j, z_i)$ is the modeled firn temperatures at time t_j and depth z_i using K_f given by estimated values of α and β. u_T is the temperature measurement uncertainty and σ_i is the standard deviation of measured temperatures at depth z_i over the period of time for which J is evaluated. The denominator normalizes the misfit according to the temperature measurement uncertainty and temperature variations observed at each depth. This normalization effectively puts more weight on misfits at depths where annual variations are still observed (z > 16 m) and avoids over-fitting at deeper depths where variations seen are mostly noise.

The global optimization method used here to minimize J is Simulated Annealing (SA), which belongs to a family of Monte Carlo methods (Sambridge and Mosegaard, 2002). The

basic concepts of SA are borrowed from problems in statistical mechanics (Sen and Stoffa, 1994) and an SA algorithm simulates the process of chemical annealing in which a melted crystalline material is cooled slowly through its freezing point, thereby approximately settling into its lowest energy state (Sambridge and Mosegaard, 2002). The performance constraint J can be viewed as the energy in the crystalline material and the optimization process as the cooling of the material. SA avoids being trapped in a local minimum of J which is a risk associated with local minimization methods such as the control method developed by MacAyeal et al. (1991). SA algorithm runs as follows (Sambridge and Mosegaard, 2002): In each step, parameters α and β are randomly perturbed. The new set of parameters is accepted if the value of J decreases. However, if J increases, the new parameters may be accepted with probability,

$$P_{accept} = \exp\left(-\frac{\Delta J}{T}\right), \tag{4.7}$$

where ΔJ is the change in J and T is the temperature parameter that starts with 1 and asymptotically approaches 0, being decreased at a rate of $0.99T$ for every 50 acceptances. If a new set of α and β is rejected, new perturbation is attempted in the next iteration. The above process is repeated until ΔJ or T reaches some threshold (1×10^{-6} in both cases). More details of the SA algorithm used here can be found in Chapter 4.1 of Sen and Stoffa (1994).

Values of α and β and root mean square errors (RMSE) at each depths are summarized in Table 4.1. β was 0 for all three sites, meaning that the equation (4.5) has a single exponent. This is to be expected because with all terms in the exponent calculated with both α and β reduce to a single number. Such form of the parameterization is close to that of Yen (1981) who uses a fixed value of K_i (2.22362 $Wm^{-1}K^{-1}$) and α = 1.885 although this is for using the ratio of snow or firn density to the density of water (1000 kgm^{-3}), not ρ_f/ρ_i. It is evident from

the values of RMSE's that the above method of parameterization has limitations. It is likely that the parameterization used here can not capture large variations in the thermal conductivity in the top several meters that actually exists (Mary Albert, personal communication). However, annual amplitudes of the temperatures at depths down to 10 m can be reasonably simulated. Therefore, it provides a path to accurate assessment of the mean thermal conductivity and this is adequate. To account for the remaining error in this parameterization, inversions by both the linearized and the RJ-MCMC methods will be carried out by varying α by ±0.1 as the sensitivity analysis. Changing α by ±0.1 corresponds to changes in amplitudes by up to 25% and changes in thermal conductivity of 11% at the maximum for each site.

Table 4.1. RMSE and the percentage of the annual amplitude in temperature explained at different depths by simulated temperatures using the thermal conductivity parameterized with α and β values as shown.

NUS07-2 $\alpha = 2.4634$ $\beta = 0$

depth (m)	RMSE (K)	annual amplitude explained (%)
0.65	0.542	98.9
1.65	0.699	98.9
2.5	0.963	88.7
3	0.922	86.1
5	0.433	113.8
10	0.140	103.5
16	0.029	-
24	0.020	-
32	0.014	-
40	0.014	-
55	0.016	-
70	0.013	-

NUS07-5 $\alpha = 2.4220$ $\beta = 0$

depth (m)	RMSE (K)	annual amplitude explained (%)
0.65	1.042	96.6
1.65	0.732	93.0
2.5	0.175	94.7
3	0.135	95.4
5	0.215	115.2
10	0.152	105.8
16	0.053	-
24	0.016	-
32	0.020	-
40	0.010	-
55	0.011	-
70	0.009	-

NUS07-7 $\alpha = 2.2913$ $\beta = 0$

depth (m)	RMSE (K)	annual amplitude explained (%)
0.65	1.100	91.3
1.65	0.543	93.1
2.5	0.395	89.8
3	0.351	90.2
5	0.316	114.7
10	0.177	92.0
16	0.056	-
24	0.019	-
32	0.022	-
40	0.021	-
55	0.016	-
70	0.023	-

NUS08-5 $\alpha = 2.3033$ $\beta = 0$

depth (m)	RMSE (K)	annual amplitude explained (%)
0.65	0.299	99.7
1.65	0.304	98.2
2.5	0.212	98.6
3	0.189	102.0
5	0.298	111.0
10	0.135	100.8
16	-	-
24	0.039	-
32	0.011	-
40	0.013	-
55	0.012	-
70	0.012	-

Vertical velocity (w)

The vertical velocity was calculated using the equation presented in Goujon et al. (2003) which is based on the ice velocity model of Lliboutry (1979) with modification in the firn where density sharply increases with depth. Using a relative vertical coordinate $\zeta = z/H$ where H is the ice sheet thickness, $w(\zeta)$ is,

$$w(\zeta) = \frac{\rho_i}{\rho}\left[w_s - (w_s - w_b)\left(\frac{m+2}{m+1}\zeta\right) \quad \left(1 - \frac{\zeta^{m+1}}{m+2}\right)\right]. \tag{4.8}$$

w_s and w_b are the vertical velocity at the surface and at the base of the ice sheet, respectively. w_s is assumed here to be equal to the accumulation rate. w_b is assumed to be 0 for NUS07-2, -5 and -7, meaning there is no melting at the base, since the condition of the ice sheet-base at each study site is unknown. To account for this unknown basal condition, however, sensitivity analyses with w_b = 5 mm/year will be carried out. NUS08-5 is considered to be over a subglacial lake (Bell et al., 2007) hence the ice sheet base is melting although the exact melting rate is not known. Here, the basal melting rate of 5 mm/year will be used and sensitivity analyses with w_b = 1mm/year and 10 mm/year will be carried out.

H is assumed to be constant with time. m is the shape parameter of the vertical velocity profile. Values of m used by Goujon et al. (2003) are 12 for Vostok (off of an ice divide) and 10 for GISP2 (ice sheet dome). NUS07-2, -5 and -7 are off of an ice divide in East Antarctica although the distance from the divide is not as great as for Vostok. Therefore, m is taken to be 11, a number between that for GISP2 and Vostok. NUS08-5 is situated approximately 40 km from the upstream edge of the subglacial lake. Vostok is situated approximately 50 km from the upstream edge of the subglacial Lake Vostok. Hence the ice flow around NUS08-5 is considered to have similar conditions to around Vostok and m = 10 is used for NUS08-5. In fact, $w(\zeta)$ calculated with m between 10 and 12 have negligible differences at all depths (not

shown) hence the choices of *m* for each site are considered suitable.

Accumulation rate

The snow accumulation rate at each respective site which is needed to calculate *w* is from McConnell (personal communication) and is derived from firn core chemistry. Accumulation rate at each site is shown in Table 4.2. These values are the mean of the past 750 years. The uncertainty of these estimates of the accumulation rate is considered to be less than 1% of the value at each site.

The temporal variability of the accumulation rate at each site has not yet been determined precisely. However, using peaks in the dielectric profiling of firn cores identified as known volcanic events, the temporal variability of the accumulation rate is estimated to be no more than 11% (Helgard Anschüetz, personal communication). To account for both the determination of the accumulation rate and the temporal variability in the uncertainty of the accumulation rate, a conservative value of 15% will be used for the sensitivity analyses in a later section.

Ice sheet thickness

The ice sheet thickness is typically obtained from radar echo sounding of the bedrock beneath the ice sheet (e.g. Tabbacco et al., 2002; Fujita et al., 2006), either from the air or the surface of the ice sheet. Continuous radar echo sounding was attempted along the entire traverse route in the 2007-08 season. Unfortunately, however, the instrument did not perform as expected and ice thickness data were not obtained. Ice thickness data used here for NUS07-2, NUS07-05 and NUS07-07 are taken from the input to the Community Ice Sheet Model (CISM), available on the internet. These ice thickness data are calculated from the surface elevation from the Digital Elevation Model (DEM) of Bamber et al. (2009) and the bedrock

topography of the BEDMAP1-Plus. Ice thickness data come in 5 km by 5 km grids. Therefore, the thickness for each site is taken from the grid that contains the location (latitude and longitude) of the site.

The uncertainty of the ice thickness in this data set can be estimated by combining the uncertainties in the DEM of Bamber et al. (2009) and the BEDMAP1-Plus. The uncertainty of the DEM in the region of the three study sites as discussed in Bamber et al. (2009) and an accompanying paper (Griggs and Bamber, 2009) is 10 m at the most. For the BEDMAP1-Plus, the uncertainty is estimated to be generally between 150 to 300 m (Lythe et al., 2001). Since the three sites are located in a region that is relatively sparse of in situ data on which the BEDMAP1-Plus is based, it is appropriate to consider that the uncertainty is close the larger end of the given range, 300 m. The uncertainty of the DEM is then negligible compared to that of the BEDMAP1-Plus. Values of the uncertainty for specific locations are not provided by Lythe et al. (2001) and hence the uncertainty in the ice thickness at the three sites is estimated to be 10% of the numbers at each site. Those numbers are then 280, 323 and 293 m, respectively, for NUS07-2, -5 and -7.

At NUS08-5, the bed reflection from the radar echo sounding was successfully obtained and the ice thickness is estimated to be 3510.0 m (Kirsty Langley, personal communication). The sources of uncertainty in this estimate are the digitization accuracy of the instrument (17 m) and the varying speed of the radar pulse in firn (15 m). Combining these two sources by the method of Root Sum of Square, the uncertainty in the ice thickness at NUS08-5 is estimated to be 22.7 m. Ice thickness at each site is shown in Table 4.2. It is assumed that the ice thickness does not change with time.

Ice sheet basal temperature

The basal boundary condition is required to drive the forward model. A prescribed

temperature is used as the basal boundary condition in this research. There are no direct measurements of the basal temperature (T_b) or heat flux at the sturdy sites. The only location near one of the study sites with the observation of the condition at and near the ice sheet base is Dome Fuji which is approximately 175 km away from NUS07-5. During the drilling of the last ~4 m of ice at Dome Fuji, more ice chip than can be created from drilling were collected, suggesting the existence of liquid water in the vicinity of the ice-bedrock interface (Motoyama et al., 2008). The inventory of Antarctic subglacial lakes (Siegert et al., 2005) show a number of subglacial lakes in the area around the ice divide of East Antarctica where the study sites are located.

Based on the two facts above, it is speculated that the basal temperatures at NUS07-2, -5 and -7 are at or near the pressure melting point of ice. Therefore, T_b varying between the pressure melting point (T_{pm}) and 10 K below the pressure melting point are used as the basal boundary condition in the forward model and when solving the inverse problem for those three sites. The pressure melting point of ice in degrees Celcius is given by (Ritz, 1992, referenced by Goujon et al., 2003),

$$T_{pm} = -7.4 \times 10^{-8} \rho_{ice}\, g\, H - 0.024 \,, \tag{4.9}$$

where ρ_{ice} is the density of ice, g is the gravitational acceleration and H is the ice sheet thickness. -7.4×10^{-8}°Cbar^{-1} is the variation coefficient of T_{pm} with pressure and 0.024 is a correction due to the air dissolution in water. T_b for each site calculated using equation (4.9) is shown in Table 4.2. The effect of using different basal temperatures in the solution of the inverse problem is discussed in a later section and it will be shown that the basal temperature is of a second order importance.

Table 4.2. Ice thickness, accumulation rate and basal temperature at each study site.

	Ice thickness (m)	Accumulation rate (mm/year water equivalent)	Basal temperature (°C)
NUS07-2	2798.4	33.35	-1.90
NUS07-5	3228.3	25.94	-2.17
NUS07-7	2929.9	29.44	-1.97
NUS08-5	3530.0	35.40	-2.41

4.2.2 Model verification

The performance of the forward model was examined using analytic solutions to PDE of heat diffusion and advection. Separate tests were conducted for cases where the heat transfer was due to only diffusion and both diffusion and advection. A uniform 3000-meter ice column (same density, thermal conductivity and specific heat capacity throughout) that was discretized as described in section 4.2 was used in both cases.

Heat diffusion aspect of the forward model was tested by taking out the advection term and imposing a time-dependent temperature variation as the boundary condition at the surface. If the surface temperature variation is assumed to be sinusoidal, the analytic solution to a heat diffusion equation is given by Paterson (1994, p.206) as,

$$T(z,t) = T_a \exp\left(-z\sqrt{\frac{\omega}{2k}}\right)\sin\left(\omega t - z\sqrt{\frac{\omega}{2k}}\right), \tag{4.10}$$

where t is time, z is the depth, k is the thermal diffusivity, T_a and $\omega/2\pi$ are the amplitude and the frequency of the variation at the surface, respectively. The forward model was run for 100 years to reduce the influence of the initial condition to negligible levels and the last one year

was used for the comparison. Table 4.3 summarizes the root mean square (RMS) error and the maximum difference in temperatures between the analytic solution and the forward model at 10 m with various time steps. The difference reduced as the time step was decreased which indicates that the heat diffusion component was being modelled properly in the forward model.

Table 4.3. Comparison of the temperature time series at 10 m from the analytic solution and the forward model

	time step (days)		
	1	0.5	0.25
RMS error (K)	0.0085	0.0043	0.0023
maximum difference (K)	0.0145	0.0079	0.0045

The second test was conducted with both of diffusive and advective terms. The analytic solution for steady, one-dimensional heat diffusion-advection is given by Paterson (1994, p218) as,

$$T(z) = T_S + \frac{\sqrt{\pi}}{2} l \left(\frac{dT}{dz}\right)_B \left[\mathbf{erf}\left(\frac{z}{l}\right) - \mathbf{erf}\left(\frac{H}{l}\right)\right], \tag{4.11}$$

where T_S is the surface temperature, $(dT/dz)_B$ is the basal temperature gradient, H is the ice thickness, k is the thermal diffusivity and erf is the error function. l is given by $l^2 = 2kH/b$ where b is the vertical advection velocity at the surface which equals the accumulation rate. The above analytic solution requires a Neumann boundary condition (temperature gradient at the boundary) at the base hence if a Dirichlet boundary condition (prescribed temperature at

the boundary) is desired, the basal temperature gradient (β_0) first needs to be calculated. This can be achieved using an equation given by Hooke (2005, p.123):

$$\beta_0 = \frac{2}{l\sqrt{\pi}} \frac{T_S - T_B}{\mathbf{erf}\left(\frac{H}{l}\right)}, \tag{4.12}$$

where T_B is the basal temperature. Solving equation (4.11) by replacing $(dT/dz)_B$ with β_0 is equivalent to obtaining the analytic solution with a Dirichlet boundary condition at the base (Hooke, 2005. p.123). To test the forward model against this analytic solution, a uniform ice column was again assumed and the vertical velocity at various depths was given by bz/H. The boundary condition at the surface (T_S) and the base (T_B) were held constant at -55 °C and -5 °C, respectively. Using a time step of 100 years, and the grid spacing as explained earlier, model was run with an initial temperature distribution that is linear between the surface and the base. The modelled temperature profile approached the analytic solution with an increasing length of time. Based on these results, it can be concluded that advective and diffusive parts were being modelled at a sufficient level.

Table 4.4. Comparison of the temperature profile from the analytic solution and the forward model.

	model time (years)			
	10,000	100,000	500,000	1,000,000
difference at 90 m (K)	0.3422	0.0057	0.00049	0.00049
RMS error (K)	1.6139	0.0227	0.0057	0.0057
maximum difference (K) (depth in m)	5.3258 (1598)	0.0746 (1568)	0.0228 (2028)	0.0228 (2028)

The above two tests indicate that the forward model properly capture the heat diffusion

and advection processes with the discretization method described above. It is well known that the solutions obtained by numerical models approach the original PDE as the grid spacing and time step are decreased (e.g. Peacock, 1987;Kolditz, 2002).

4.3 Linearized inversion method

The first inversion method follows the approach of Parker (1994), with modifications in some details by Clow (unpublished). A non-linear problem of heat transfer in firn-ice column is linearized and the inverse problem that involves continuous functions is solved by numerical approximation and applying techniques of linear algebra. The use of the actual term 'linearized inversion' follows Sambridge and Mosegaard (2002).

The non-linearity of heat transfer in a firn-ice column arises due mainly to the temperature-dependent thermal properties (see section 4.2.1). However, the thermal conductivity changes only by approximately 0.5% with 1 K change in temperature. Variations of the surface temperature dealt with in this research, as will be shown later, are 2 K at most, leading to 1% change in thermal conductivity. The specific heat capacity is constant at low temperatures encountered in this research. The assumption of a constant accumulation rate and vertical velocity throughout time as discussed in section 4.2.1 and the lack of temperature-dependence leads to a linear treatment of the otherwise non-linear advection term. Therefore, it can be said that the heat transfer in firn-ice is weakly non-linear and it is appropriate to linearize the problem.

For many geophysical problems, there is a linear functional relationship between the observational data and the model which can be represented in a form,

$$d_j = \left(g_j, m\right) = \int_0^a g_j(x, y)\, m(y)\, dy, \qquad j = 1, 2, \ldots, N, \tag{4.13}$$

where m is the model defined on the interval [0, a], d_j is the jth datum and g_j is the jth operator that relates m and d_j called 'representer function' (Parker, 1977; Oldenburg, 1984). x and y are variables of space or time. If we let $\mathbf{d} = (d_1, d_2, \ldots, d_N)$ and $G = (g_1, g_2, \ldots, g_N)$, a forward problem is to solve for $\mathbf{d}$ given G and m, and the inverse problem is to solve for m given $\mathbf{d}$ and G. Equation (4.13) is in fact a linear forward model written as an inner product (Truffer, 2004). In the context of the borehole paleothermometry, g_j are continuous functions describing the response of firn or ice layer at selected depths to the initial condition, boundary conditions and the internal heat source if it exists.

4.3.1 Representer functions

Representer functions must be prescribed to solve an inverse problem with the linearized inversion method. As mentioned above, representer functions describe the response of firn or ice at different depths to the initial condition, boundary conditions and the source term. This means that parameters of m are the initial condition and the histories of boundary conditions and the source term. However, the quantity of interest here is only the surface boundary condition, or the surface temperature history. To isolate the surface temperature history as the only unknown quantity, it is first assumed that the source term is negligible, as discussed in section 4.2.

The effect of the initial condition is handled by subtracting it from the observed data. The initial condition, which is the firn-ice temperature profile at a time t_0, is obtained using a forward model. Since there is no available knowledge of what the initial condition is, a steady state temperature profile is used. The forward model is run with a surface temperature that gives a temperature that matches the measured value at 90 m for each respective site, and basal temperatures T_b varying between the pressure melting point and 10 K lower than the pressure melting point. Then, the modeled temperatures are subtracted from the measured

values. The surface temperature used to obtain the steady state profile is often called the pre-observational mean temperature T_{POM} (e.g. Hartmann and Rath, 2005; Hopcroft et al., 2007) which is the term of choice hereinafter. The time t_0 is set at 500 years before present, procedure for selecting it is explained in the next section. Since different values of the basal temperature lead to different initial conditions, the inversion is performed with a number of basal temperatures to examine the effect of the basal temperature in inverted surface temperature history. Section 4.5 includes further details on how exactly the basal temperatures are dealt with.

It is further assumed that the deepest point of the data (80 and 90 m) is well outside of the influence of the change in basal temperature condition that might happen within the time scales we are concerned with. This assumption is shown to be valid by Goujon et al. (2003) who modeled the temperature evolution in the ice sheet for Vostok, East Antarctica, where the conditions (temperature, accumulation rate, ice sheet thickness) are similar to those at the four sites of this research. It should be noted that this assumption together with the treatment of the ice sheet basal temperature in deriving an initial condition effectively assumes that the basal temperature is constant throughout the history at a value used to obtain the initial condition.

Having reduced the model to be comprised only of the surface temperature history, the representer functions corresponding to the surface temperature need to be derived. This is an easy procedure if an analytic solution of equation (4.1) exists, as representer functions can be derived from the Green's function solution of the partial differential equation. However, exact representer functions can not be obtained analytically since the firn and ice are non-uniform media with varying thermal properties and vertical speed at different depths. Representer functions are then numerically approximated by driving a forward model with an impulsive, delta-like function then following the response of the firn and ice with time.

The numerical approximation of the Dirac delta function (hereinafter referred to as δ-function) needs to be found first since the representer function g_j describes the response of firn or ice to δ-function occurring at time t_0 at the surface. This is achieved by driving the forward diffusion-advection model with the surface boundary condition represented by Figure 4.3 for 10 days at time steps of 60 seconds. Then, the output of the forward model at an arbitrary depth close to the surface, 0.5 m for this research, is compared with analytically derived representer function for diffusion-only case for the same depth. The representer function g_j for diffusion-only heat transfer process for a depth z at time t since t_0 is given by (Clow, unpublished),

$$g_j = \frac{z}{\kappa\sqrt{4\pi\kappa}\left(t - t_0\right)^{3/2}} \exp\left[-\frac{z^2}{4\kappa\left(t - t_0\right)}\right], \tag{4.14}$$

where $\kappa = K/\rho c$ is the thermal diffusivity of firn at depth z. Density (ρ), thermal conductivity (K) and heat capacity (c) are calculated from equations introduced in section 4.2.1. The value of Δm that gives the smallest RMS difference between the representer function calculated by equation 4.15 and numerical output at depth z is taken as the approximation to the δ-function.

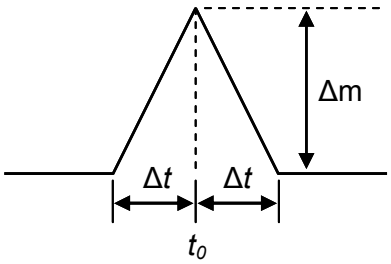

Figure 4.3. Graphical representation of the delta-like function used to numerically derive representer functions. Adapted from Clow (unpublished).

Once the approximate δ-function is found, the forward model is driven with it for the length of time of the inversion. Numerical outputs at depths corresponding to those of observations are taken as representer functions g_j. In section 4.5, it will be shown that a satisfactory solution to the inverse problem can be gained using representer functions derived with the above described method.

4.3.2 Selecting t_0, the time of the initial condition

t_0, the time of the initial condition, is selected by inspecting what is called the 'thermal response function' (Clow, unpublished). Thermal response functions are the response of firn-ice column to the δ-function at given times and indicate the depth over which the surface boundary condition at different times in the past spread over time. It is desirable to set t_0 far enough back in time so the signal of the initial condition has little to no effect in the solution of the model m.

Thermal response functions are derived by driving the forward model with a δ-function, in a method similar method to deriving representer functions, then taking numerical outputs at different times. Figure 4.4a and b show thermal response functions calculated for NUS07-2 for 5, 10, 20, 50, 100 and 500 years after the input of the δ-function. It can be seen in Figure 4.4a and b that only a small portion of the response to the δ-function from 500 years before present is left within the top 90 m. Comparison of the integrals of the thermal response function for the top 90 m and the whole ice sheet reveals that about 8% of the signal is contained in the top 90 m. It can be interpreted that any events preceding 500 years before present hence the initial condition set at 500 years before present has little effect in the firn temperature profile of today. It is evident that setting the initial condition further back in time will guarantee that the effect of the initial condition to be smaller. However, 500 years is the practical length of time for the inverse problem to be solved by the Monte Carlo inversion

method (further explanations in section 4.4.2). Also, thermal response functions for all other sites have negligible differences. Therefore, since a small percentage of the signal from 500 years before present is contained in the top 90 m and to conform to the Monte Carlo method, the initial condition is set at 500 years before present.

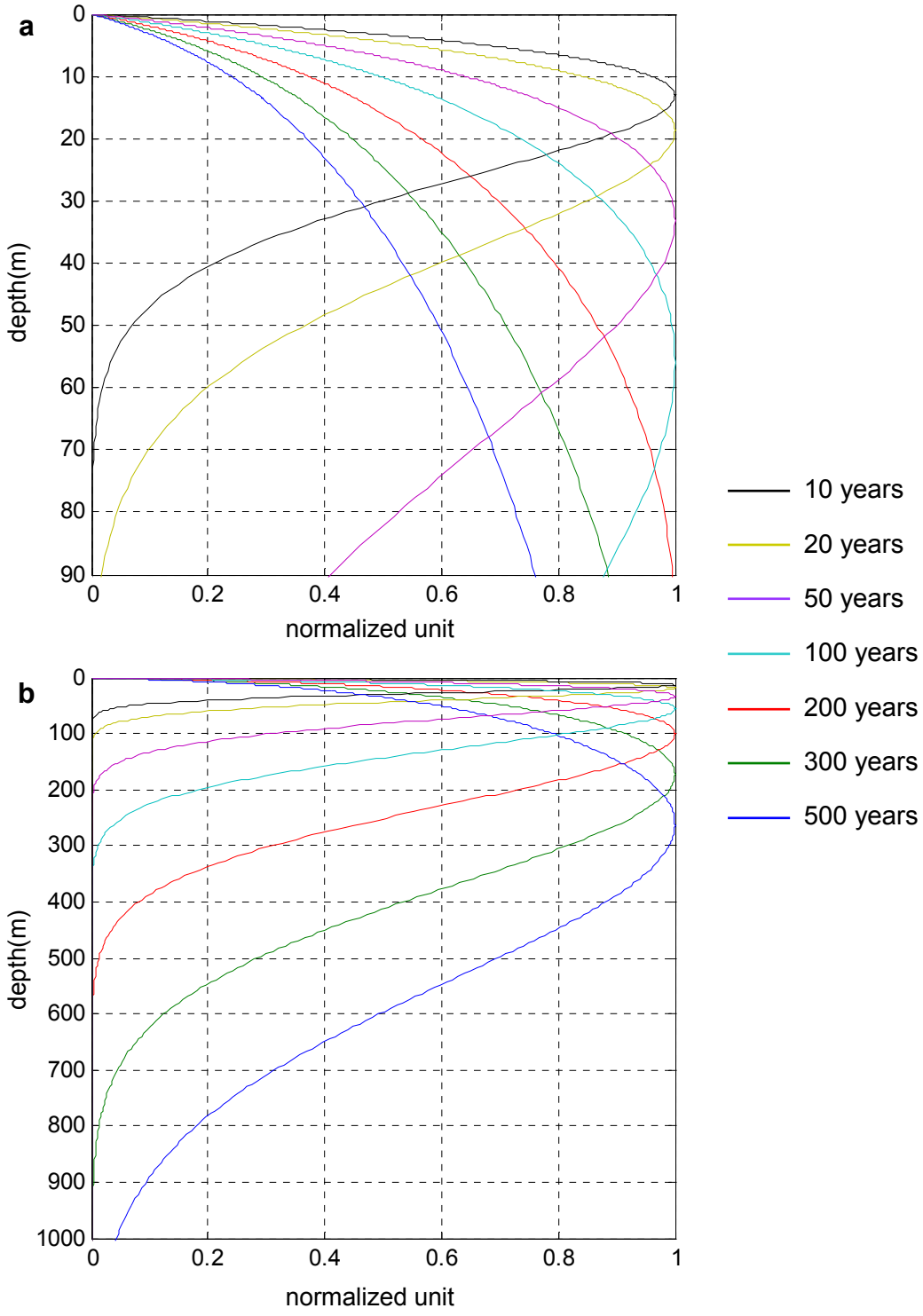

Figure 4.4. Thermal response functions at different times for **a.** the top 90 m and **b.** 1000 m of the ice sheet. Conditions at NUS07-2 were used to derive these thermal response functions.

4.3.3 Solution strategy

The model m is a continuous function lying in an infinite-dimensional space called the 'model space'. This means that the solution contains in principle an infinite number of variables (Parker, 1977). Since only a finite set of data can be obtained in reality, the inverse problem is as underdetermined as it can be and infinitely many solutions exist for m (e.g. Parker, 1977; Truffer, 2004). This 'non-uniqueness' of the model is made more severe as data errors or noise increases (Oldenburg, 1984). To overcome this difficulty, regularization is utilized, where a well-behaved model is selected from the infinite set that satisfies the data, within some imposed constraints (Parker, 1994).

To find m, we demand that m has the minimum magnitude, as measured by a scalar functional called the 'model norm', denoted by $||m||$ (Waddington et al., 2007). The norm of choice here is the '2-norm' which corresponds to the ordinary length of a vector (Euclidean norm). The model norm can be written as $||m||_2$ with the subscript 2 denoting the 2-norm. The heat transfer process is diffusive in nature and smears out the details of the boundary conditions over time. This leads us to intuitively seek m that is smooth and with the least amount of oscillations to prevent ourselves from accepting solutions that may show features that are far too detailed in time than expected (i.e., annual oscillations from 50 years ago).

Data **d** contain uncertainties so it is undesirable to fit them exactly. Rather, data should be fit within some tolerance Θ which is based on uncertainties of the data σ (Parker, 1994),

$$\Theta = \sigma N^{1/2}\left[1 - \frac{1}{4N} + \frac{1}{32N^2} + O\left(N^{-3}\right)\right]. \tag{4.15}$$

If a prediction functional $F[m]$, or the forward problem, is defined as,

$$F[m] = Gm, \tag{4.16}$$

the difference between the observational data **d** and the result of the prediction functional scaled by data uncertainties gives a 'misfit functional',

$$\delta[m] = \left\| \Sigma^{-1} \left(\mathbf{d} - F[m] \right) \right\|_2 \tag{4.17}$$

where Σ is a vector of standard deviations of data (σ_j's). We seek a model that gives a misfit functional within Θ. It turns out that the smoothest model has the largest allowable misfit (Parker, 1994), hence we seek a condition $\delta[\mathbf{m}] = \Theta$.

Constraints used for the regularization of the model *m* can now be stated as: find *m* that 1) has the smallest norm and 2) gives the misfit functional equaling the tolerance *Θ*. Two constraints have to be met simultaneously and the Lagrange multiplier *v* is used to form a functional,

$$U[m, \nu] = \|m\|^2 - \nu \left(\Theta^2 - \delta^2[m] \right). \tag{4.18}$$

m and *v* can be found by setting the gradient of *U* with respect to *m* and *v* equal 0.

4.3.4 Solution procedure - true norm-minimizing solution

To actually obtain the solution in the above manner, the true norm-minimizing solution developed by Clow (unpublished) is followed. Unless otherwise stated, materials presented in this section are from Clow (unpublished). This method approximates the model *m* by a linear combination of orthonormal basis functions that span the model space. The solution is obtained by a linear combination of the 'natural modes' of the physical system the problem is dealing with.

As the first step, space and time variables are cast into dimensionless form to increase

the numerical stability. Dimensionless time is defined as,

$$\tau \equiv \frac{t}{t^*}, \tag{4.19}$$

where t^* is the time scale of the problem which can be chosen to be some convenient number. Here, t^* = 100 years was used. Time running backwards is defined as,

$$\eta = \tau - \tau_0, \tag{4.20}$$

where τ_0 is the time of initial condition (t = 0). Clow (unpublished) found that further numerical stability is gained if η is cast into a logarithmic scale,

$$\chi = \ln(\eta). \tag{4.21}$$

The dimensionless depth is defined as,

$$\zeta \equiv \frac{z}{z^*}, \tag{4.22}$$

where z^* is the vertical extent of the solution domain. z^* is 90 m for NUS07-2, -5 and -7, and 80 m for NUS08-5.

The computation in reality requires problem to be solved in a finite-dimensional form. Therefore, m is numerically approximated and treated as a vector **m** whose components are samples of the surface temperature history at L points. For the approximate problem, the prediction functional, can be written as,

$$\mathbf{F}[\mathbf{m}] = G\,W\,\mathbf{m}, \tag{4.23}$$

where G is a $N \times L$ matrix of representer functions where the j^{th} row is the representer $g_j(\tau)$ sampled from χ_1 to χ_L,

$$G = \begin{bmatrix} g_1(\chi_1) & \rightarrow & g_1(\chi_L) \\ g_2(\chi_1) & \rightarrow & g_2(\chi_L) \\ & \vdots & \\ g_N(\chi_1) & \rightarrow & g_N(\chi_L) \end{bmatrix}. \tag{4.24}$$

W is the diagonal matrix of size $L \times L$ of quadrature weights providing a numerical quadrature approximation for functions like $\mathbf{m}$ and G (Parker, 1994),

$$W = \text{diag}(w_1, w_2, \ldots, w_L). \tag{4.25}$$

The numerical quadrature rule used here is the trapezoidal rule and the quadrature weights w_k are,

$$w_k = \frac{1}{2}[(\chi_2 - \chi_1), (\chi_3 - \chi_1), (\chi_4 - \chi_2), \ldots, (\chi_{k+1} - \chi_{k-1}), \ldots, (\chi_L - \chi_{L-1})]. \tag{4.26}$$

Using this quadrature weights, the numerical approximation of the model norm $\|m\|$ can be defined as,

$$\|R\,\mathbf{m}\| = \|m\| \tag{4.27}$$

where R is called the regularizing matrix. For the 2-norm that is used here, R is,

$$R = W^{1/2} = \mathrm{diag}\left(w_1^{1/2}, w_2^{1/2}, \ldots, w_L^{1/2}\right). \tag{4.28}$$

With the above definitions, misfit functional (4.17) can now be rewritten as,

$$\delta[\mathbf{m}] = \left\| \Sigma^{-1} \left(\mathbf{d} - \mathbf{F}[\mathbf{m}] \right) \right\|_2 \tag{4.29}$$

and the functional (4.18) as,

$$U[\mathbf{m}, \nu] = \|R\,\mathbf{m}\|^2 - \nu\left(\Theta^2 - \delta^2[\mathbf{m}]\right). \tag{4.30}$$

In expanding equation (4.30), it is useful to define a data vector scaled by the uncertainty matrix Σ^{-1},

$$\mathbf{e} = \Sigma^{-1}\,\mathbf{d}, \tag{4.31}$$

and a new model vector,

$$\mathbf{y} = R\,\mathbf{m}. \tag{4.32}$$

The misfit functional (4.29) then becomes,

$$\begin{aligned} \delta[\mathbf{m}] &= \left\| \Sigma^{-1} \left(\mathbf{d} - \mathbf{F}[\mathbf{m}] \right) \right\|_2 \\ &= \left\| \Sigma^{-1} \left(\mathbf{d} - GW\,\mathbf{m} \right) \right\|_2 \\ &= \left\| \mathbf{e} - \Sigma^{-1} GW R^{-1} \mathbf{y} \right\|_2 \\ &= \left\| \mathbf{e} - A_1 \mathbf{y} \right\|_2, \end{aligned} \tag{4.33}$$

where matrix A_1 is $\Sigma^{-1}GWR^{-1}$. A_1 can be factorized using the Singular Value Decomposition, or SVD (e.g. Strang, 2009) as,

$$A_1 = V\, S^T\, U^T, \tag{4.34}$$

assuming the $L > N$. U ($L \times L$) and V ($N \times N$) are orthogonal matrices and S is comprises of a diagonal and a zero matrix,

$$S = \begin{bmatrix} S_1 \\ O \end{bmatrix}, \tag{4.35}$$

where O is a matrix of the appropriate size filled with zeros and S_1 is,

$$S_1 = \mathrm{diag}(s_1, s_2, \ldots, s_N), \tag{4.36}$$

where s_k are singular values of A_1. The misfit functional is rewritten as,

$$\begin{aligned} \delta[\mathbf{m}] &= \left\| \mathbf{e} - V\, S^{\mathrm{T}}\, U^{\mathrm{T}}\, \mathbf{y} \right\|_2 \\ &= \left\| V^{\mathrm{T}}\, \mathbf{e} - S^{\mathrm{T}}\, U^{\mathrm{T}}\, \mathbf{y} \right\|_2 \\ &= \left\| \left(V^{\mathrm{T}}\, \mathbf{e}\right) - \left[S_1\, O^{\mathrm{T}}\right] \left(U^{\mathrm{T}}\, \mathbf{y}\right) \right\|_2 \\ &= \left\| \tilde{\mathbf{e}} - \left[S_1\, O^{\mathrm{T}}\right] \tilde{\mathbf{y}} \right\|_2 \end{aligned} \tag{4.37}$$

where new vectors are defined with coordinate rotation by the matrices V^{T} and U^{T},

$$\tilde{\mathbf{e}} = V^{\mathrm{T}}\, \mathbf{e} \tag{4.38}$$

$$\tilde{\mathbf{y}} = U^{\mathrm{T}}\, \mathbf{y}. \tag{4.39}$$

The submatrix O^{T} has no effect so the misfit (squared) can be written in terms of a sum as,

$$\delta^2[\mathbf{m}] = \sum_{i=1}^{N} (\tilde{e}_i - s_i \tilde{y}_i)^2 . \tag{4.40}$$

Recall that the model norm is given by,

$$\| \mathbf{m} \| = \| R\, m \|_2 = \| \mathbf{y} \|_2 = \| \tilde{\mathbf{y}} \|_2 . \tag{4.41}$$

Since $\tilde{y}_i = 0$ for $i > N$, $\| \tilde{\mathbf{y}} \|_2 = \| \tilde{\mathbf{y}}_{\mathrm{t}} \|_2$. Thus the model norm reduces to,

$$\| \mathbf{m} \| = \| \tilde{\mathbf{y}}_{\mathrm{t}} \|_2 . \tag{4.42}$$

The Euclidean norm is used so the model norm squared becomes,

$$\| \mathbf{m} \|^2 = \sum_{i=1}^{N} \tilde{y}_j . \tag{4.43}$$

Returning to the model vector **m**,

$$\mathbf{m} = R^{-1}\, \mathbf{y} = R^{-1}\, U\, \tilde{\mathbf{y}} . \tag{4.44}$$

The above equation can be interpreted as an expansion in a set of basis functions,

$$\mathbf{m} = \sum_{j=1}^{N} \tilde{y}_j\, \Psi_j , \tag{4.45}$$

where the basis functions Ψ_j are the columns of $R^{-1}U$,

$$R^{-1}\,U\ = \left[\Psi_1, \Psi_2, \cdots, \Psi_N\right], \tag{4.46}$$

and $\tilde{\mathbf{y}}$ is a vector of expansion coefficients. Basis functions, calculated by using conditions at NUS07-2, are shown in normal time scale in Figure 4.5 and in logarithmic time scale in Figure 4.6. Basis functions for sites other than NUS07-2 are not shown here since they look almost identical.

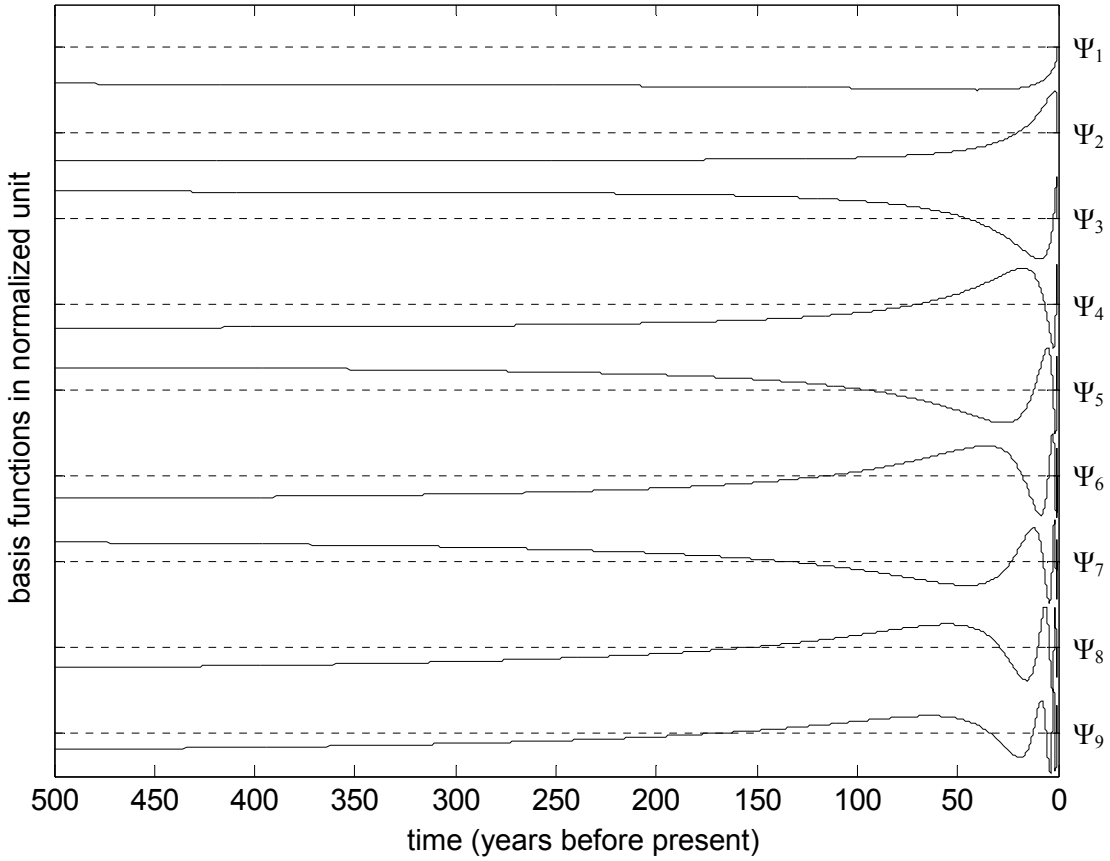

Figure 4.5. Basis functions Ψ_j in normal time scale. Each function has been scaled since the amplitudes vary greatly. Dotted lines are zero-levels for each function.

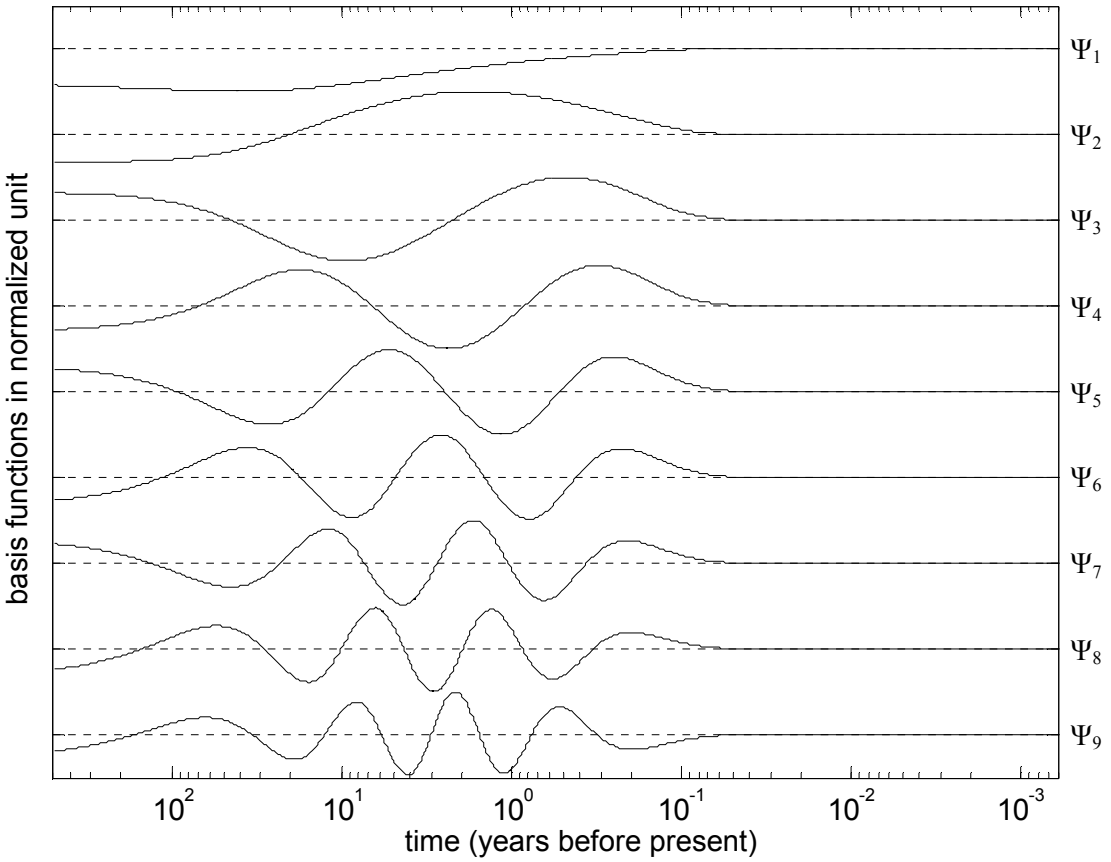

Figure 4.6. Basis functions Ψ_j in logarithmic time scale. Each function has been scaled since the amplitudes vary greatly. Dotted lines are zero-levels for each function.

Now, the functional (4.30) can be written as,

$$\begin{aligned} U[\mathbf{m},\nu] &= \|\tilde{\mathbf{y}}\|_2^2 - \nu\left[\Theta^2 - \|e - S_1\tilde{\mathbf{y}}_t\|_2^2\right] \\ &= \sum_{j=1}^{N}\tilde{y}_j{}^2 - \nu\left[\Theta^2 - \sum_{j=1}^{N}(\tilde{e}_j - s_j\tilde{y}_j)^2\right]. \end{aligned} \tag{4.47}$$

The derivative with respect to ν is,

$$\frac{\partial U}{\partial \nu} = -\left(\Theta^2 - \delta^2[\mathbf{m}]\right), \tag{4.48}$$

which is zero when,

$$\Theta = \|\tilde{\mathbf{e}} - S_1\tilde{\mathbf{y}}_t\|_2. \tag{4.49}$$

Setting the gradient of U with respect to the model coefficient vector to zero, $\partial U/\partial\tilde{y}_i = 0$. Looking at the expression for U in terms of sums,

$$\begin{aligned} \frac{\partial U}{\partial \tilde{y}_j} &= 2\tilde{y}_j - 2\nu s_j(\tilde{e}_j - s_j\tilde{y}_j) \\ &= 2(1+\nu s_j{}^2)\tilde{y}_j - 2\nu s_j\tilde{e}_j. \end{aligned} \tag{4.50}$$

Setting the gradient to zero,

$$\begin{aligned} (1+\nu_0 s_j{}^2)\tilde{y}_j &= \nu_0 s_j\tilde{e}_j \\ \left(\frac{1}{\nu_0 s_j{}^2}+1\right)\tilde{y}_j &= \left(\frac{\tilde{e}_j}{s_j}\right) \\ \tilde{y}_j &= \omega_j\left(\frac{\tilde{e}_j}{s_j}\right), \qquad j=1,2,\cdots,N, \end{aligned} \tag{4.51}$$

where

$$\omega_j = \frac{1}{\left(\frac{1}{\nu_0 \, s_j^{\,2}} + 1 \right)} \, . \tag{4.52}$$

ω_j weights on singular values s_j. Basis functions associated with small singular values contain a large amount of oscillations that would increase the model norm if equally weighted as basis functions with large singular values have small influence on the solution of m.

Finally, the model with the constrains of the minimum norm a fit within the tolerance is found by,

$$\mathbf{m}_0 = \sum_{j=1}^{N} \tilde{y}_j \, \Psi_j \, . \tag{4.53}$$

4.3.5 Error and resolution analysis

The significance of the regularized model is assessed with uncertainties in the inverted model and the temporal resolution scale of the model given by the resolving function. The uncertainty in the inverted model is estimated from the standard deviation of the expansion coefficients since $\mathbf{m}_0$ consists of basis functions Ψ_j that are scaled by expansion coefficients $\tilde{y}_i$ as shown in equation (4.53). The variance of $\tilde{y}_i$ are calculated as (Clow, unpublished),

$$\begin{aligned} \mathbf{VAR}\left[\tilde{y}_j\right] &= \mathbf{VAR}\left[\frac{\omega_j \, \tilde{e}_j}{s_j}\right] \\ &= \frac{\omega_j^{\,2}}{s_j^{\,2}} \mathbf{VAR}\left[\tilde{e}_j\right] \\ &= \frac{\omega_j^{\,2}}{s_j^{\,2}} , \end{aligned} \tag{4.54}$$

hence the standard deviation of $\tilde{y}_i$ is,

$$\sigma_{\tilde{y}_j} = \frac{\omega_j}{s_j}. \tag{4.55}$$

The variance of the model at time τ_k (k = 1 to L) is,

$$\begin{aligned} \mathbf{VAR}[m_k] &= \mathbf{VAR}\left[\sum_{j=1}^{N} \tilde{y}_j \, \Psi_{jk}\right] \\ &= \sum_{j=1}^{N} {\Psi_{jk}}^2 \, \mathbf{VAR}[\tilde{y}_j] \\ &= \sum_{j=1}^{N} \frac{{\omega_j}^2 \, {\Psi_{jk}}^2}{{s_j}^2}. \end{aligned} \tag{4.56}$$

The standard deviation of the model is then,

$$\sigma_{m_k} = \left[\sum_{j=1}^{N} \frac{{\omega_j}^2 \, {\Psi_{jk}}^2}{{s_j}^2}\right]^{1/2}, \tag{4.57}$$

where m_k and Ψ_{jk} are the k^{th} elements of vectors $\mathbf{m}_0$ and Ψ_j .

The smoothness criterion used for regularizing a model can prevent spurious details to arise. However, it can also limit the ability to resolve real structures at fine temporal scales (Waddingtion et al., 2007). In fact, the regularized model may be interpreted as the result of smoothing the real model by a set of narrowly peaked functions called resolving functions (Parker, 1994). Therefore, temporal resolution scale of the model can be examined by resolving functions and the spread which is derived from resolving functions. Resolving functions are also found for L different times, by running the forward model with a δ-function and then inverting the result using the same Lagrange multiplier used to find the model (Parker, 1994; Truffer, 2004). The half-width of the resolving functions is called the spread which is often used to measure the physical scale of details than can be resolved with the

inverse method, as was done in e.g. Harris and Chapman (1998) and Truffer (2004). Following this approach, the regularized model is viewed as consisting of the weighted average of the true model over the time period of the spread.

4.4 Monte Carlo inversion method

Monte Carlo methods are defined as experiments making use of random numbers to solve problems that are either probabilistic or deterministic in nature (Sambridge and Mosegaard, 2002). It is important to state that the above meaning applies to either simulation of actual random processes (a probabilistic problem) or the use of random numbers to solve problems that do not involve random process (deterministic problem; Sambridge and Mosegaard, 2002). It is obvious that the borehole paleothermometry problem is a deterministic problem: there is only one surface temperature history that leads to the observation of subsurface temperature distribution and it did not happen at random. Therefore, the Monte Carlo method solves the problem with a probabilistic approach. The linearized method of the last section solves the problem with a deterministic approach. There are several variants of Monte Carlo inversion techniques, a good review of which is given by Sambridge and Mosegaard (2002).

4.4.1Bayesian inference

Here, the inverse problem is cast into a Bayesian formulation and the solution of the problem is given as the probability density function (PDF) of the model parameters. Bayesian inference provides a framework for combining the *a priori* model information with the information contained in the data to arrive at a more refined statistical distribution (Scales and Snieder, 1997). The probability distribution of the model parameter vectors conditioned on the data and prior information is given by Bayes' law and is termed the posterior (e.g.

Malinverno, 2002; Hopcroft et al., 2007),

$$p(\mathbf{m} \mid \mathbf{d}, \wp) = \frac{p(\mathbf{m} \mid \wp) \times p(\mathbf{d} \mid \mathbf{m}, \wp)}{p(\mathbf{d}, \wp)}, \tag{4.58}$$

where p(...) stands for probability, 'a | b' implies conditional dependence of a on b (a given b), **m** and **d** are the model and data vectors and $\wp$ is the prior information or hypothesis underlying the model formulation. With these definitions, $p(\mathbf{d} \mid \mathbf{m}, \wp)$ is the probability of observing the data given the model and the prior information $\wp$, and $p(\mathbf{m} \mid \wp)$ is the probability distribution of the model parameters given the prior information (Hopcroft et al., 2007). The denominator of (4.58) is commonly called the 'marginal likelihood' or 'evidence' and is defined as (Sambridge et al., 2006),

$$p(\mathbf{d}) = \int p(\mathbf{d} \mid \mathbf{m}) \times p(\mathbf{m})\, d\mathbf{m}. \tag{4.59}$$

The evidence is the integral of the numerator of (4.58) that normalizes the posterior pdf (Malinverno, 2000). The above equation indicates that the evidence is not directly a function of the model (Malinverno, 2002; Sambridge et al., 2006). For this reason as well as the fact that it can be difficult to calculate, the evidence is typically ignored for geophysical inverse problems (Sambridge et al., 2006). In words, equation (4.58) can be written as (e.g. Sambridge et al., 2006; Hopcroft et al., 2009),

$$\text{posterior} = \frac{\text{likelihood} \times \text{ prior}}{\text{evidence}}. \tag{4.60}$$

The prior probability distribution used in inverse problems introduces information into the model so that the inverse solution is constrained in some sense (Hopcroft et al., 2007). In

the linearized method, the constraint on the model was placed by the smoothness criterion in regularization process.

4.4.2 Reversible Jump Markov Chain Monte Carlo

The posterior PDF is determined here by using the Reversible Jump Markov chain Monte Carlo (RJ-MCMC). RJ-MCMC was first introduced by Green (1995) and has subsequently been employed in geophysical problems, mainly solid earth geophysics, by several authors (e.g. Malinverno, 2002; Sambridge et al., 2006). RJ-MCMC was applied to borehole paleothermometry problem by Hopcroft et al. (2007; 2009) where surface temperature histories in the northern hemisphere (mainly from the United Kingdom) were inverted from terrestrial borehole temperature profiles and results that are coherent with other borehole temperature inversions and multi-proxy surface temperature reconstructions (e.g. Briffa and Osborn, 2002; Beltrami and Bourlon, 2004) were obtained.

RJ-MCMC was chosen over other Monte Carlo inversion methods because of its unique capability to jump between parameter subspaces of differing dimensionality (Green, 1995). In other words, "the number of unknowns itself is unknown" and the dimension of the parameter space is a variable to be solved for (Sambridge et al., 2006). In the context of borehole paleothermometry, dimension of the parameter space includes the number of the surface temperature time-points; the more time-points there are, the more complex the surface temperature history is and vice-versa. It is important to note that the surface temperature history, a continuous function, is treated as a series of linear segments. The nodes of these segments are the temperature time-points.

Previous examples of borehole paleothermometry problems on ice sheet locations that used Monte Carlo methods were solved for fixed-dimensions. Dahl-Jensen et al. (1998) divided the surface temperature history into 125 intervals starting with a 10 years at the most

recent time and increasing to 25k years at the end of the history (450k years before present). Barrett et al. (2009) used fixed time intervals of 15 years for the entire length of the history (300 years). Such practice can lead to a surface temperature history with more detail than can be supported by data. For example, the surface temperature history of Barrett et al. (2009) shows a temperature increase of approximately 0.2 K between ~1760 and 1775 AD followed by a decrease of about the same amount in the next 15 years. Reflecting on the resolution analysis of Clow (1992), a climatic event of such magnitude and duration occurring ~230 years ago can not be resolved from data of Barrett et al. (2009) - temperatures measured at 10 different depths down to 300 m depth and with an estimated uncertainty of 0.01 K. Without a resolution analysis such as the one described for the linearized inversion, which is the case for Barrett et al. (2009), results can potentially be over-interpreted. Because of its parsimonious nature, RJ-MCMC preferentially samples simpler models provided that they can adequately explain or fit the data (Hopcroft et al., 2007), hence avoiding a risk of resolving features or events that are not warranted by data.

RJ-MCMC consists of two-stage process of proposing a model probabilistically and then accepting or rejecting this proposed model. The new model $\mathbf{m}'$ is proposed by drawing from a probability $q(\mathbf{m}' \mid \mathbf{m})$ such that a newly proposed model $\mathbf{m}'$ is conditional only on the current model $\mathbf{m}$. For a proposal without a change in dimensions, the newly proposed model is accepted with an acceptance probability,

$$\alpha = \min\left[1,\ \frac{p(\mathbf{m}'|\wp)}{p(\mathbf{m}|\wp)} \cdot \frac{p(\mathbf{d}|\mathbf{m}')}{p(\mathbf{d}|\mathbf{m})} \cdot \frac{q(\mathbf{m}|\mathbf{m}')}{q(\mathbf{m}'|\mathbf{m})}\right], \tag{4.61}$$

or in simpler terms,

$$\alpha = \min\left[1,\ (\text{prior ratio}) \cdot (\text{likelihood ratio}) \cdot (\text{proposal ratio})\right], \tag{4.62}$$

which is know as the Metropolis-Hastings rule (Metropolis and Ulam, 1949; Hastings, 1970). The more general form of the acceptance probability that accounts for dimension-change is,

$$\alpha = \min\left[1,\ \frac{p(\mathbf{m}'|\wp)}{p(\mathbf{m}|\wp)} \cdot \frac{p(\mathbf{d}|\mathbf{m}')}{p(\mathbf{d}|\mathbf{m})} \cdot \frac{q(\mathbf{m}|\mathbf{m}')}{q(\mathbf{m}'|\mathbf{m})} \cdot |\mathbf{J}|\right], \tag{4.63}$$

or,

$$\alpha = \min\left[1,\ (\text{prior ratio}) \cdot (\text{likelihood ratio}) \cdot (\text{proposal ratio}) \cdot (\text{Jacobian})\right]. \tag{4.64}$$

The Jacobian **J** accounts for the transformation from the current model **m** to the proposed model **m**' and is given by,

$$|\mathbf{J}| = \left|\frac{\partial(\mathbf{m}', \mathbf{u}')}{\partial(\mathbf{m}, \mathbf{u})}\right|, \tag{4.65}$$

where **u** and **u**′ are vectors of random numbers used to transform the current model to the proposed model. The Jacobian ensures that the probability of sampling different dimensions is not artificially biased (P. Hopcroft, personal communication). For fixed-dimension cases, the Jacobian is 1 and discarded. The exact forms of the acceptance probability are presented in Appendix B of Hopcroft et al. (2007).

If the newly proposed model is accepted, then previous model **m** is replaced by **m**′ and moves to the next iteration. After an initial 'burn-in' period in which the random walker moves towards the high posterior probability region, the chain samples a desired posterior PDF (Malinverno, 2002). This means that the algorithm returns model parameters that are distributed in the posterior PDF and a good estimate of the true probability distribution is given (e.g. Gilks et al., 1996). An MCMC algorithm effectively has a memory mechanism

that makes the chain stay in the high posterior probability region of model space and thus it is much more efficient than Monte Carlo methods such as the one employed by Dahl-Jensen et al. (1998) where models are chosen independently and tested against data (Malinverno, 2002).

Model setup

Following the procedure of Hopcroft et al. (2007), the surface temperature history is set up as a series of linear segments with nodes of these segments being k surface temperature history time-points, represented by Figure 4.7. The number of k is varied between 2 and 15 with a minimum case (k = 2) having time-points at the present and L (length of time inverted for). For the time before L, the pre-observational mean surface temperature (T_{POM}) is defined and together with the basal temperature (T_b) it gives the steady state temperature profile in the firn-ice column that is used as the initial condition for the forward model.

The model parameter vector is then,

$$\mathbf{m} \in \{ \mathbf{T}, \mathbf{t}, T_b, T_{POM} \}, \tag{4.66}$$

where **T** and **t** are vectors of temperatures and time-points, respectively, T_b is the basal temperature and T_{POM} is the pre-observational mean surface temperature. Parameters of **m** are used in the forward model to obtain a simulated temperature profile from which temperature values at depths corresponding to the measured temperatures are extracted to construct a vector $\mathbf{d}_{\text{sim}}$. The forward model is run at time steps of 1/12 year for the most recent ten years then one year for the rest of the period.

The length of time inverted for, or L, is 500 years in this research. It was shown in section 4.3.2 that there is little effect of the initial condition set at 500 years before present in

today's temperature profile hence the dependence of the inverted model on the initial condition is minimal. Another important consideration in selecting L is the computational time. RJ-MCMC is a computationally expensive method since several hundred thousand samples are required to define the posterior PDF. Therefore, the time required for one iteration should be kept to a minimum. The longer the L, the longer the one forward model run within one iteration and hence the longer the whole run of RJ-MCMC. Given the available computational resources for this research, one run of the RJ-MCMC for surface temperature sampling typically took 3.5 to 4 days with L = 500 years. This was determined to be a practically feasible amount of time to conduct the research in a reasonable time-frame.

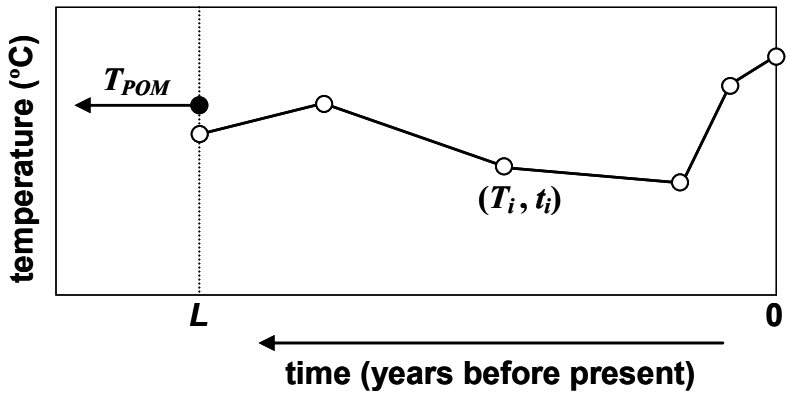

Figure 4.7. Setup of the surface temperature history. Adapted from Hopcroft et al., (2007).

Prior

The prior on the surface temperature values is set to a multivariate Gaussian distribution centered on the pre-observational mean temperature (T_{POM}), found by running an exploratory RJ-MCMC simulation before the actual surface temperature history sampler ,

$$p(\mathbf{T}|\wp) = \frac{1}{\left[(2\pi)^k \det C_{pr}\right]^{1/2}} \cdot \exp\left[-\frac{1}{2}\left(\mathbf{T}-\mathbf{T}_{\text{prior}}\right)^{\mathrm{T}} C_{pr}^{-1}\left(\mathbf{T}-\mathbf{T}_{\text{prior}}\right)\right], \quad (4.67)$$

where **T** is a vector containing current model values of the surface temperature, $\mathbf{T}_{prior}$ is a vector of prior mean values and k is the number of surface temperature time-points. C_{pr} is a diagonal matrix with entries equal to 1.0 meaning that there is no correlation assumed on the prior information. It can be seen from equation (4.67) that for the case a constant surface temperature history, the prior calculated with a lower *k* is higher than with a higher *k*. Therefore, a model with lower *k* would be accepted even with the same data fit and this is the parsimony enforced by the RJ-MCMC algorithm.

Positions of surface temperature time-points are drawn as the order statistics from a uniform distribution over the time interval that is inverted for (Green, 2001; Hopcroft et al., 2007). The prior probability on the time-points is,

$$p(\mathbf{t}|\wp) = \frac{k!\, I\left[0 < t_1 < t_2 < \ldots < t_k < L\right]}{L^k}, \quad (4.68)$$

where **t** is a vector containing time-points, *L* is the length of the time domain ($L = t_{\max} - t_{\min}$).

The prior on the number of time-points *k* is set to a uniform distribution between 2 and 15. *k* directly relates to the resolution of the inverted surface temperature history. The resolution of the surface temperature histories derived from the borehole paleothermometry with similar measurement uncertainty as in this research have been shown to be low in general (e.g. Clow, 1992; Beltrami and Bourlon, 2004). However, there is actually no information on the dimensionality of the surface temperature history required by data, other than 'it should be low'. Utilizing a uniform distribution is an appropriate measure to overcome this difficulty since the algorithm is designed to search for the appropriate

dimensionality by itself.

The prior on the basal temperature is set uniform over the interval of the pressure melting point of ice (T_{pm}), which is site-specific and calculated using equation (4.9), and 10 K lower than T_{pm}. The prior on T_{POM} is uniform over the interval of -50 and -60°C.

Likelihood

The likelihood depends on the data misfit in a least-squares sense,

$$p(\mathbf{d}_{\text{obs}} \mid \mathbf{m}, \wp, k) = \frac{1}{\left[(2\pi)^n \det C_d\right]^{1/2}} \cdot \exp\left[-\frac{1}{2}(\mathbf{d}_{\text{sim}} - \mathbf{d}_{\text{obs}})^{\text{T}} C_d^{-1} (\mathbf{d}_{\text{sim}} - \mathbf{d}_{\text{obs}})\right], \quad (4.69)$$

where there are n data points, $\mathbf{d}_{\text{sim}}$ and $\mathbf{d}_{\text{obs}}$ are vectors of modeled and observed firn temperatures, respectively. C_d is a diagonal matrix with entries equal to the variance of the measurement uncertainty. In practice, the likelihood decreases as the quadratic form ($\mathbf{d}_{\text{sim}}$ - $\mathbf{d}_{\text{obs}}$)$^{\text{T}}$ C_d^{-1} ($\mathbf{d}_{\text{sim}}$ - $\mathbf{d}_{\text{obs}}$) becomes larger. Therefore, it quantifies how likely the proposed model is in light of the data (Malinverno, 2002).

Proposal functions

At each iteration of the RJ-MCMC, one of the following types of a new model proposal is selected at random which is the same as the procedure of Hopcroft et al. (2007):

(i) Perturb one temperature value T_i

(ii) Perturb one time value t_i

(iii) Create a new surface temperature time-point (birth)

(iv) Delete a surface temperature time-point (death)

(v) Perturb T_b and T_{POM}.

The probability of selecting one of these proposals is 1/5 except when the number of

surface temperature time-points reaches k_{min} or k_{max}. When $k = k_{min}$, probability of proposal types (iv) and (v) are set to 0. When $k = k_{max}$, proposal types (iii) and (v) are set to 0. Proposal type (v) is set to 0 to improve efficiency (Hopcroft et al., 2007).

Execution of each proposal type follows the procedure presented in Appendix A of Hopcroft et al. (2007). The only difference from the practice of Hopcroft et al. (2007) is the standard deviation of the proposal for the new temperature value in a birth (σ_T^b) where 2.5×10^{-4} is used instead of 1×10^{-6}.

Sampling of the posterior distribution

The RJ-MCMC sampler starts off in the region of low probability and move towards the posterior PDF. This transition is called the 'burn-in' period. Following the practice of Malinverno (2002), burn-in period is estimated to end the first time that the standard deviation of the total data misfit is less than the standard deviation of the expected measurement errors.

Determining when a large enough number of samples were obtained to characterize the posterior PDF and to stop the MCMC sampler is still an active area of research (Malinverno, 2002; see e.g. Gilks et al. 1996 and Robert and Casella, 2004 for discussions). A practical criterion is to continue the iterations until the characteristics of the posterior PDF stop changing significantly (Malinverno, 2002). In exploratory RJ-MCMC simulations, typically, characteristics of the posterior PDF derived from 350,000 and 400,000 samples were not significantly different. Therefore, RJ-MCMC was stopped when 400,000 samples were obtained after the burn-in period.

Quantifying the posterior distribution

The posterior probability can be quantified in terms of the expectation values of the model

(Hopcroft et al., 2007). Samples of the posterior PDF generated by the RJ-MCMC can be used to calculate the expectation value as,

$$E[f(m)] = \frac{1}{n}\sum_{1}^{n} f(m). \tag{4.70}$$

where $f(m)$ is the model value (Gilks et al., 1996). The expectation value is in fact the posterior mean which is calculated by integrating across all models weighted by their posterior probability values (Hopcroft et al., 2007).

The 95% confidence interval is calculated by eliminating the 2.5% of the lowest and highest surface temperature values at time-points along the 500 years inverted for. This gives a range of the surface temperature history which has a 95% probability of enclosing the true model (Hopcroft et al., 2007).

4.5 Synthetic example

4.5.1 Synthetic surface temperature history and data

Two inverse methods described in the previous sections will now be applied to an example where synthetic data is created from a known surface temperature history, shown in Figure 4.8. The surface temperature history was created by first defining a history that is indicated by the red solid line in Figure 4.8. Then, adding normally distributed noise on top of it with a standard deviation of 0.2 K. To create synthetic data from this surface temperature history, density, thermal properties, vertical speed and ice thickness of NUS07-2, together with the pre-observational mean surface temperature (T_{POM}) of -54°C and the basal temperature (T_b) of -2°C were used.

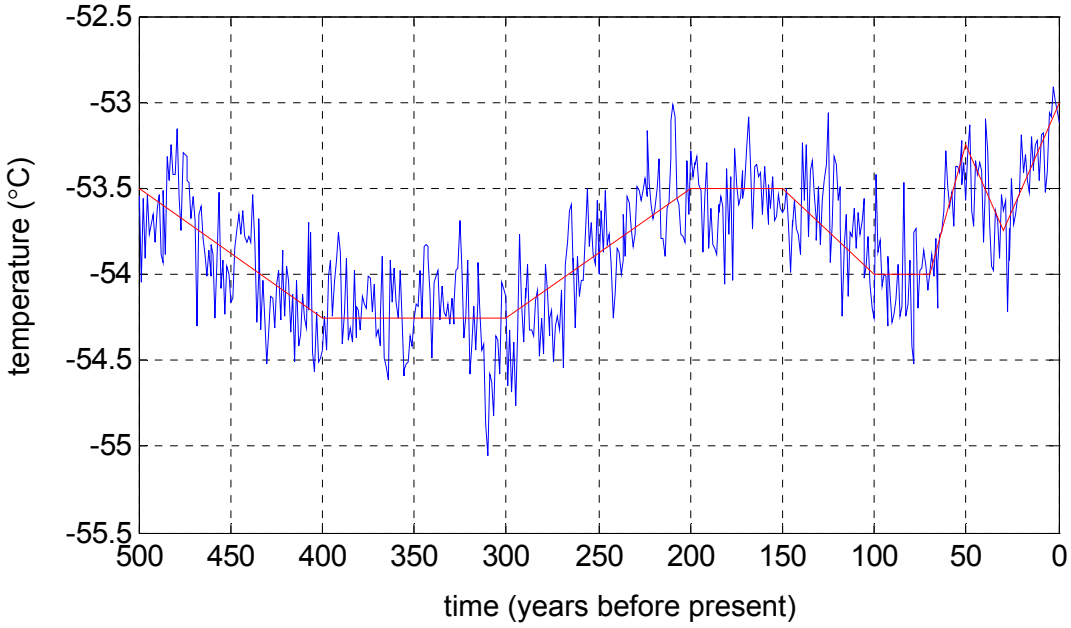

Figure 4.8. Surface temperature history used to create synthetic data (blue). Surface temperature history of red line was used as the baseline and normally distributed noise of standard deviation equaling to 0.2 K was added.

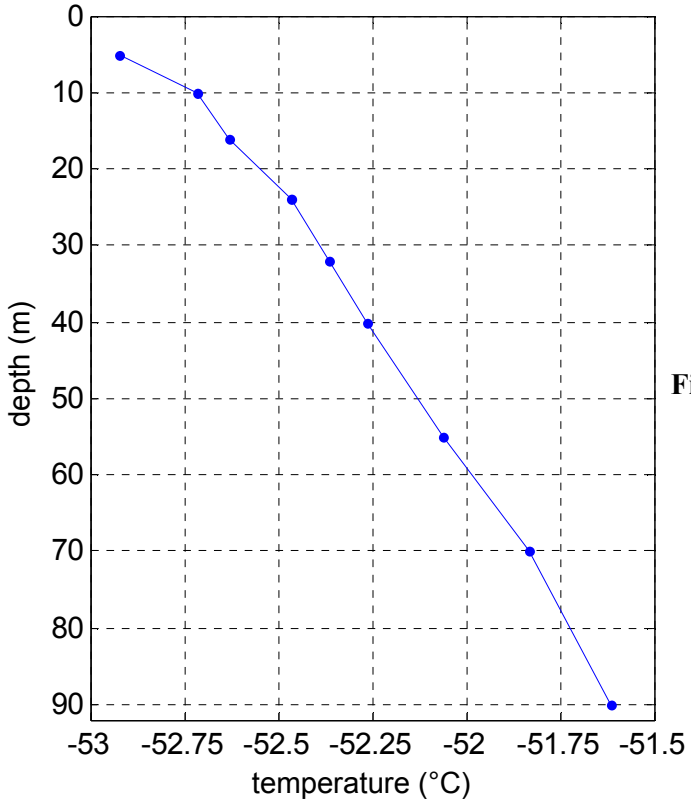

Figure 4.9. Synthetic data created from the surface temperature history shown in Figure 4.8. Noise equaling the measurement uncertainty of ATPUs (0.03 K) was added to the terminal temperature profile output by running the forward model with the synthetic surface temperature history.

4.5.2 Applying the linearized inversion method

The linearized inversion method deterministically gives a solution of the surface temperature history for one basal temperature T_b value. For this reason, the effect of different T_b in the surface temperature history is first examined.

Figure 4.10 shows models of the surface temperature history inverted from the synthetic data shown in Figure 4.9, using T_b between -11.9°C and -1.9°C (the pressure melting point of ice at NUS07-2) at 1 K increment. The largest spread in the inverted surface temperatures, 0.36 K, is at 500 years before present (b.p.), when the initial condition is set. T_b is prescribed when deriving the initial condition, as explained in section 4.3.1. hence T_b has the largest influence in setting up the initial condition. T_b = -1.9°C (-11.9°C) results in the lowest (highest) estimate of the surface temperatures for most of the time. However, the spread of surface temperature histories in the most recent ~30 years is much less at around 0.1 K which indicates a reasonable robustness of the solutions for the recent several decades against the choice of the pre-observational mean surface temperature (T_{POM}) and the basal temperature (T_b).

From this point onward, results from the linearized inversion method will be shown with the model inverted with T_b that is 5 K below the pressure melting point T_{pm} with error bounds from standard deviations of the model with T_b at T_{pm} and 10 K below T_{pm}. The model and its error bounds derived in such a way for the synthetic example are shown in Figure 4.11 for 500 years and Figure 4.12 for the most recent 100 years. Included in Figure 4.11 and 4.12 are resolving functions and spreads for selected time-points which indicate the temporal resolution scale in the inverted surface temperature history as explained in section 4.3.5. The inverted value of the T_{POM} or the surface temperature used to derive the initial condition was -53.72°C whereas the true T_{POM} was -54°C.

The feature of the inverted model that is perhaps the most obvious in Figure 4.11 is the

little change for times beyond ~50 years b.p. and the inconsistency with variations in the true surface temperature history. On the multi-century time scale, the true surface temperature varies by approximately 1 K which is not captured at all by the inverted model. The error bounds also only increase by approximately 0.08 K from 100 to 500 years b.p. This behavior can be explained in terms of resolving functions. For 100 and 250 years b.p., resolving functions look almost identical, resembling a step function rather than the δ-function which is their original form. It must then be interpreted, following the description of Parker (1994), that the lack of variations beyond ~100 years b.p. is because data contain little information from this time period and the inverted model of the surface temperature history shows only small deviations from the surface temperature used to derive the initial condition which is the T_{POM}. The resolving function for 50 years b.p. looks different from those of 100 and 250 years b.p. with a broad peak near 50 years b.p. and a sharper increase to this peak from the present. This is indicating that the data contain more information from 50 years b.p. compared to earlier times. The inverted temperature for 50 years b.p. is higher by 0.06 K than at 100 years b.p. which can be considered to be reflecting mostly T_{POM} but also including some influence from the times more recent than 50 years b.p. when the true temperature is actually higher.

Looking at more recent times in Figure 4.12, the model follows the true surface temperature history rather well back to approximately 20 years b.p., although interannual variations are not captured. More defined peaks of resolving functions compared to earlier times give some confidence to the fidelity of the inverted model for this time period. However, the resolving functions progressively become wider in a non-linear fashion and the spread increases from approximately 12 years for 5 years b.p. to 50 years for 20 years b.p. Therefore, the close matches between the inverted and the true temperatures around 20 years b.p. should be interpreted with caution. Going further back in time, the event between 70 years and 30 years b.p. (approximately 0.75 K warming from around 70 years to 50 years b.p.

then subsequent cooling of ~0.5 K to 30 years b.p.) is not represented in the inverted model. This can be considered as a result of the smearing of the event as indicated by the resolving function for 50 years b.p. What is conclusive then is that the long-term increase from the T_{POM} to the present is captured well. However, the exact timing of the onset and the magnitude of the warming trend can not be determined without ambiguities except for the past ~15 to 20 years.

It should be noted that the inverted model shows a sharp drop within the most recent 2 years. This is a combined result of the true signal and the artifact of the method. The true surface temperature history has 0.2 K decrease from 3 years to 0 years b.p. Since this is a recent event, its signal is in data. However, the inverted temperature at 0 years b.p. is equal to T_{POM} which is 0.6 K lower than that of the true history. This occurs since all of the basis functions Ψ_j (see section 4.3.4) have values of 0 at 0 years b.p. hence the inverted surface temperature for 0 years b.p. inevitably becomes T_{POM}. Also, the data used for the inversion is the annual mean below 5 m hence the data lack in constraints and there are no meanings to any details within the most recent year shown in the inverted surface temperature.

Figures 4.13 a through d show the sensitivity of the inversion results to perturbation in thermal conductivity parameterization (a), accumulation rate (b), ice sheet thickness (c) and the basal melt rate (d). Only the most recent 100 years are shown since the inverted temperatures beyond 100 years b.p. show no changes and are only indicative of T_{POM}, as described above. In all cases, the general shape of the curve is preserved. There are small deviations in the inverted temperatures for the most recent ~15 to 20 years which corroborate the inference about the past ~20 years made by examining the single inverted model and associated resolving functions.

In order to account for the sensitivity of the inverted model to the various parameters, error bounds obtained from the sensitivity tests were combined by the method of root sum of

squares (RSS). The inverted model with the error bounds calculated as such is shown in Figure 4.14. It should be noted that the error bounds shown here indicate the maximum range of errors since each sensitivity test was carried out with what is considered as the upper and lower bounds of each parameter from available data and knowledge.

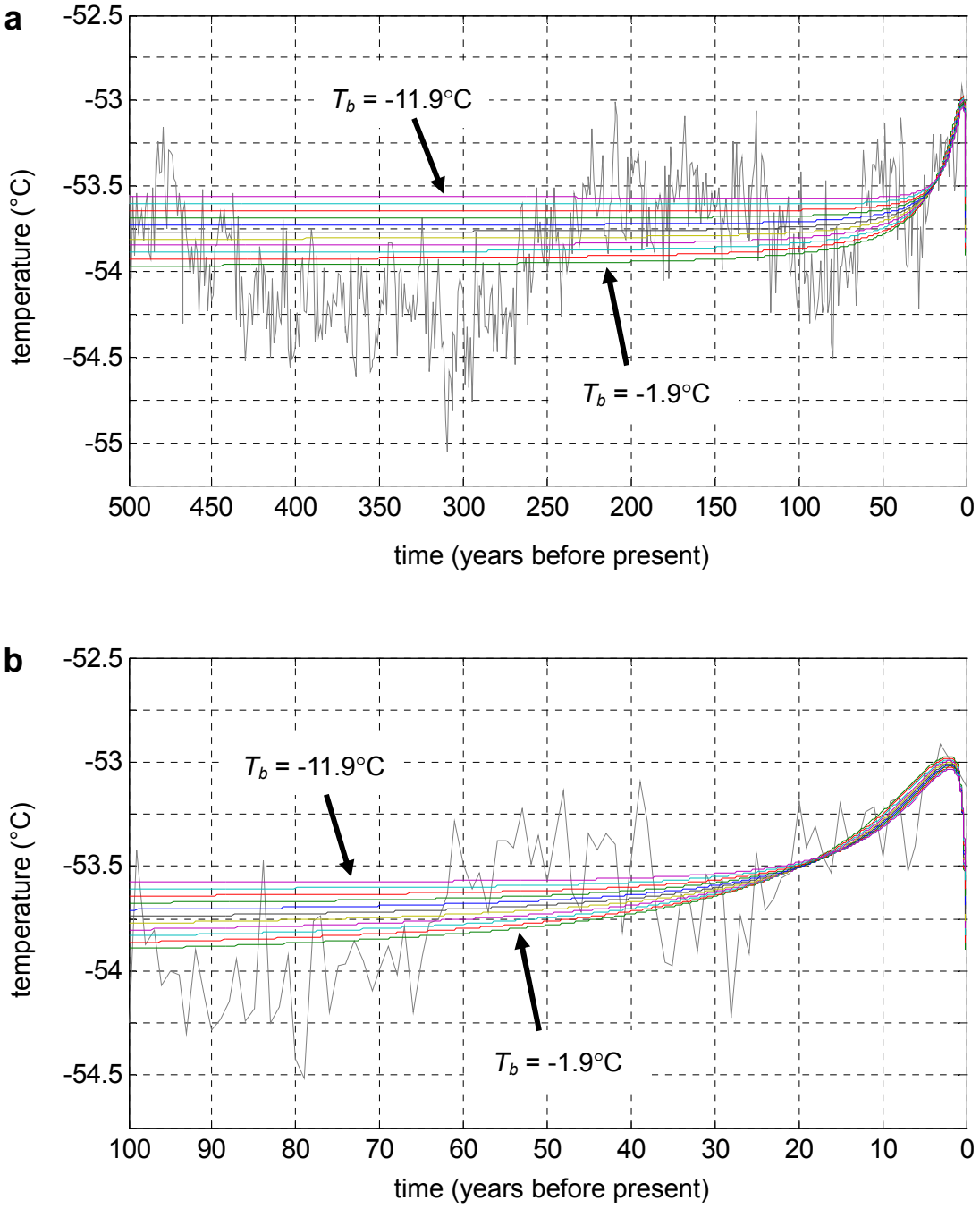

Figure 4.10. Surface temperature histories inverted using the linearized method with different basal temperatures T_b. **a**. for the entire length of time of inversion (500 years) and **b**. the most recent 100 years. Gray line is the true surface temperature history.

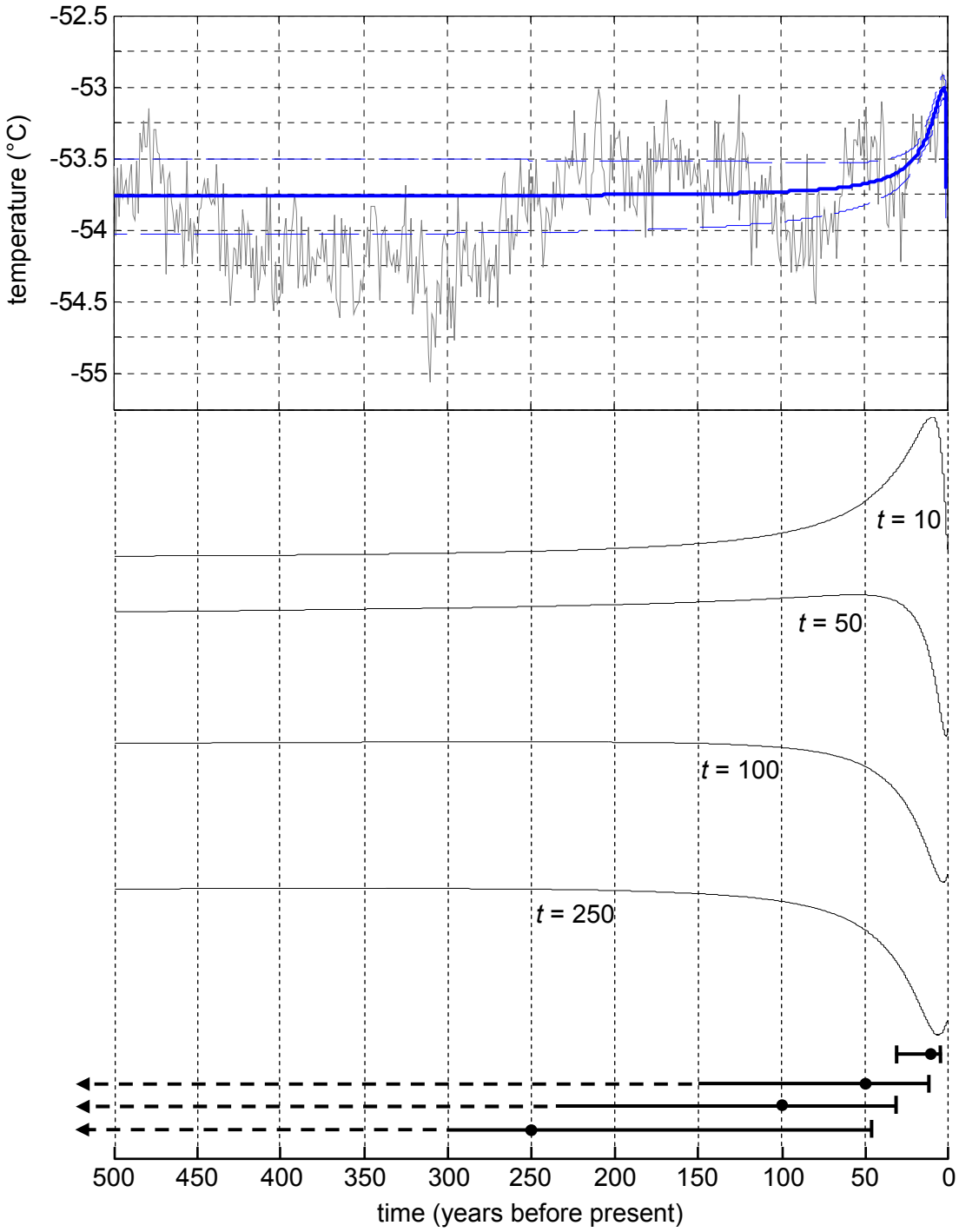

Figure 4.11. Surface temperature history inverted using the linearized method with T_b = -5.9°C for 500 years (blue solid line) with the one standard deviation error bounds (blue dashed lines). Gray solid line is the true surface temperature history. Four black solid lines are the resolving functions for different time-points with their respective spread indicated by horizontal error bars below.

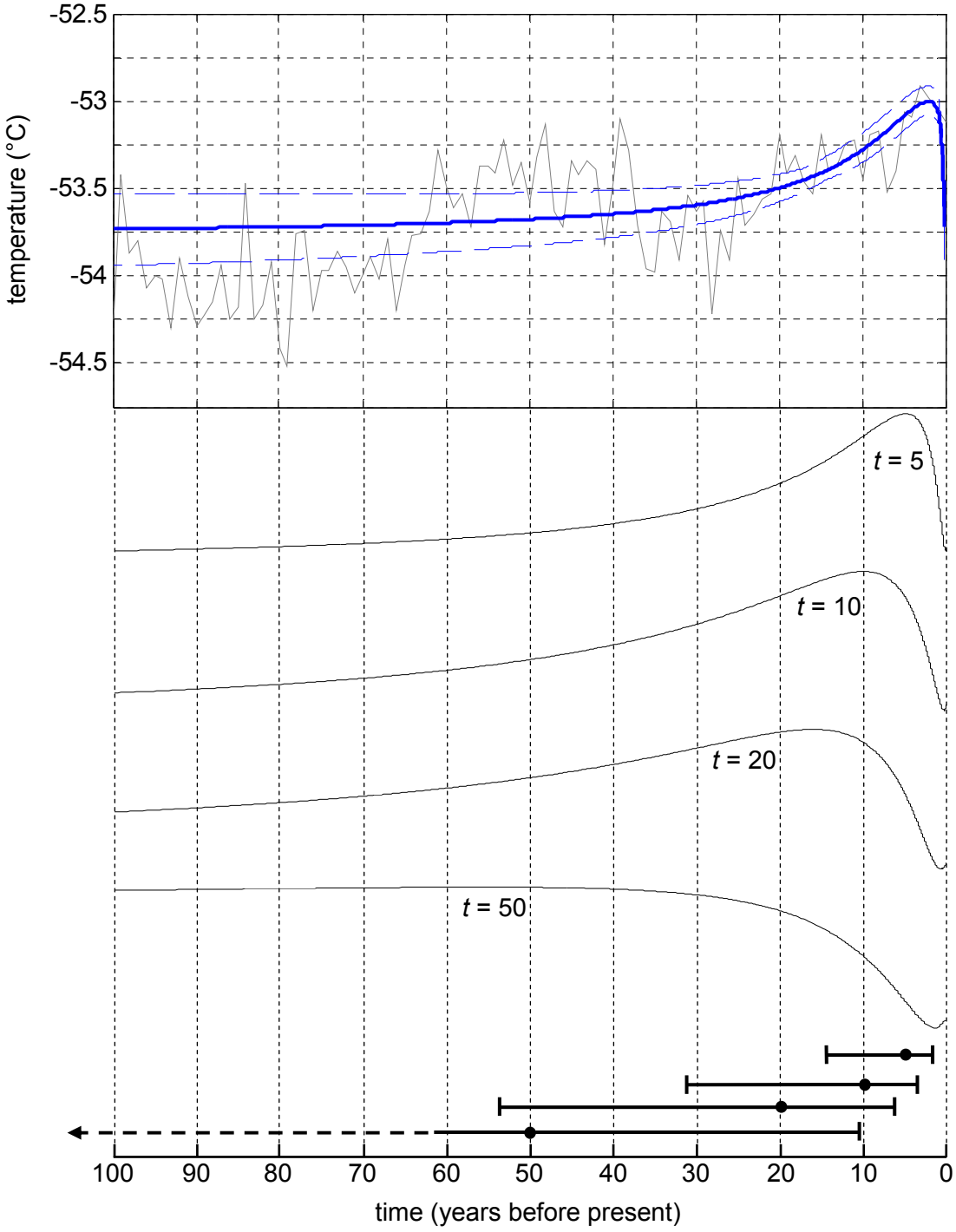

Figure 4.12. Surface temperature history inverted, same as Figure 4.11 but for the most recent 100 years (blue solid line) with the one standard deviation error bounds (blue dashed lines). Gray solid line is the true surface temperature hisotry. Four black solid lines are the resolving functions for different time-points with their respective spread indicated by horizontal error bars below.

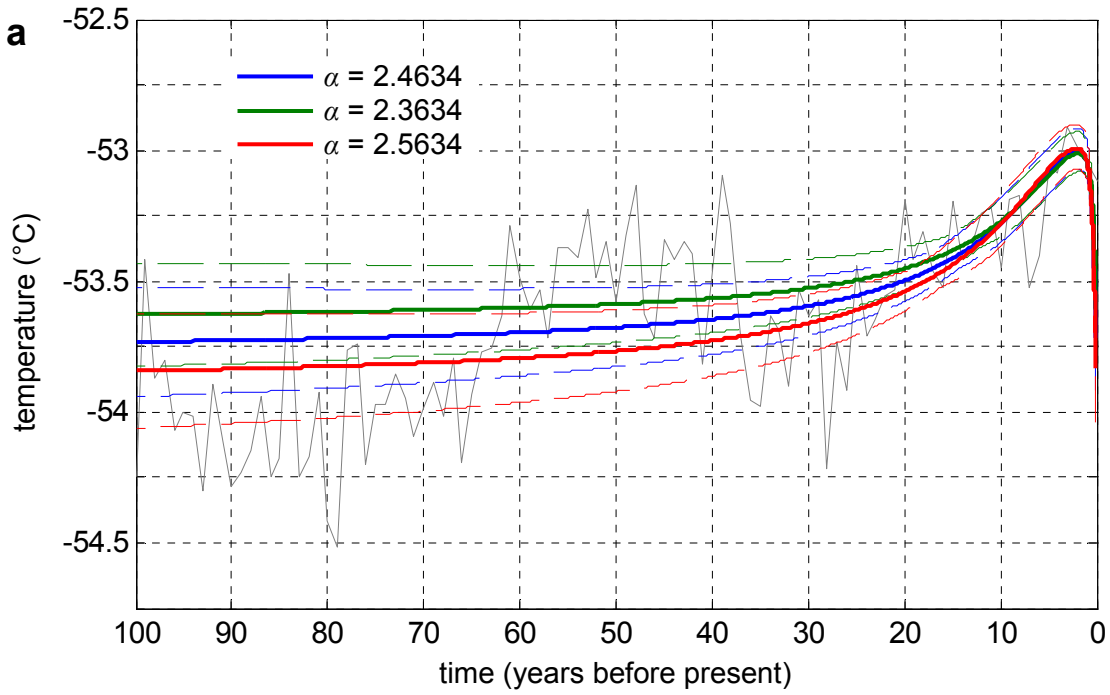
a
-52.5
-53
-53.5
-54
-54.5
temperature (°C)
α = 2.4634
α = 2.3634
α = 2.5634
100
90
80
70
60
50
40
30
20
10
0
time (years before present)

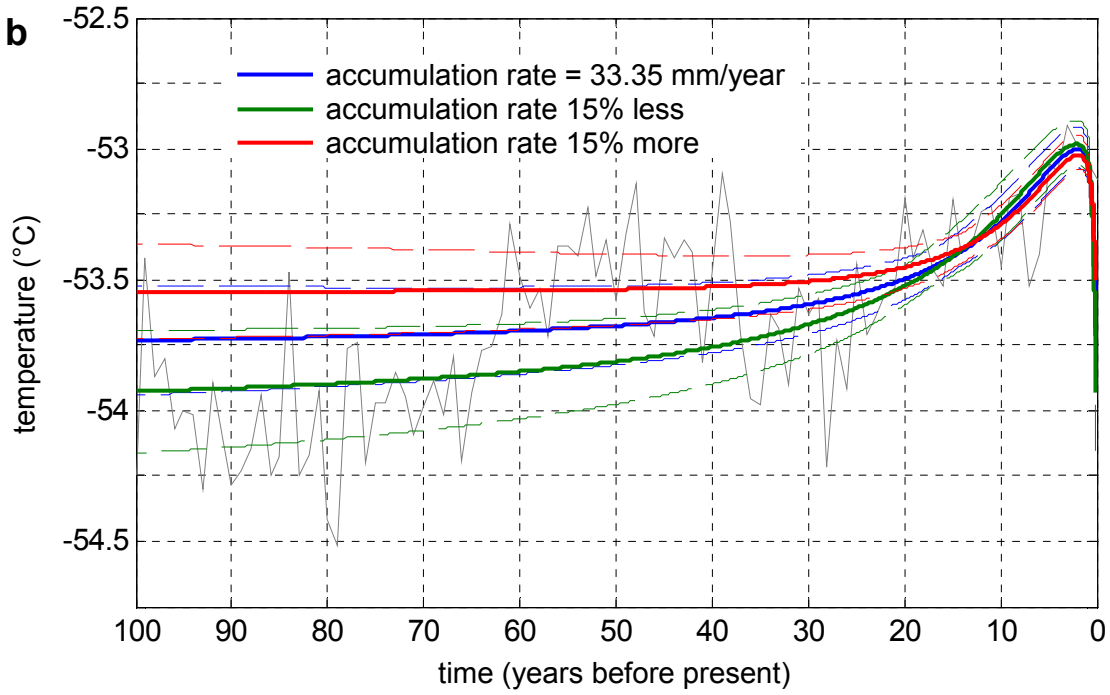
b
-52.5
-53
-53.5
-54
-54.5
temperature (°C)
accumulation rate = 33.35 mm/year
accumulation rate 15% less
accumulation rate 15% more
100
90
80
70
60
50
40
30
20
10
0
time (years before present)

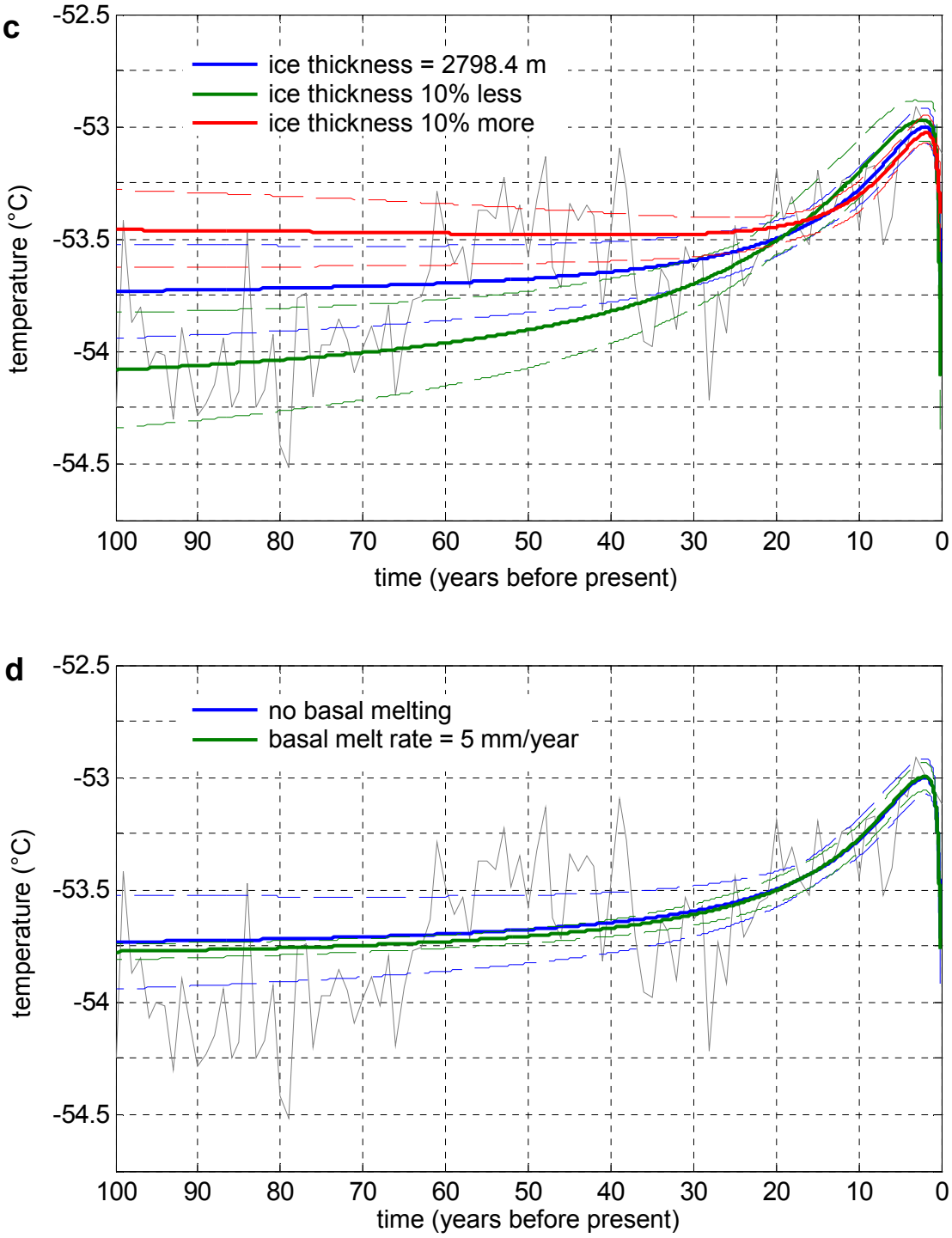

Figure 4.13. Surface temperature history inverted using the linearized method with different values of **a**. α, **b**. accumulation rate, **c**. ice sheet thickness and **d**. basal melt rate. Dashed lines indicate the one standard deviation error bounds. Gray solid line is the true surface temperature history.

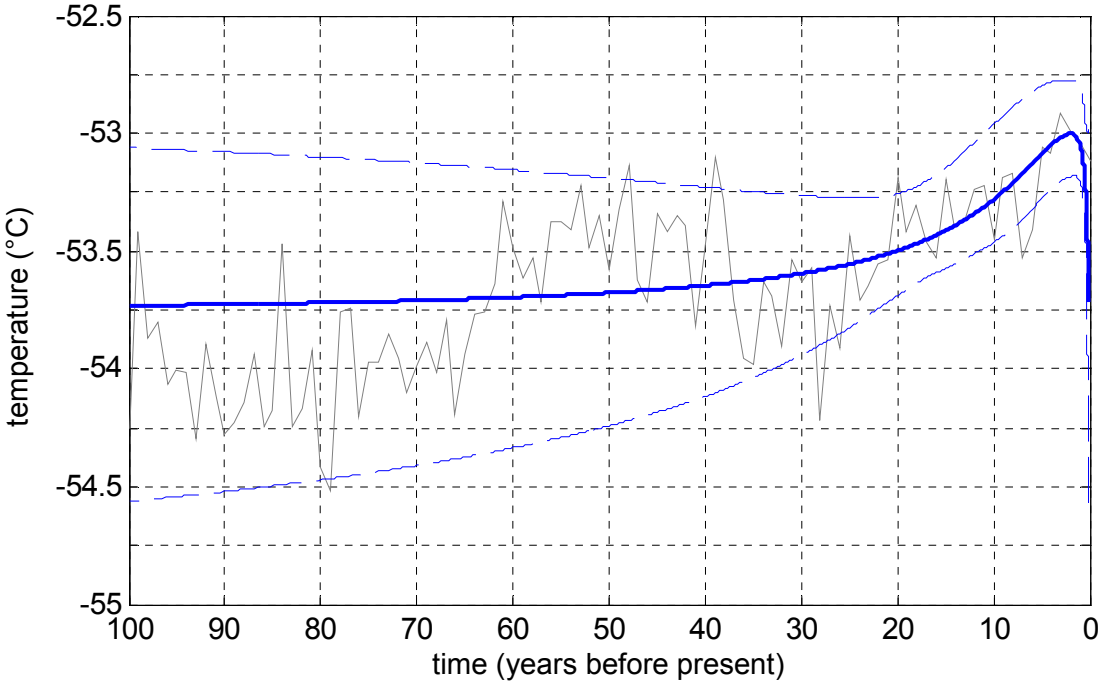

Figure 4.14. Surface temperature history inverted without perturbations in various parameters (solid blue line) and error bounds calculated by combining those from sensitivity analyses to different values of α, accumulation rate, ice sheet thickness and basal melt rate (dashed blue line). Gray solid line is the true surface temperature history.

Section 4.3.2 of this chapter discussed the justification for setting the initial condition at 500 years b.p. To demonstrate that this is in fact appropriate, inversion was performed with the time of initial condition set at 1000 years b.p. The synthetic surface temperature history shown in Figure 4.8 was first extended to 1000 years b.p. (Figure 4.15). The pre-observational mean surface temperature (T_{POM}) was set to -53.5°C in this case and the basal temperature (T_b) was again set to -2°C. New synthetic data shown in Figure 4.16 was created from this extended surface temperature history with the same procedure described in section 4.5.1 and the inversion performed using the new data. Figure 4.17 shows the two models of the surface temperature history and their associated error bounds derived by using

synthetic data created from the 500-year long surface temperature history (blue solid and dashed lines), which is the same as Figure 4.14, and at 1000-year long surface temperature history (green solid and dashed lines). It is apparent that the two models are very similar to each other and are well within each other's error bounds. The noticeable differences occur for times beyond 50 years b.p. where the two models start diverging and the temperatures for the times of initial condition differ by approximately by 0.1 K. However, as already discussed earlier in this section, inverted temperatures beyond ~50 years b.p. are strongly influenced by the T_{pom} and do not reflect details in the true surface temperature even in the decadal time-scale. Therefore, noticeable differences in inverted surface temperature histories resulting from setting the initial condition at 500 and 1000 years b.p. only occur beyond the time-scale over which data can resolve. It can then be concluded that 500 years b.p. is an appropriate time for the initial condition to be placed.

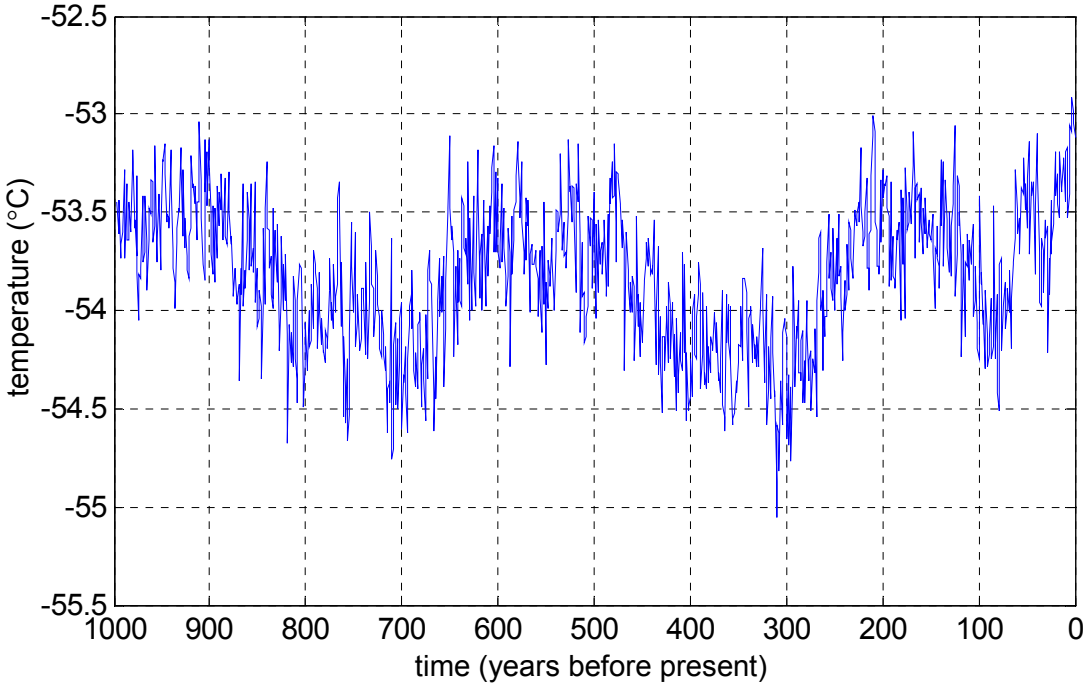

Figure 4.15. Synthetic surface temperature history that is extended to 1000 years b.p. Temperatures between 0 and 500 years b.p. are the same as the synthetic surface temperature history shown in Figure 4.8

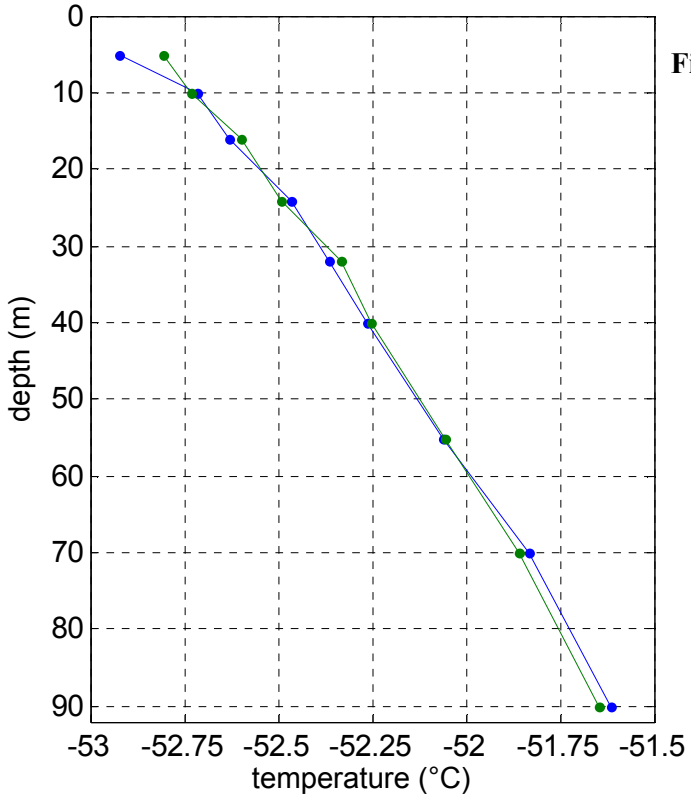

Figure 4.16. Synthetic data created from the 500-year long surface temperature history shown in Figure 4.8 (blue) and 1000-year long history shown in Figure 4.15 (green). Data from 500-year long surface temperature history is the same as in Figure 4.9. Noise equaling the measurement uncertainty of ATPUs (0.03 K) was added to the terminal temperature profile output by running the forward model with the 1000-year long history.

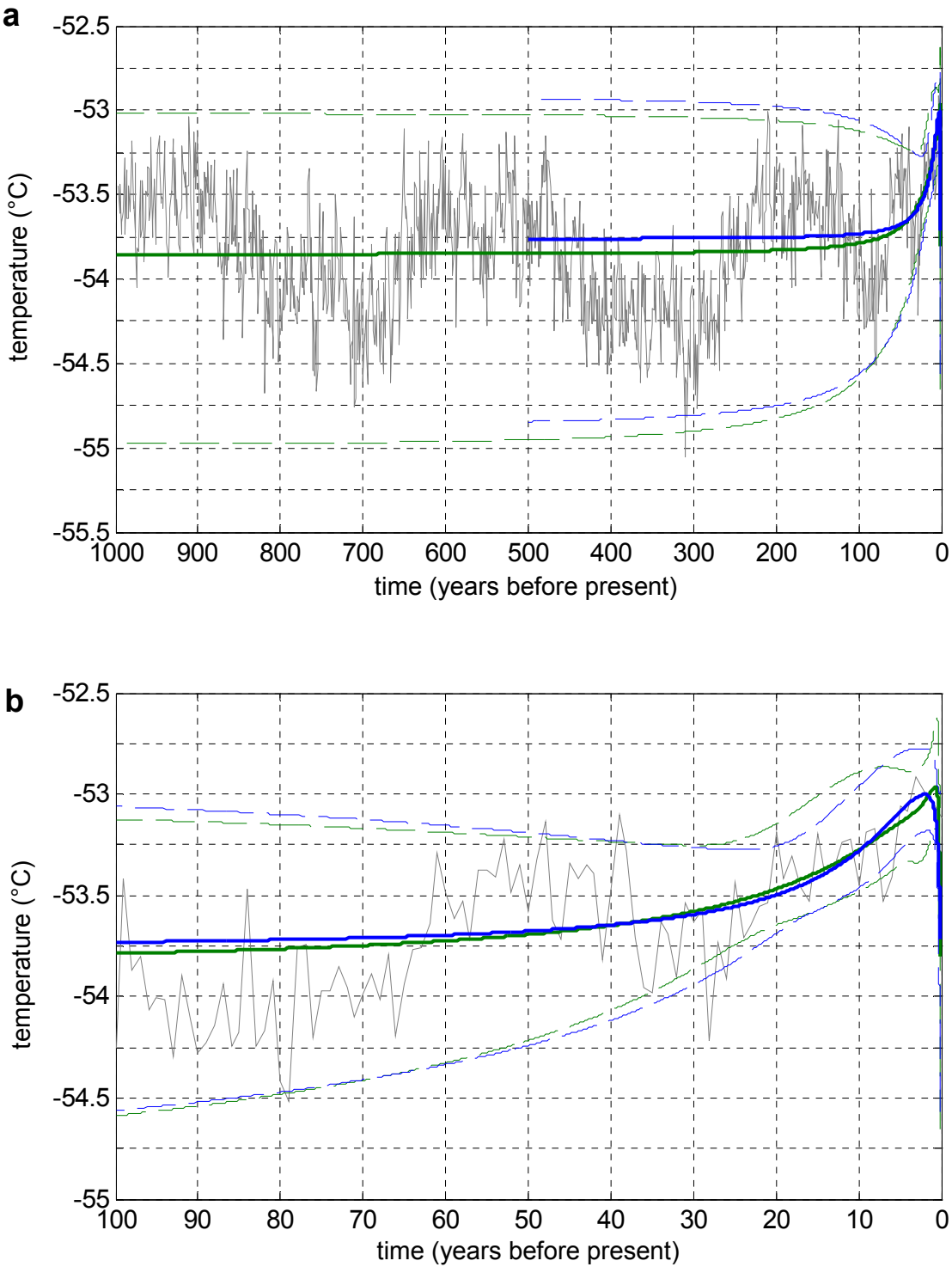

Figure 4.17. Surface temperature history inverted using the linearized method with synthetic data created with the 500-year long surface temperature history (blue) and 1000-year long history for **a.** 1000 years and **b.** is for the most recent 100 years.

4.5.3 Applying the RJ-MCMC

Figure 4.15 shows the result of the surface temperature history inversion by RJ-MCMC as the posterior PDF with the mean and the 95% confidence intervals indicated by the thick line and dashed lines, respectively. The maximum likelihood model, one of 400,000 model samples that make up the posterior PDF, is included in Figure 4.18 to highlight the fact that the posterior mean consists of individual models that are not smooth and look quite different from the mean.

The posterior mean model shows large departures from the true model beyond 100 years b.p. The inverted model shows decrease in temperature between ~100 and 170 years b.p. then a steady increase to 500 years b.p. although the true surface temperature history is more complex than that. The 95% confidence interval encloses almost all the true model for beyond ~70 years b.p. However, the interval is much wider than the range of temperatures in the true model and it widens with increasing time into the past. These features demonstrate the diminishing knowledge of the surface temperature history as you go further back in time and the inverted model for beyond ~100 years b.p. is unreliable.

Above points can be illustrated better by looking at the posterior and the prior PDFs for instantaneous times (Figure 4.19). The prior used here has the mean and the standard deviation of -53.9°C and 1 K. The posterior PDFs have sharper peaks and show large differences from the prior PDFs for recent times. Further back in time, the posterior PDFs become progressively closer to the prior. The posterior and the prior for 500 years b.p. are effectively the same meaning that there was no useful information about the surface temperature for 500 years b.p. in the data.

Concentrating now on the most recent 100 years (Figure 4.19b), the posterior mean follows the true model in a broad sense. Also, the 95% confidence interval encloses the general features underlying the true model, i.e. the synthetic history before the noise was

added (red solid line in Figure 4.8). On the interannual time scale, the true model often lies outside of the 95% confidence interval although this is to be expected from the experimental set-up and the purpose of the inversion here is not to capture those details. However, like the linearized inversion method, the event between 70 and 30 years b.p. is not represented well. Rather, the posterior mean appears to be representative of the warming of approximately 1 K since around 70 to 80 years b.p.

For the pre-observational mean surface temperature (T_{POM}) and the basal temperature (T_b), the prior distributions were uniform over ranges of -60 to -50°C and -11.9 to -1.9°C, respectively. The posterior for T_{POM} shown in Figure 4.20a can reasonably be approximated by a Gaussian distribution which leads to the mean and the 95% confidence interval (2 standard deviations) of -53.4 ± 0.6°C. Since the true T_{POM} was -54°C, the RJ-MCMC was able to obtain the value of T_{POM} just within the error bound, meaning that the data contains little signal of T_{POM}, just enough to get a rough estimate of it. On the other hand, the posterior for T_b is a uniform random which is no different from the prior, indicating that there is no information about T_b in the data. In other words, the basal temperature of the interior of ice sheet can not be constrained from the temperature profile of the upper 90 m.

The number of surface temperature points (k) ranged between 3 and 8 (Figure 4.21). The majority of sampled models consisted of 4 or 5 time points: 32% and 45% for k = 4 and 5, respectively. This denotes that the samples of the model are simple and made up of just a few linear segments, reflecting the low resolution expected from the level of the measurement uncertainty and the depth over which the temperature profile extends. The maximum likelihood model in Figure 4.18a is in fact a good example that has only two inflection points within 500 years.

The posterior PDF obtained by combining results of all the sensitivity tests is shown in Figure 4.23. The two posterior PDFs look virtually the same. It might be expected that the

95% confidence interval may become wider since distinctive differences in the posterior PDFs are seen for sensitivity tests for the thermal conductivity parameterization (Figure 4.122a) and ice thickness (Figure 4.22c). The number of samples that lie outside of the 95% confidence interval for the no-perturbations case do indeed increase as a result. However, this is offset by the posterior PDFs of the accumulation rate (Figure 4.22b) and the basal melt rate (Figure 4.22d) that have identical PDFs to the no-perturbations case which add more samples close to the mean.

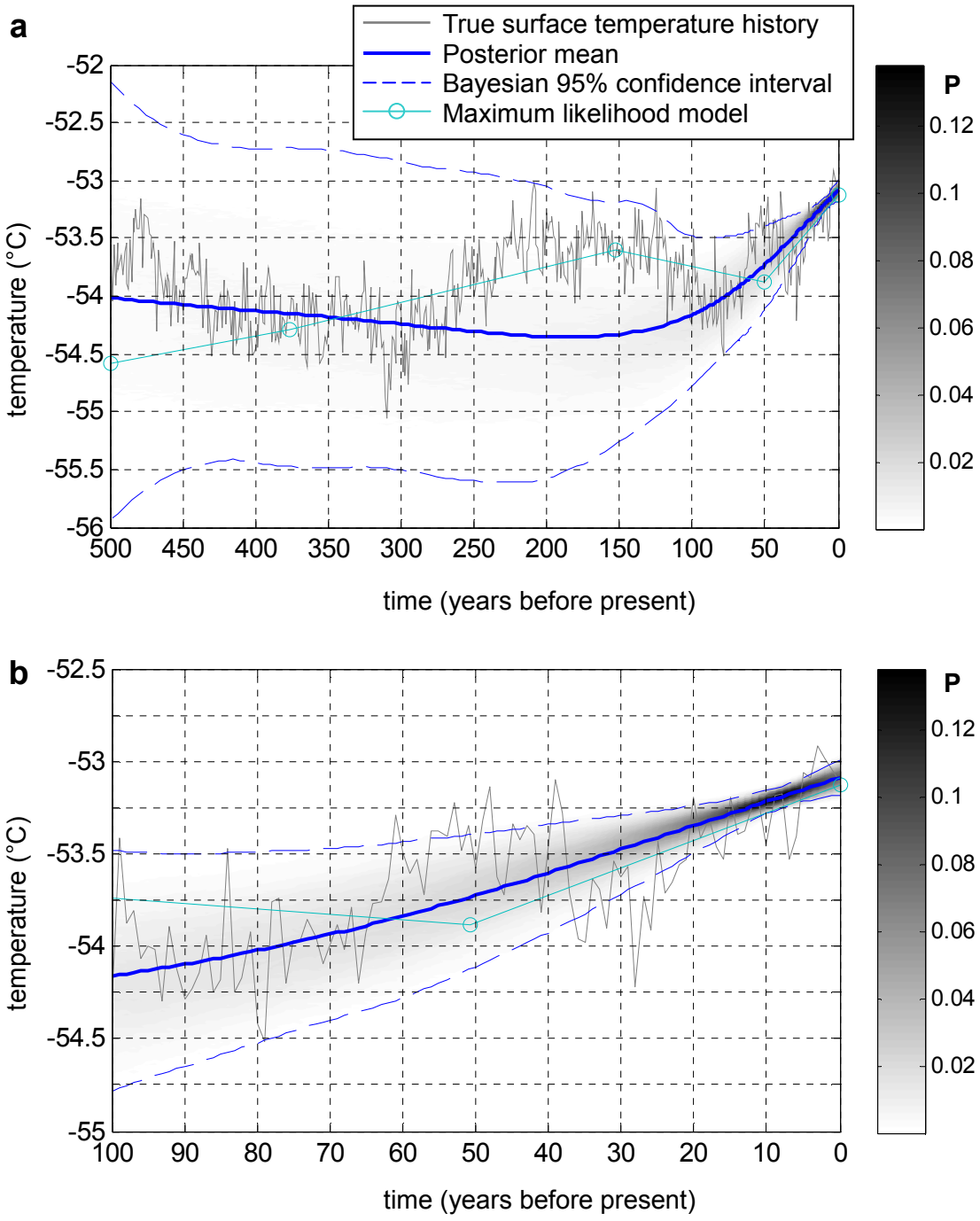

Figure 4.18. Surface temperature history inverted using the RJ-MCMC for **a**. 500 years and **b**. the most recent 100 years. Gray scale indicates the posterior PDF.

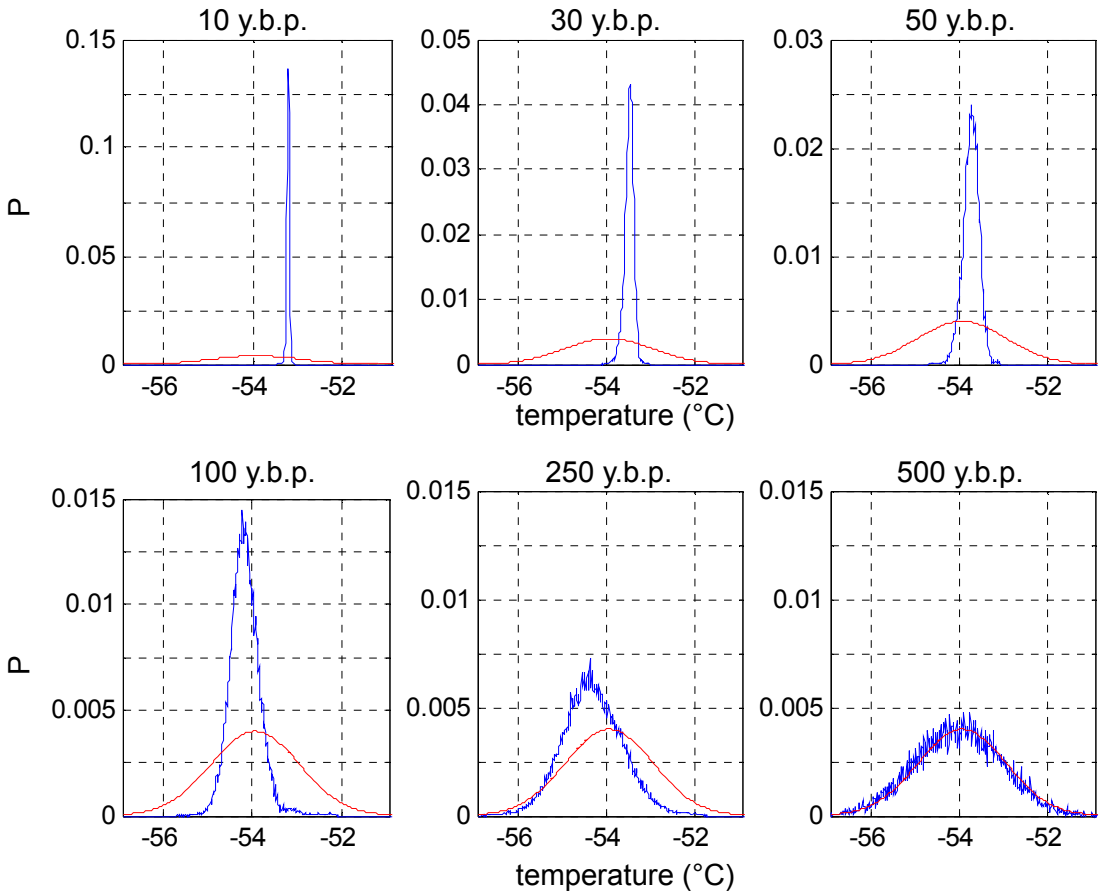

Figure 4.19. Posterior PDF for different times before present (blue) and the prior PDF (red). Notice that the scale of the probability changes between plots.

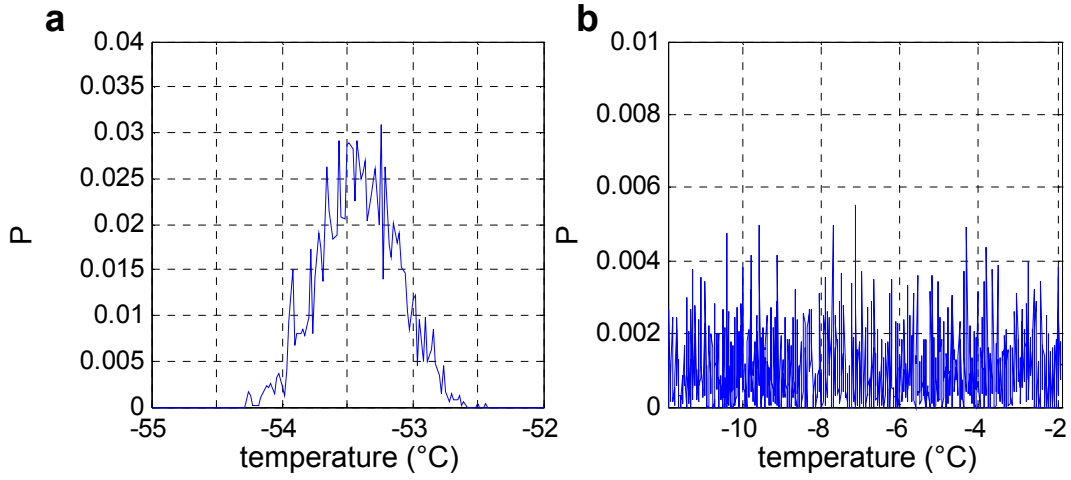

Figure 4.20. Posterior PDF for **a**. pre-observational mean temperature T_{POM} and **b**. basal temperature T_b.

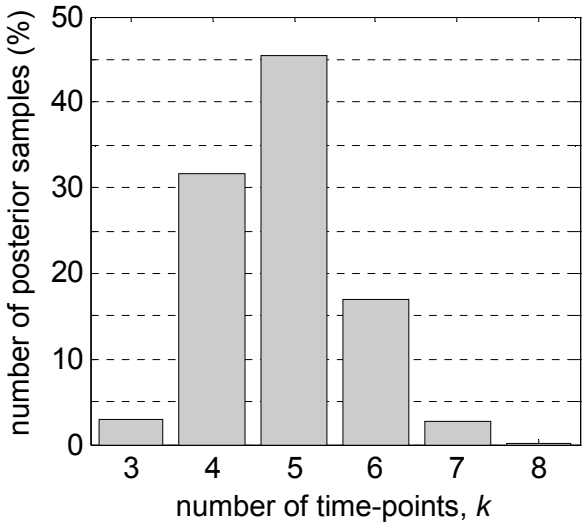

Figure 4.21. Posterior distribution of number of surface temperature history time-points *k*.

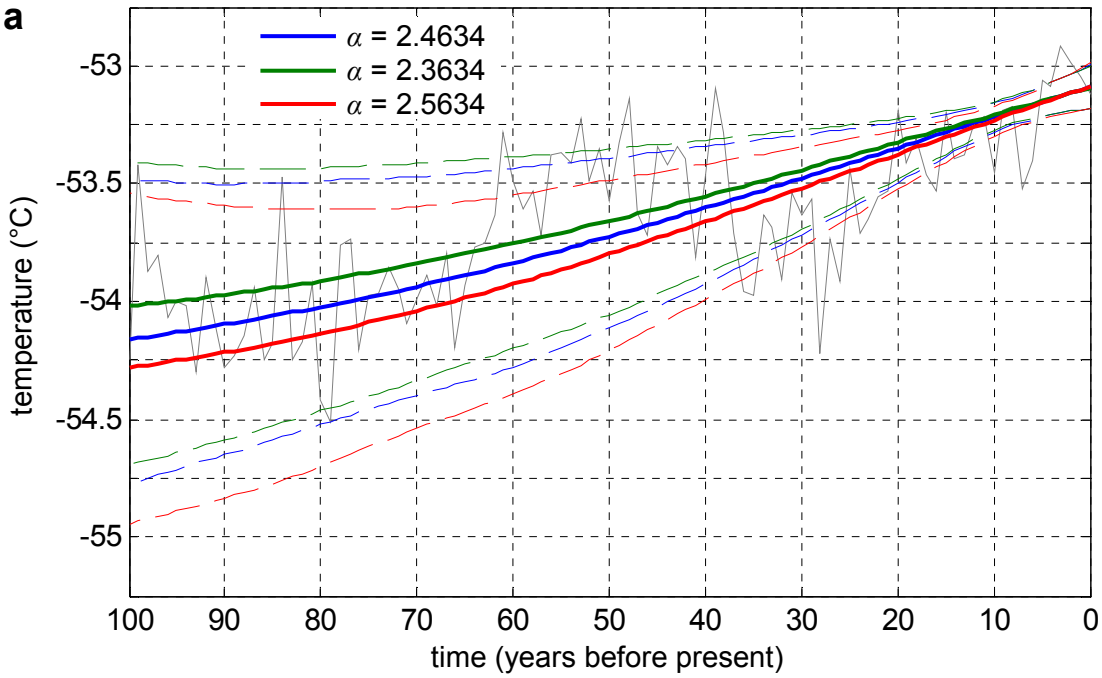
a
α = 2.4634
α = 2.3634
α = 2.5634
-53
-53.5
-54
-54.5
-55
temperature (°C)
100
90
80
70
60
50
40
30
20
10
0
time (years before present)

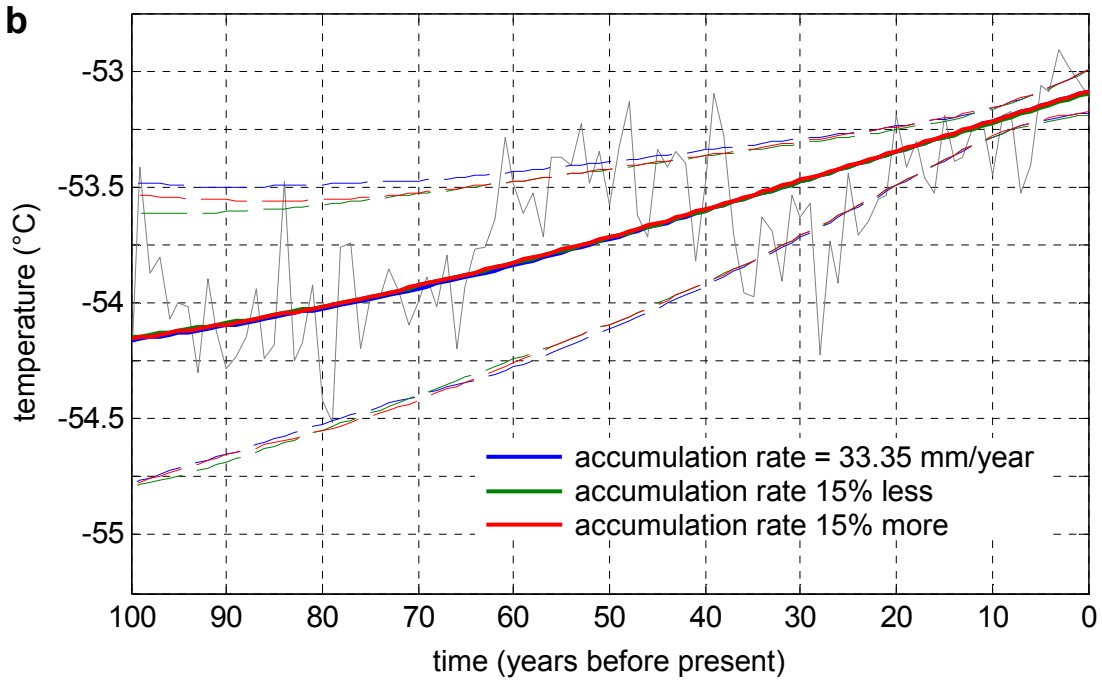
b
-53
-53.5
-54
-54.5
-55
temperature (°C)
accumulation rate = 33.35 mm/year
accumulation rate 15% less
accumulation rate 15% more
100
90
80
70
60
50
40
30
20
10
0
time (years before present)

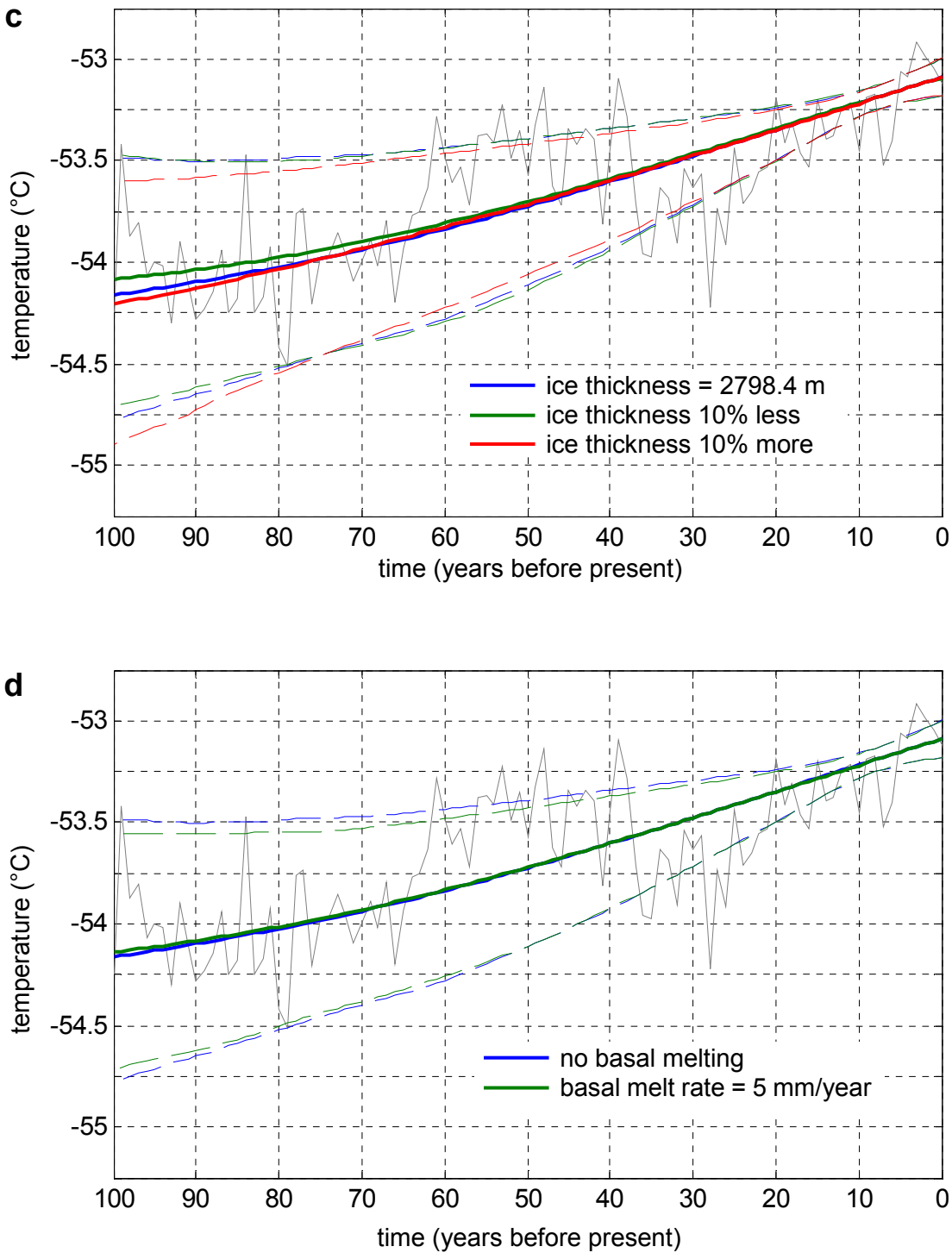

Figure 4.22. Surface temperature history inverted using the RJ-MCMC with different values of **a**. α, **b**. accumulation rate, **c**. ice sheet thickness and **d**. basal melt rate. Dashed lines indicate the 95% confidence interval. Gray solid line is the true surface temperature history.

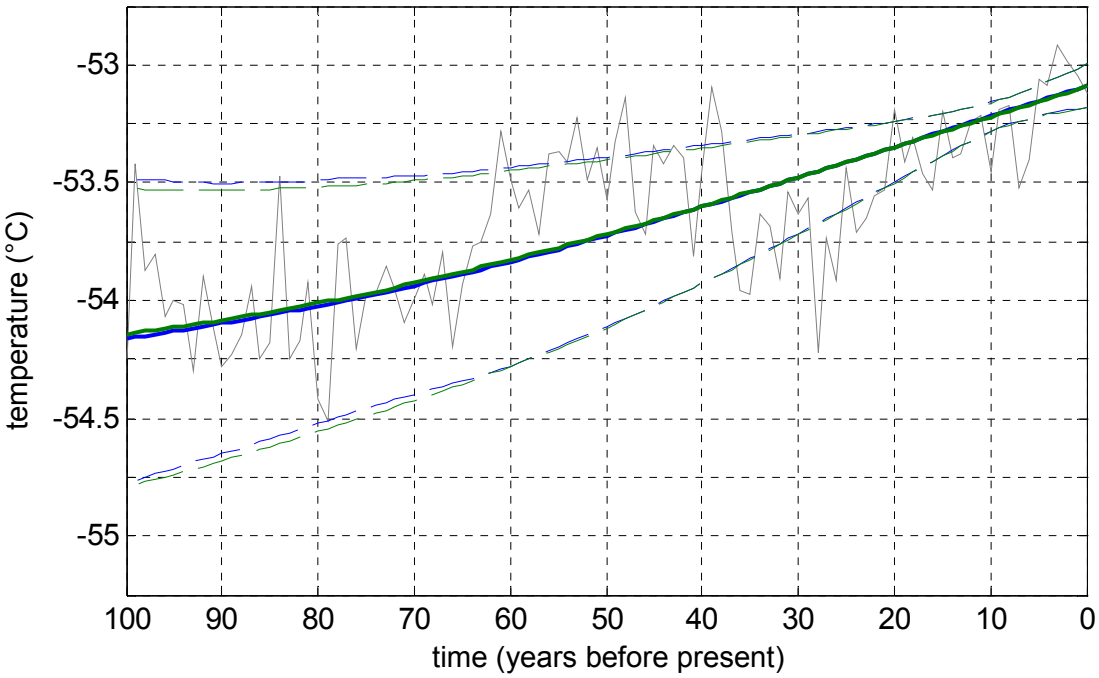

Figure 4.23. Surface temperature history inverted without perturbations in various parameters (blue) and error bounds calculated by combining those from sensitivity analyses to different values of α, accumulation rate, ice sheet thickness and basal melt rate (green). Gray solid line is the true surface temperature history.

As was done for the linearized inversion method, inversion was performed with the 1000-year long synthetic surface temperature history with synthetic data shown in Figure 4.16. Figure 4.24 shows the two models of the surface temperature history and their associated error bounds derived by using synthetic data created from the 500-year long surface temperature history (blue solid and dashed lines), which is the same as Figure 4.23, and at 1000-year long surface temperature history (green solid and dashed lines). Much like the example with the linearized inversion, significant differences between the two surface temperature histories are seen for times beyond 100 years b.p. which is beyond the time-scale over which data can resolve. Therefore, 500 years b.p. is considered to be an appropriate time

for the initial condition to be placed for both the linearized and the RJ-MCMC methods and the initial condition is set at 500 years b.p. for all inversion calculations in the rest of this research.

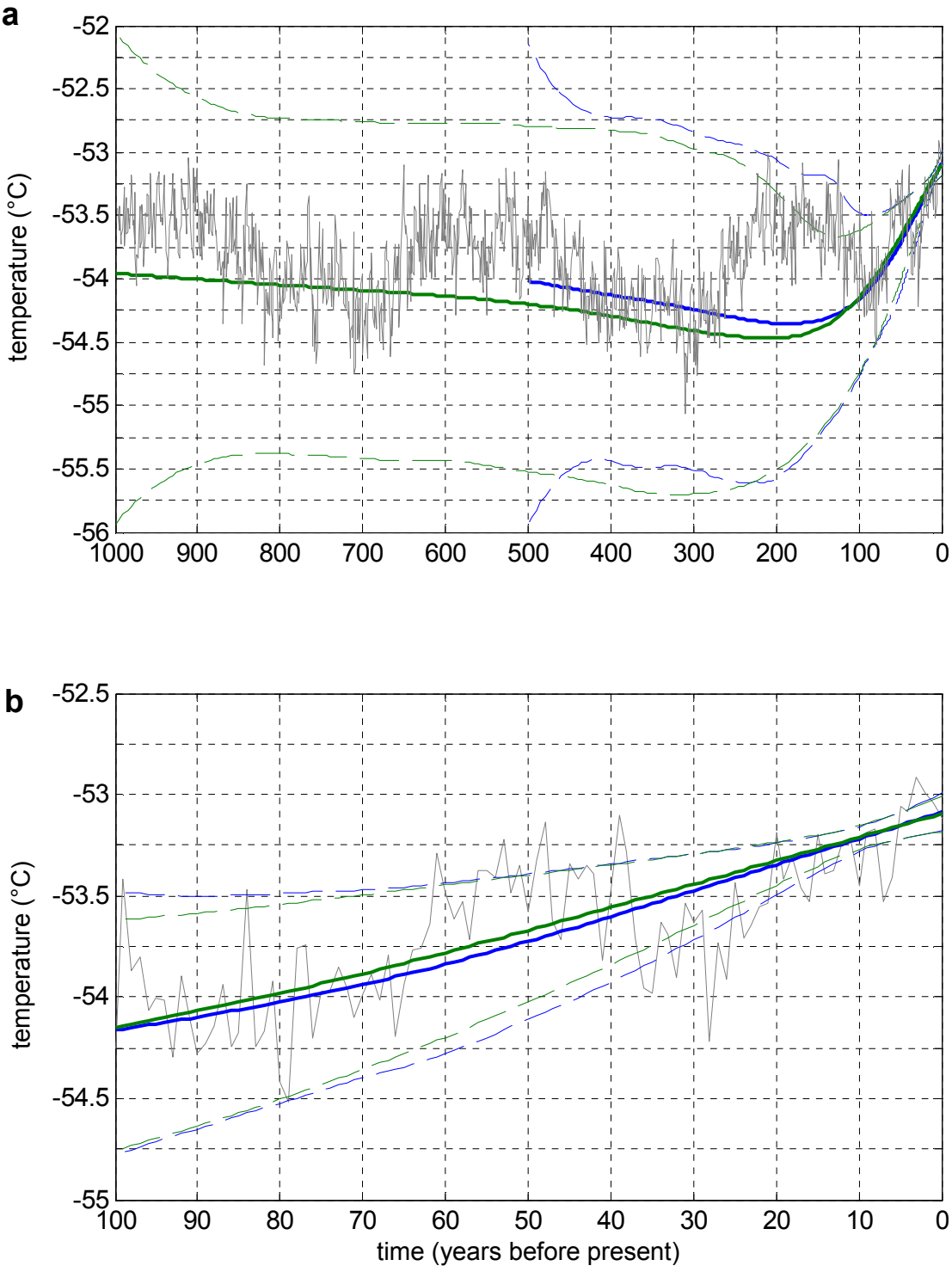

Figure 4.24. Surface temperature history inverted using the linearized method with synthetic data created with the 500-year long surface temperature history (blue) and 1000-year long history for **a.** 1000 years and **b.** is for the most recent 100 years.

4.5.4 Comparing the results from the linearized inversion and the RJ-MCMC

Models of the surface temperature history inverted by the linearized inversion and the RJ-MCMC are plotted together in Figure 4.25 along with the true surface temperature history. The inverted models obtained from both the linearized inversion and RJ-MCMC show warming towards the present. However, the inferences made about this warming trend from the two models could differ. The model from the linearized inversion is indicating that the warming started around 40 years b.p. and there was an acceleration in the rate in the most 20 years. On the other hand, the model from the RJ-MCMC shows a constant warming rate since around 100 years b.p. Qualitatively speaking, the model from linearized inversion appears to be following the true surface temperature history better than the one from the RJ-MCMC, particularly in the most recent 20 years. However, the model from the RJ-MCMC seem to be representing the temperature increase from around 80 years b.p. Therefore, the two models are both capturing aspects of the true surface temperature history and neither method can be concluded to be better than the other.

A quantitative way to assess the performance of the inversion is to examine data simulated by inverted models of the surface temperature histories and calculate the misfit from the observed data. Figure 4.26a shows the firn temperatures simulated by surface temperature histories shown in Figure 4.25 that were obtained by the linearized inversion and the RJ-MCMC together with the observed synthetic data. The total misfit δ can be calculated as,

$$\delta = \sqrt{\left(\mathbf{d}_{\text{sim}} - \mathbf{d}_{\text{obs}}\right)^{\text{T}} \left(\mathbf{d}_{\text{sim}} - \mathbf{d}_{\text{obs}}\right)}, \tag{4.71}$$

where $\mathbf{d}_{\text{sim}}$ and $\mathbf{d}_{\text{obs}}$ are vectors of simulated and observed firn temperatures. δ for the linearized inversion and the RJ-MCMC are 0.083 and 0.071, respectively. The expected total

misfit, calculated by equation (4.15) presented in section 4.3.3 with $\sigma = 0.03$ K, is 0.088. As anticipated, both the linearized inversion and the RJ-MCMC create data that fit within the expected misfit. This means that the inverted models of the surface temperature histories, however different they may look, are consistent with the observed data within the measurement uncertainty. It is tempting to state that the model obtained by the RJ-MCMC is more reliable than that obtained by the linearized inversion since the total data misfit is lower. However, a small misfit can also mean an over-fit which in the presence of the measurement uncertainty is undesirable (e.g. Parker, 1994; Aster et al., 2005). This misfit-test hence reinforces the qualitative statement made earlier on the performance of both methods.

The synthetic data example of this section demonstrates that inferences that could be made from the inversion of the borehole temperature data with the linearized inversion method and the RJ-MCMC can be summarized as follow:

- The direction of the surface temperature trend for the past several decades can be provided with certainty.
- Any magnitude and the duration of the trends should be interpreted with caution.

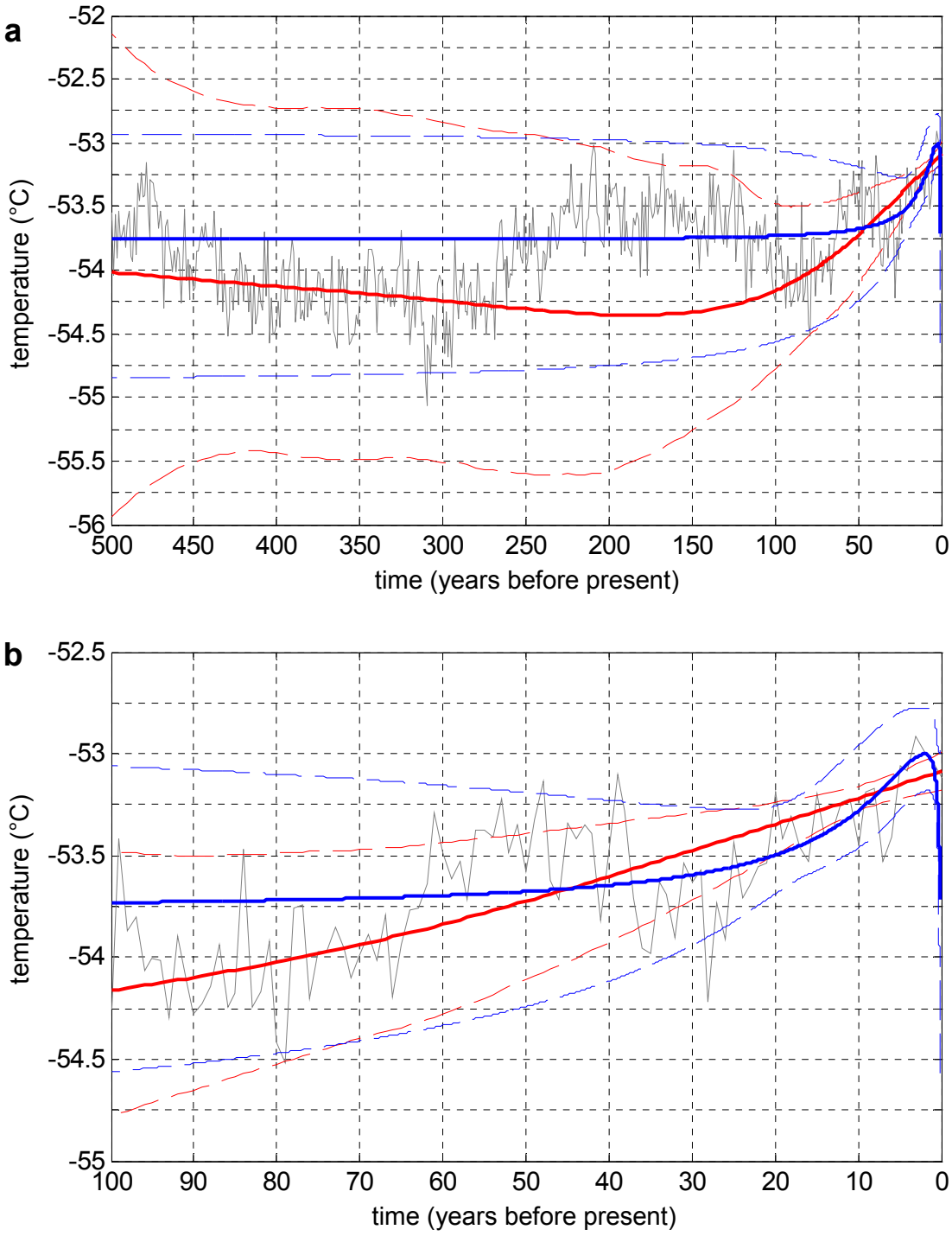

Figure 4.25. Surface temperature history inverted using the linearized method (blue) and RJ-MCMC (red) with the true surface temperature history (gray) for **a**. 500 years and **b**. the most recent 100 years.

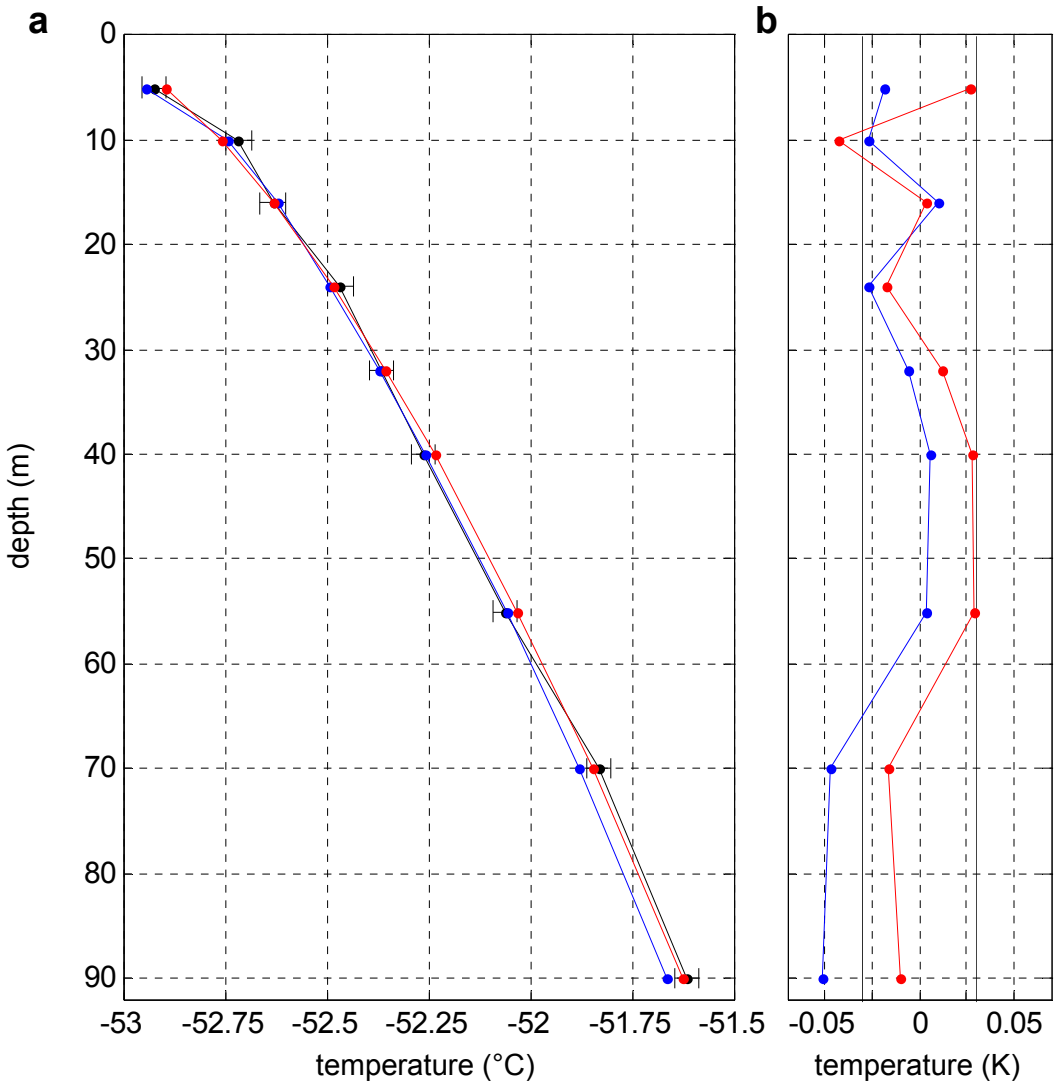

Figure 4.26. a. Synthetic data from the true surface temperature history (black) and those derived from inverted surface temperature histories by linearized inversion method (blue) and RJ-MCMC (red). Error bars on black line indicate the standard uncertainty of temperature measurements with ATPUs (0.03 K). **b**. Data misfit of linearized inversion (blue) and RJ-MCMC, with the standard uncertainty of measurements (black solid lines) The total misfit are 0.085 and 0.071 for linearized inversion and RJ-MCMC, respectively. The expected misfit is 0.088.

Chapter 5

SURFACE TEMPERATURE TRENDS IN EAST ANTARCTICA

5.1 Introduction

In the previous chapter, it was shown through the use of a synthetic example that the firn temperature data extending down to 90 m is useful in inferring the surface temperature trend on multi-decadal time scale. Both the linearized inversion and the RJ-MCMC will now be applied to firn temperature data obtained in East Antarctica, to examine the surface temperature trends of the recent several decades. Then, the recent climate trends of East Antarctica will be discussed in light of these results and existing results by other authors.

5.2 Inverted surface temperature histories at each site

5.2.1 NUS07-2

Models of the surface temperature history inverted by both methods look quite similar (Figure 5.1), except the most recent 5 years. The model from the linearized inversion (blue solid line in Figure 5.1) shows an increase of approximately 0.7 K between ~5 years and 1 year b.p. then a decrease although this decrease within the most recent year has no meaning as explained in section 4.5.2. On the other hand, the model from the RJ-MCMC shows no such features and displays a constant increase since ~60 years b.p. Details in the most recent ~5 years in the model inverted by the linearized inversion could be a result of the better fit to the measured data than the RJ-MCMC. Data misfits for 10, 16 and 24 m, where the firn

temperature shows an increase towards the surface, are smaller in the data simulated by the linearized inversion than the RJ-MCMC (Figure 5.2b). The increase in the surface temperature in the most recent ~5 years can be considered to be reflecting this temperature increase from 24 to 10 m. Conversely, this can also be interpreted to be a result of over-fitting the observational data. The observational data are associated with the standard uncertainty (0.03 K) meaning that the true temperature value lies within the error bar shown in Figure 5.2a with 66.7% probability, centered at the measured value. Therefore, better fits to parts of or all of observed temperatures do not necessarily indicate the inverted model to be a 'better model', especially if the total misfit is below the tolerance which is the case for both the linearized inversion and the RJ-MCMC.

The trends calculated from the model inverted by the linearized inversion and the RJ-MCMC between 10 and 50 years b.p., when the two models start diverging from each other, are 0.28 ± 0.04 K/decade and 0.27 ± 0.08 K/decade, respectively. Reflecting upon the synthetic example of the previous chapter, it is likely that the true surface temperature history is enclosed by the error bounds indicated by dashed lines. As stated in the previous chapter, trends beyond ~30 years b.p. need to be interpreted with caution. However, two models follow each other more closely compared to the synthetic example and are well within the error bounds of each other between 10 and 50 years b.p. Therefore, it is highly likely that the true surface temperature trend at this site for the past ~50 years is as described above.

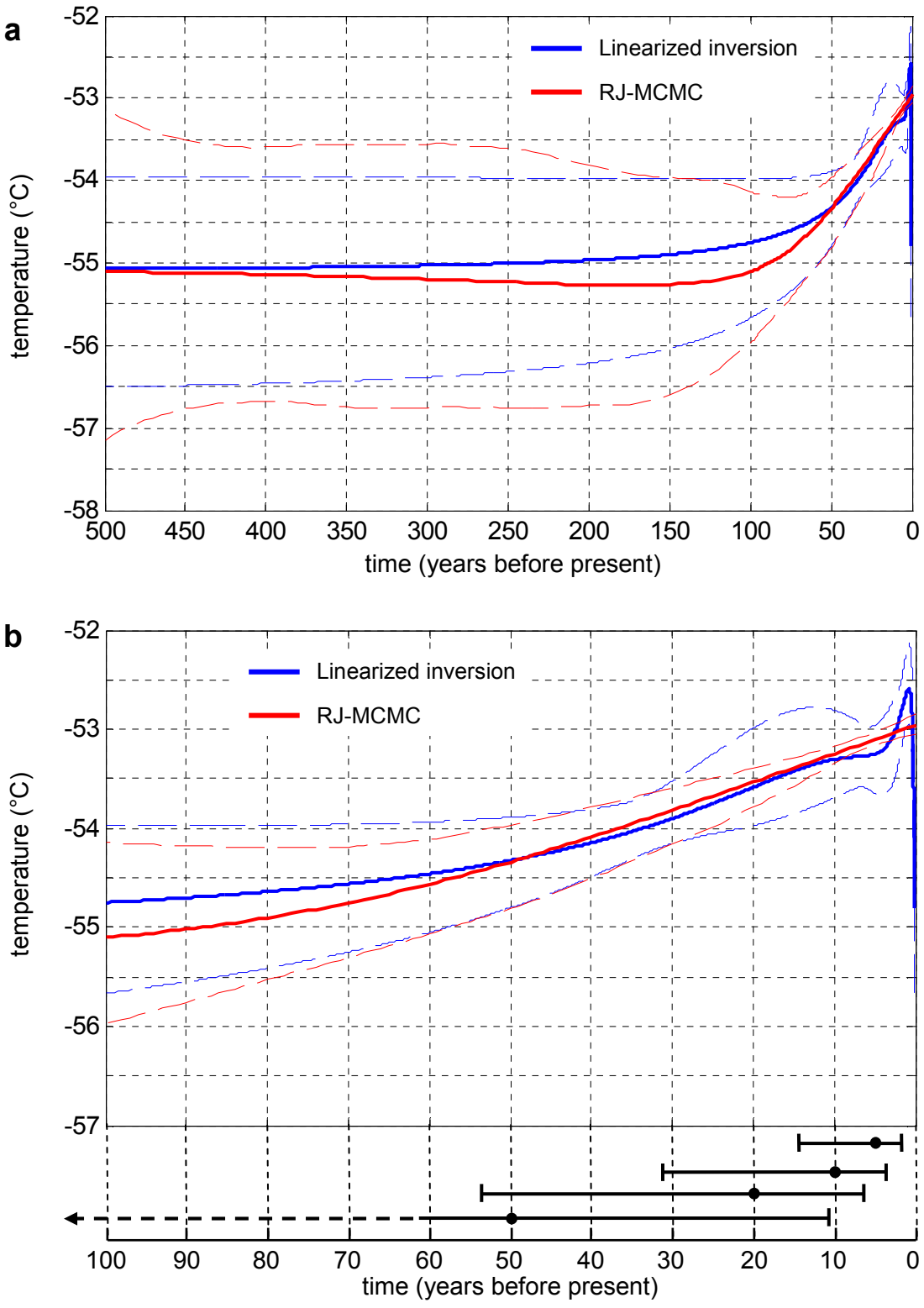

Figure 5.1. Surface temperature history at NUS07-2 inverted using the linearized method (blue) and RJ-MCMC (red) for **a**. 500 years and **b**. the most recent 100 years with spreads for 5, 10, 20 and 50 years b.p.

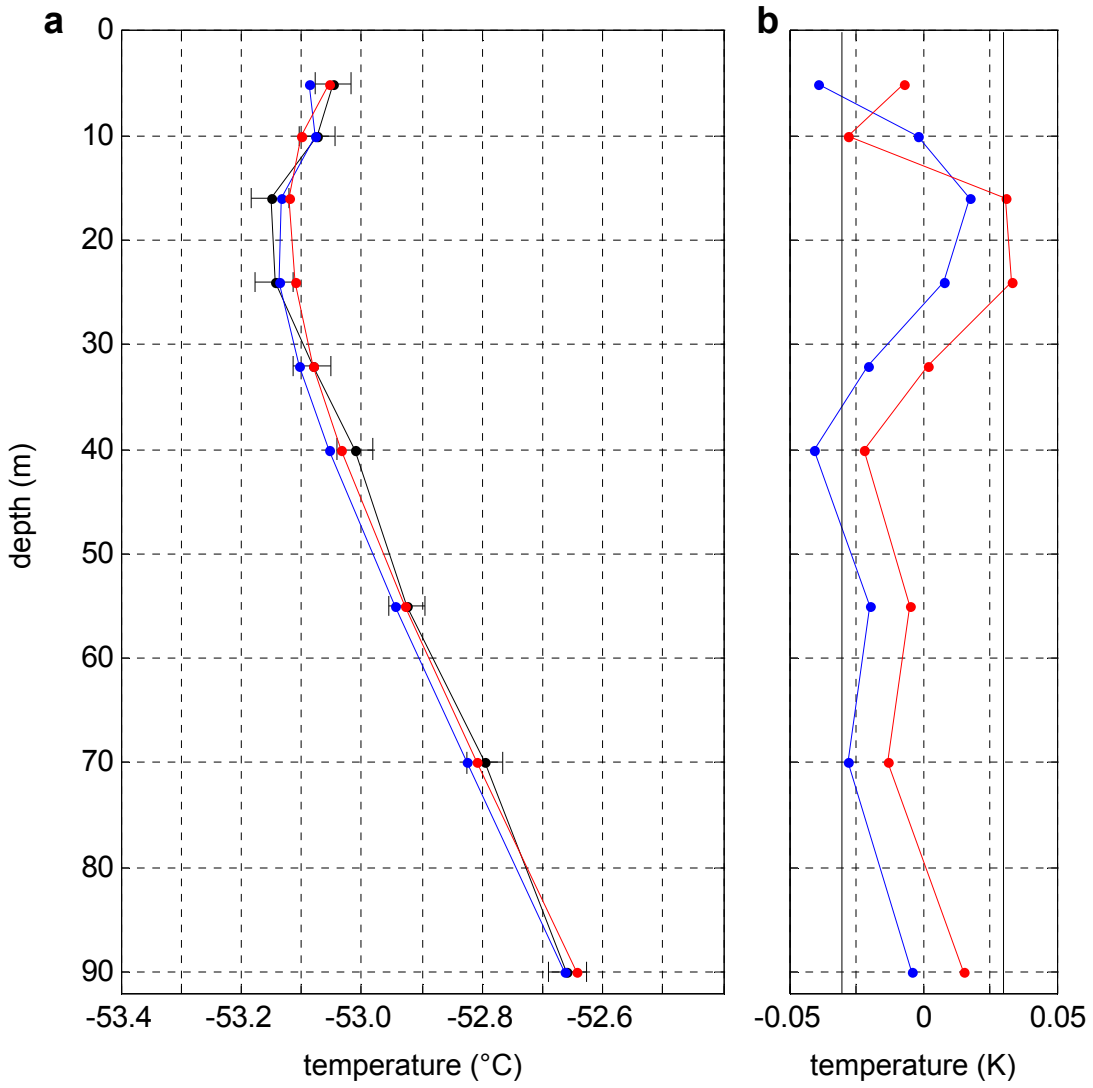

Figure 5.2. a. Observed data at NUS07-2 (black) and those derived using surface temperature histories inverted by linearized inversion method (blue) and RJ-MCMC (red). Error bars on black line indicate the standard uncertainty of temperature measurements with ATPUs (0.03 K). **b**. Data misfit of linearized inversion (blue) and RJ-MCMC, with the standard uncertainty of measurements (black solid lines) The total misfit are 0.072 and 0.062 for linearized inversion and RJ-MCMC, respectively. The expected misfit is 0.088.

5.2.2 NUS07-5

A consistent feature in the models inverted by both methods is the recent sharp increase in the temperature. The linearized inversion shows an increase of 1.38 ± 0.22 K in the most recent 5 years, excluding the sharp drop within the most recent year. RJ-MCMC shows an increase of 1.38 ± 0.63 K in the last 10 years. In the model from the linearized inversion, there is an event where the temperature decreases by -0.23 ± 0.26 K from around 13 to 5 years b.p. However, the error bounds seen around this time period (Figure 5.3b) are large and the 95% confidence interval exceeds the amount of decrease indicated. This event also occurs within the spread calculated for 10 years b.p., meaning that such an event can not be resolved from the given data. Therefore, it is unlikely that this surface temperature decrease did actually occur.

Quite different conclusions can be drawn from the two models beyond the most recent decade. More or less constant warming trend of 0.17 ± 0.03 K from around 100 to 13 years b.p. is shown by the model from the linearized inversion whereas no significant change is shown by the model from the RJ-MCMC before 10 years b.p. However, the two models create simulated data that fit the observed data within the tolerance. Hence the two models are both possible surface temperature histories at this site and it is unclear whether the surface temperature has been increasing or not beyond the most recent decade. It is clear tough, that a significant amount of warming has occurred at this site, whether it's confined to the most recent several years or it has been going on a for longer period of time.

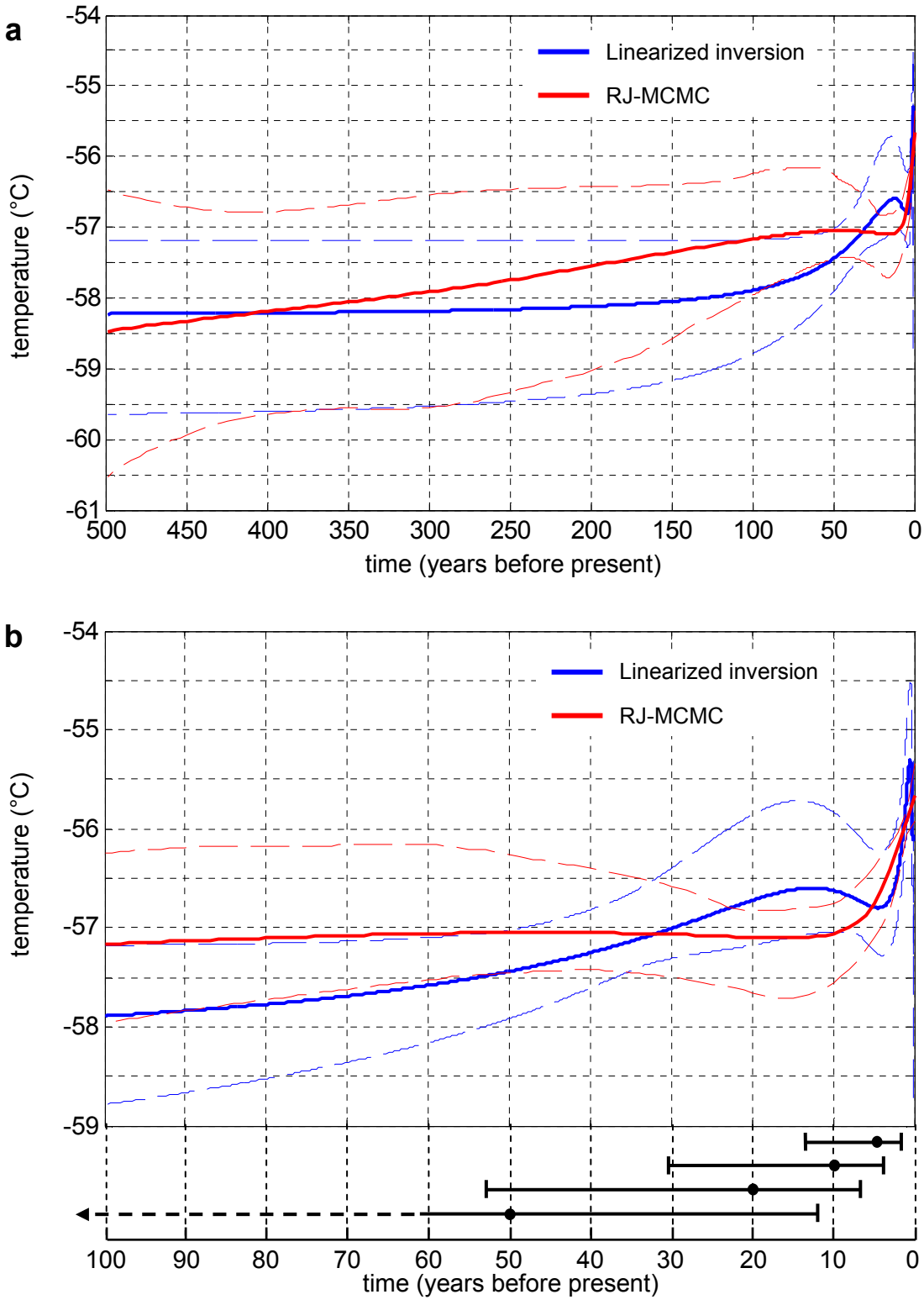

Figure 5.3. Surface temperature history at NUS07-5 inverted using the linearized method (blue) and RJ-MCMC (red) for **a**. 500 years and **b**. the most recent 100 years with spreads for 5, 10, 20 and 50 years b.p.

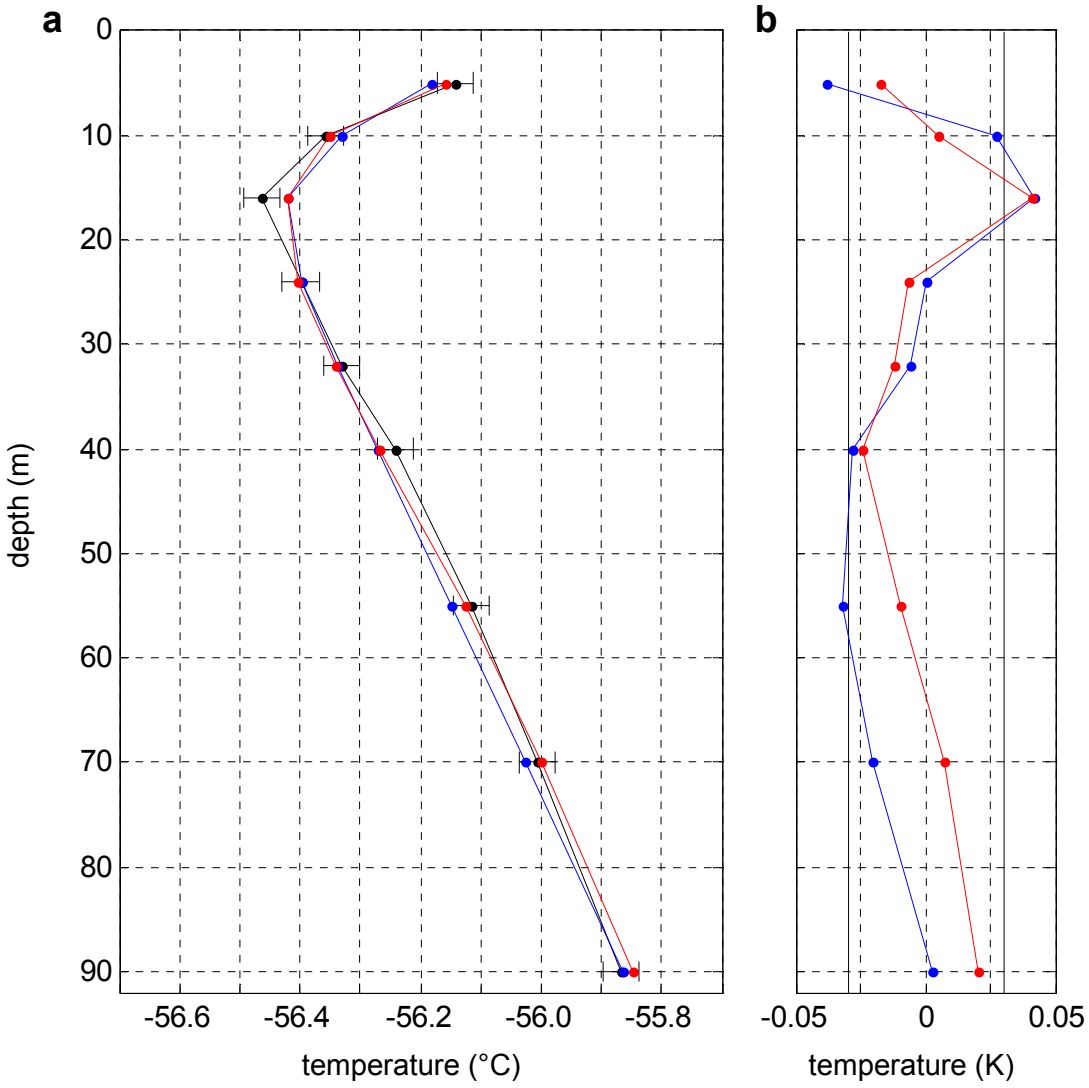

Figure 5.4. a. Observed data at NUS07-5 (black) and those derived using surface temperature histories inverted by linearized inversion method (blue) and RJ-MCMC (red). Error bars on black line indicate the standard uncertainty of temperature measurements with ATPUs (0.03 K). **b**. Data misfit of linearized inversion (blue) and RJ-MCMC, with the standard uncertainty of measurements (black solid lines) The total misfit are 0.079 and 0.058 for linearized inversion and RJ-MCMC, respectively. The expected misfit is 0.088.

5.2.3 NUS07-7

Similar to NUS07-5, the two models show a fair agreement in the most recent several years; a significant amount of warming in the most recent 5 years. The linearized inversion shows an increase of approximately 0.45 K between 5 and 1 year b.p. which translates to the trend of 1.52 ± 0.30 K/decade. For the same period of time, the RJ-MCMC shows an increase of 0.59 K or 1.56 ± 1.10 K/decade. Although the errors associated with trends in the time period are large, particularly for the RJ-MCMC, the two numbers are similar hence the significant warming of the recent 5 years is likely a true event.

Between 5 and ~30 years b.p., two models show approximately the same amount of surface temperature increase but of differing rates. Looking at the period between 33 years b.p. and 5 years b.p. where the two models cross for a convenience of comparison, the linearized inversion indicates an almost linear trend of 0.26 ± 0.04 K/decade. On the other hand, the model inverted by the RJ-MCMC shows almost no change until 25 years b.p. and then a non-linear increase of 0.74 K to 5 years b.p. Considering that the two models stay within each other's error bounds for this time period (and for all other times), as well as the fact that either methods can not exactly invert the true model even at 30 years b.p. as shown in the previous chapter, it can only be stated that the surface temperature increased by around 0.70 to 0.75 K between ~30 and 5 years b.p. However, how this increase occurred, either at a constant rate or not, is not clear.

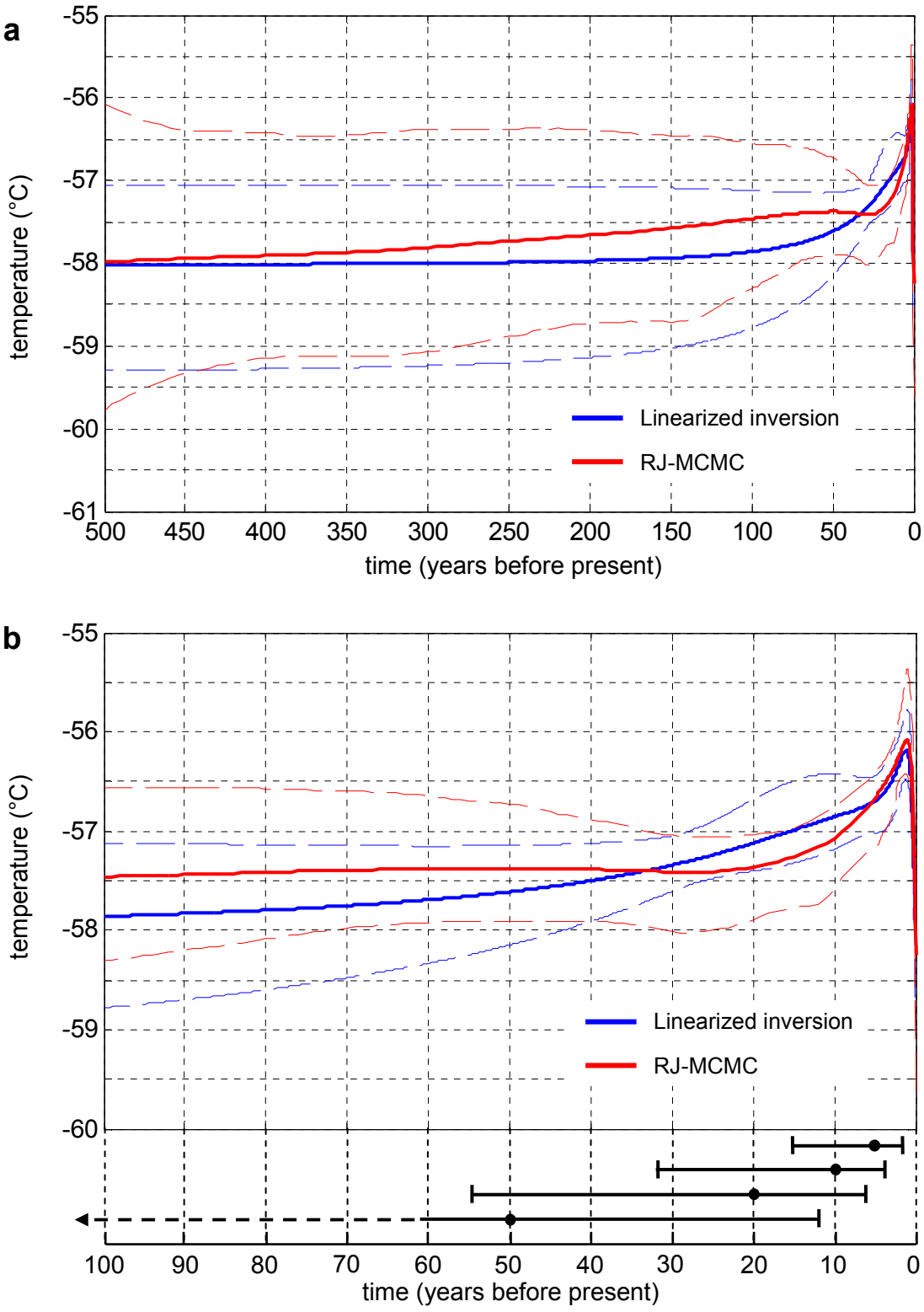

Figure 5.5. Surface temperature history at NUS07-7 inverted using the linearized method (blue) and RJ-MCMC (red) for **a**. 500 years and **b**. the most recent 100 years with spreads for 5, 10, 20 and 50 years b.p.

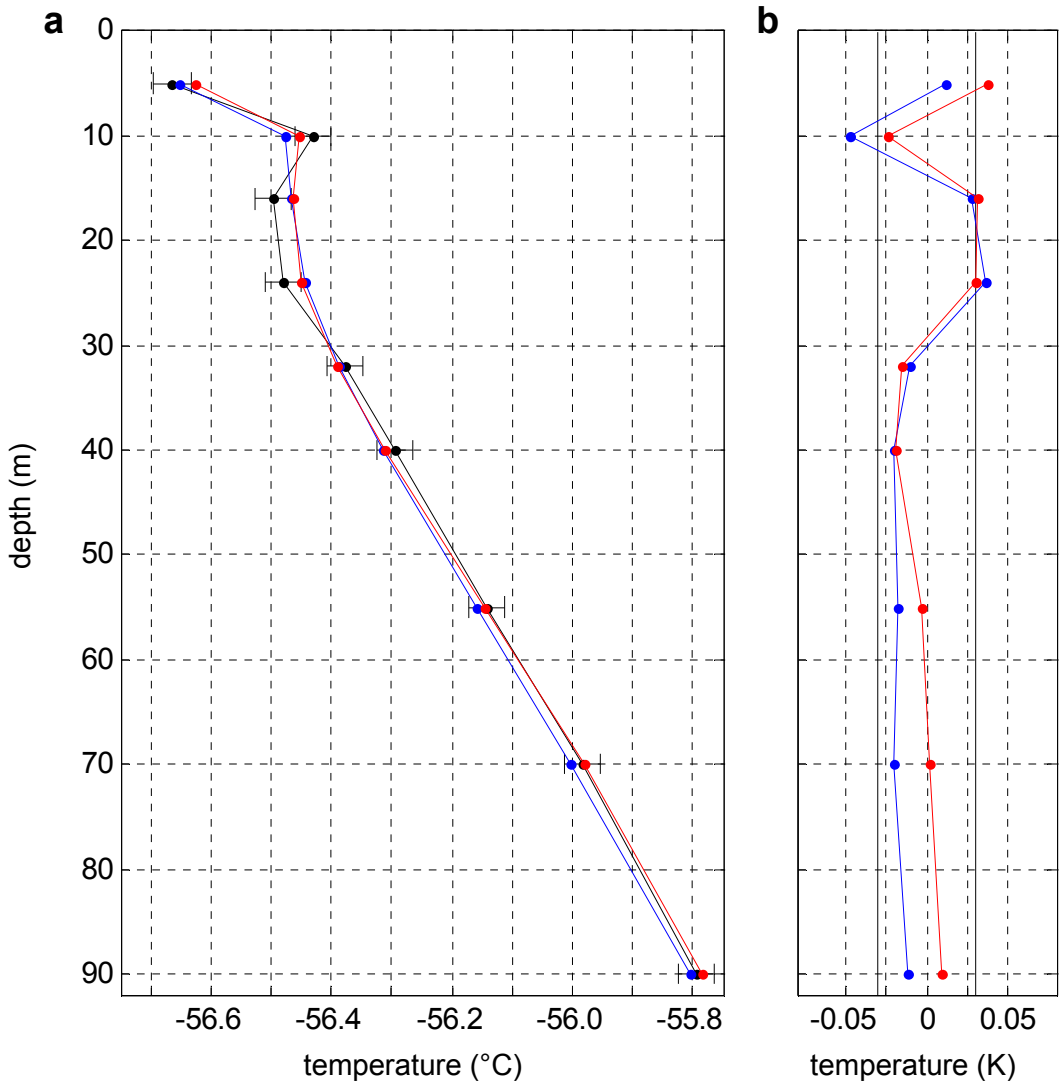

Figure 5.6. a. Observed data at NUS07-7 (black) and those derived using surface temperature histories inverted by linearized inversion method (blue) and RJ-MCMC (red). Error bars on black line indicate the standard uncertainty of temperature measurements with ATPUs (0.03 K). **b**. Data misfit of linearized inversion (blue) and RJ-MCMC, with the standard uncertainty of measurements (black solid lines) The total misfit are 0.077 and 0.068 for linearized inversion and RJ-MCMC, respectively. The expected misfit is 0.088.

5.2.4 NUS08-5

Both models indicate a large amount of temperature increase within the most recent two years; 2.48 K and 2.60 K from the linearized inversion and the RJ-MCMC, respectively. This is most likely reflecting a large amount of increase from 10 to 5 m depths in the measured temperature profile (Figure 5.8a). It can be thought that the two consecutive anomalously warm years. In any case, it is not surprising to see such an event in the inverted models since the signal from the most recent several years should be well resolved as can be seen from resolving functions. Also, this type of short event is not a climatological signal that is the focus of this research.

Beyond 2 years b.p., it appears that there is a slight cooling to no trend. The model from the linearized inversion displays a cooling trend of -0.11 ± 0.08 K/decade between 30 and 2 years b.p. and almost no change before this time period. In the model from the RJ-MCMC, the trend stays constant at -0.02 ± 0.06 K/decade for the same time period as well as beyond 30 years b.p. It is important to note that the error bounds associated with the trends from both models are either comparable to the actual number for the trend or exceeds it which was not the case for any other sites. Moreover, the two models stay within the error bounds of each other. For these reasons, it can be said that this site has experienced slight cooling to no significant change in the surface temperature for the past several decades except the most recent 2 years.

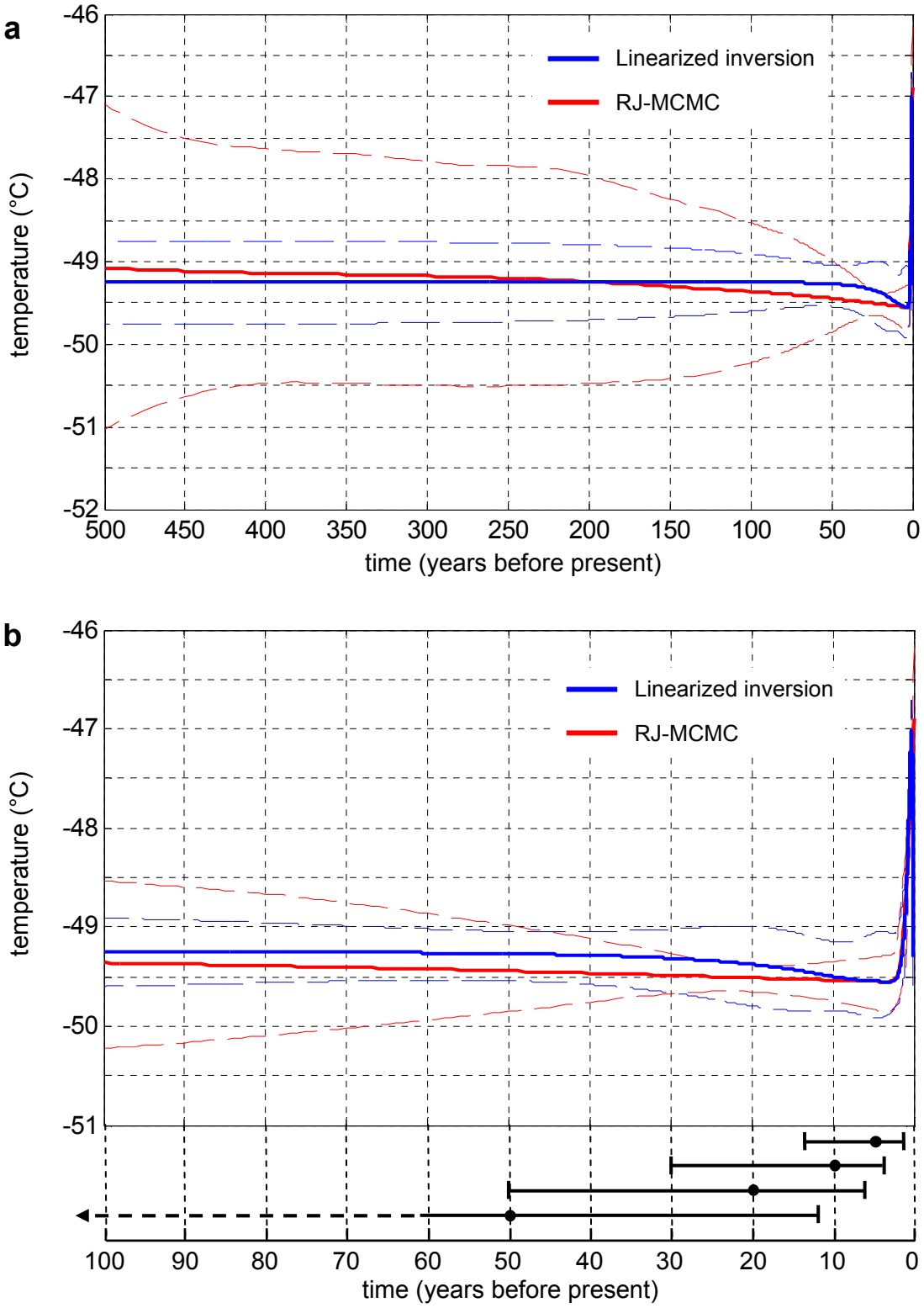

Figure 5.7. Surface temperature history at NUS08-5 inverted using the linearized method (blue) and RJ-MCMC (red) for **a**. 500 years and **b**. the most recent 100 years with spreads for 5, 10, 20 and 50 years b.p.

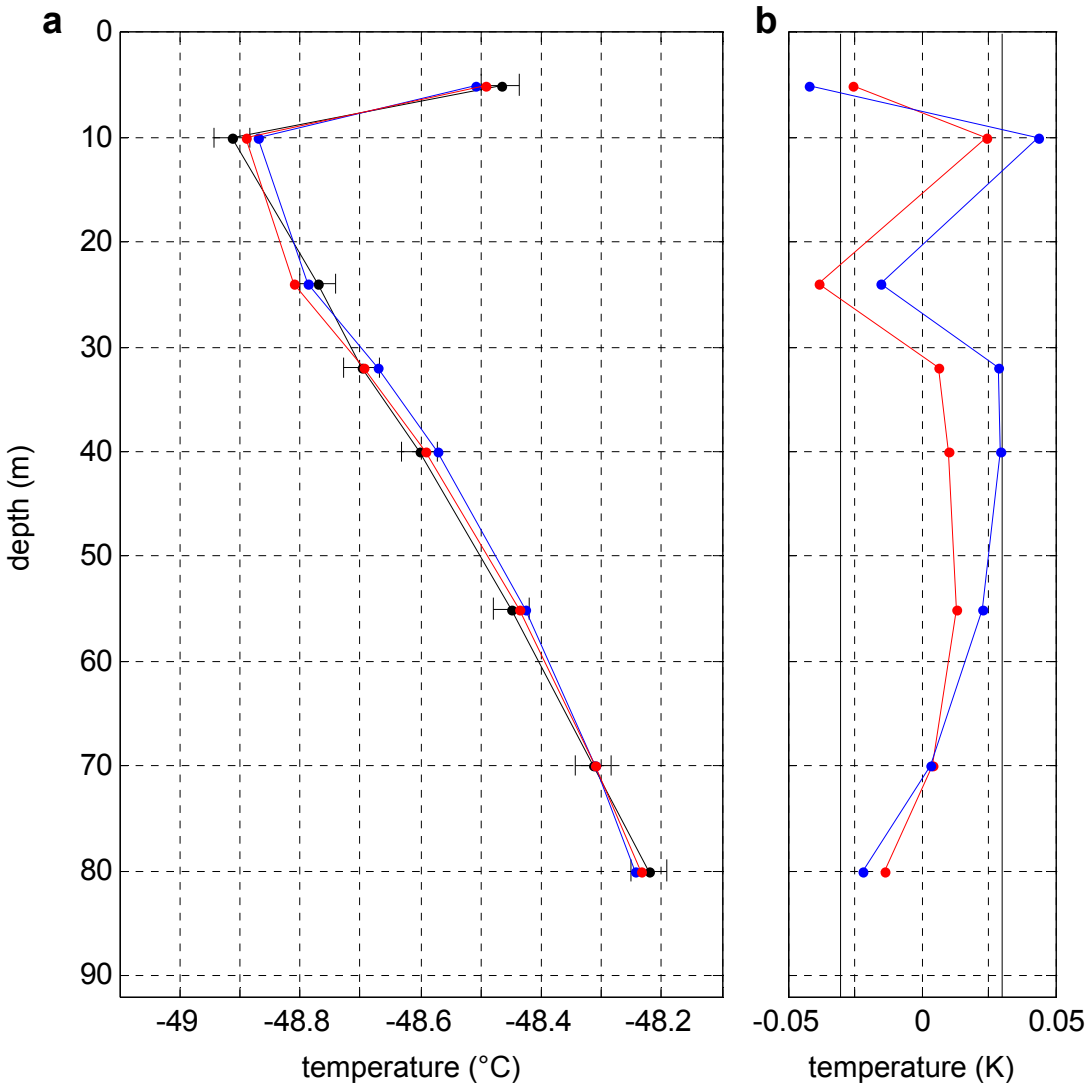

Figure 5.8. a. Observed data at NUS08-5 (black) and those derived using surface temperature histories inverted by linearized inversion method (blue) and RJ-MCMC (red). Error bars on black line indicate the standard uncertainty of temperature measurements with ATPUs (0.03 K). **b**. Data misfit of linearized inversion (blue) and RJ-MCMC, with the standard uncertainty of measurements (black solid lines) The total misfits are 0.816 and 0.057 for linearized inversion and RJ-MCMC, respectively. The expected misfit is 0.082.

5.3 Comparison with existing temperature records and reconstructions

Before beginning the discussion, readers are reminded that the surface temperature histories derived by both the linearized and the RJ-MCMC inversion methods are of the *skin-surface* temperature, not the *near-surface air* temperature. Although they are not exactly the same physical quantities, comparisons will be made on the assumption that they are closely related and they do not differ significantly on annual and longer-term basis (e.g. Comiso, 2000).

The inverted surface temperature histories at NUS07-2, -5 and -7, despite some discrepancies in details between models derived by the two inversion methods, indicate warming trends within the recent several decades. A clearly different pattern from those three sites, slight cooling to no change, is seen at NUS08-5. NUS07-2, -5 and -7, sites along the route of the Traverse in the 2007-08 season, are 1000 to 1200 m higher in altitude than NUS08-5 (Figure 2.3). When above facts are considered, a broad pattern of the recent surface temperature trends in East Antarctica, at least in the Dronning Maud Land sector is, warming trend near the ice divide and cooling to no change off the divide.

The only available long-term station records from the interior of East Antarctica exist at Vostok and South Pole which are approximately 1000 and 870 km away from the nearest site (NUS07-7), respectively. Despite the great distance from the study sites, Vostok is at 3488 m above sea level and just off of the ice divide, hence it can be considered to have conditions that are similar to the near-divide sites, NUS07-2, -5 and -7. On the other hand, South Pole and NUS08-5 are both off the divide, around 800 to 1000 m lower in altitudes than near-divide sites. Although there are Automatic Weather Stations scattered in the general region of the study sites, their records are too short and often intermittent for useful comparisons. Therefore, the results of the borehole paleothermometry will first be compared with records from Vostok and South Pole followed by temperature reconstructions covering the entire Antarctic Ice Sheet.

Mean annual temperature records at Vostok and South Pole, and their linear trends are shown in Figure 5.9. As outlaid in Chapter 1, trends calculated from station temperature records at the continental locations in Antarctica are statistically not significant and can vary depending on a time period examined. Moreover, the Vostok record has data gaps even in recent times. Nevertheless, the long-term trends are in broad agreement, at least the direction of the trend, with the pattern of the surface temperature trends derived from borehole paleothermometry. The trend at Vostok for 1958-2009 period is positive, 0.15 ± 0.18 K/decade. This trend is much smaller than the trend at NUS07-2 where a relatively constant surface temperature change going back to about 50 years ago is shown. When compared to results from NUS07-5 and -7 that indicate accelerated warming starting some time between ~30 years ago and the present, the magnitude is again much smaller. There does appear to be an increase in the temperature in the Vostok record since the mid 1980s which would then be in line with results at those two sites that are in fact closer to Vostok than NUS07-2. However, 5 out of 24 years since 1985 is missing on top of the brevity of the period for determining a climate trend. Hence it is premature to conclude that this is indeed the case. In any case, the inverted surface temperature histories at three near-divide sites and the Vostok record all show positive trends.

The slight cooling to no significant trend shown in the inverted surface temperature history at NUS08-5 is in closer agreement to the trend at the nearest station, South Pole which is -0.03 ± 0.06 K/decade between 1958 and 2008. The distance to South Pole from NUS08-5 is approximately 790 km and from the next closest study site, NUS07-7 where a warming trend was shown, is ~860 km. Although the distances to South Pole are not significantly different, altitudes are. NUS08-5 is at 2544 m above sea level, about 300 m lower in altitude than South Pole and NUS07-7 is at 3716 m, ~880 m higher than South Pole. Because of the lower altitude and the topography of the Antarctic Ice Sheet, NUS08-5 and South Pole are in

the katabatic wind zone where the mean wind speed is generally higher than the region around the ice divide (e.g. Parish and Bromwich, 2007) and the climate regime is slightly different. The difference in the surface temperature trends could therefore be linked to the characteristics of the study sites.

Near-surface air temperature reconstruction of Steig et al. (2009) and Monaghan et al. (2009) both show a long term weak warming trend for the region of the study sites. NUS07-2, -5 and NUS08-5 are in an area of a statistically significant trend of around 0.1 K/decade for 1957-2006, and statistically not significant but the same magnitude is shown for the location of NUS07-7 in Steig et al. (2009). On the other hand, all four sites are included in a basin indicated by Monaghan et al. (2009) with a trend between 0.0 and 0.1 K/decade that is statistically not significant for 1960-2008. Hence trends at three near-divide sites agree with the positive trends shown both by Steig et al. (2009) and Monaghan et al. (2009) although magnitudes differ.

Significant warming trends of comparable magnitudes to those shown at NUS07-5 and -7 by borehole paleothermometry are indicated by the reconstruction of Monaghan et al. (2008) for the period 1992-2005. (Note that Monaghan et al. (2009) is an updated version of Monaghan et al. (2008). However, the examination of the recent time period was only carried out in the older study.) As can be seen in Figure 5.10c, a large portion of East Antarctic interior, including locations of NUS07-5 and -7, is shown to be warming at a rate in excess of 0.8 K/decade. A similar pattern is shown by the clear-sky skin-surface temperatures derived from the satellite IR data that is completely independent from the Monaghan reconstruction. However, this strong warming trend is also shown for the location of NUS08-5. Inverted surface temperature history there shows slight cooling to no change until 2007, including the recent 10 to 20 years when the resolution is still reasonably good. Therefore, even though the inverted surface temperatures at near-divide sites show fair coherence with reconstructions

using the spatial extrapolation technique and satellite IR data, there are some disagreement between the spatial patterns shown by the borehole paleothermometry and the reconstruction based on station records and satellite IR data.

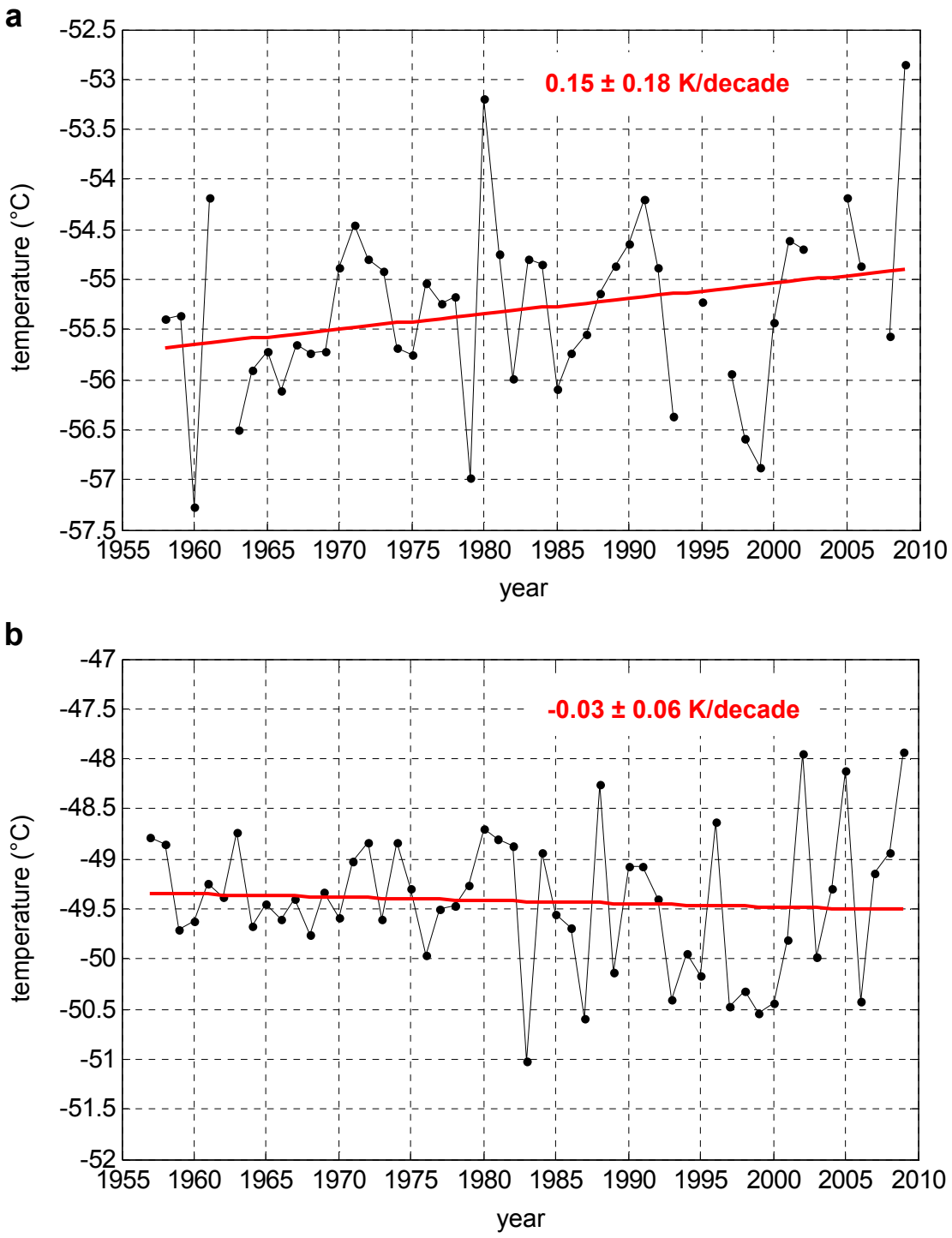

Figure 5.9. Mean annual near-surface air temperatures recorded at **a**. Vostok for 1958-2009 and **b**. at South Pole. Red solid lines are the linear fit to the data and their linear trends and the 95% confidence interval are written above in red letters.

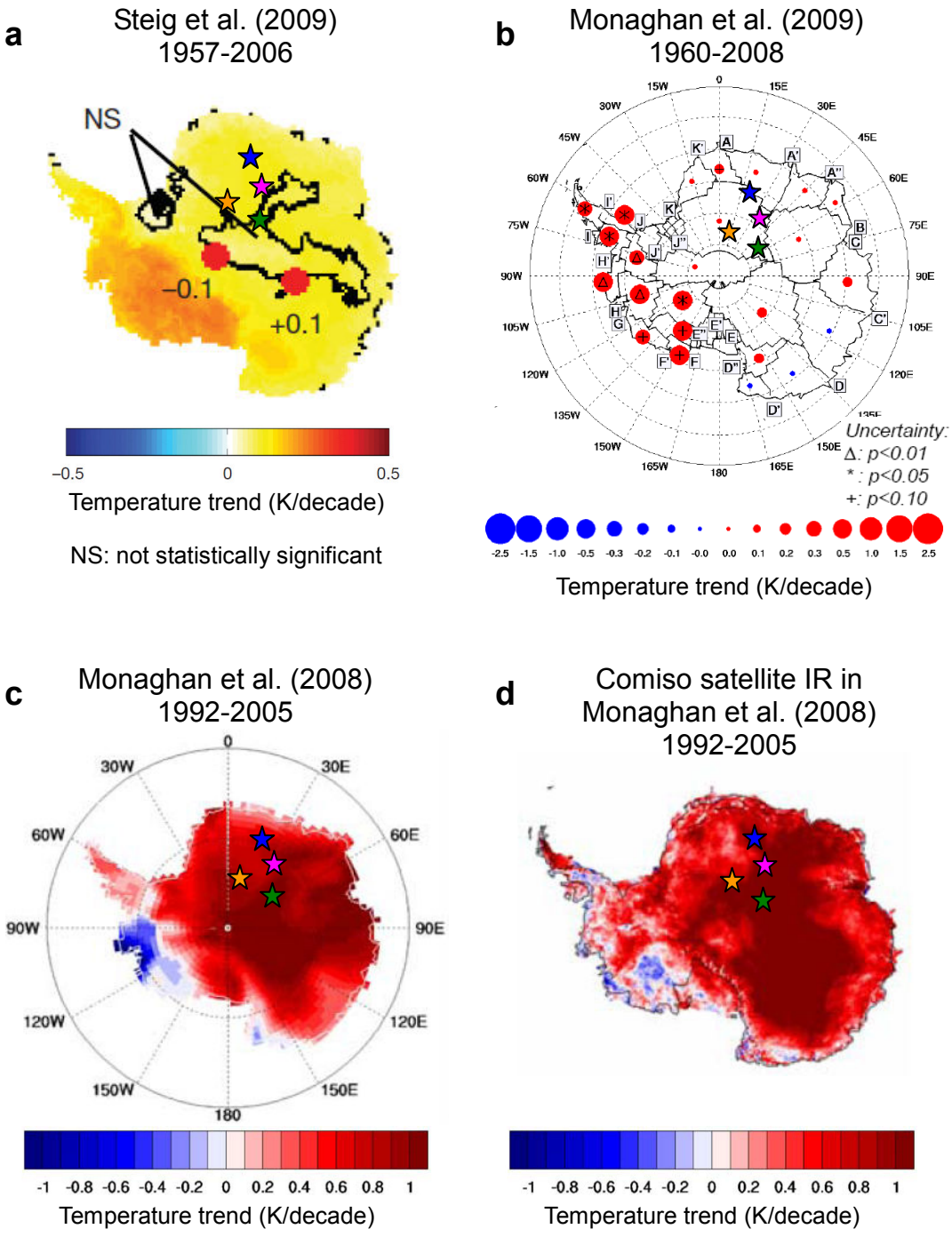

Figure 5.10. Maps of near-surface air temperature trends of **a**. Steig et al. (2009), **b**. Monaghan et al. (2009), **c**. Monaghan et al. (2008) and **d**. the skin-surface temperature trends of Comiso satellite IR, mentioned in Monaghan et al. (2008). Stars indicate the locations of the study sites in this research, blue: NUS07-2, pink: NUS07-5, green: NUS07-7 and orange: NUS08-5.

An interesting pattern of temperature trends are seen in the mid-troposphere which may be related to the pattern at the surface. Turner et al. (2006) found a warming trend of 0.5 to 0.7 K/decade in winter time (June-August) at the 500-hPa level between 1971 and 2003, from radiosonde temperature profiles. Although this strong, statistically significant warming trend is in winter, Figure 5.11 shows that 7 out of 8 stations in East Antarctica show warming on annual basis, 3 of which (South Pole, Syowa and Casey) are statistically significant trends between 0.2 and 0.4 K/decade. Monaghan et al. (2009) applied the same kriging-like spatial extrapolation technique as in Monaghan et al. (2008) to radiosonde data from stations indicated in Figure 5.12b and reconstructed the 500 hPa temperature for 1960-2007 period. A statistically significant warming was identified over the entire Antarctica and trends for the East Antarctic interior are around 0.4 K/decade (Figure 5.12a). The mean surface pressure at Dome Fuji and Plateau Station which are at similar altitudes and relatively close to the near-divide sites are around 600 hPa (Table 5.1). On the other hand, the mean surface pressure at South Pole is 681.2 hPa hence the surface pressure at NUS08-5 which is ~300 m lower in altitude is estimated to be higher than at South Pole. Therefore, NUS07-2, -5 and -7 are close to the mid-troposphere where a warming trend is observed than NUS08-5. It is not known how the 500-hPa level is connected with the surface around the ice divide in East Antarctica. However, it is possible that the three sites along the ice divide display the similar trends to the 500-hPa level since the surface is closer to the mid-troposphere than at NUS08-5 and South Pole and a stronger coupling of the surface and the 500-hPa level may exist.

Table 5.1 Observed mean annual pressures, altitude, period of observation and the data sources for stations near the study sites of this research. Data sources are Yamanouchi et al. (2003) for Dome Fuji, Schwerdtfeger (1970) for Plateau Station and Turner et al. (2004) updated in 2010 for Vostok and South Pole.

	Dome Fuji	Plateau Station	Vostok	South Pole
mean surface pressure (hPa)	598.6	609.2	624.5	681.2
altitude (m)	3810	3625	3488	2835
period of observation	1995-1997	1966-1968	1958-2008	1958-2009

It is worth noting that the skin-surface temperature trend from the satellite IR data of Comiso (2000), mentioned in Steig et al. (2009), displays exactly this pattern. Figures 5.12a to c show trends of the skin-surface temperature for 1982-1999 with different cloud masking techniques. Figure 5.12a was produced from data of Comiso (2000) who used a combination of channel differencing and daily differencing. Figures 5.12b and c are produced by applying an additional cloud masking (thresholding technique; see Steig et al. 2009 for details) with different threshold values. It is clear that introducing the thresholding technique has a significant impact in the temperature trends. Steig et al. (2009) states that the very strong trends shown in Figure 5.12a are not supported by the ground-based observations. However, the ground-based observations used to justify this statement are only from South Pole and Vostok for the interior of East Antarctica and none from the region where the study sites of this research are located. One must keep in mind that the trend map of Comiso (2000) shown in Figure 5.12a is for the 1982-1999 period and results of this research extends for further 9 years for NUS07-2, -5 and -7 and 10 years for NUS08-5. Also, the magnitudes of trends can not be determined unambiguously by borehole paleothermometry. However, at least the pattern shown in Figure 5.12a is supported by the inverted surface temperature histories. This raises the possibility that, despite the limitations in the satellite IR data, the earlier reconstruction using them may have been indicating a realistic true pattern of the surface

temperature trends. Extending the satellite IR record to present without the thresholding technique, as well as re-examining and validating the cloud masking will help to clarify if this is the case.

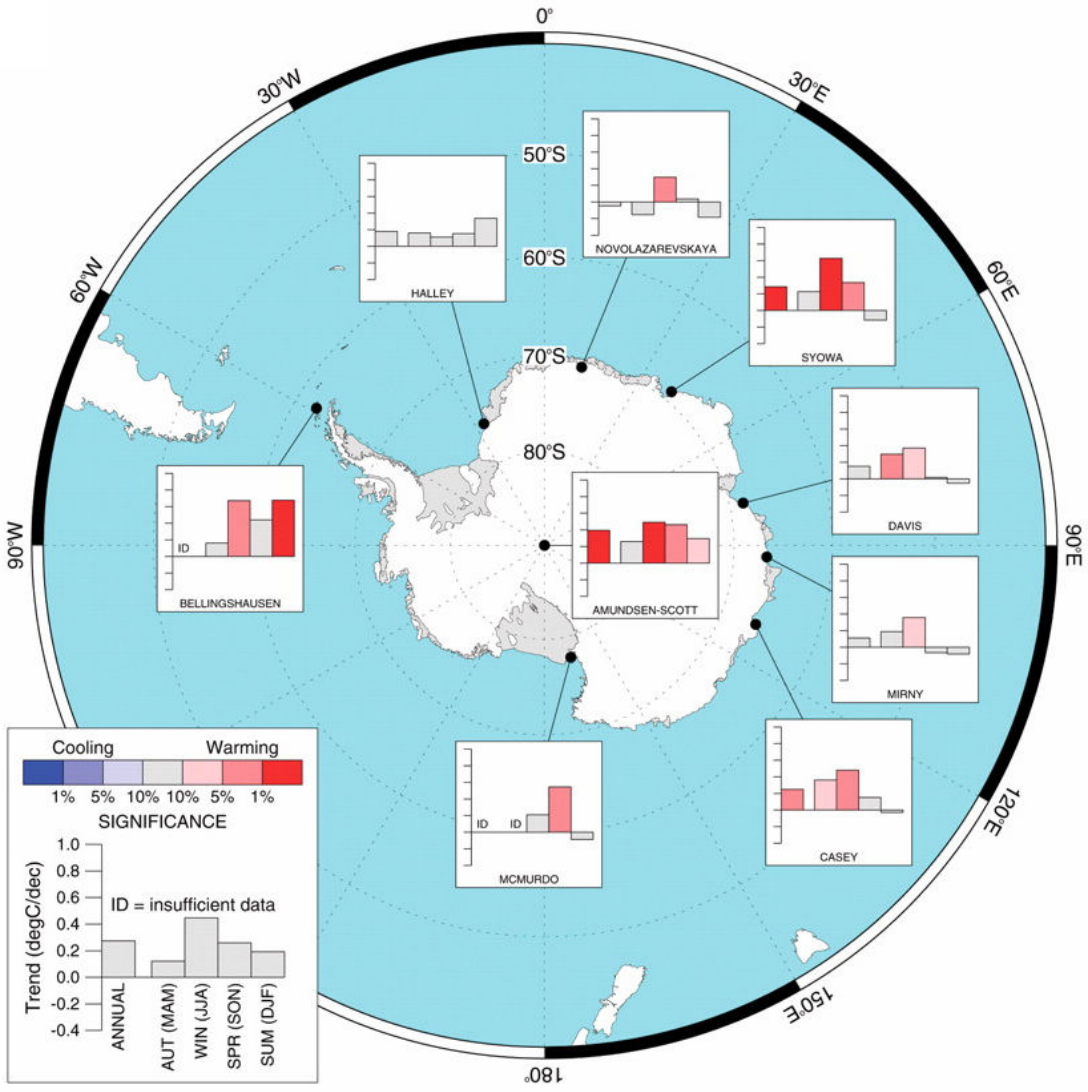

Figure 5.11. Annual and seasonal 500 hPa temperature trends from 1971 to 2003 for nine radiosonde stations with long records. From Turner et al. (2006).

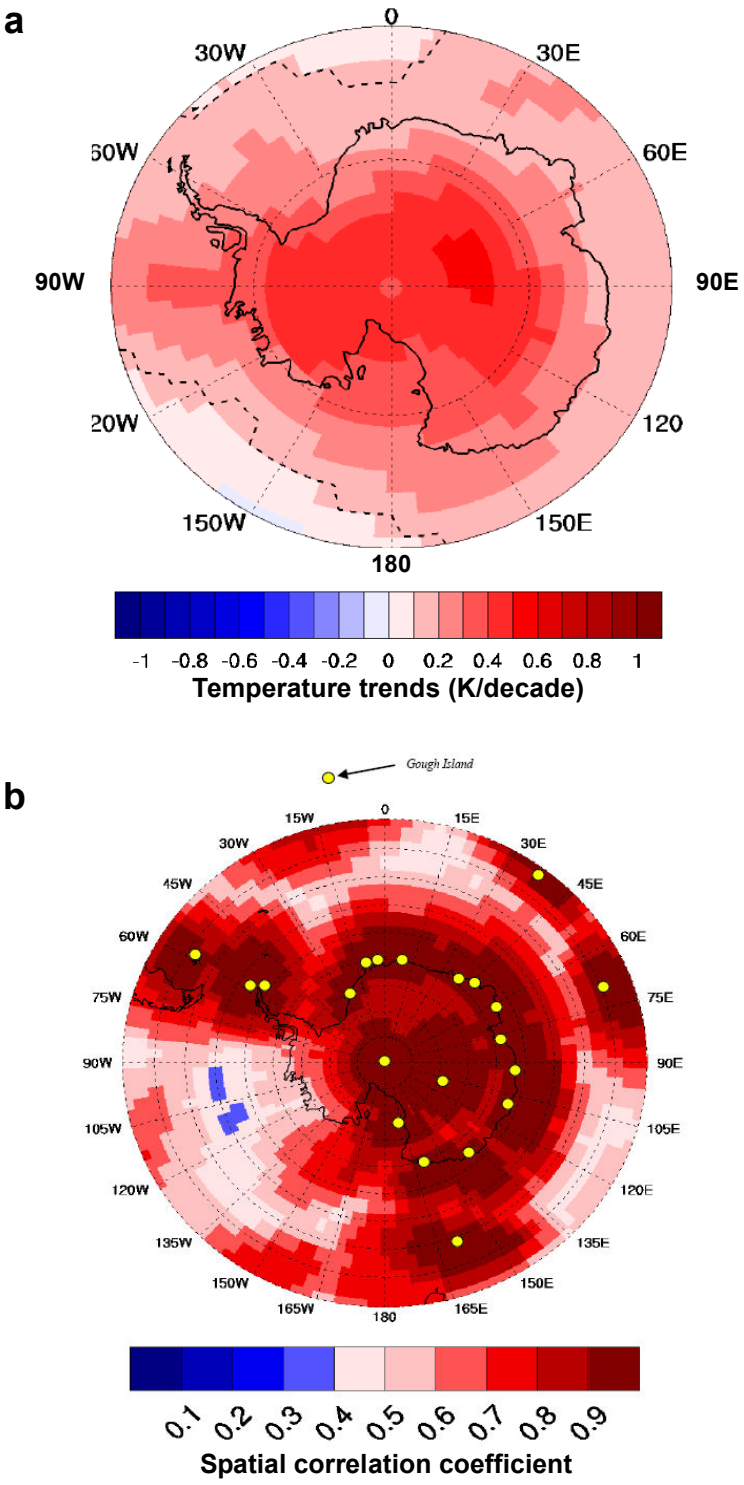

Figure 5.12. a. Annual 500 hPa temperature trends from 1960 to 2007 and **b**. locations of stations (yellow dots) and the maximum absolute value of the Pearson's correlation coefficient (shading) used in the 500 hPa temperature reconstruction. From Monaghan et al. (2009).

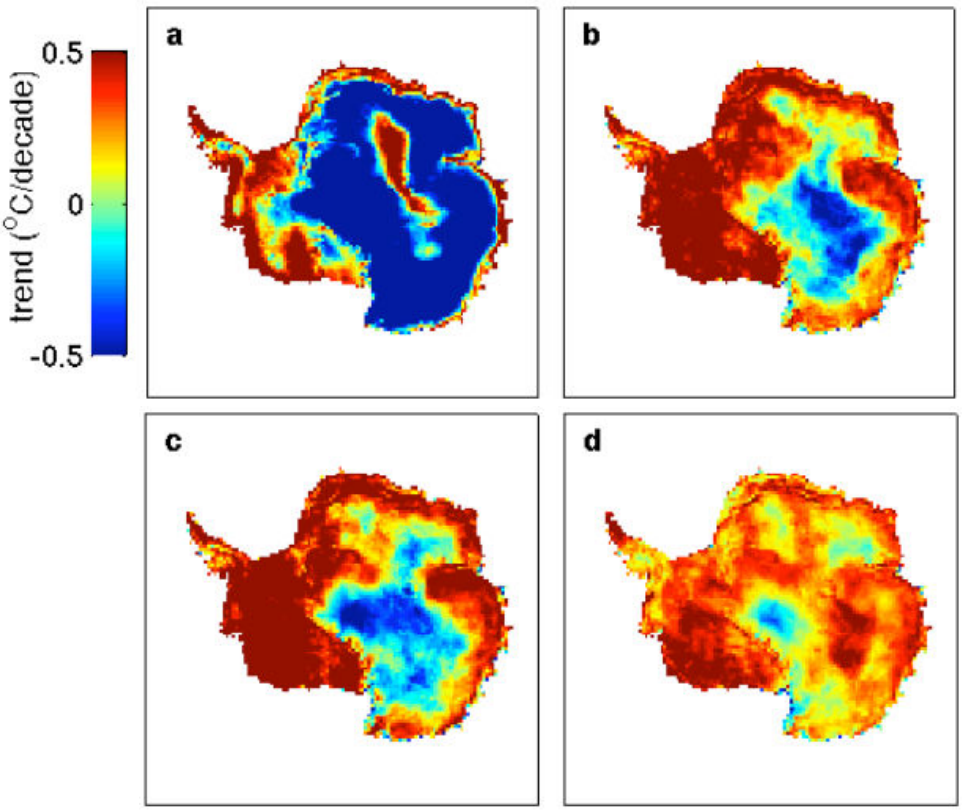

Figure 5.13. Maps of skin-surface temperature trends from AVHRR satellite IR data for 1982-1998 with cloud masking used in **a**. Comiso (2000), **b**. Monaghan et al. (2008) and **c**. Steig et al (2009). **d**. shows the same as **c** but for 1982-2006. From Steig et al. (2009).

Chapter 6

COMPARISON WITH HISTORICAL DATA

6.1 Introduction

So far in this dissertation, surface temperature histories at four sites in the interior of East Antarctica were derived only by applying geophysical inverse methods to borehole firn temperature profiles. From this present day data, an inference of the surface temperature change pattern in the recent decades was made. In this chapter, the reliability of these data will be explored with the available data from the past. The purpose of the Traverse and this research is to obtain *in situ* data to investigate the climate trends from places rarely visited and without long-term meteorological measurements. However, the Traverse visited locations of historical visits and research stations with some scientific data. The newly obtained data can be compared with these measurements and possibly validated. Here, meteorological measurements at Plateau Station and borehole temperature measurements at the Pole of Inaccessibility, made in the 1960s, will be compared to some of the results presented in Chapter 5.

6.2 Meteorological measurements at Plateau Station, 1966-68

The U.S. Antarctic Program established Plateau Station at 79.25°S, 40.56°E in December 1965 for the purpose of supporting the South Pole-Queen Maud Land Traverses and carrying out various scientific research studies at a high altitude and high polar latitude. It was

operated continuously until January 1969. During this time, meteorological measurements were made using a 32-m profiling tower. Firn temperatures were also measured over a course of a year in 1967, down to a depth of 10 m. Plateau Station is situated 126 km east of NUS07-5 and approximately 50 m higher in altitude. Although there are numerous research papers written using meteorological data from Plateau Station (e.g. Kuhn et al., 1975 and references therein), raw data are not available. Only monthly mean air temperatures for 1967 and 1966-98 period, and the annual mean 10-meter firn temperature for 1967 were found in published and archived literature. This limits the analyses in this section to be only qualitative.

The inverted surface temperature histories from this research are of the skin-surface temperature, whereas the meteorological measurements from Plateau Station are temperatures of the overlying air or the sub-surface. In the interior of Antarctica, it is expected that the skin-surface temperature is on average lower than the air temperature because of the inversion layer that exists for much of the year (e.g. King and Turner, 1997; van den Broeke et al, 2005). A strong inversion layer was observed to persist throughout the year at Plateau Station (Riordan, 1977). Therefore, a direct comparison of the air temperatures and inverted surface temperatures can not be carried out and an estimate of the skin-surface temperature at Plateau Station is needed. With a lack of radiation data to conduct a surface energy balance modeling approach (e.g. van den Broeke et al., 2004), the only way to estimate the skin-surface temperature is to use the 10-m firn temperature as a proxy for the annual mean skin-surface temperature which is often done on dry-snow areas of polar ice sheets (e.g. Schytt, 1958; Paterson, 1994).

Table 6.1 summarizes the 10-m firn temperature, air temperature and their differences for Plateau Station and elsewhere on the high-altitude region of the Antarctic plateau. The 10-m firn temperature measured at Plateau Station in 1967 hence the estimate of the skin-surface

temperature is -60.5°C. The difference between the 1.5-m air and the skin-surface temperatures is 4.6 K which is much larger than what was observed at many sites. Although this number appears anomalously large, it is not unrealistic since a difference of 5.0 K has been recorded at Dome A recently (Ma et al., 2010). Dome A is situated ~400 m higher than Plateau Station at the highest point on the ice sheet. Plateau Station is also located near the main ice ridge. This similar geographic setting of the location of these two stations may explain their larger apparent inversion strength.

Table 6.1. Comparison of 10-m firn temperatures and annual mean air temperatures from high-altitude Antarctic plateau sites. This table is based on Table 4 in Loewe (1970) with data for Plateau Station from Weller and Scwerdtfeger (1977) and Kuhn (1969), and Dome A from Ma et al. (2010) added. *: the temperature at 0.1 m depth was used to approximate the skin-surface temperature in Ma et al. (2010).

station	altitude (m)	10-m firn temperature (°C)	air temperature (°C)	difference (K)	observation period
Plateau	**3672**	**-60.5**	**-55.9**	**4.6**	**1967**
Pionerskaya	2740	-39.4	-38.0	1.4	1956-58
South Pole	2835	-50.8	-49.3	1.5	1957-67
Vostok	3488	-57.3	-55.6	1.7	1958-57
Komsomolskaya	3500	-53.9	-52.5	1.4	1958
Dome A	4093	-56.6*	-51.6	5.0	2005-07

As discussed in Chapter 4, a surface temperature history obtained by the linearized inversion method is a collection of weighted averages of the true surface temperature over some period of time. The spread for 42 years b.p. (1967) shown in Figure 6.1 indicates that temperature for this time is in fact a weighted average over a long period of time up to around 10 years b.p. and time when the averaging starts can not be defined from the data. In case of

the RJ-MCMC, the resulting surface temperature history is the statistical mean of many surface temperature histories that fit the criteria of data misfit and the prior information. Therefore, surface temperatures for an instantaneous time can not be picked from inverted surface temperature histories and directly compared with the surface temperature for 1967 at Plateau Station. However, both of the inverted surface temperature histories are around 3 K higher than the surface temperature at Plateau Station throughout a long period of time surrounding 1967 (Figure 6.1). As a more direct comparison, the mean annual 10-m firn temperature in 2008-09 measured with ATPU was -56.4°C as shown in Figure 5.4a in the previous chapter. This is 4.1°C higher than the Plateau Station measurement.

Those large differences may be explained by the distance between the two sites and their different setting with respect to local topography. Figure 6.2 shows the altitude profiles for ±100 km from each location along the line of the maximum slope, extracted from ICESat Digital Elevation Model of Zwally et al. (2003). It is clear that NUS07-5 is on a steeper slope at a 100-km scale. Moreover, Plateau Station is only approximately 80km away from a ridge. The closest ridge to NUS07-5, which is in fact Dome Fuji, is ~170 km away (not shown). Because of the steeper slope and greater distance to the closest ridge, NUS07-5 probably experiences stronger inversion (katabatic) wind than at Plateau Station. In general, a higher wind speed weakens the inversion strength due to the turbulent mixing of the air inside the inversion layer (e.g. King and Turner, 1997; van As et al., 2007). This has been shown to be the case in Dronning Maud Land by Kane (1970) who analyzed the relationship between the slope gradient and the 10-m firn temperatures measured during the U.S. South Pole-Queen Maud Land Traverses I and II and found the warmest spots corresponded with areas of high slope. The inversion strength could therefore be weaker at NUS07-5 which could explain the higher surface temperature given by inversion than at Plateau Station for 1967.

It is also possible that some part of the difference is due to Plateau Station experiencing

anomalously cold conditions for the few years prior to 1967. It is well-known that the temperatures at depths in firn and ice show lagged responses to variations at the surface (e.g. Paterson, 1994) and the lag at 10 m depth to an annual temperature cycle at the surface is about half a year at Plateau Station (Weller and Schwerdtfeger, 1977). Climate variations on longer time scale, e.g., two or three cold years could reach 10 m with even longer lag. The lack of available data for the seasons before 1967 as of this writing makes it impossible to speculate further.

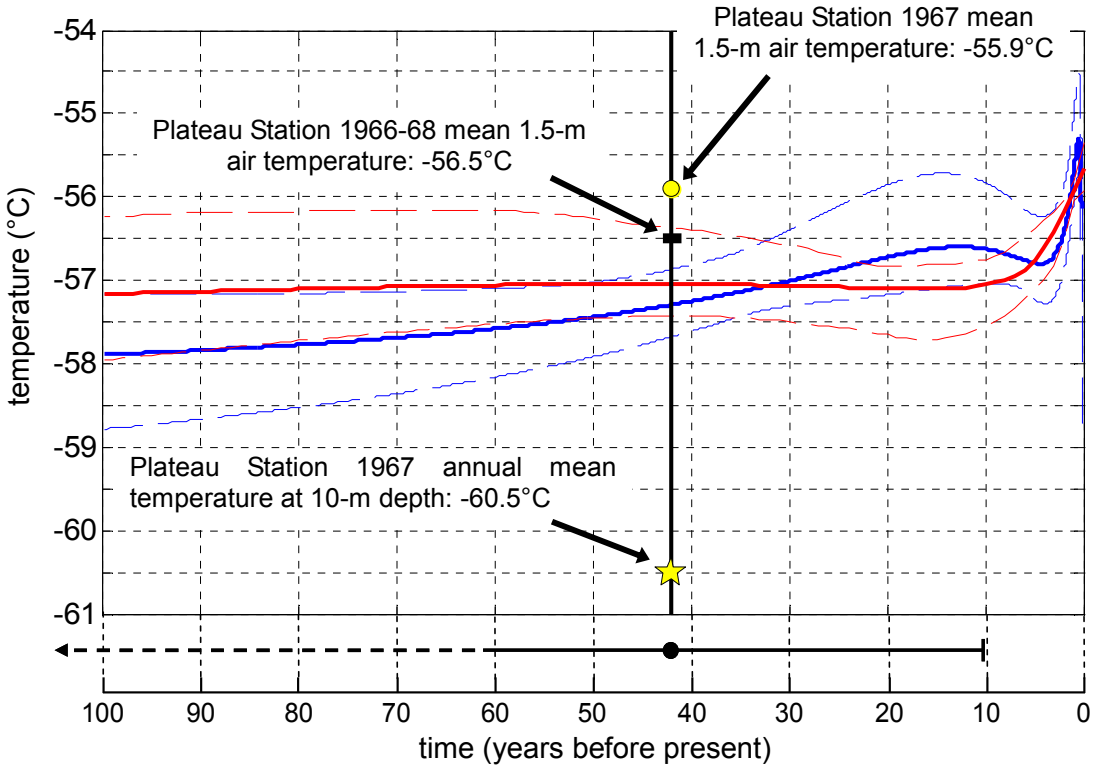

Figure 6.1. Inverted surface temperature histories at NUS07-5 from the linearized inversion (blue) and RJ-MCMC (red) for the past 60 years, and meteorological and firn temperature measurements at Plateau Station, situated 126 km away from NUS07-5. Spread for 42 years b.p. (1967) is also shown at the bottom.

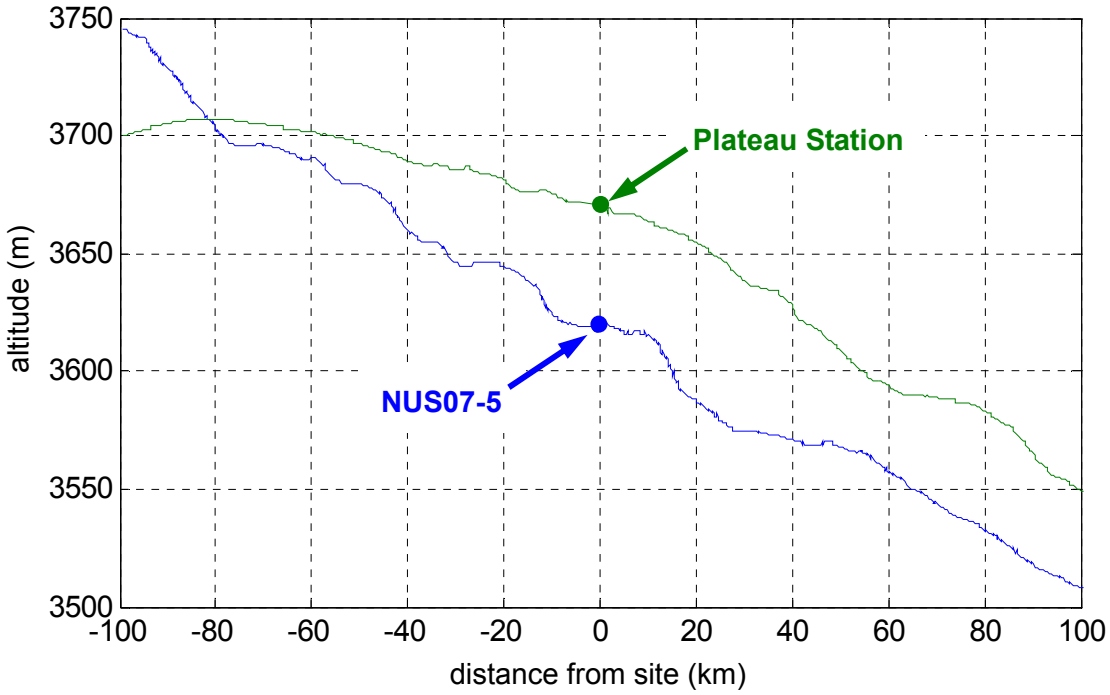

Figure 6.2. Altitude profiles along the line of maximum slope for ±100 km, centered at Plateau Station and NUS07-5.

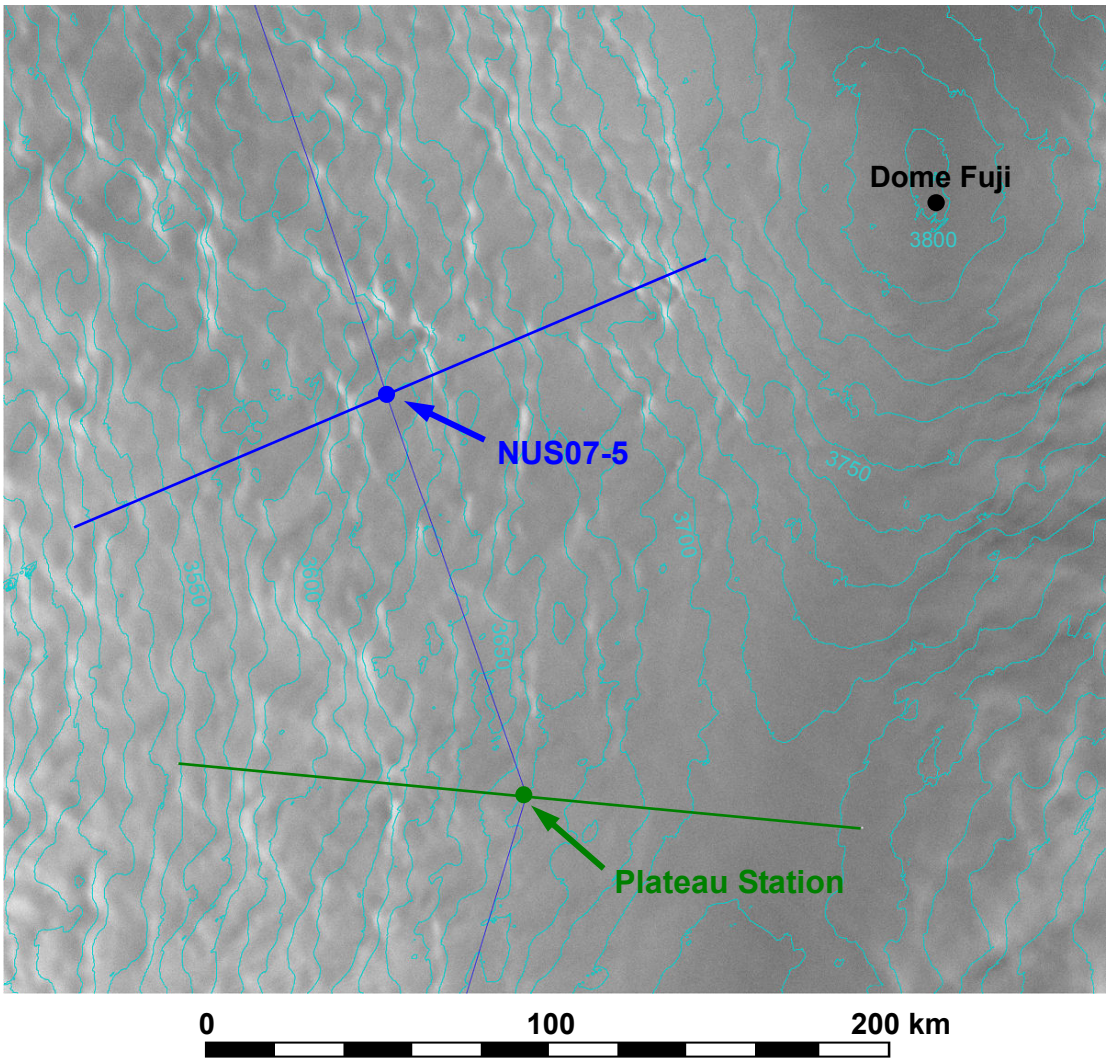

Figure 6.3. A map around NUS07-5 and Plateau Station with elevation from ICESat DEM of Zwally et al. (2003) laid over RADARSAT-1 SAR mosaic image of Jezek et al. (2002). Lines of slope from where altitude profiles in Figure 6.2 for NUS07-5 and Plateau Station were taken are indicated by blue and green lines, respectively. Elevation contour interval is 10 m.

6.3 Borehole temperature measurements at the Pole of Inaccessibility, 1964 and 1965

Pole of Inaccessibility served as a hub for the U.S. South Pole-Queen Maud Land (SPQML) Traverses of 1964-65 and 1965-66, as well as several Soviet traverses. Firn temperature measurements were made by a Soviet traverse of 1963-64 and the U.S. SPQML Traverse of 1964-65 in a 47-m borehole that was drilled in 1958 (Cameron et al., 1968). Locations of this older borehole and the one drilled during the Norwegian-U.S. Traverse are separated by approximately 4 km hence the two boreholes can be considered to be at virtually the same location.

Temperature profiles measured by the Soviet traverse and the U.S. SPQML Traverse are shown in Figure 6.4., along with the profiles measured by the ATPU. Unfortunately, the details on the measurements made by the Soviets (uncertainty, sensors and the measurement device used etc.) can not be found. Also, the Soviet data appear somewhat unreliable. Temperatures between 7 and 22 m for the Soviet profile show larger variations than measurements made by ATPU or the U.S. SPQML Traverse. Temperatures at 32 m and deeper are all the same which seems unrealistic considering the gradients seen at depths shallower than 32 m. For these reasons, detailed analysis will be done using data from the U.S. SPQML Traverse. The Soviet data will be considered only supplementary.

It is important to note that the older measurements were made in an open borehole. Several investigators have used temperatures measured in open boreholes on Antarctic and Greenland Ice Sheets for surface temperature inversions (Alley and Koci, 1990; Nicholls and Parren, 1993). Alley and Koci (1990) found that in a 217-m open borehole at GISP2 in Greenland (measurements were made after the first season of GISP2 ice core drilling in 1989), temperatures at 15 m and deeper were reproducible to ±0.01 K when repeated measurements were made up to 25 days after the drilling. However, an experiment to monitor open-borehole temperatures and the atmospheric pressure by Clow et al. (1996) at Taylor Dome C borehole

in Antarctica revealed temperature fluctuations with the standard deviation of 0.02 to 0.03 K correlated well with atmospheric pressure fluctuations. Based on these facts, an additional uncertainty of ±0.02 K is added to the quoted uncertainty of ±0.05 K for measurements by the U.S. SPQML Traverse.

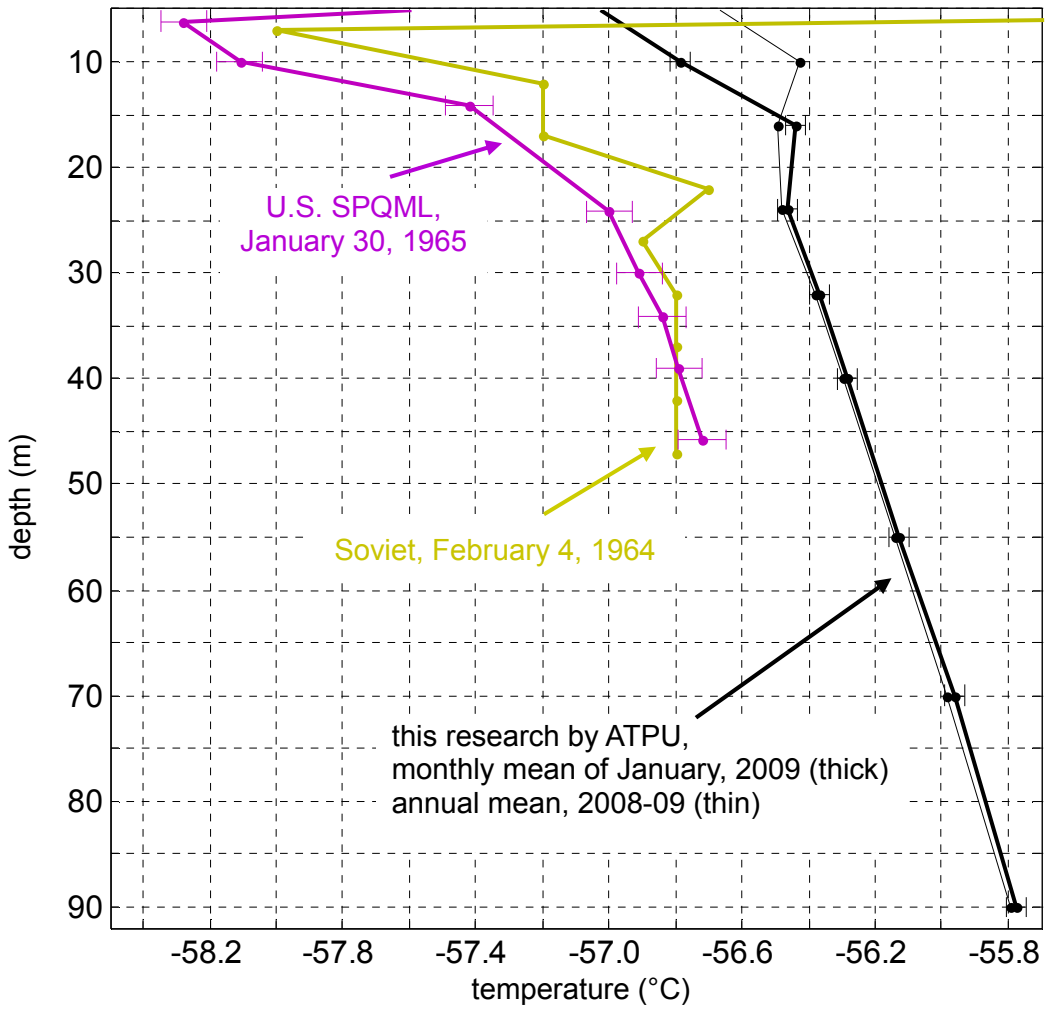

Figure 6.4. Firn temperature profiles at the Pole of Inaccessibility (NUS07-7) measured by the Soviet traverse on February 4, 1964 (dark yellow), by the U.S. SPQML Traverse on January 30, 1965 (purple) and the monthly mean for January, 2009 by this study (black) with their respective measurement uncertainties. The uncertainty for the measurement by Soviets is unknown. The older data are from Cameron et al. (1968).

An obvious difference between the profiles measured in the 1960s and recently is the offset between the profiles. The profile measured by the ATPU shows temperatures systematically higher by approximately 0.5 K, ignoring differences seen at 10 m and above where seasonal variations still persist. Profiles measured by both the US SPQML and the Soviet traverses, who presumably used different measurement devices, are systematically lower than the modern measurement. This provides enough evidence to determine that the firn temperatures were in fact lower in the 1960s, even though some doubts remain about measurements by the Soviet traverse. The question is then, can this offset be explained by climatic changes shown by the inverted surface temperature histories?

To answer this, the forward model was run with inverted surface temperature histories up to 1965 and the resulting simulated temperature profiles compared. Blue and red thin lines in Figure 6.6 are the simulated profiles at 1965 (45 years b.p.) obtained from surface temperature histories inverted by the linearized inversion and the RJ-MCMC, respectively, that are shown by blue and red solid lines in Figure 6.4. Although both of these profiles are closer to the older measurements than profile measured in 2008-09, there are still around 0.2 to 0.3 K offset from the profile in 1965. This implies that the surface temperatures were probably lower for some extended period prior to 1965.

When the errors in the parameters used to calculate the inverted temperatures are accounted for, however, lower temperatures measured in 1965 can reasonably be simulated. Error bounds indicated by dashed lines in Figure 6.5 are derived by accounting for uncertainties in thermal conductivity, accumulation rate, ice thickness, and basal melt rate. Of those parameters, accumulation rate and ice thickness create the largest spread of surface temperatures for times before 20 years b.p (Figure 4.13 and 4.19 in Chapter 4). Light blue solid line in Figure 6.5 is the surface temperature history inverted by the linearized inversion with the accumulation rate and the ice thickness lower by 15% and 10%, respectively, which

are the lower uncertainty bounds for both parameters as discussed in Chapter 4.2. Pink line with circles is one sample of the posterior Probability Density Function of the surface temperature history derived by the RJ-MCMC, also with lower accumulation rate and ice thickness. Firn temperature profiles simulated for 1965 by these two surface temperature histories are also shown in Figure 6.6. The profile simulated with surface temperature history from the linearized inversion (light blue solid line) lies within the measurement uncertainty of the profile in 1965 between 24 and 38 m. On the other hand, profile from the RJ-MCMC is within the uncertainty of 1965 data only at 24 m, although the offset has been reduced. The better fit to the older profile by the surface temperature history from the linearized inversion is a result of lower temperatures for several decades leading up to 1965 than in the history from the RJ-MCMC.

There are still distinct differences between temperatures measured in 1965 and those simulated by surface temperature histories inverted with lower accumulation rate and ice thickness, particularly for depths above 15 m and below 40 m. This is probably due to the inverted surface temperatures being smooth. Interannual and decadal variability in the years preceding 1965 can not be recovered from the modern data since there is no resolving power for short time periods in the past. This is well indicated by the spread for 1965 shown in Figure 6.5b. In order to obtain a better fit to the U.S. SPQML data, interannual to decadal time scale details in the surface temperature history are required. For example, there probably was some degree of cooling for several years or a decade, or close to no change up to 1965, judging from the curvature of this profile. To actually recover details around 1965 (or for any time point when data are available), inverse methods need to be modified so multiple data measured at different times can be incorporated.

The result of the comparative analysis in this section indicates that the surface temperatures around 1965 (45 years b.p.) were 0.3 to 0.5 K lower than originally estimated by

the two inverse methods although these numbers were within the error bounds. If this revised inversion is accepted, the warming trend is then stronger by approximately 0.1 K/decade. This exercise highlights the difficulty in obtaining a precise magnitude of the surface temperature trend from the borehole paleothermometry. It is apparent that the parameters used in the inversion methods need refined values, and reduced errors on the values would permit more precise estimates within the limits imposed by thermal diffusion. However, the analysis of the 1965 data shows the potential for improvement in the inversion of modern firn thermal profiles if some valid, well-characterized older data can be found.

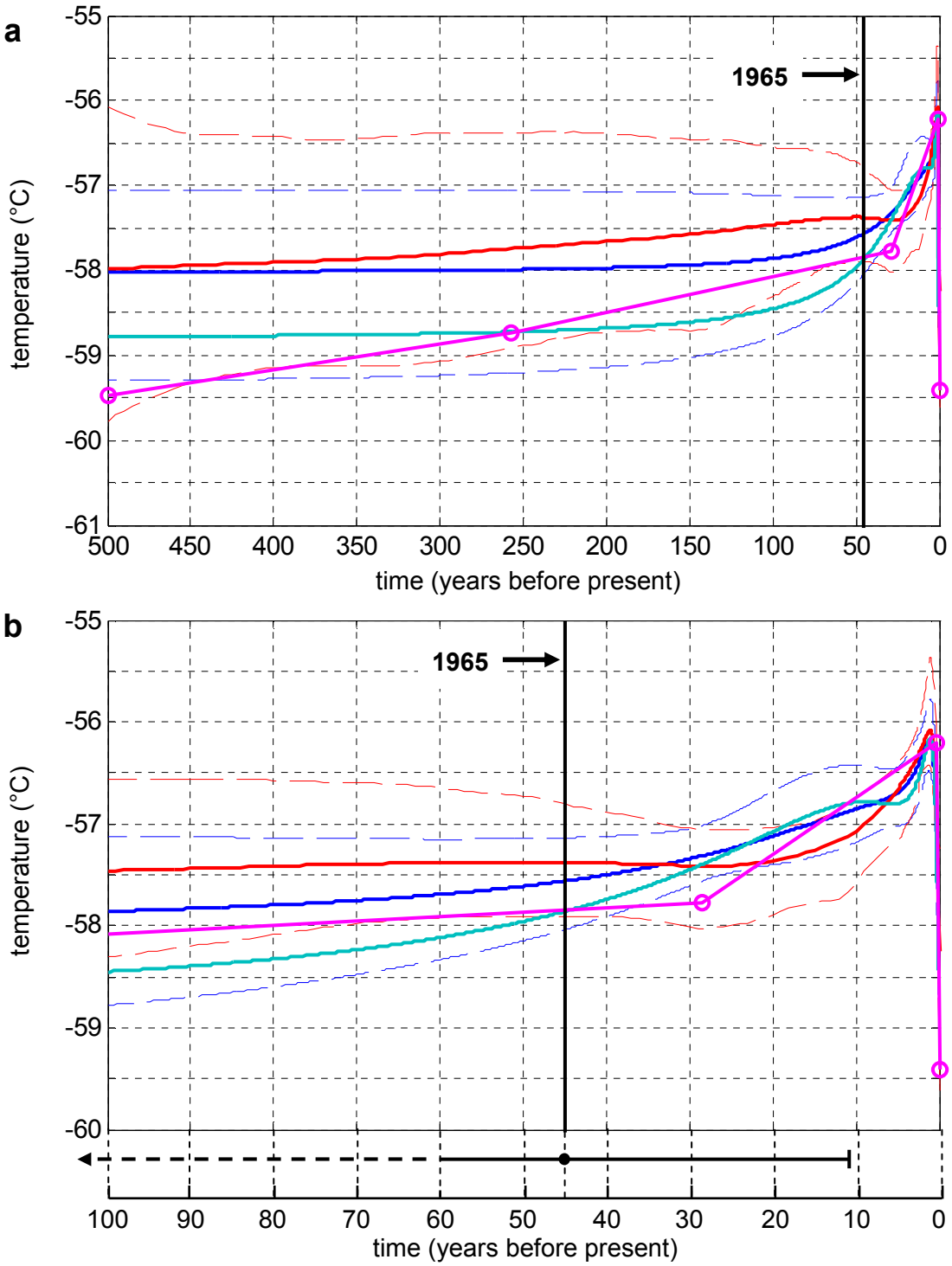

Figure 6.5. Surface temperature history at NUS07-7 inverted using the linearized method (blue) and RJ-MCMC (red) for **a**. 500 years and **b**. the most recent 100 years and the spread for 45 years b.p. (1965). Blue and red lines are the same as in Figure 5.5 in Chapter 5. Light blue line is the surface temperature inverted by linearized inversion with accumulation rate -15% and ice thickness -10%. Pink line with circles is one model obtained by RJ-MCMC with accumulation rate -15% and ice thickness -10%.

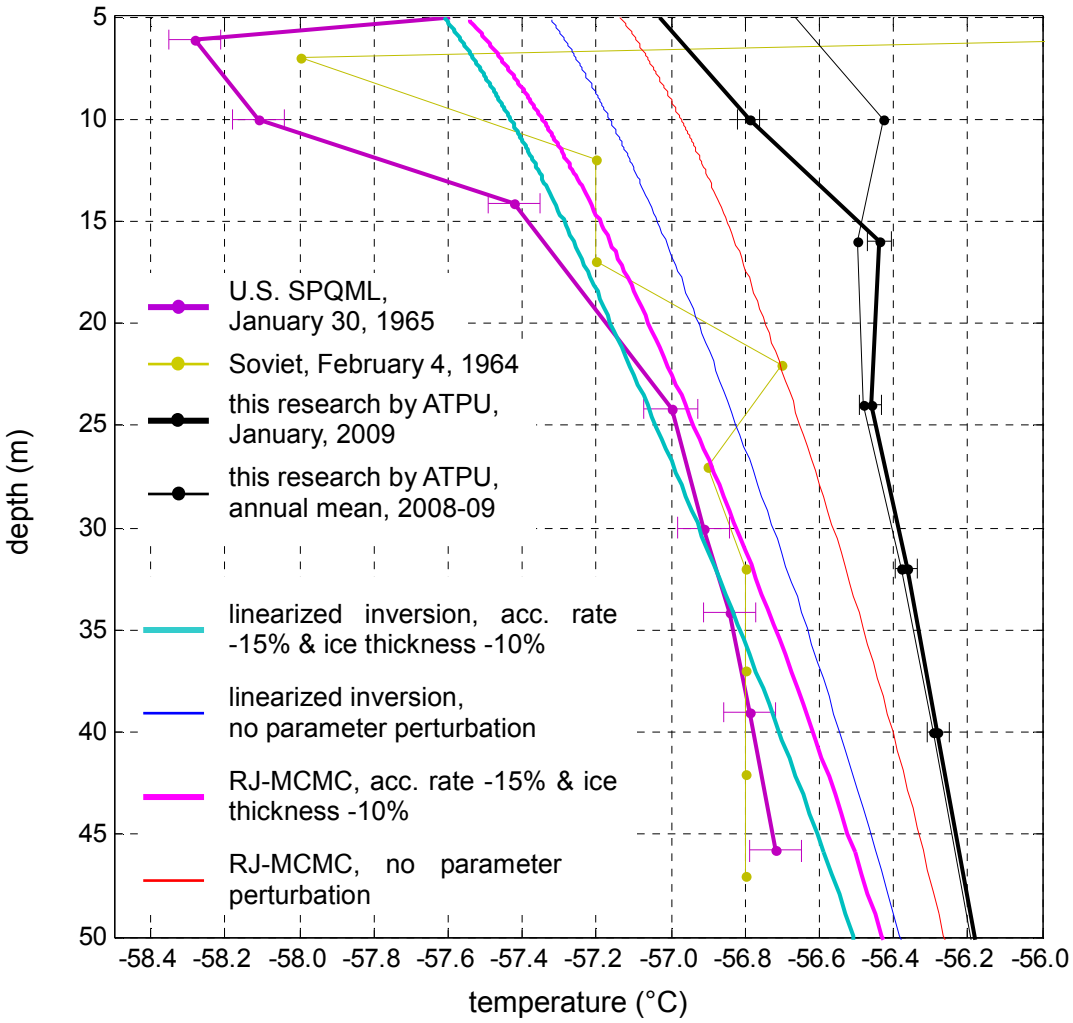

Figure 6.6. Measured and simulated firn temperature profiles at the Pole of Inaccessibility (NUS07-7). Measured profiles are the same as in Figure 6.2. Simulated profiles were obtained by running the forward model with inverted surface temperature histories shown in Figure 6.5 up to 1965.

Chapter 7

SUMMARY AND FUTURE DIRECTIONS

7.1 Summary

The climate trend of the Antarctic interior remains less clear than much of the rest of the globe because of a lack of long-term weather records. Recent studies utilizing sparse available records, satellite data, and models have estimated a warming trend of approximately 0.1 to 0.2 K/decade in Antarctica for the past 50 years. Despite these recent developments, trends in a large part of East Antarctica are still ambiguous since statistical significance can not be established. This dissertation research was carried out with the aim of contributing a new and independent estimate of the surface temperature trends for the past several decades in Dronning Maud Land sector of East Antarctica. Specific objectives were: 1) to determine the surface temperature trends in the interior of East Antarctica for the past several decades; 2) in order to achieve 1), develop an automated firn temperature profiling system that is easily deployed in a traverse set-up, and make high-precision firn temperature profile measurements and; 3) apply geophysical inverse methods to the obtained firn temperature profiles.

Chapter 3 provided a description of the Automated Temperature Profiling Units (ATPUs) that were deployed at four sites in East Antarctica during the Norwegian-U.S. IPY Scientific Traverse of East Antarctica. ATPUs can be set up in the field within 24 hours and measure near-hourly firn temperatures with the standard uncertainty of 0.03 K.

In Chapter 4, two geophysical inverse methods, the linearized inversion method and the Reversible Jump Markov Chain Monte Carlo (RJ-MCMC), as well as the forward model

required to solve the inverse problem were introduced. A synthetic data example was used to demonstrate important concepts in interpreting surface temperature histories derived by the two inverse methods: the direction of the surface temperature trend for the past several decades can be provided with certainty; any magnitude and the duration of the trends should be interpreted with caution.

The linearized inversion and the RJ-MCMC were applied to firn temperature profiles from four sites in East Antarctica and their results presented in Chapter 5. At NUS07-2, trends calculated from inverted surface temperature histories by the linearized inversion and the RJ-MCMC since 50 years b.p., when the two models start diverging from each other, were 0.28 ± 0.04 K/decade and 0.27 ± 0.08 K/decade, respectively. At NUS07-5, surface temperature histories from the two methods showed noticeable differences. The linearized inversion indicated a more or less constant warming trend of 0.17 ± 0.03 K until 13 years ago whereas the RJ-MCMC showed no change in the same time period. However, a sharp increase in the temperature of around 1.3 to 1.4 K within the most recent decade was a consistent feature in the surface temperatures inverted by both methods. At NUS07-7, the surface temperature increase of 0.70 to 0.75 K between ~30 and 5 years ago was shown by both methods although the linearized inversion showed constant increase whereas the RJ-MCMC showed non-linear increase. At NUS08-5, cooling trend of -0.11 ± 0.08 K/decade between 30 and 2 years b.p. and almost no change before this time period was derived from the linearized inversion. In the surface temperature history from the RJ-MCMC, the trend was constant at -0.02 ± 0.06 K/decade for the same time period as well as beyond 30 years b.p.

Although surface temperature histories inverted by the two inversion methods showed differences in details at some sites, an emerging picture of the surface temperature trends in Dronning Maud Land sector of East Antarctica is, a warming trend near the ice divide and cooling to no change off the divide. This pattern had not been shown by existing

Antarctic-wide near-surface air temperature reconstructions. However, the 500-hPa level temperature was recently found to be warming at a rate of 0.5 K/decade since 1960 (Monaghan et al., 2009). It is speculated that the significant warming trends seen at the three near-divide sites may be connected to this mid-tropospheric warming because the surface pressure is closer to the 500-hPa level than NUS08-5 which is located off the divide although the exact mechanism of the coupling of the mid-troposphere and the surface the vertical atmospheric circulation remain to be investigated.

In Chapter 6 historical data from Plateau Station and the Pole of Inaccessibility were compared with inverted surface temperatures at NUS07-5 and -07, respectively. The 10-m firn temperature measured at Plateau Station in 1967 was used as a proxy for the skin-surface temperature. The inverted temperature for 1967 at NUS07-5 was around 3 K higher than the surface temperature at Plateau Station. An inspection of the surface slope around Plateau Station and NUS07-5, which are separated by 126 km, revealed that NUS07-5 situated further away from the nearest ice ridge and on a steeper slope than Plateau Station. It is estimated that such site characteristics induces stronger katabatic wind which causes turbulent mixing within the surface inversion layer hence the mean surface temperature is higher at NUS07-5 than at Plateau Station. The analysis of the firn temperature profile measured by the U.S. SPQML Traverse in 1965 and the modern data showed an offset of about 0.5 K, the modern data being warmer than older data. This offset could not first be explained by surface temperature histories originally inverted by the two inverse methods. However, when uncertainties in forward model input parameters (accumulation rate and ice sheet thickness in this case) were accounted for, a reasonable agreement between the older measurements and simulated profiles was obtained. This exercise showed the difficulty in obtaining a precise magnitude of the surface temperature trend from the borehole paleothermometry, as well as the potential for improvement in the inversion of modern firn thermal profiles if some valid,

well-characterized older data can be found.

The pattern of the surface temperature trends in East Antarctica indicated by this research, a warming trend near the ice divide and cooling to no change off the divide, has neither been shown nor discussed by published investigations. The only exception is the skin-surface temperature reconstruction from satellite infrared data by Comiso (2000) which has since been revised, however, and no longer shows the same pattern (Steig et al., 2009). Based on sparse station records, Turner et al. (2009) suggested that the pattern of the near-surface air temperature trend in Antarctica for the past 50 years is warming Peninsula, little change to some cooling across the rest of the continent. And this is related to the positive trend in the Southern Annular Mode (SAM) driven in part by the depletion of stratospheric ozone in spring time and greenhouse gas increases (Thompson and Solomon, 2002; Gillet et al., 2008). This SAM-related mechanism can not explain the pattern shown by this research since the implication of the former is that the Antarctic interior cools (e.g. van den Broeke and van Lipzig, 2004). Recently published results of Monaghan et al. (2009) and Steig et al. (2009) utilizing spatial extrapolation techniques revealed that the warming trend is not confined to the Antarctic Peninsula area but is rather spread over the whole continent. In particular, West Antarctica is warming at a statistically significant and faster rate than East Antarctica. In explaining such a pattern, Steig et al. (2009) used a general circulation model to show that for West Antarctica and the Peninsula at least, the warming trend is related to regional changes in atmospheric circulation and associated changes in sea surface temperature and sea ice in Amundsen and Bellingshausen Seas. However, again, such results do not offer a satisfactory explanation for the pattern indicated by this research since both Monaghan et al. (2009) and Steig et al. (2009) show a uniform, modest amount of warming (0.0 to 0.1 K/decade) for the interior Dronning Maud Land.

The newly proposed pattern of the surface temperature trends do not appear to be related

to well-studied atmospheric circulation patterns and oceanic influences at this point. The strong warming trend in the mid-troposphere, which was suggested to be related to the warming at the ice sheet surface near the ice divide in East Antarctica, is a recently discovered phenomenon and causal relation to the large scale synoptic, ozone depletion and related changes in the SAM, or other phenomena need to be found. Therefore, the driver of climate trends in the interior of the East Antarctic Ice Sheet and their connection to the larger scale climate still remains unclear.

7.2 Future directions

Research questions to be pursued in the future are, what is the relation of trends seen at the ice sheet skin-surface from the borehole paleothermometry to the mid-tropospheric trends and how could such a pattern of surface temperature trends arise? A few avenues exist to seek answers to these questions such as the study of atmospheric circulation with global and regional models and/or reanalysis data, and surface energy balance studies. Firn temperature distribution, from which surface temperature histories were inverted, is mainly a result of the energy exchange at the ice sheet surface. Therefore, surface temperature trends found in this dissertation are likely a result of changes in one or more components of the surface energy balance (SEB). Using reanalysis-derived surface meteorology such as ERA-40, NCEP-2 and JRA-25, the individual components of the SEB can be perturbed in order to quantify the amount of change required in each term to reproduce observed surface temperature trends. The quality of these reanalyses outputs over Antarctica improve after 1979 (Bromwich et al., 2007). This coincides with the time period with relatively high confidence in the inverted surface temperatures.

Optical remote sensing could aid the SEB study since albedo, which controls the

shortwave radiation flux can be derived using satellite measurements from sensors such as AVHRR and MODIS, although limited to clear-sky conditions and when the sun is above the horizon. Surface albedo obtained by satellite sensors is an available and independent data set that could be used to assess the results of SEB simulations. Although observations of surface albedo by these sensors are limited to clear-sky conditions and when the sun is above the horizon, AVHRR data set is now almost 30 years long starting in 1981, coinciding with the time period with relatively high confidence in surface temperature histories inverted from the borehole paleothermometry and reliable time period of reanalyses fields. Additionally, thermal infrared channels of AVHRR and MODIS provide the surface skin temperature that can be used as an input in simulating firn temperature distributions. Therefore it will serve as important complementary data to look at the variations in shortwave energy flux. MODIS data will provide an independent cross-check of AVHRR for the last decade.

It must be noted that the surface temperature inversion from borehole paleothermometry is by no means perfect and there is room for improvement. To solve the inverse problem, parameters that influence heat diffusion and advection in the ice sheet (thermal conductivity, ice sheet thickness, accumulation rate and basal melt rate) were measured in firn cores or derived from available data sets. The analysis of the older data presented in Chapter 6 highlighted the need for refined values of these parameters. For example, accumulation rates used for each sites were the mean of the past 750 years derived from firn core chemistry. All the results so far were obtained by using constant accumulation rates since accumulation rate history or the relation between the surface temperature and accumulation rate have not yet been determined for each study sites. It is expected that these information will become available in the future as detailed firn core analysis progress. It's been suggested that the accumulation rate has not changed significantly in East Antarctica for the past 50 years (Monaghan et al., 2006) hence the results of the surface temperature inversion are not

expected to change vastly. However, the accuracy is expected to increase since time-varying accumulation rate history is more realistic than constant accumulation rate.

Similar investigation should be carried out in West Antarctica in order to obtain a clearer picture of recent climatic change in Antarctica as a whole. Steig et al. (2009) and Monaghan et al. (2009) showed that West Antarctica experienced a statistically significant warming trend of ~0.2 to 0.3 K/decade in the near-surface air temperature for the past 50 years whereas changes in East Antarctica are not statistically significant (Figure 5.10a and b in Chapter 5). It would be interesting to see trends from reconstructions of Steig et al. (2009) and Monaghan et al. (2009) compare with those from the borehole paleothermometry. The outcome of the borehole paleothermometry in West Antarctica could either confirm the near-surface air temperature trends so far inferred, or emphasize the need for the investigation into the coupling of the near-surface air and the surface skin temperatures.

References

Anderson, V. H. (1958). *USNC-IGY Antarctic Glaciological Data Field Work 1957-1958*, **Report 825-1-Part II**, Ohio State University Research Foundation.

Arblaster, J.M., G. A. Meehl (2006). Contributions of external forcings to southern annular mode trends, *J. Climate*, **19,** 2896-2905.

Arthern, R. J., D. P. Winebrenner, and D. G. Vaughan (2006). Antarctic snow accumulation mapped using polarization of 4.3-cm wavelength microwave emission, *J. Geophys. Res.*, **111**, D06107, doi:10.1029/2004JD005667.

Bamber, J.L., J. L. Gomez-Dans and J. A. Griggs (2009). A new 1km digital elevation model of the Antarctic derived from combined satellite radar and laser data – Part 1: Data and methods, *The Cryosphere*, **3**, 101-111.

Banta, J. R., J. R. McConnell, M. M. Frey, R. C. Bales, and K. Taylor (2008). Spatial and temporal variability in snow accumulation at the West Antarctic Ice Sheet Divide over recent centuries, *J. Geophys. Res.*, **113**, D23102, doi:10.1029/2008JD010235.

Barrett, B. E., K. W. Nicholls, T. Murray, A. M. Smith, and D. G. Vaughan (2009). Rapid recent warming on Rutford Ice Stream, West Antarctica, from borehole thermometry, *Geophys. Res. Lett.*, **36**, L02708, doi:10.1029/2008GL036369.

Beltrami, H. & Mareschal, J.C. (1995). Ground temperature from borehole temperature data: Resolution and limitations, *GlobalPlanet. Changes*, **11**, 57-70.

Bindschadler, R. A., X. Chen and R. L. Vornberger (1997). Surface velocity and strain rates at the onset of ice stream D, West Antarctica, *Ant. J, Rev.*, **32**, 41-43.

Bodeker, G. E., H. Shiono, and H. Eskes (2005). Indicators of Antarctic ozone depletion, *Atmos. Chem. Phys.*, **5**, 2603-2615.

Bohlander, J. and T. Scambos, compilers (2001). *THERMAP Antarctic Ice Sheet Temperature Data.* Boulder, CO: National Snow and Ice Data Center. Digital media.

Brandt, R. E. and S. G. Warren (1997): Temperature measurements and heat transfer in near-surface snow at the South Pole. J. Glaciol., 43, 339-351.

Bromwich, D. H. and Fogt, R. L. (2004). Strong trends in skill of the ERA-40 and NCEP/NCAR reanalyses in the high and middle latitudes of the southern hemisphere, 1958-2001. *J. Climate*, **17**, 4603-4619.

--- , --- , K. I. Hodges and J. E. Walsh (2007). A tropospheric assessment of the ERA-40, NCEP, and JRA-25 global reanalyses in the polar regions, *J. Geophys. Res.*, **112**, D10111, doi:10.1029/2006JD007859.

Cazenave, A. and W. Llovel (2010). Contemporary sea level rise, *Ann. Rev. Mar. Sci.*, **2**,

145-173.

Chapman, W.L., and J.E. Walsh (2007). A synthesis of Antarctic temperatures, *J. Climate*, **20**, 4096-4117.

Clow, G. D. (1992). The extent of temporal smearing in surface temperature histories derived from borehole temperature measurements, *Palaeogeog., Palaeoclim., Palaeoecol.*, **98**, 81-86.

---, R. W. Saltus and E. D. Waddington (1996). A new high-precision borehole-temperature logging system used at GISP2, Greenland, and Taylor Dome, Antarctica, *J. Glaciol.*, **42**, 576-584.

--- (2008), USGS Polar Temperature Logging System, Description and Measurement Uncertainties, *U.S. Geological Survey Techniques and Methods*, **2–E3**, 24 p.

--- (unpublished). *Inverse theory*, and *Inversion of simple 1D conduction problem*, personal notes of G. D. Clow.

Cole, J. E., D. Rind, R. S. Webb, J. Jouzel and R. Healy (1999). Climatic controls on $\delta^{18}O$ variability of precipitation; simulated influence of temperature, precipitation amount and vapor source region, *J. Geophys. Res.*, **104**, 12,223-14,235.

Comiso, J. C. (2000). Variability and Trends in Antarctic Surface Temperatures from In Situ and Satellite Infrared Measurements, *J. Climate*, **13**, 1674-1696.

Dahl-Jensen, D. and S. Johnsen (1986). Paleotemperatures still exist in the Greenland ice sheet, *Nature*, **320**, 250-232.

---, D., K. Mosegaard, N. Gundestrup, G. D. Clow, S. J. Johnsen, A. W. Hansen, and N. Balling. (1998). Past temperatures directly from the Greenland Ice Sheet, *Science*, **282**, 268–271.

Dalrymple, P. C. (1966). A physical climatology of the Antarctic plateau, in *Studies in Antarctic meteorology, Antarctica*, *Ant. Res. Ser.*, **9**, Rubin, M. J. ed., 195-231, AGU, Washington D.C.

---, H. H. Lettau and S. H. Wollaston (1966). South Pole micrometeorology program: data analysis, in *Studies in Antarctic meteorology, Antarctica*, *Ant. Res. Ser.*, **9**, Rubin, M. J. ed., 13-57, AGU, Washington D.C.

Firestone, J. (1995). Resolving the Younger Dryas event through borehole thermometry, *J. Glaciol.*, **41**, 39-50.

Fujita, S., H. Maeno and K. Matsuoka (2006). Radio wave depolarization and scattering within ice sheets: A matrix based model to link radar and ice core measurements and its application, *J. Glaciol.*, **52**, 407-424.

Fujita, K. and O. Abe (2006). Stable isotopes in daily precipitation at Dome Fuji, East Antarctica, *Geophys. Res. Lett.*, **33**, doi:10.1029/2006GL026936.

Garrett, K. W. and H. M. Rosenberg (1974). The thermal conductivity of epoxy-resin/powder composite materials, *J. Phys. D: Appl. Phys.*, **7**, 1247-1258.

Gilks, W.R., S. Richardson and D. Spiegelhalter, eds. (1996). *Markov Chain Monte Carlo in Practice*, Chapman and Hall, London, U.K.

Gillett, N. P., D. A. Stone, P. A. Stott, T. Nozawa, A. Y. Karpechko, G. C. Hergel, M. F. Wehner and P. D. Jones (2008). Attribution of polar warming to human influences, *Nat. Geosci.*, **1**, 750-754.

Giovinetto, M (1960). *USNC-IGY Antarctic Glaciological Data Field Work 1957-1958*, **Report 825-2-Part IV**, Ohio State University Research Foundation.

---, M. B., N. M. Waters, and C. R. Bentley (1990). Dependence of Antarctic surface mass balance on temperature, elevation and distance to open water, *J. Geophys. Res.*, **95**, 3517-3531.

Goldthwait, R. P. (1958). *USNC-IGY Antarctic Glaciological Data, Field Work 1957 and 1958*, **Report 825-1-Part II**, Ohio State University Research Foundation.

Goujon, C., J.-M. Barnola, and C. Ritz (2003). Modeling the densification of polar firn including heat diffusion: Application to close-off characteristics and gas isotopic fractionation for Antarctica and Greenland sites, *J. Geophys. Res.*, **108(D24)**, 4792, doi:10.1029/2002JD003319.

Haran, T., J. Bohlander, T. Scambos, T. Painter, and M. Fahnestock compilers (2006). *MODIS mosaic of Antarctica (MOA) image map*. Boulder, Colorado USA: National Snow and Ice Data Center. Digital media.

Harris, R. N. and D. S. Chapman (1998). Geothermics and climage change 1. Analysis of borehole temperatures with emphasis on resolving power, *J. Geophys. Res.*, **103(B4)**, 7363-7370.

Hartmann, A. and V. Rath, (2005) Uncertainties and shortcomings of ground surface temperature histories derived from inversion of temperature logs, *J. Geophys. Eng.*, **2(4)**, 299-311.

Hegerl, G.C., F. W. Zwiers, P. Braconnot, N.P. Gillett, Y. Luo, J.A. Marengo Orsini, N. Nicholls, J.E. Penner and P.A. Stott (2007). Understanding and Attributing Climate Change. In: *Climate Change 2007: The Physical Science Basis. Contribution of Working Group I to the Fourth Assessment Report of the Intergovernmental Panel on Climate Change*, Solomon, S., D. Qin, M. Manning, Z. Chen, M. Marquis, K.B. Averyt, M. Tignor and H.L. Miller (eds.), Cambridge University Press, Cambridge, United Kingdom and New York, NY, USA.

Hines, K. M., D. H. Bromwich, and G. J. Marshall (2000). Artificial surface pressure trends in the NCEP–NCAR reanalysis over the Southern Ocean. *J. Climate*, **13**, 3940–3952.

Hooke, R.L.B. (2005). *Principles of Glacier Mechanics*, 2nd ed., Cambridge University Press,

Cambridge, U.K.

Intergovernmental Panel on Climate Change (2007). *Climate Change 2007: Synthesis Report. Contribution of Working Groups I, II and III to the Fourth Assessment Report of the Intergovernmental Panel on Climate Change* [Core Writing Team, Pachauri, R.K and Reisinger, A. (eds.)]. IPCC, Geneva, Switzerland.

Jacka, T. H. and W. F. Budd (1991). Detection of temperature and sea-ice-extent changes in the Antarctic and Southern Ocean, *Proc. Int. Conf. on the Role of the Polar Regions in Global Change*, Fairbanks, AK, Univ. of Alaska, Geophysical Institute, 63-70.

--- and W. F. Budd (1998). Detection of temperature and sea-ice-extent changes in the Antarctic and Southern Ocean, 1949-96, *Ann. Glaciol.*, **27**, 553-559.

Jacobel, R. W., B. C. Welch, E. J. Steig and D. P. Schneider (2005). Glaciological and climatic significance of Hercules Dome, Antarctica: An optimal site for deep ice core drilling, *J. Geophys. Res.*, **110**, F01015, doi: 10.1029/2004JF000188.

Jezek, K., and RAMP Product Team (2002). *RAMP AMM-1 SAR Image Mosaic of Antarctica*. Fairbanks, AK: Alaska SAR Facility, in association with the National Snow and Ice Data Center, Boulder, CO. Digital media.

Jones, P. D. (1995). Recent variations in mean temperature and the diurnal temperature range in the Antarctic, *Geophys. Res. Lett.*, **22**, 1345-1348.

Jouzel, J., et al. (1997). Validity of temperature reconstruction from water isotopes in ice cores, *J. Geophys. Res.*, **102**, 26,471-26,487.

Kameda, T., H. Motoyama, S. Fujita and S. Takahashi (2008). Temporal and spatial variability of surface mass balance at Dome Fuji, East Antarctica, by the stake method from 1995 to 2006, *J. Glaciol.*, **54**, 107-116.

Kaye, G. W. C. and T. H. Laby (1995). *Tables of physical and chemical constants*, 15th ed. Longman, Essex, England.

Koloditz, O. (2002). *Computational methods in environmental fluid mechanics*, Springer, Berlin, Germany.

Kuhn, M. H. (1969). Preliminary report on meteorological studies at Plateau Station, Antarctica, 1967, Univ. Melbourne, Met. Dept.

--- (1971). Messung und Analyse der spektralen transparenz der Ostantarktischen atmosphäre, Ph.D. dissertation, Univ. of Innsbruck, Innsbruck.

---, A. J. Riordan and I . A. Wagner (1975). The climate of Plateau Station, in *Proc. Twenty-fourth Alaska Science Conference, Fairbanks, Alaska, August 15 to 17, 1973*, 255-267, Geophysical Institute, University of Alaska, Fairbanks, AK.

Kwok R., and J. C. Comiso (2002). Spatial patterns of variability in Antarctic surface temperature: Connections to the Southern Hemisphere Annular Mode and the Southern

Oscillation. *Geophys. Res. Lett.*, **29**, 1705, doi:10.1029/2002GL015415.

Liston, G.E. and J-G. Winther (2005). Antarctic surface and subsurface snow and ice melt fluxes. *J. Clim*, **18**,1469-1481.

Lliboutry, L. (1979). A critical review of analytical approximate solutions for steady state velocities and temperatures in cold ice-sheets, *Z. Gletscherkd. Glazialgeol.*, **15**, 135-148.

Ma, Y, L. Bian, C. Xiao, I. Allison and X. Zhou (2010). Near surface climate of the traverse route from Zhongshan Station to Dome A, East Antarctica, *Ant. Sci.*, **22**, 443-459.

MacAyeal, D. R., J. Firestone, E. Waddington (1991). Paleothermometry by control methods, *J. Glaciol.*, **37**, 326-338.

---, T. A. Scambos, C. L. Hulbe and M. A. Fahnestock (2003). Catastrophic ice-shelf break-up by an ice-shelf-fragment-capsize mechanism, *J. Glaciol.*, **49**, 22-36.

Manabe, S. and R. J. Stouffer, (1980). Sensitivity of a global climate model to an increase of CO2 in the atmosphere, *J. Geophys. Res.*, **85(C10)**, 5529–5554.

Marshall, G. J. (2003). Trends in the southern annular mode from observations and reanalyses. *J. Climate*, **16**, 4134-4143.

--- (2007). Half-century seasonal relationships between the Southern Annular Mode and Antarctic temperature. *Int. J. Climatol.*, **27**, 373-383.

--- (2010, July 9). An observation-based Southern Hemisphere Annular Mode Index, http://www.antarctica.ac.uk/met/gjma/sam.html, accessed August 4, 2010.

Mayewski, P.A., et al. (2009). State of the Antarctic and Southern Ocean climate system, *Rev. Geophys.*, **47**, RG1003, doi:10.1029/2007RG000231.

Meehl, G. A. et al. (2007). Global Climate Projections. In: *Climate Change 2007: The Physical Science Basis. Contribution of Working Group I to the Fourth Assessment Report of the Intergovernmental Panel on Climate Change* [Solomon, S., et al. (eds.)]. Cambridge Univ. Press.

Monaghan, A. J., D. H. Bromwich, W. Chapman, and J. C. Comiso (2008). Recent variability and trends of Antarctic near-surface temperature, *J. Geophys. Res.*, **113**, D04105, doi:10.1029/2007JD009094.

Motoyama, H., N. Hirasawa, K. Satow, and O. Watanabe (2005). Seasonal variations in oxygen isotope ratios of daily collected precipitation and wind drift samples and in the final snow cover at Dome Fuji Station, Antarctica, *J. Geophys. Res.*, **110**, D11106, doi:10.1029/2004JD004953.

Neumann, T. A. (2003). Effects of firn ventilation on geochemistry of polar snow. Ph.D dissertation, University of Washington, Seattle.

Nicholas, J. V., and D. R. White (2001). *Traceable temperatures*, 2nd ed., Wiley, West Sussex,

U.K.

Nicholls, K.W. and J.G. Paren. (1993). Extending the Antarctic meteorological record using ice-sheet temperature profiles, *J. Climate*, **6**(1), 141-150.

Nicholls, R. J. and A. Cazanave (2010). Sea-level rise and its impact on coastal zones, *Science*, **328**, 1517-1519.

Noone, D. (2008). The influence of midlatitude and tropical overturning circulation on the isotopic composition of atmospheric water vapor and Antarctic precipitation, *J. Geophys. Res.*, **113**, D04102, doi:10.1029/2007JD008892.

---, and I. Simmonds (2002). Associations between $\delta^{18}O$ of water and climate parameters in a simulation of atmospheric circulation for 1979–95, *J. Climate.*, **15**, 3150–3169.

Oldenburg, D. W. (1984). An introduction to linear inverse theory, *IEEE Trans. Geosci. Remote Sensing*, **GE-22**, 665-674.

Parker, R. L. (1977). Understandig Inverse Theory, *Ann. Rev. Earth Palanet. Sci.*, **5**, 35-64.

---. (1994). *Geophysical Inverse Theory*, Princeton University Press, Princeton.

Patankar, S. V. (1980). *Numerical Heat Transfer and Fluid Flow*, Hemisphere Publishing, New York.

Paterson, W. S. B. (1994).*The Physics of Glaciers,* 3rd ed., Butterworth-Heinemann, Oxford, U.K.

Peacock, S. M. (1987). Thermal modeling of metamorphic pressure–temperature–time paths: a forward approach. In: *Short Courses in Geology*, **7,** American Geophysical Union, Washington D.C., 57-102.

Pirrit, J. and G. A. Doumani (1961). *USNC-IGY Antarctic Glaciological Data, Field Work 1959*, **Report 968-2**, Ohio State University Research Foundation.

Press, W.H., B. P. Flannery, S. A. Teukolsky, and W. T. Vettering (2007). Numerical recipes in C: the art of scientific computing. Cambridge University Press, 3rd edition.

Raper, S. C. B., T. M. L. Wigley, P. D. Mayes, P. D. Jones and M. J. Salinger (1984). Variations in surface air temperatures. Part 3: The Antarctic, 1957–82. *Mon. Wea. Rev*. **112**, 1341–1353.

Rignot, E., J.L. Bamber, M. R. van den Broeke, C. Davis, Y. Li, W. J. van de Berg and E. van Meijgaard (2008). Recent Antarctic ice mass loss from radar interferometry and regional climate modeling, *Nat. Geosci.*, **1**, 106-10.

Riordan, A. J. (1977). Variation of temperature and air motion in the 0- to 32-meter layer at Plateau Station, Antarctica, in *Meteorological studies at Plateau Station, Antarctica*, *Ant. Res. Ser.*, **25**, Businger, J.A. ed., 113-127, AGU, Washington D.C.

Robert, C. P. and G. Casella (2004). *Monte Carlo Statistical Methods*, 2nd ed., Springer, New York.

Scambos, T. A., C. L. Hulbe, M. A. Fahnestock, J. Bohlander (2000). The link between climate warming and break-up of ice shelves in the Antarctic Peninsula, *J. Glaciol.*, **46**, 516-530.

Schneider, D. P., E. J. Steig and T. can Ommen (2005). High-resolution ice-core stable-isotopic records from Antarctica: towards interannual climate reconstruction, *Ann. Glaciol.*, **41**, 63-70.

---, E. J. Steig, T. D. van Ommen, D. A. Dixon, P. A. Mayewski, J. M. Jones, and C. M. Bitz (2006). Antarctic temperatures over the past two centuries from ice cores, *Geophys. Res. Lett.*, **33**, L16707, doi:10.1029/2006GL027057.

Schwander, J., T. Sowers, J.-M. Barnola, T. Blunier, A. Fuchs, and B. Malaizé (1997). Age scale of the air in the summit ice: Implication for glacial-interglacial temperature change, *J. Geophys. Res.*, **102**, 19,483-19,493.

Schwerdtfeger, W. (1970). Theory and observations of the wind in the friction layer over the Antarctic plateau, *Ant. J. U.S.*, **5**, 175-176.

Severinghaus, J.P., M. R. Albert, Z. R. Courville, M.A. Fahnestock, K. Kwamura, S. A. Montzka, J. Mühle, T. A. Scambos, E, Shields, C. A. Shuman, M. Suwa. P. Tans and R. F. Weiss (2010). Deep air convection in the firn at a zero-accumulation site, central Antarctica, *Earth Planet. Sci. Lett.*, doi:10.1016/j.epsl.2010.03.003.

Shepherd, A. and D. Wingham (2007). Recent sea-level contributions of the Antarctic and Greenland ice sheets, *Science*, **315**, 1529-1532.

Stearns, C. R. and G. A. Weidner (1993). Sensible and latent heat flux estimates in Antarctica, in *Antarctic Meteorology and Climatology: Studies Based on Automatic Weather Stations*, *Ant. Res. Ser.*, **61**, Bromwich, D. H. and C. R. Stearns ed., 109-138, AGU, Washington D.C.

Steig, E. J., D. P. Schneider, S. D. Rutherford, M. E. Mann, J. C. Comiso, and D. T. Shindell (2008). Warming of the Antarctic ice sheet surface since the 1957 International Geophysical Year, *Nature*, **457**, 459-463.

Tabacco, I.E., C. Bianchi, A. Zirizzotti, E. Zuccheretti, A. Forieri and A. Della Vedova (2002). Airborne radar survey above Vostok region, east Antarctica: ice thickness and Lake Vostok geometry. *J. Glaciol.*, **48**, 62-69.

Tanner, B. D. (1990). Automated Weather Stations, in *Remote Sens. Rev.*, vol 5, pt. 1: *Instrumentation for studying vegetation canopies for remote sensing in optical and thermal infrared regions*, edited by N. S. Goel and J. M. Norman, 73-98.

Taylor, B. N. and C. E. Kuyatt (1994). Guidelines for evaluating and expressing the uncertainty of NIST measurement results, *NIST Technical Note*, **1297**, National Institute of Standards and Technology, 20p.

Thomas, R. H., D. R. MacAyeal, D. H. Eilers and D. R. Gaylord (1984). Glaciological studies on the Ross Ice Shelf, Antarctica, 1973-1978, in *The Ross Ice Shelf: Glaciology and Geophysics, Ant. Res. Ser.*, **42**, edited by C. R. Bentley and D. E. Hayes, 21-53.

---, E. Rignot, G. Casassa, P. Kanagaratnam, C. Acuña, T. Akins, H. Brecher, E. Frederick, P. Gogineni, W. Krabill, S. Manizade, H. Ramamoorthy, A. Rivera, R. Russell, J. Sonntag, R. Swift, J. Yungel, J. Zwally (2004). Accelerated sea-level rise from West Antarctica, *Science*. **306**, 255-258.

Thompson, D. W. J., and J. M. Wallace (2000). Annular modes in the extratropical circulation. Part I: Month-to-month variability. *J. Climate*, **13**, 1000–1016.

---, and S. Solomon (2002). Interpretation of recent Southern Hemisphere climate change. *Science*, **296**, 895–899.

Trenberth, K.E., P.D. Jones, P. Ambenje, R. Bojariu, D. Easterling, A. Klein Tank, D. Parker, F. Rahimzadeh, J.A. Renwick, M. Rusticucci, B. Soden and P. Zhai (2007). Observations: Surface and Atmospheric Climate Change. In: *Climate Change 2007: The Physical Science Basis. Contribution of Working Group I to the Fourth Assessment Report of the Intergovernmental Panel on Climate Change*, Solomon, S., D. Qin, M. Manning, Z. Chen, M. Marquis, K.B. Averyt, M. Tignor and H.L. Miller (eds.), Cambridge University Press, Cambridge, United Kingdom and New York, NY, USA.

Truffer, M. (2004). The basal speed of valley glaciers: an inverse approach, *J. Glaciol.*, **50**, 236–242.

Turner, J., S. R. Colwell, G. J. Marshall, T. A. Lachlan-Cope, A. M. Carleton, P. D. Jones, V. Lagun, P. A. Reid and S. Iagovkina (2004). The SCAR READER Project: Toward a High-Quality Database of the Mean Antarctic Meteorological Observations, *J. Climate.*, **17**, 2890-2896.

---, S. R. Colwell, G. J. Marshall, T. A. Lachlan-Cope, A. M. Carleton, P. D. Jones, V. Lagun, P. A. Reid and S. Iagovkina (2005). Antarctic climate change during the last 50 years, *Int. J. Climatol.*, **25**, 279-294.

---, J. E. Overland and J. E. Walsh (2007). An Arctic and Antarctic perspective on recent climate change, *Int. J. Clim.*, **27**, 277-293.

--- et al. (2009). The Instrumental Period. In: *Antarctic Climate Change and the Environment*, Turner, J., R. Bindschadler, P. Convey, G. di Prisco, E. Fahrbach, J. Gutt, D. Hodgsion, P. Mayewski and C. Summerhayes (eds.), Scientific Committee on Antarctic Research, Scott Polar Research Institute, Cambridge, UK.

van As, D., M. R. van den Broeke, M. M. Helson (2007). Strong-wind events and their impact on the near-surface climate at Kohnen Station on the Antarctic Plateau, *Ant. Sci.*, **19**, 507-519.

van den Broeke, M. R., D. van As, C. Reijmer and R. van de Wal (2004). Assessing and improving the quality of unattended radiation observations in Antarctica, *J. Atmos.*

Ocean. Tech., **21**, 1417-1431.

--- (2005). Sensible heat exchange at the Antarctic snow surface: a study with automatic weather stations, *Int. J. Climatol.*, **25**, 1081-1101.

van Lipzig, N. P. M. and E. van Meijgaard (2002). Temperature Sensitivity of the Antarctic Surface Mass Balance in a Regional Atmospheric Climate Model, *J. Climate.*, **15**, 2758-2774.

Vaughan, D. G., J. L. Bamber, M. Giovinetto, J. Russell, and A. P. R. Cooper (1999). Reassessment of net surface mass balance in Antarctica, *J. Climate.*, **12**, 933– 946.

---, G. J. Marshall,W. M. Connolley, C. Parkinson, R. Mulvaney, D. A. Hodgson, J. C. King, C. J. Pudsey, and J. Turner (2003). Recent rapid regional climate warming on the Antarctic Peninsula, *Clim. Change*, **60**, 243-274.

Velicogna, I. (2009). Increasing rates of ice mass loss from the Greenland and Antarctic ice sheets revealed by GRACE, *Geophys. Res. Lett.*, **36**, L19503, doi:10.1029/2009GL040222.

Vieli, A., A. J. Payne, A. Shepherd and Z. Du (2007). Causes of pre-collapse changes of the Larsen B ice shelf: Numerical modelling and assimilation of satellite observations, *Earth Planet. Sci. Lett*. **259,** 297-306.

Waddington, E. D., T. A. Neumann, M. R. Koutnik, H-P. Marshall and D. L. Morse (2008). Inference of accumulation-rate patterns from deep layers in glaciers and ice sheets, *J. Glaciol.*, **53**, 694-712.

Weller, G. E., and P. Schwerdtfeger (1971). New data on the thermal conductivity of natural snow, *J. Glaciol.*, **10**, 309–311.

---, and P. Schwerdtfeger (1977). Thermal properties and heat transfer processes of low-temperature snow, in *Meteorological studies at Plateau Station, Antarctica*, *Ant. Res. Ser.*, **25**, Businger, J.A. ed., 27-34, AGU, Washington D.C.

Werner, M., and M. Heimann (2002). Modeling interannual variability of water isotopes in Greenland and Antarctica, *J. Geophys. Res.*, **107**, 4001, doi:10.1029/2001JD900253.

Yamanouchi, T., N. Hirasawa, M. Hayashi, S. Takahashi and S. Kaneto (2003). Meteorological characteristics of Antarctic inland station, Dome Fuji, *Mem. Natl. Inst. Polar Res., Spec. Issue*, **57**, 94-104.

Zwally, H. J. and J. Li. (2002). Seasonal and interannual variations of firn densification and ice-sheet surface elevation at the Greenland summit. *J. Glaciol.*, **48**, 199-207.

Zwally, H.J., R. Schutz, C. Bentley, J. Bufton, T. Herring, J. Minster, J. Spinhirne, and R. Thomas (2003). GLAS/ICESat L2 Antarctic and Greenland Ice Sheet Altimetry Data V001. Boulder, CO: National Snow and Ice Data Center. Digital media.

Appendix A

BOREHOLE BACK-FILLING

Temperatures in the deep borehole were recorded during the back-filling, as discussed in section 3.3. Figures A.1 through A.3 show recorded temperatures. Measurements were made at 1-minute interval.

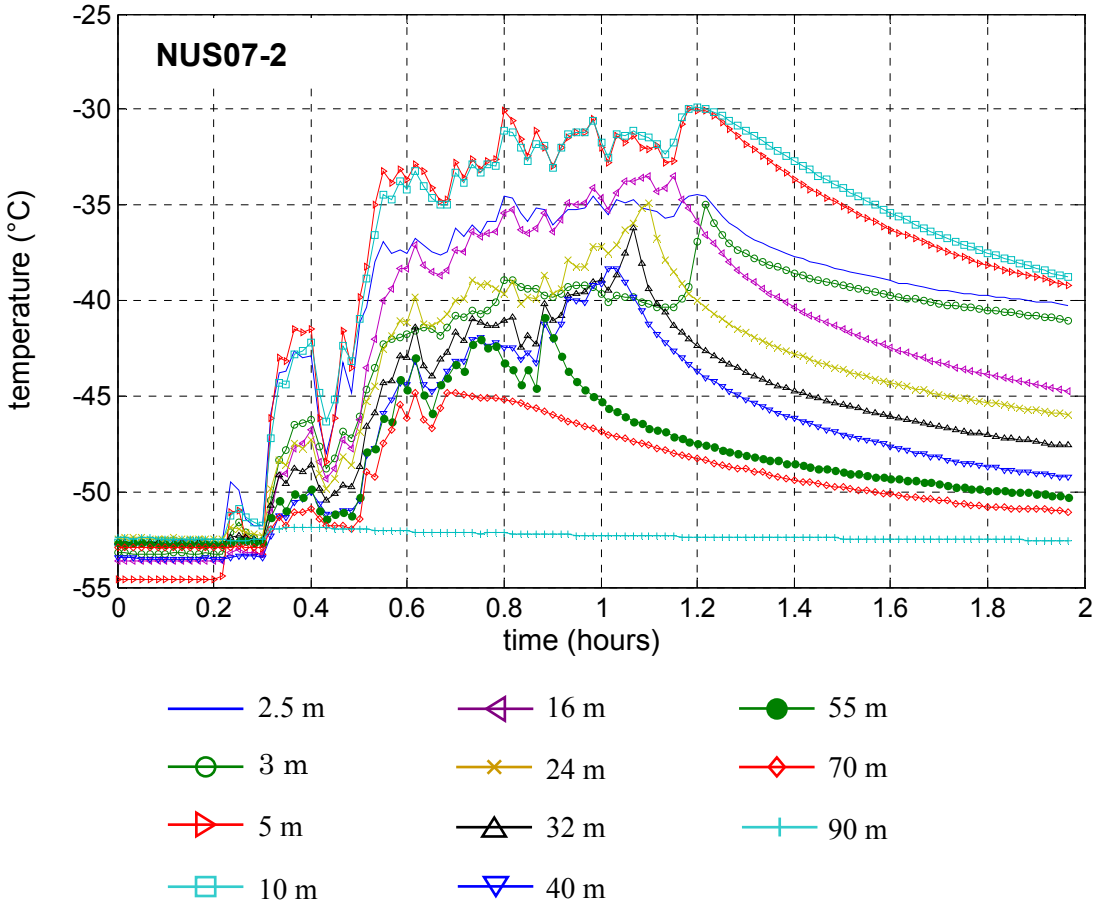

Figure A.1. Temperatures recorded during back-filling of the deep borehole at NUS07-2.

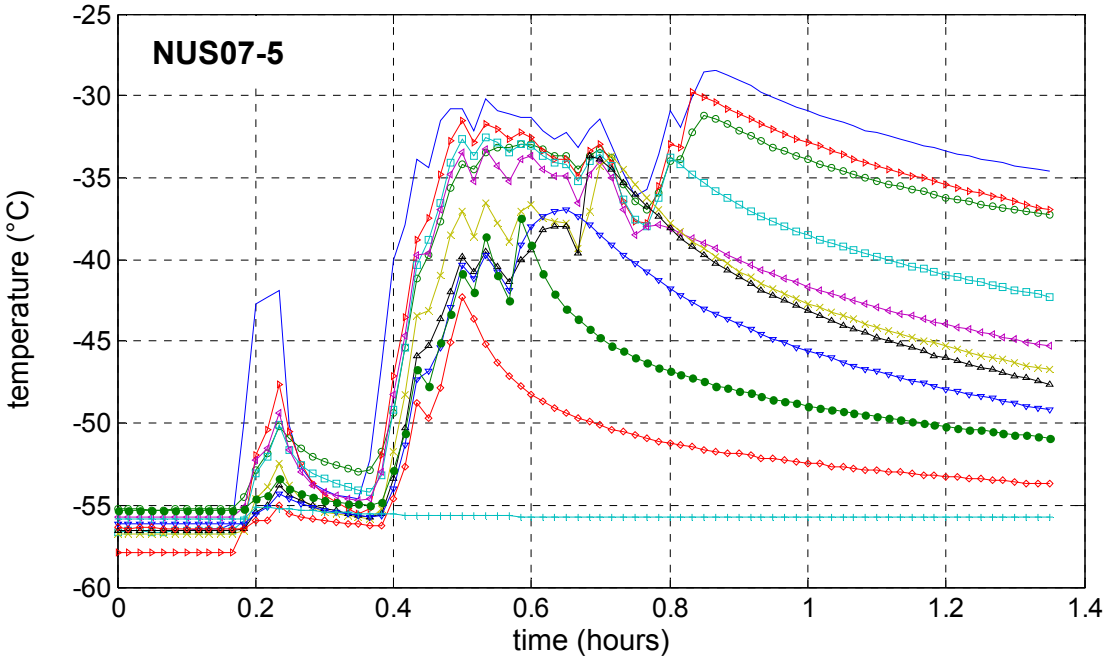

Figure A.2. Temperatures recorded during back-filling of the deep borehole at NUS07-5. Legends are the same as Figure A.1.

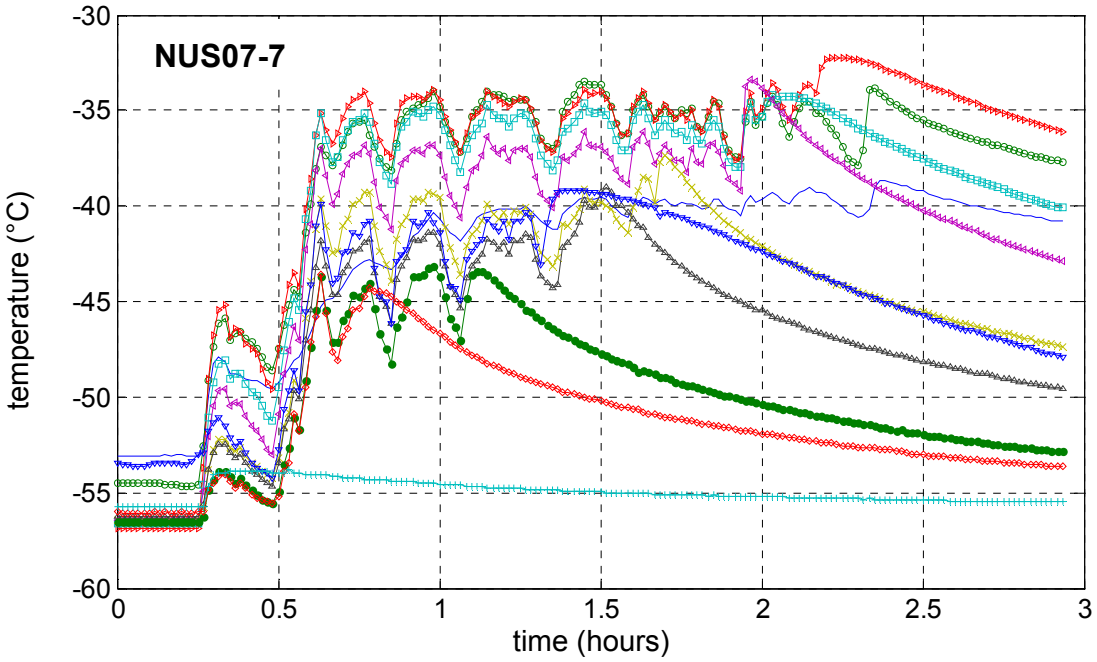

Figure A.3. Temperatures recorded during back-filling of the deep borehole at NUS07-7. Legends are the same as Figure A.1.

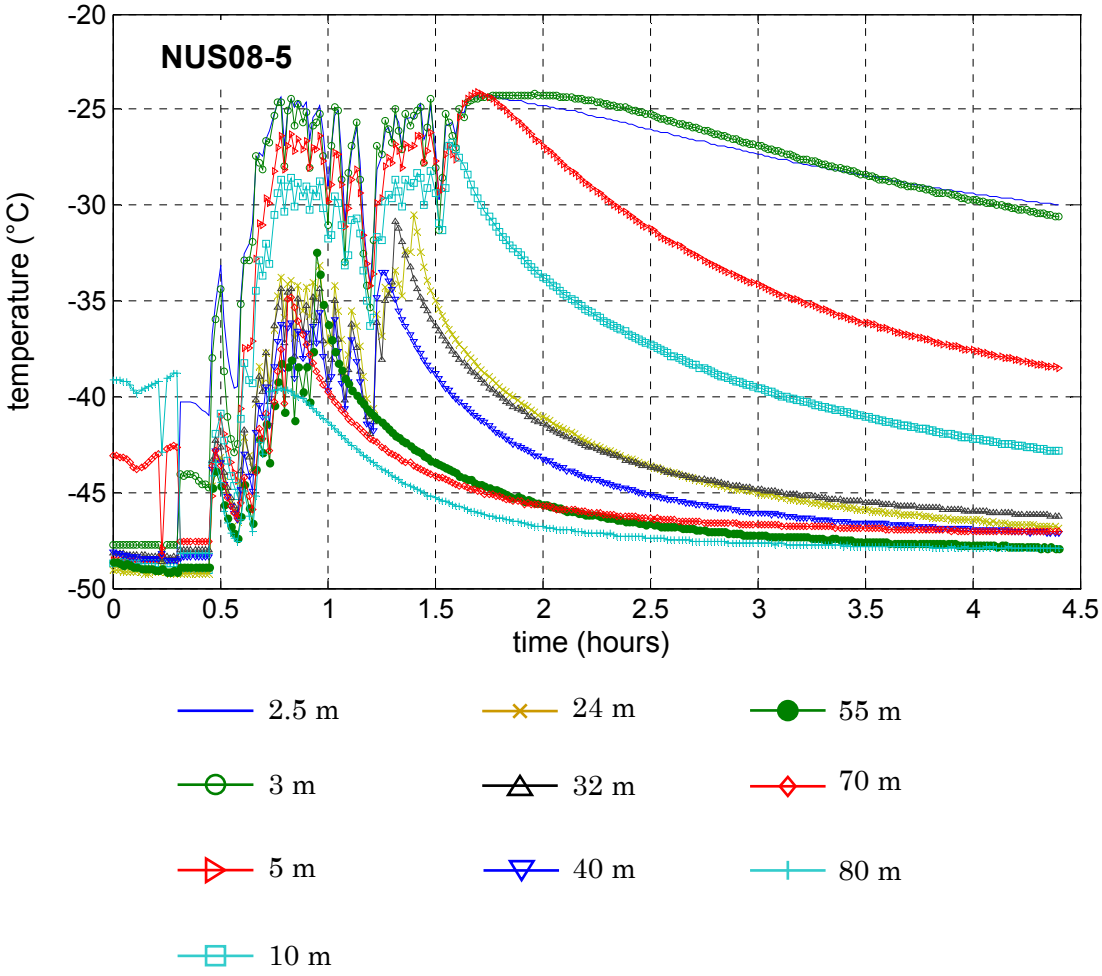

Figure A.4. Temperatures recorded during back-filling of the deep borehole at NUS08-5.

Appendix B

DISCRETIZATION OF PARTIAL DIFFERENTIAL EQUATION

A partial differential equation (4.1), describing the one-dimensional heat diffusion-advection is solved by closely following the discretization method of Patankar (1980). However, Patankar (1980) only presents an unsteady-state solution for heat conduction in one chapter and steady-state solution of a general fluid diffusion-advection in another chapter. This appendix is intended to present the derivation of the discretization equation of an unsteady-state solution of heat diffusion-advection which was arrived by combining materials in Chapters 4 and 5 of Patankar (1980) as well as following many of the practices of Neumann (2003). The discretization equation will be derived for a cluster of grid-points shown in Figure B.1, focusing on the grid point P.

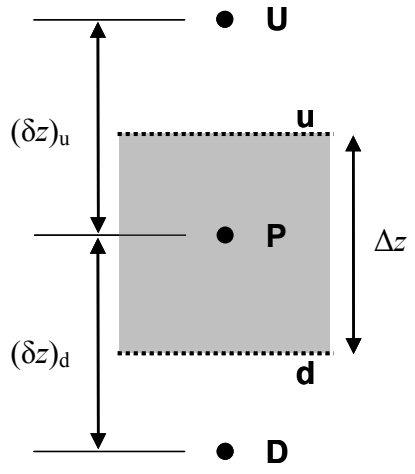

Figure B.1. Representation of the grid-point cluster for deriving the discretization equation. U, P and D are grid points upwards, inside and downwards of the control volume of interest, respectively. u and d are interfaces at the upwards and downwards of the control volume of interest, respectively. $(\delta z)_u$ and $(\delta z)_d$ are distances between grid points U and P, and P and D, respectively. Δz is the size of the control volume surrounding the grid point P. Adapted from Patankar (1980).

It is convenient to start by defining a new term J that describes the total energy flux in the positive z direction,

$$J = K\frac{\partial T}{\partial z} - \rho c w T . \tag{B.1}$$

Using equation (B.1), equation simplifies to,

$$\rho c \frac{\partial T}{\partial t} = \frac{\partial J}{\partial z} . \tag{B.2}$$

The above expression is integrated over the control volume surrounding the grid point P and over the time interval from t to $t + \Delta t$,

$$\rho c \frac{\Delta z}{\Delta t}\left(T_{\mathrm{P}} - T_{\mathrm{P}}{}^{0}\right) = J_{\mathrm{d}} - J_{\mathrm{u}} \tag{B.3}$$

where $T_{\mathrm{P}}{}^{0}$ and T_{P} are the temperature at grid point P at time t ("old" time step) and $t + \Delta t$ ("new" time step), respectively, and J_{d} and J_{u} are total integrated fluxes at interfaces d and u, respectively. Equation (B.3) assumes that T_{P} of the new time step prevails over the time interval Δt. This assumption leads to the fully implicit scheme which is the chosen method of solving the discretization equation.

By employing the fully implicit scheme, right hand side of equation (B.3) can in fact be treated independently as a steady-state diffusion-advection equation since J_{d} and J_{u} depend only on values of T at grid points for a single time step (Neumann, 2003). This means that the right hand side of equation (B.2) can be expressed as,

$$\frac{d}{dz}\left(\rho c w T\right) = \frac{d}{dz}\left(K\frac{\partial T}{\partial z}\right) , \tag{B.4}$$

and the right hand side of equation (B.3) as,

$$J_{\mathrm{d}} - J_{\mathrm{u}} = 0 . \tag{B.5}$$

The exact solution of equation (B.4) for an interface d located between grid points P and D is,

$$\frac{T - T_{\mathrm{P}}}{T_{\mathrm{D}} - T_{\mathrm{P}}} = \frac{\exp\left(P_{\mathrm{d}}\, \mathrm{d} / \left(\delta z\right)_{\mathrm{d}}\right) - 1}{\exp(P_{\mathrm{d}}) - 1} \tag{B.6}$$

where T is the temperature at d and P_{d} is the Peclet number defined by,

$$P_{\mathrm{d}} = \frac{\left(\rho c w\right)_{\mathrm{d}}}{K_{\mathrm{d}} / \left(\delta z\right)_{\mathrm{d}}} . \tag{B.7}$$

The Peclet number is the ratio of the strengths of diffusion and advection (Patankar, 1980). To simplify the above expression for future uses, new symbols F_{d} and D_{d} are defined as follows,

$$F_{\mathrm{d}} = \left(\rho c w\right)_{\mathrm{d}} , \qquad D_{\mathrm{d}} = \frac{K_{\mathrm{d}}}{\left(\delta z\right)_{\mathrm{d}}} . \tag{B.8}$$

Using the exact solution (B.6), an expression for J_{d} can be obtained as,

$$J_{\mathrm{d}} = F_{\mathrm{d}} \left(T_{\mathrm{P}} + \frac{T_{\mathrm{P}} - T_{\mathrm{D}}}{\exp(P_{\mathrm{d}}) - 1} \right). \tag{B.9}$$

Changing subscripts for grid positions in equations (B.6) through (B.8), similar expression for J_{u} can be obtained as,

$$J_{\mathrm{u}} = F_{\mathrm{u}} \left(T_{\mathrm{U}} + \frac{T_{\mathrm{U}} - T_{\mathrm{P}}}{\exp(P_{\mathrm{u}}) - 1} \right). \tag{B.10}$$

Substituting equations (B.9) and (B10) into equation (B.3) leads to a discretization equation that can readily be used and this formulation is called the exponential scheme in Patankar (1980). However, exponentials are expensive to compute hence a scheme that is easier to compute and has the qualitative behavior of the exponential scheme is needed. There are several different schemes presented by Patankar (1980). Now a generalized formulation containing functions that can be substituted to implement different schemes will be derived. To start, a new function J^* is defined, which is a normalized flux (Neumann, 2003),

$$J^* \equiv \frac{J\delta z}{K} = PT - \frac{dT}{d\left(\mathrm{d}/\delta z\right)} \tag{B.11}$$

For a flux at an interface d located between grid points P and D again, the value of T at the interface will be some weighted average of T_P and T_D while the gradient $dT/d(\mathrm{d}/\delta z)$ will be some multiple of $T_\mathrm{D} - T_\mathrm{P}$. Thus, Patankar (1980) expresses J_d^* as,

$$J_\mathrm{d}^* = P\left[\alpha T_\mathrm{P} + (1-\alpha)T_\mathrm{D}\right] - \beta\left(T_\mathrm{D} - T_\mathrm{P}\right), \tag{B.12}$$

where α and β are dimensionless multipliers that depend on P. J_d^* can be simplified to,

$$J_\mathrm{d}^* = BT_\mathrm{P} - AT_\mathrm{D}, \tag{B.13}$$

where A and B are dimensionless coefficients of T for ahead of the interface and behind the interface, respectively, which define how T_P and T_D are weighted by a function of the Peclet number at the interface to determine the flux of T (Neumann, 2003). J_u^* can similarly be deduced as,

$$J_u^* = BT_U - AT_P \,. \tag{B.14}$$

There are useful properties of A and B identified by Patankar (1980):

$$B = A + P \tag{B.15a}$$

$$A(-P) = B(P) \tag{B.15b}$$

$$B(-P) = A(P) \tag{B.15c}$$

$$A(P) = A(|P|) + \max(-P, 0) \tag{B.15d}$$

$$B(P) = A(|P|) + \max(P, 0) \tag{B.15e}$$

where max(X, Y) denote the greater of X and Y. Using the property (B.15a), equations (B.13) and (B.14) can be rewritten as,

$$J_d^* - P_d T_P = A(T_P - T_D), \tag{B.16}$$

$$J_u^* - P_u T_P = B(T_U - T_P). \tag{B.17}$$

Substituting the definition of the Peclet number P from equations (B.7) and (B.8),

$$J_d - F_d T_P = A D_d (T_P - T_D), \tag{B.18}$$

$$J_u - F_u T_P = B D_u (T_U - T_P). \tag{B.19}$$

Above two expressions can be rewritten by again using the definition of the Peclet number and properties (B.15d) and (B.15e),

$$J_d = F_d T_P + \left[D_d A(|P_d|) + \max(-F_d, 0)\right](T_P - T_D), \tag{B.20}$$

$$J_u = F_u T_P + \left[D_u A(|P_u|) + \max(F_u, 0)\right](T_U - T_P). \tag{B.21}$$

These are the final form of J_d and J_u that can be substituted into equation (B.3). Doing so, the final discretization equation is then,

$$\begin{aligned}\rho c \frac{\Delta z}{\Delta t}\left(T_P - T_P{}^0\right) = {} & F_d T_P + \left[D_d A(|P_d|) + \max(-F_d, 0)\right](T_P - T_D) \\ & - F_u T_P + \left[D_u A(|P_u|) + \max(F_u, 0)\right](T_U - T_P).\end{aligned} \tag{B.22}$$

Since equation (B.22) is rather tedious, it is simplified to a form,

$$a_P T_P = a_D T_D + a_U T_U + b, \tag{B.23}$$

where coefficients are defined as,

$$a_D = D_d A(|P_d|) + \max(-F_d, 0), \tag{B.22a}$$

$$a_U = D_u A(|P_u|) + \max(F_u, 0), \tag{B.22b}$$

$$a_P = a_D + a_U + F_D - F_U + b, \tag{B.22c}$$

$$b = a_P{}^0 T_P{}^0, \tag{B.22d}$$

$$a_P{}^0 = \rho c \Delta z / \Delta t. \tag{B.22e}$$

The function $A(|P|)$ is the function that can be modified according to the scheme of choice, presented in Table 5.2 of Patankar (1980). In this research, the power law scheme is used where the function is in a form,

$$A(|P|) = \max\left(0, (1 - 0.1|P|)^5\right). \tag{B.23}$$

Patankar (1980) recommends the use of the power law scheme because of the efficiency in computation and its better ability to approximate the exact form (exponential scheme) than other schemes. It was found that with Matlab®, the software used to perform all computations in this research, exponential scheme was just as efficient as the power law scheme in terms of the computational time required. However, the power law scheme achieved better results in the model verification described in section 4.2.2, yielding smaller RMS errors between analytical and modeled solutions.

For each grid point along the firn-ice column of interest, a discretization equation in a form of (B.23) is derived, leading N equations where N is the number of grid points. By expanding and rearranging equations, they can be organized into a "tri-diagonal" system of equations which can be efficiently solved by Thomas algorithm (see for example Press et al. (2007), for details on solving tri-diagonal system of equations).

The discretization equation derived above is a linear algebraic equation although equation (4.1) is in fact non-linear because of the temperature-dependence of thermal conductivity (see section 4.2.1 for discussion of thermal conductivity). Non-linearity is usually handled by iteration (Patankar, 1980). However, rather than performing iterations, thermal conductivity for the new time step ($t + \Delta t$) is calculated using temperatures of the current time step (t), which is in fact the characteristic of the explicit scheme. This opposes the fully implicit scheme that is used to solve the discretization equation. The approach taken here is justified for the following reasons:

-Thermal conductivity changes only by approximately 0.5% with 1 K change in temperature. Variations of the surface temperature derived by the inverse method are 3 K at most, leading to ~1.5% change in thermal conductivity.

-Time steps (t) employed in the discretization equation are small, 1 year at most). The temperature change at annual time step is 2 K at most. Therefore, errors in thermal

conductivity introduced in one time step is minimal, much smaller than 1%.

-Iterating within each time step would increase the computation time by a tremendous amount, making the Monte Carlo inverse method impossible to be solved in any practical time-frame using available computational resources.

Appendix C

TEMPERATURE MEASUREMENTS AT SHALLOW DEPTHS

In this appendix, time series of temperatures measured down to 10 m, both in the shallow and deep borehole, are presented. The intention of this appendix is to show the expected behavior of temperature variations in the firn i.e. damping of short-term temperature variations with increasing depths. For the inversion of surface temperature history at each study site, which was the primary objective of this dissertation research, temperature measurements from 5 m and deeper were used. Measurements in the shallow borehole were used for the parameterization of the thermal conductivity profile, discussed in Chapter 4.2.1.

For NUS07-2, -5 and -7, the data logger program to obtain measurements from the shallow hole unfortunately contained an error which made the resistance readings less sensitive than intended. As a result, the resolution of measurements at these depths was an order of magnitude lower than sensors in the deep borehole. However, this is considered to have no significant effect in results of this research since only measurements from 5 m and deeper were used in the actual inversion of surface temperature histories. For the parameterization of the thermal conductivity, only measurements from 0.15, 0.65 and 1.5 m depths were used. At those depths, short-term fluctuations (daily to multiple-days) of up to several Kelvins are present. Therefore, it is considered that the effect of the decreased resolution is minimal.

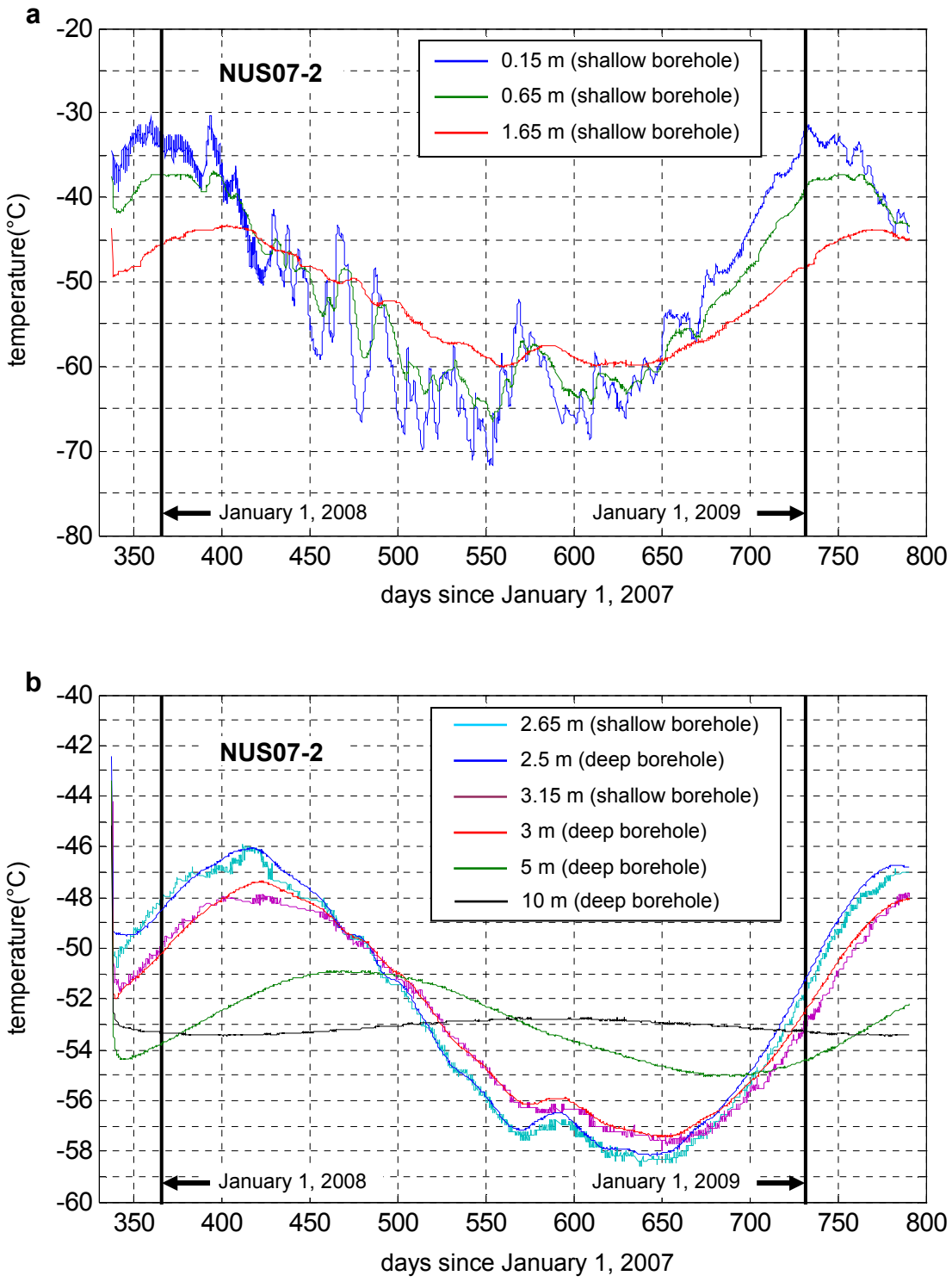

Figure C.1. Time series of temperatures at NUS07-2, **a.** 0.15 to 1.65 m, and **b.** 2.5 to 10 m.

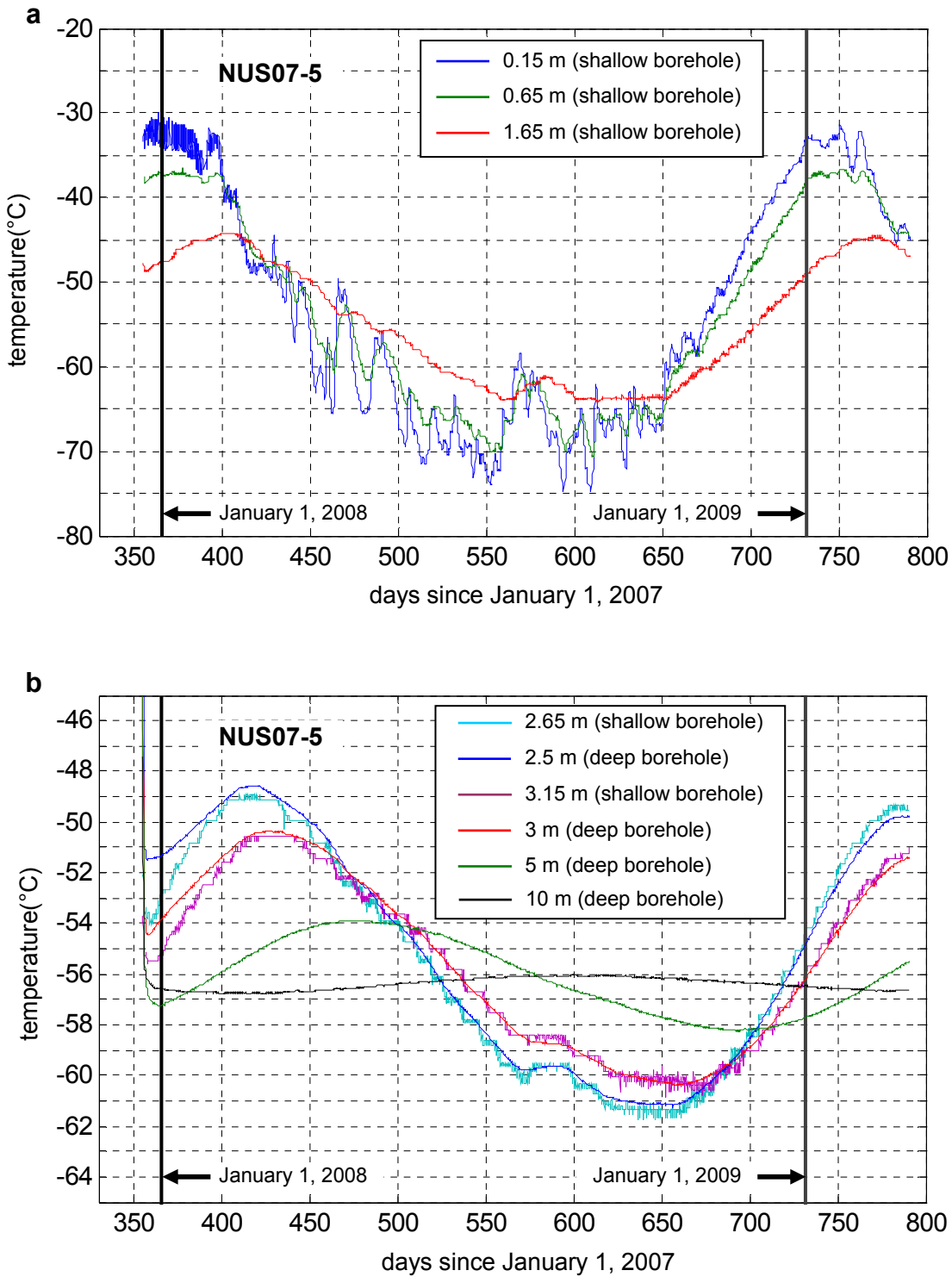

Figure C.2. Time series of temperatures at NUS07-5, **a.** 0.15 to 1.65 m, and **b.** 2.5 to 10 m.

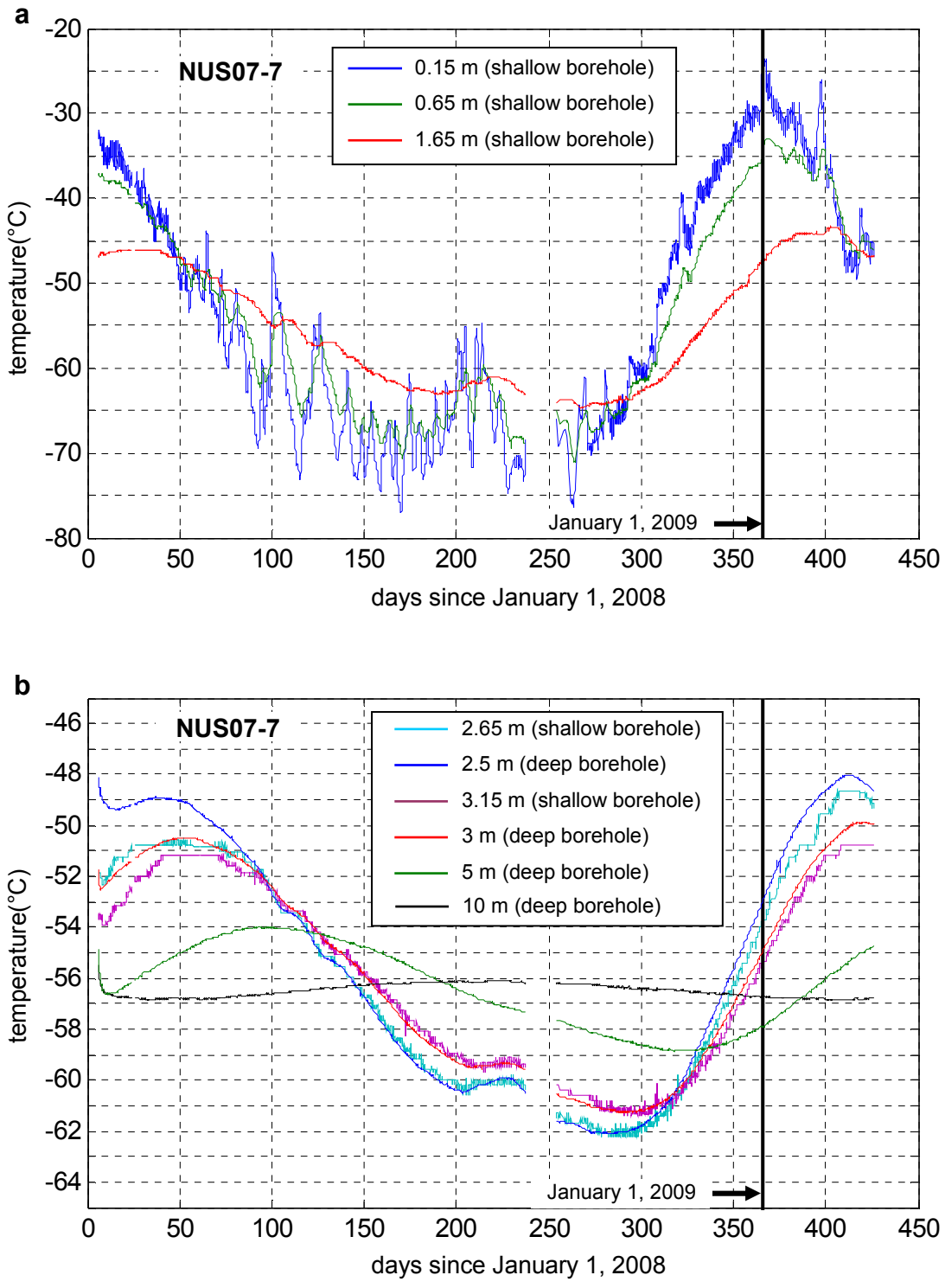

Figure C.3. Time series of temperatures at NUS07-7, **a.** 0.15 to 1.65 m, and **b.** 2.5 to 10 m.

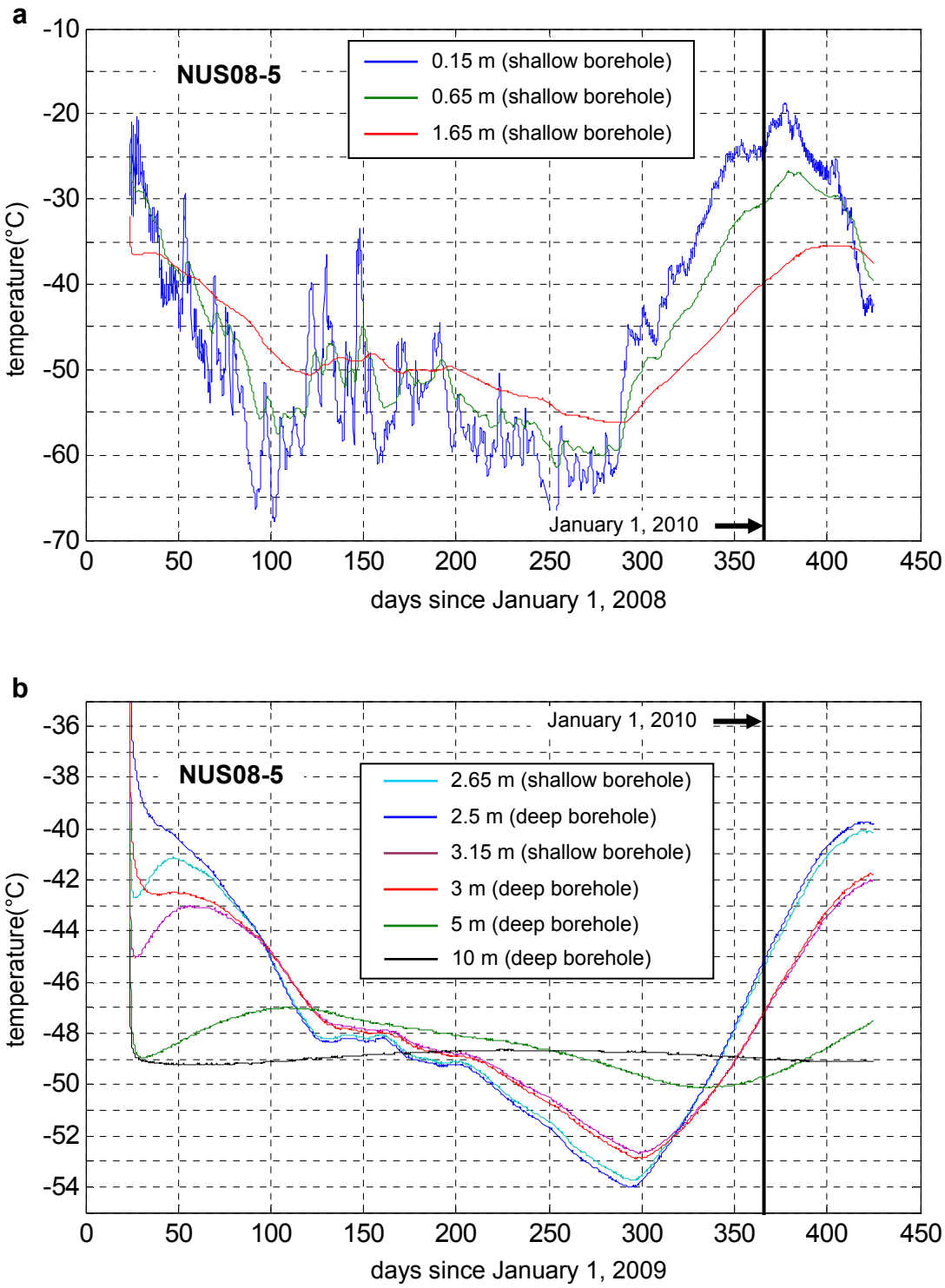

Figure C.4. Time series of temperatures at NUS08-5, **a.** 0.15 to 1.65 m, and **b.** 2.5 to 10 m.

Appendix D

SIMULATION OF TEMPERATURE PROFILES IN THE PAST

In Chapter 6.3, a comparative analysis of the firn temperature profiles measured in the 1965 and those simulated by the inverted surface temperatures was presented. The procedure involved driving the forward model with surface temperature histories derived by both the linearized inversion and the RJ-MCMC methods up to a time when the historical measurement was made. This appendix is intended to demonstrate that such a procedure can provide a meaningful validation on the inverted surface temperature histories by applying the same procedure to the synthetic example used in Chapter 4.

The thick black line in Figure D.1 is the 'true temperature profile' for 1965, obtained by running the forward model with the synthetic true surface temperature history shown in Figure 4.8. Compared to the synthetic data for present (green line), the true temperature profile for 1965 is lower at all depths, by approximately 0.1 K between depths of 40 to 90 m, increasing towards the surface to about 0.3 K at 5 m depth. Blue and red lines in Figure D.1 are simulated temperature profiles for 1965 by running the forward model with the surface temperature histories inverted by the linearized inversion and RJ-MCMC, respectively, which were shown in Figure 4.24. Both of these profiles show systematically lower temperatures than the synthetic data for the present. The profile simulated by the surface temperature history from the linearized inversion shows a close match to the true profile for depths below 30 m. The profile simulated by the surface temperature history from the RJ-MCMC also shows a close match to the true profile for 70 m and below.

Although there are differences between the true and simulated temperature profiles, lower temperatures in 1965 were reasonably simulated by the two inverted surface temperature histories.

Differences are considered to be the result of details in the true surface temperature history being smeared out and the limited resolving power of the data used in the inversion, i.e. the event between ~70 and 30 years b.p. not being captured by inverted histories. Nevertheless, the ability to produce firn temperature profiles close to the true one in the past indicates that the borehole paleothermometry method used in this research can in fact capture the gross surface temperature history of the past several decades and the validation procedure of Chapter 6.3 is a meaningful analysis.

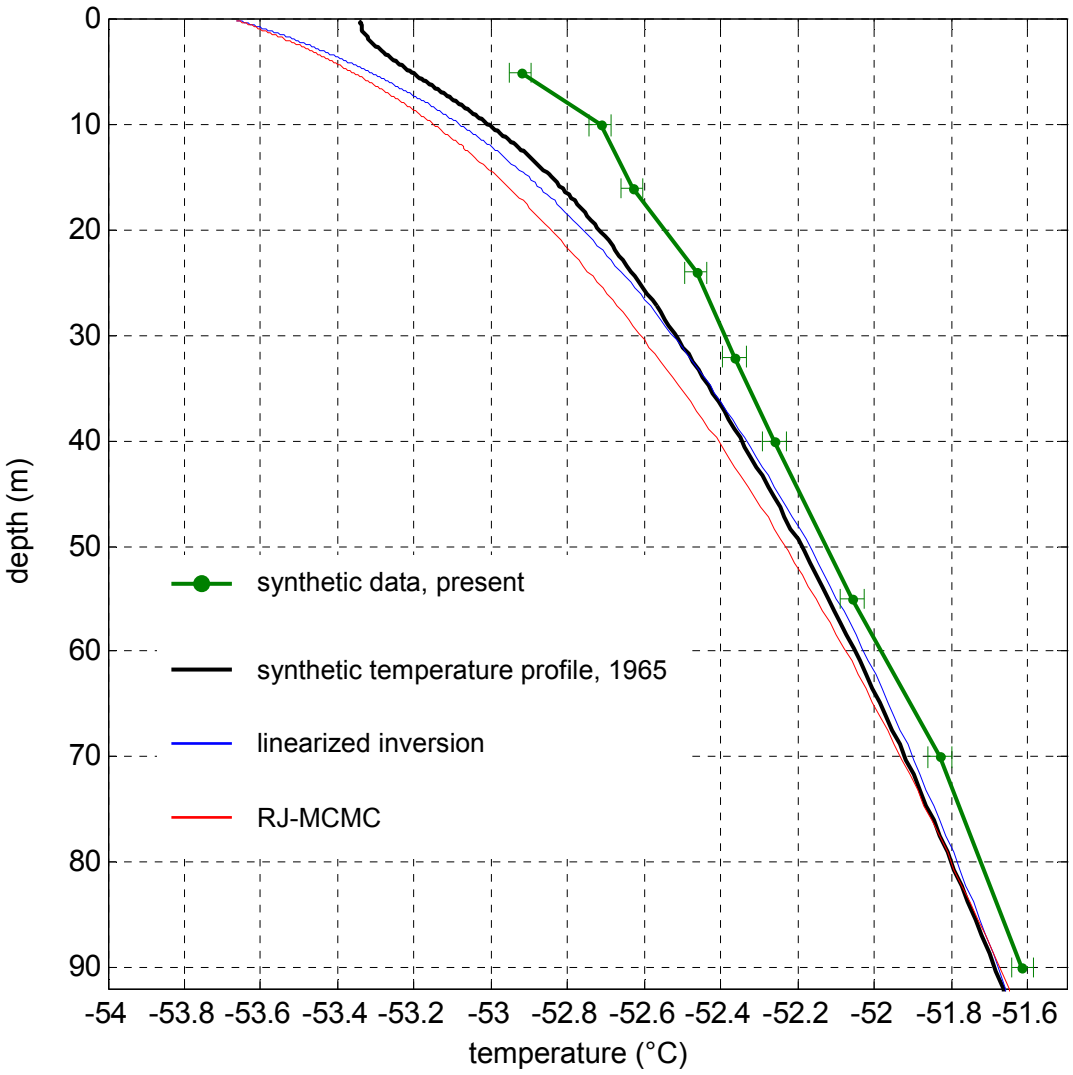

Figure D.1. Synthetic data for present and temperature profiles simulated for 1965. Simulated profiles were obtained by running the forward model with the synthetic surface temperature history shown in Figure 4.8 (thick black), and surface temperature histories inverted by the linearized inversion (blue) and RJ-MCMC (red), shown in Figure 4.24.